Interferometric Gates for All-Optical Signal Processing

vorgelegt von
Diplom-Physiker
Colja Schubert
aus Berlin

von der Fakultät II - Mathematik und Naturwissenschaften
der Technischen Universität Berlin
zur Erlangung des akademischen Grades
Doktor der Naturwissenschaften
Dr. rer. nat.

genehmigte Dissertation

Promotionsausschuss :

Vorsitzender: Prof. Dr. rer. nat. Gebhard von Oppen
Berichter: Prof. Dr.-Ing. Hans Joachim Eichler
Berichter: Prof. Dr. rer. nat. Hans-Georg Weber

Tag der wissenschaftlichen Aussprache: 26. April 2004

Berlin 2004
D 83

Abstract

This work investigates all-optical interferometric gates based on Semiconductor Optical Amplifiers (SOA) for all-optical signal processing. The objective is to realize gates for applications in high bit rate transmission systems (160 Gbit/s and above) based on optical time division multiplexing (OTDM). In OTDM systems, a high TDM bit rate of 160 Gbit/s is realized on a single wavelength by bit-interleaving a number of optical signals with a lower bit rate (base data rate). The gating times needed in 160 Gbit/s OTDM systems are on the order of ps, which cannot be realized with electrical gates. Over the last three years, the base data rate in OTDM systems has increased from 10 to 40 Gbit/s. The influence of the higher base data rate on SOA based interferometric gates is addressed in detail within this work.

Interferometric gates consist of a nonlinear medium, in this case an SOA, incorporated in an interferometer setup. The switching effect is based on cross-phase modulation (XPM) in the nonlinear medium. Thus the response of the SOA refractive index upon saturation by a strong optical pulse and the associated phase shift (phase dynamics) is of major importance. The phase dynamics of SOAs, operated in conventional and gain-transparent (GT) mode, are measured in this work under different operation conditions. Based on the results, the SOAs are compared with respect to interferometric switching and the optimum operation parameters are derived.

Subsequently, interferometric SOA gates based on three different interferometer setups, namely the Semiconductor Laser Amplifier in a LOop Mirror (SLALOM), the Mach-Zehnder Interferometer (MZI) and the Ultrafast-Nonlinear Interferometer (UNI) are realized using GT-SOAs. The gates are characterized by switching window measurements. The switching windows are evaluated using different criteria, such as the switching window width and the on-off contrast ratio to compare the gates with respect to their application in OTDM systems. Switching window widths of 3 to 4 ps and on-off contrast ratios above 25 dB ($\approx$ 316:1) are achieved.

Finally, the most promising gates are tested in OTDM system experiments as demultiplexer, add-drop multiplexer and sampling gate, at TDM bit rates up to 160 Gbit/s and base data rates of 10 Gbit/s and 40 Gbit/s. Error-free operation of a GT-UNI gate as 160 Gbit/s demultiplexer at 10 and 40 Gbit/s base data rate is demonstrated in the laboratory as well as in a field experiment. Using a GT-UNI with a modified configuration, add-drop multiplexing at 160 Gbit/s is achieved for the first time with an SOA based gate.

Zusammenfassung

Die vorliegende Arbeit untersucht rein-optische Interferometerschalter basierend auf Halbleiterlaserverstärkern (SOA) bezüglich ihrer Anwendung in der optischen Signalverarbeitung. Das Ziel ist die Entwicklung von Schaltern für Anwendungen in hochbitratigen Übertragungssystemen ($\geq$160 Gbit/s) basierend auf optischer Zeitmultiplextechnik (optical time division multiplexing - OTDM). In OTDM-Systemen werden hohe Übertragungsdatenraten von 160 Gbit/s auf einer einzigen Wellenlänge durch zeitliches Verschachteln optischer Signale niedrigerer Datenrate (Basisdatenrate) erreicht. In solchen 160 Gbit/s OTDM-Systemen werden Schaltzeiten in der Größenordnung weniger Pikosekunden benötigt, die mit elektrischen Schaltkonzepten nicht erreichbar sind. Im Laufe der letzten drei Jahre ist die Basisdatenrate in OTDM-Systemen von 10 auf 40 Gbit/s angestiegen. Deshalb wird insbesondere der Einfluß einer erhöhten Basisdatenrate auf das Schaltverhalten von SOA-basierten Interferometerschaltern im Detail betrachtet.

Interferometerschalter bestehen aus einem nichtlinearen Medium, in diesem Fall einem SOA, eingefügt in ein Interferometer. Der Schalteffekt beruht auf Kreuzphasenmodulation im nichtlinearen Medium. Deshalb ist die Brechungsindexänderung im SOA durch starke optische Steuerpulse und die damit verbundene Phasenänderung für ein optisches Signal (Phasendynamik) von besonderer Bedeutung. Im Rahmen dieser Arbeit wurde die Phasendynamik von konventionell und Gewinn-Transparent (GT) betriebenen SOAs unter verschiedenen Operationsbedingungen untersucht. Basierend auf diesen Messungen wurden die SOAs im Hinblick auf ihren Einsatz in Interferometerschaltern verglichen und die optimalen Betriebsparameter bestimmt.

Im folgenden wurden drei Interferometerschalter mit GT-SOAs als nichtlinearem Medium und unterschiedlichen Konfigurationen – Semiconductor Laser Amplifier in a LOop Mirror (SLALOM), Mach-Zehnder Interferometer (MZI), Ultrafast-Nonlinear Interferometer (UNI) – realisiert. Zur Charakterisierung der Schalter und einem Vergleich bezüglich der Anwendung in OTDM-Systemen, wurden Schaltfenster gemessen und mittels verschiedener Kriterien, z.B. der Schaltfensterbreite und des Schaltkontrastes, ausgewertet. Schaltfensterbreiten von $3-4$ ps und Schaltkontraste über 25 dB ($\approx$ 316:1) wurden erreicht.

Abschließend wurden die besten Schalter für Anwendungen als Demultiplexer, Add-Drop Multiplexer und zum Abtasten hochbitratiger Datensignale in 160 Gbit/s OTDM-Sytemen mit 10 und 40 Gbit/s Basisdatenrate getestet. Fehlerfreies Demultiplexen von 160 Gbit/s auf die Basisdatenraten 10 und 40 Gbit/s mit einem GT-UNI Schalter konnte sowohl im Labor als auch in einem Feldexperiment demonstriert werden. Mit einem GT-UNI in einer modifizierten Konfiguration konnte zum ersten Mal Add-Drop Multiplexen bei 160 Gbit/s mit einem SOA-basierten Schalter gezeigt werden.

Contents

Chapter 1

Introduction

The use of light for transmission in telecommunication has become ubiquitous. Todays networks typically consist of network nodes, built of electronic boxes (switches and routers) interconnected by optical pipes (point-to-point optical transmission systems). Each pipe can provide a large capacity (several terabit per second) by using wavelength division multiplexing (WDM) to carry many optical channels simultaneously on the same fiber. The bottlenecks are still the network nodes, where signal processing is performed in the electrical domain. All-optical signal processing for application in telecommunication networks has been studied extensively over the last decade, because signal processing in the optical domain offers a number of advantages. Using optical processing makes opto-electrical/electro-optical conversion in the network nodes unnecessary, which can potentially be more cost-effective. Moreover, the bandwidth of the signal can be significantly larger, compared to electrical processing, because the optical signal processor can work at higher bit rates. This enables optical transmission systems where the bit rates in a single wavelength channel can exceed the bandwidth of presently available electronics (40 Gbit/s). Such high bit rates (160 Gbit/s and above) are achieved by bit-interleaving a number of lower bit rate optical data channels to a high bit rate data signal. This technique is called optical time division multiplexing (OTDM) [1]. OTDM can be used in conjunction with WDM to form high-capacity all-optical core networks [2]. In this work, all-optical interferometric gates based on semiconductor optical amplifiers are investigated as optical signal processors. Applications of such gates in optical transmission systems using OTDM are discussed in detail.

1.1 All-Optical Switching in OTDM Systems

The typical setup of an **Optical Time Division Multiplexing** system is shown schematically in Fig. 1.1 [3, 4]. An optical pulse source generates a pulse train with a repetition frequency that corresponds to the so called base data rate (e.g. 40 GHz). The generated optical pulse train is coupled into four optical branches. The pulse train in each branch is then intensity modulated and the four modulated pulse trains (the base rate channels, 40 Gbit/s) are bit-interleaved in a passive multiplexer (MUX) to form a high bit rate optical data stream (160 Gbit/s, called TDM bit rate). To avoid interference effects between neighboring base rate channels, the pulse width has to be significantly shorter than the bit period in the multiplexed data stream (a full width half maximum

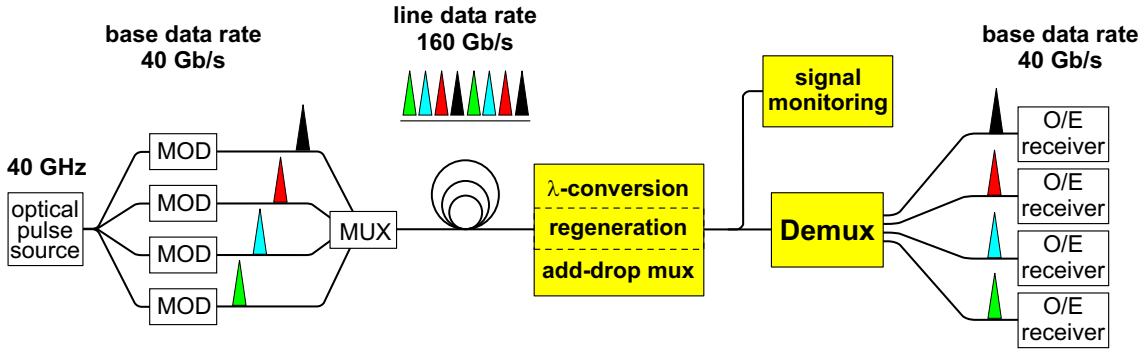

Figure 1.1: Typical setup of an OTDM transmission system with 40 Gbit/s base data rate and a TDM bit rate of 160 Gbit/s.

(FWHM) of about one fourth of the bit period, which means $\leq$ 1.8 ps at 160 Gbit/s, is normally sufficient [5]). After the multiplexer the data stream can no longer be handled by opto-electronic receivers and electrical signal processors. Operations like signal regeneration, wavelength conversion, add-drop multiplexing and signal monitoring have to be performed in the optical domain. This includes also demultiplexing (DEMUX), which is needed at the end of an OTDM transmission line to separate the bit-interleaved channels for further electrical signal processing. All these operations can be realized by all-optical gates. The base data rate is normally chosen to match the highest bit rate that can be handled by the opto-electronic receivers. In this work all-optical gates for systems with 10 Gbit/s and 40 Gbit/s base data rate are investigated. The TDM bit rate in an OTDM system is limited by the width of the optical pulses. The pulse sources available for this work [6] generate pulses with about 1.3 ps width (FWHM). This allows TDM bit rates of up to 160 Gbit/s (single polarization) without significant interference effects between neighboring pulses.

Typically an all-optical gate performs an **AND** operation between an optical signal controlling the gate (control port) and a second optical signal propagating through the gate (data port). Figs. 1.2 to 1.6 illustrate how all-optical gates can be used to realize the operations needed in an OTDM system.

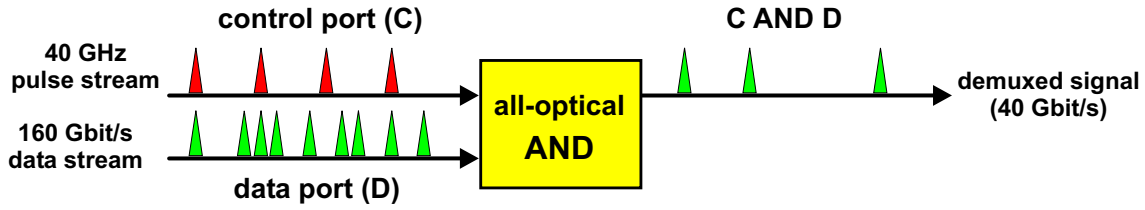

Figure 1.2: All-optical AND gate operated as demultiplexer.

For **demultiplexing** (Fig. 1.2), one of the bit-interleaved base rate channels has to be extracted from the high bit rate data stream. This is achieved by using a periodic pulse train at the base data rate in the control port of the gate and inserting the data signal into

the data port. At the output, the so called demultiplexed signal, which is one of the base rate channels, leaves the gate. The gating window has to be broad enough to extract one complete pulse, but small enough to suppress the pulses from all other channels. Which channel is demultiplexed can be chosen by changing the temporal position of the control pulses with respect to the data signal. Different from the demultiplexer shown in Fig. 1.1, this configuration can only extract one base rate channel at a time. In a complete system, the data signal is split into four branches and one demultiplexer is needed in each branch.

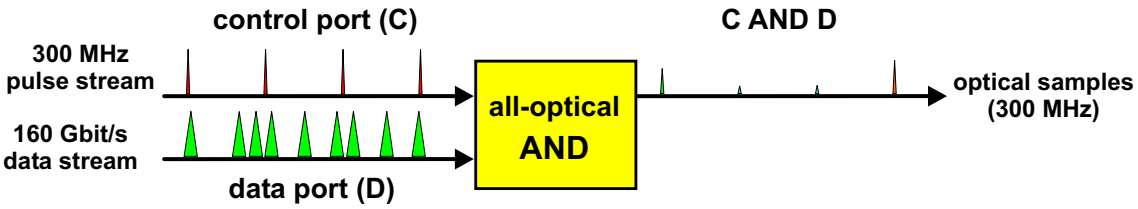

Figure 1.3: All-optical AND gate operated as sampling gate.

For **signal monitoring** (Fig. 1.3) an image of the data signal has to be generated at the full TDM bit rate (e.g. 160 Gbit/s) [7]. This is achieved by an optical sampling technique, where the gate is used to extract optical samples from the data stream. In this case, the gate is controlled by a pulse train, of which the repetition rate (the so called sampling rate) is on the order of a few hundred MHz. The repetition rate is limited by the analogue-to-digital conversion, which is needed to further process the generated samples. The sampling rate is not an exact multiple of the TDM bit rate, so that the sampling pulses scan periodically through the data signal. Here the gating window has to be as small as possible to achieve a high temporal resolution of the sampling system [8].

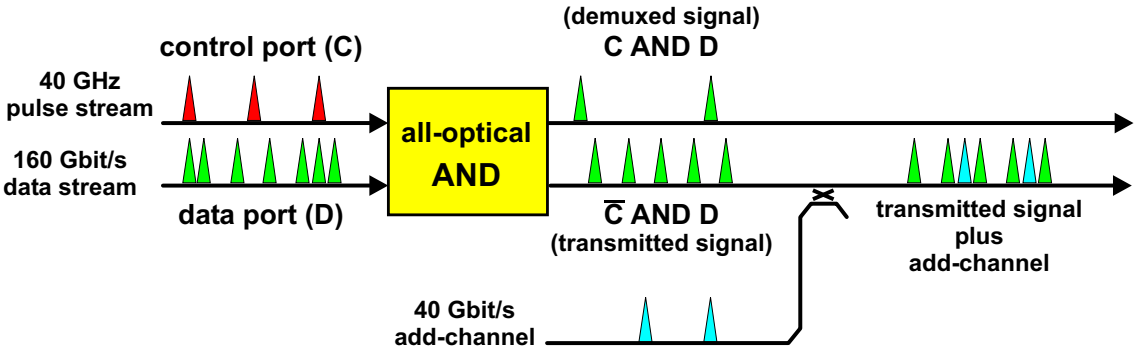

Figure 1.4: All-optical AND gate operated as add-drop multiplexer.

In **add-drop multiplexing** (Fig. 1.4), one channel is extracted at the base data rate, like in demultiplexing and replaced by a new channel (add-channel). To realize this operation, the so called transmitted signal is needed in addition to the demultiplexed signal. The transmitted signal is complementary to the demultiplexed signal and contains the bit-interleaved data stream with empty time slots at the position of the extracted

channel. The new channel can then be inserted passively into the emptied time slots in the transmitted signal. The interferometric gates discussed in this work provide the required demultiplexed and transmitted signal at their outputs (see Fig. 1.7).

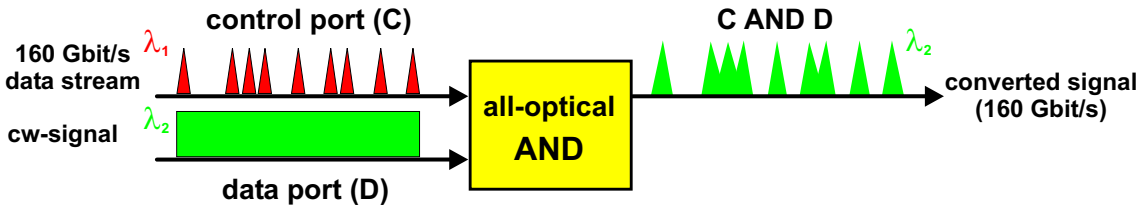

Figure 1.5: All-optical AND gate operated as wavelength converter.

In **wavelength conversion** (Fig. 1.5), a data signal with a specific wavelength λ_1 is converted to another wavelength λ_2 at the full TDM bit rate. For this operation the all-optical AND gate is operated with the data pulse stream in the control port. For the data port, a cw signal with wavelength λ_2 is used. At the output, the wavelength converted data signal leaves the gate, with a shape and temporal position as given by the data signal in the control port of the gate.

The configuration described for wavelength conversion can also be used for **signal regeneration** (Fig. 1.6). A periodic pulse train (clock signal) with a repetition frequency corresponding to the full TDM bit rate has to be used instead of the cw signal. The regeneration relies on the fact that in this configuration the shape of the wavelength converted signal is mainly determined by the undistorted clock signal in the data port. This is of course only true, if a gating window with a square like shape is realized.

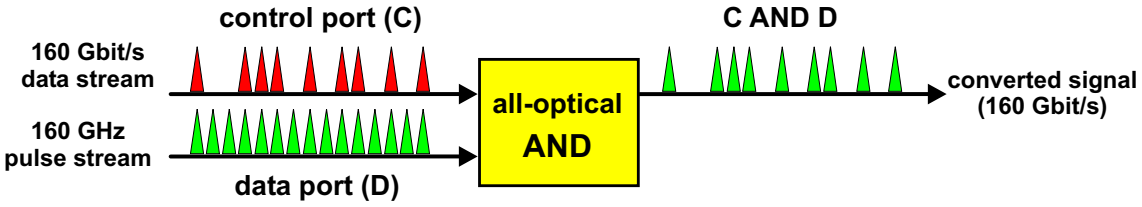

Figure 1.6: All-optical AND gate operated as signal regenerator.

The control and the data signal have to be synchronized for most signal processing functions mentioned above. The recovery of the base rate clock signal from the data signal at the full TDM bit rate is a complex task and beyond the scope of this work. Clock recovery up to 160 Gbit/s has been realized using phase locked loops based on all-optical switches [9, 10] and electro-absorption modulators [11, 12, 13]. A number of high bit rate transmission experiments with such clock recoveries have been performed [12, 13, 14, 15]. Instead of recovering the base rate clock from the full TDM bit rate, it is sometimes possible to transmit the base rate clock on a separate wavelength channel.

1.2 Operation Principle of All-Optical Gates

The operation principle of an **all-optical gate** is based on the alteration of the transmission properties of a nonlinear medium by optical control pulses. In principle, every medium showing an optical nonlinearity can be used in an all-optical gate. A high nonlinear coefficient and a fast response time of the nonlinear effect are generally important. Particularly the response time has to be sufficiently fast to enable short gating times (on the order of a few picoseconds). Polarization independence and a large optical bandwidth are also desirable properties.

Especially two nonlinear media are widely used for all-optical gates in applications for telecommunication, the semiconductor optical amplifier (SOA) [16, 17, 18, 19] and a special type of silica fiber with enhanced nonlinearity, so called highly nonlinear fiber (HNLF) [20]. The nonlinear properties of these media can differ significantly, since the interaction of an optical wave with the medium can either be resonant or non-resonant, depending on the energy levels (transition frequencies) of the medium and the frequency of the optical wave. In silica fiber, where the transition frequencies of the medium are far away from the optical frequencies used in telecommunication (around 1.3 µm and 1.5 µm), the interaction with the data signal is non-resonant and the nonlinearities are also called non-resonant. In general non-resonant nonlinearities have a very fast response time on the order of a few femtoseconds, but the nonlinear coefficient is comparably small. High optical powers (several watt peak power) or a long interaction length (several hundred meter) are needed to achieve reasonable nonlinear effects. In contrast, the SOA requires far lower powers (below one watt) using a very short interaction length (SOA chip length is typically a few hundred micrometer). This is due to the resonant nature of the SOA nonlinearity, which leads to an effective nonlinear coefficient about eight orders of magnitude higher as compared to ordinary fiber [21]. The disadvantage of the SOA as nonlinear medium is however, that most nonlinear effects are associated with the dynamics of the carrier density. As a result, the response time is limited by the recovery time of the carrier density in the SOA (carrier density dynamics), which is typically a few hundred picoseconds.

Two different types of nonlinear effects can be used to realize all-optical gates. The first type includes nonlinear effects in which new frequency components are generated by the data and control signal inside the medium (e.g. four-wave mixing (FWM) or second-harmonic generation (SHG)). The second type includes nonlinear effects in which the phase or amplitude of the data signal propagating through the medium is altered by changes of the nonlinear refractive index or gain, induced by optical control signals (e.g. cross-phase modulation (XPM), cross-amplitude modulation (XAM), cross-gain modulation (XGM)). This work will concentrate on so called interferometric gates, with SOAs as nonlinear media. Interferometric gates use the phase shift in the data signal induced by a nonlinear refractive index change (XPM), which belongs to the second type of nonlinear effects.

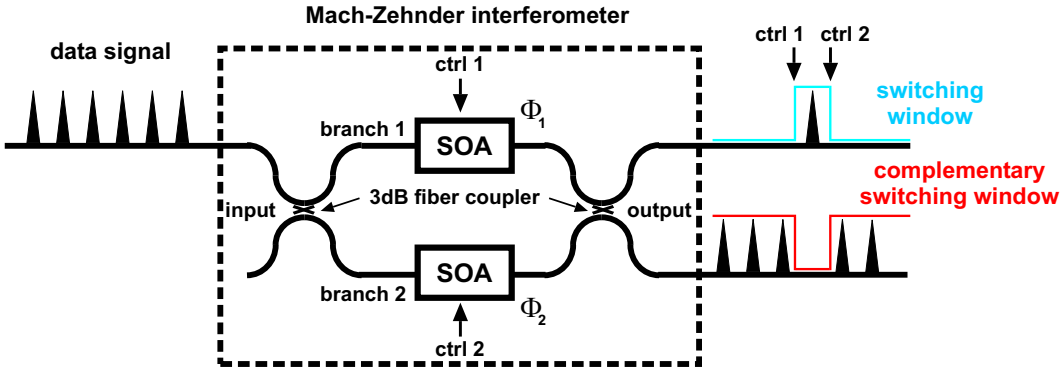

Figure 1.7: Schematic depiction of an all-optical Mach-Zehnder Interferometer switch based on SOAs as nonlinear medium.

Mach-Zehnder Interferometer Switch: An example of an interferometric gate is shown schematically in Fig. 1.7. It consists of a nonlinear medium (in this case SOAs) incorporated in an interferometer setup (in this case a Mach-Zehnder Interferometer). The operation principle is as follows: The optical data signal is split at the input fiber coupler into two signal components with equal amplitudes (3 dB $\cong$ 50 %). The signal components travel through different interferometer branches (branch 1 and branch 2) and interfere at the output fiber coupler. Depending on the phase difference $\Phi_1 - \Phi_2$ between both signal components, the interference can be constructive or destructive. We assume that the phase difference is such, that the interference is destructive in the upper output and therefore constructive in the lower output. As a result the data signal will leave the gate through the lower output. If a control signal (ctrl 1) is inserted into the SOA in branch 1, a nonlinear refractive index change occurs and the phase Φ_1 of the data signal component travelling through the upper interferometer branch will change. In the ideal case of a π phase shift, the interference at the output coupler will then be constructive in the upper output and destructive in the lower output. This means that the data signal is switched from the lower to the upper output. By inserting a second control pulse (ctrl 2) into the SOA in branch 2, inducing the same refractive index change, the interferometer is balanced again and the data signal is switched back to the lower output. The change of the transmission to the output ports, also depicted in Fig. 1.7, are called switching window and complementary switching window. For most applications only one output is used, except for add-drop multiplexing, where also the complementary switching window is needed (see Fig. 1.4).

Compared to non-interferometric gates, especially those based on cross gain modulation, the interferometric switch offers two main advantages. First, the transmittance of the interferometer can be completely changed from 1 to 0, which enables very high on-off ratios. Second, the interferometer is only sensitive to differences between the phase of the interferometer branches. This is used to realize a differential switching scheme, which enables narrow switching windows in interferometric switches with SOAs as nonlinear media. In the following, the different switching schemes are discussed.

Switching Schemes: In the switching scheme explained above, a phase shift was induced in both interferometer branches. This is called differential switching scheme. In principle, it is sufficient to use a phase shift in only one branch, the non-differential switching

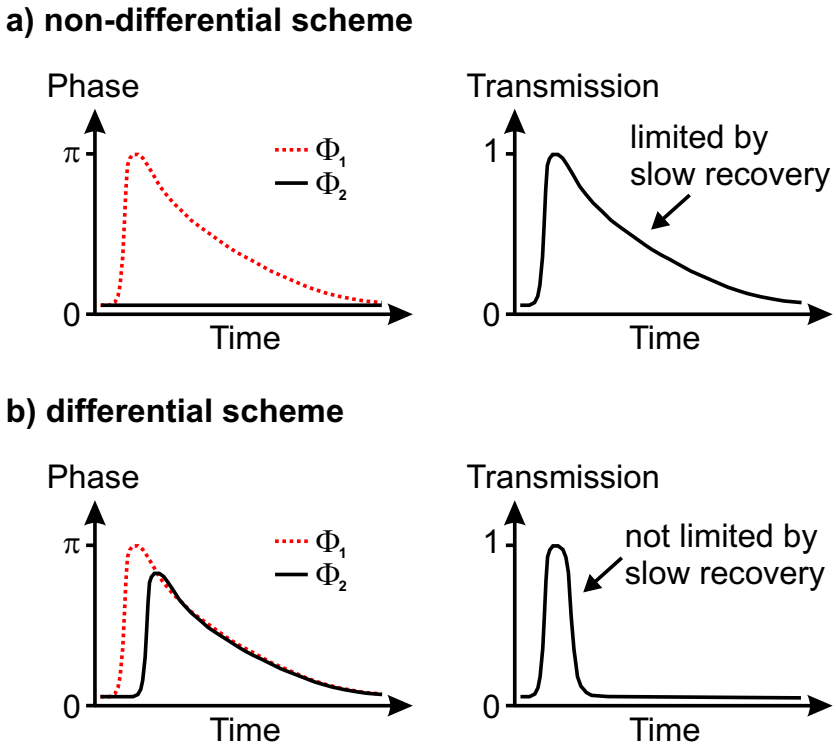

Figure 1.8: Schematic depiction of the phase change and the corresponding transmission through an interferometric switch based on SOAs operated in a) non-differential scheme and b) differential scheme. Φ_1 and Φ_2 are the induced phase changes for the separated data signal components.

scheme. But the width of the switching windows will then be limited by the time needed for the refractive index to reach its initial value again (recovery time). This is illustrated in Fig. 1.8 for an SOA based switch. The phase change, induced in the SOA by the nonlinear refractive index change, is followed by a slow recovery. The origin of this slow recovery will be discussed in section 3. In the non-differential scheme (Fig 1.8 a)), the phase change is induced for one of the two data components (Φ_1), while the phase of the other component remains unchanged (Φ_2). This results in a broad switching window, limited by the slow recovery. In the differential scheme (Fig 1.8 b)), both data components experience the phase change, but at slightly different times. As the transmission through the interferometer depends on the phase difference, this results in a narrow switching window, which is no longer limited by the slow recovery. The width of the switching window is given by the temporal delay between both phase curves. However, the recovery time is still important if we increase the frequency of the control pulses. In this case, the time for the carrier density in the SOA to reach its initial value is reduced, which leads to a lower maximum phase change (see 3.2.2).

The interferometric switch discussed above was based on SOAs. Highly nonlinear fibers are used as nonlinear medium in interferometric switches, very similar to SOAs. If theses two nonlinear media are compared regarding applications for fast optical switching, the following differences are obvious:

- Due to the non-resonant nature of the fiber nonlinearity, the response time in fibers

is fast, compared to SOAs and not limited by a slow recovery process. This makes a differential switching scheme unnecessary to achieve narrow switching windows.

- The effective nonlinearity in fibers is eight orders of magnitude lower compared to SOAs. This means that a long interaction length (several hundred meter) is needed to achieve sufficient cross-phase modulation.
- The cross-phase modulation in fibers depends on the state of polarization of the two light signals.
- The induced phase shift is independent of the repetition frequency of the control pulses.

1.3 Present State of the Art of Interferometric Gates

In this section, the present state of the art of interferometric gates and the contributions of this work are discussed. Interferometric gates based on SOAs and HNLF have been realized for a number of applications in OTDM systems with high TDM bit rates. They are summarized in Table 1.1. For different interferometric and non-interferometric switching configurations, the table lists the highest data rate achieved in the applications so far and the nonlinear effect that was used. The abbreviations are explained in Appendix B.

Demultiplexer: The highest TDM bit rate achieved in demultiplexing a single polarization data signal is 640 Gbit/s with the Nonlinear Optical Loop Mirror (NOLM), a fiber based interferometric gate. Gates based on SOAs were used at 160 Gbit/s and 336 Gbit/s. In addition to configurations with hybrid fiber-chip setups (GT-UNI, GT-MZI, SLALOM), SOA based gates were also realized as monolithically integrated devices (InP integrated MZI) or integrated in a silica waveguide structure (hybrid integrated MZI). For completeness, Table 1.1 also lists so called electro-optical gates, based on electro-absorption modulators (EAM). Details about EAMs in general may be found in [22, 23]. In these non-interferometric switches, an electrical control signal changes the absorption coefficient of an EAM to gate the data signal. Demultiplexing of up to 160 Gbit/s data signals has been shown with such devices. Even 320 Gbit/s were achieved using an EAM with integrated photo diode (PD-EAM), where the control signal was optical instead of electrical.

Sampling Gate: The sampling gate offering the highest temporal resolution was based on second-harmonic generation (SHG) in periodically poled $LiNbO_3$. This gate enabled eye diagram measurements of a 640 Gbit/s data signal. Sampling gates based on SOAs were used for monitoring data signals up to 320 Gbit/s.

Add-Drop Multiplexer: The data rate limit for add-drop multiplexing is 160 Gbit/s so far, realized with hybrid setups based on SOAs or HNLF. Add-drop multiplexing with monolithically integrated SOA gates has been shown up to 80 Gbit/s.

Wavelength Converter and 3R-Regenerator: Also in wavelength conversion and 3R-regeneration the highest data rate achieved was 160 Gbit/s. The 160 Gbit/s wavelength converter was based on SOAs (polarization discriminating Mach-Zehnder Interferometer, PD-MZI), while the 160 Gbit/s 3R-regenerator was fiber based (Kerr-Switch). Note that 3R-regeneration with interferometric gates, such as the two configurations listed under 3R-regenerator in Table 1.1, involves a wavelength conversion (see Fig. 1.6).

The contribution of this work to the present state of the art of interferometric gates is indicated in Table 1.1 by an asterisk ($*$). The objective of this work was to investigate

Effect	Medium	Configuration	Result	Year	Ref.
Demultiplexer					
XPM	SOA	hybrid integrated MZI	336 to 10.5 Gbit/s	2002	[24]
XPM	SOA	GT-UNI*	160 to 10/40 Gbit/s	2001	[25, 26]
XPM	SOA	GT-MZI*	160 to 10 Gbit/s	2000	[27]
XPM	SOA	InP integrated MZI	160 to 10 Gbit/s	2001	[28, 29]
XPM	SOA	SLALOM	160 to 10 Gbit/s	1994	[30, 31]
FWM	SOA	single pass	160 to 10/40 Gbit/s	2002	[32, 33, 34]
XPM	HNLF	NOLM	640 to 10 Gbit/s	2000	[35]
XAM	EAM	single pass	160 to 40 Gbit/s	2002	[36]
XAM	EAM	double pass	160 to 40 Gbit/s	2003	[37]
XAM	EAM	PD-EAM	320 to 10 Gbit/s	2003	[38]
Sampling Gate					
XPM	SOA	GT-UNI*	160/320 Gbit/s	2002	[39, 40]
XPM	HNLF	NOLM	160 Gbit/s	2002	[41]
FWM	SOA	single pass	160 Gbit/s	2001	[42]
SHG	$ppLiNbO_3$	single pass	640 Gbit/s	2003	[43]
Add-Drop Multiplexer					
XPM	SOA	GT-UNI*	160 to 10 Gbit/s	2003	[44]
XPM	SOA	InP integrated MZI	80 to 10 Gbit/s	2000	[45]
FWM	HNLF	single pass	160 to 10 Gbit/s	2002	[46]
Wavelength Converter					
XPM	SOA	DIC	100 Gbit/s	2000	[47]
XPM	SOA	PD-MZI	168 Gbit/s	2000	[48]
3R-Regenerator					
XPM	SOA	PD-MZI	84 Gbit/s	2000	[48, 49]
XPM	HNLF	Kerr-Switch*	160 Gbit/s	2002	[50, 51]

Table 1.1: Summary of signal processing functions realized using optical gates. The abbreviations are explained in Appendix B.

interferometric gates based on SOAs for the applications listed in Table 1.1 at a TDM bit rate of 160 Gbit/s and an increased base data rate of 40 Gbit/s. For all applications, interferometric gates were realized in this work in hybrid fiber-chip setups. For the demultiplexer, sampling gate and add-drop multiplexer, SOAs were used as nonlinear medium. In the case of wavelength conversion and 3R-regeneration, the SOA based gates were inapplicable and a fiber based solution, the Kerr-Switch, was chosen. Error-free performance

at 160 Gbit/s was demonstrated for all applications, in the case of add-drop multiplexing and 3R-regeneration for the first time.

1.4 Objective and Outline of this Work

Objective: As was mentioned in the previous section, the objective of this work is to investigate interferometric gates based on SOAs. The focus is on their application for all-optical signal processing, in particular in OTDM systems at a TDM bit rate of 160 Gbit/s. In detail, the investigations include:

- Direct measurements of the phase dynamics in different types of SOAs under various operation conditions. The aim is to find the optimum operation parameters for the use of SOAs in interferometric gates.
- Comparison of interferometric gates based on SOAs in different configurations, with respect to applications in OTDM systems. This will be done using switching window measurements.
- Test of the interferometric gates in an OTDM system for applications like demultiplexing, add-drop multiplexing and in a sampling system up to a TDM bit rate of 160 Gbit/s. The gates are tested in back-to-back configurations (without transmission over a fiber span) and in transmission experiments.

Over the past three years, the base data rate in OTDM systems has increased from 10 Gbit/s to 40 Gbit/s. For applications like demultiplexing, a higher base data rate means a higher repetition rate of the control signal. In the SOA, the response time is limited by the slow carrier density dynamics, so that the higher control pulse rate can have a severe influence on interferometric gates based on SOAs. Therefore the effect of a higher control pulse rate of 40 GHz is of major importance in all the investigations listed above.

Outline: The theoretical background on interferometric switching is provided in **Chapter 2**. In the first part, the basic nonlinear properties of a dielectric medium are discussed. The nonlinear refractive index change, induced by optical control signals, is derived. Prior to the discussion of the resonant nonlinearities in SOAs, presented in chapter 3, the simpler case of an isotropic, non-resonant medium, such as an optical fiber is considered. This is followed in the second part of this chapter by a description of the different types of two beam interferometers using the Jones formalism. Finally, the Jones formalism is applied to calculate the transmittance function of two simple types of interferometric gates based on HNLF, the NOLM and the Kerr-Switch.

In **Chapter 3** the Semiconductor Optical Amplifier is discussed. In the first part, a description of SOAs and their nonlinear properties relevant for interferometric switching is given. This includes a phenomenological model for the carrier density dynamics in the active region of the SOA, which can be used to derive the gain and refractive index changes, induced by optical control pulses. The SOAs investigated in this work are operated in two different modes, called the conventional and the gain-transparent mode. The differences between both operation modes are briefly addressed. In the second part of this chapter, measurements of the gain and refractive index (phase) changes in an SOA upon saturation

by a strong optical pulse, so called gain and phase dynamics, are presented. The influence of the gain and phase dynamics on the switching performance of interferometric gates based on SOAs is discussed under various operation conditions.

In **Chapter 4**, the Jones formalism derived in chapter 2 was used to calculate the transmittance functions for three different types of interferometric gates based on SOAs, the Semiconductor Laser Amplifier in a LOop Mirror (SLALOM), the Mach-Zehnder Interferometer (MZI) switch and the Ultrafast-Nonlinear Interferometer (UNI). Switching window measurements for these switches under various operation conditions are presented. The three investigated switches are compared in view of their application in OTDM systems. The comparison is based on the evaluation of the measured switching windows using different criteria, in particular the switching window width, the on-off contrast ratio, the maximum transmittance and the integrated contrast ratio (ICR).

Chapter 5 presents applications of the investigated interferometric gates based on SOAs as demultiplexer, add-drop multiplexer and optical sampler in an OTDM system. The experiments were performed at a base data rates of 10 Gbit/s and 40 Gbit/s and TDM bit rates up to 160 Gbit/s and included back-to-back measurements as well as transmission over fiber spans. As will be shown in chapter 3, SOA based gates are not suitable for wavelength conversion and signal regeneration at high TDM bit rates. Therefore these operations were implemented using the fiber based Kerr-Switch, presented in chapter 2.

Finally, the obtained results are summarized and discussed in **Chapter 6** and a short outlook is given.

Chapter 2

Basics of Interferometric Switching

The following chapter will provide a brief theoretical description to present the main formulas used to describe interferometric switching. Starting from the wave equation in nonmagnetic, dielectric media the nonlinear propagation effects of optical waves are discussed for the special case of a non-resonant, isotropic medium. The more complicated resonant case, which is relevant for the description of the nonlinear properties of semiconductor optical amplifiers (SOA), will be discussed in chapter 3. A complete theoretical investigation of the nonlinear effects is beyond the scope of this work. Therefore the description will mainly concentrate on the optically induced refractive index changes in the medium, which lead to a phase shift of the optical wave used in interferometric switches. For a deeper insight into the matter a number of references are given. In the second part of this chapter we introduce the Jones formalism, which enables a unified mathematical description of the interferometers considered in this work. Using this formalism it will be shown that the transmission properties of all three interferometers are governed by simple interference equations with very similar form. In the last part of this chapter the derived formulas are applied to interferometric switches. As example simple gates based on HNLF as nonlinear medium are chosen.

2.1 Wave Equation and Nonlinear Effects

The propagation and nonlinear interaction of optical fields is governed by Maxwell's equations [52, 53]. Based on Maxwell's equations it is possible to derive a wave equation for the optical field, which describes the propagation through a medium. In the case of nonmagnetic, charge free, dielectric media (magnetization, current density and charge density are zero), such as optical fibers, this wave equation is [20]

$$\nabla^2 \underline{\mathbf{E}} - \frac{1}{c^2}\frac{\partial^2}{\partial t^2}\underline{\mathbf{E}} = \frac{1}{\varepsilon_0 c^2}\frac{\partial^2}{\partial t^2}\underline{\mathbf{P}} \,, \tag{2.1}$$

where ε_0 is the electric permittivity of free space and c is the speed of light in vacuum. $\underline{\mathbf{E}}$ is the electric field vector of the optical field and $\underline{\mathbf{P}}$ is the polarization density arising inside the medium in response to the optical field.

It is sometimes useful to consider the frequency-domain. In this case the wave equation is written as

$$\nabla^2 \underline{\widetilde{\mathbf{E}}}(\omega) + \frac{\omega^2}{c^2}\underline{\widetilde{\mathbf{E}}}(\omega) = -\frac{\omega^2}{\varepsilon_0 c^2}\underline{\widetilde{\mathbf{P}}}(\omega) \tag{2.2}$$

The Fourier transform $\underline{\widetilde{\mathbf{E}}}(\omega)$ and $\underline{\widetilde{\mathbf{P}}}(\omega)$ of the electric field $\underline{\mathbf{E}}(\mathrm{t})$ and the polarization density $\underline{\mathbf{P}}(\mathrm{t})$ are given by

$$\underline{\widetilde{\mathbf{E}}}(\omega) = \frac{1}{2\pi}\int_{-\infty}^{+\infty} d\tau\, \underline{\mathbf{E}}(\tau)\, \mathrm{e}^{i\omega\tau} \tag{2.3}$$

$$\underline{\widetilde{\mathbf{P}}}(\omega) = \frac{1}{2\pi}\int_{-\infty}^{+\infty} d\tau\, \underline{\mathbf{P}}(\tau)\, \mathrm{e}^{i\omega\tau}\ . \tag{2.4}$$

Please note that $\underline{\widetilde{\mathbf{E}}}(\omega)$ and $\underline{\widetilde{\mathbf{P}}}(\omega)$ are in general complex (indicated by the tilde). To solve the wave equation 2.1 or 2.2 the constitutive relation between $\underline{\mathbf{P}}$ and $\underline{\mathbf{E}}$ is needed.

In general $\underline{\mathbf{P}}$ is a complicated function of $\underline{\mathbf{E}}$ and can be separated into a part, which is linear in $\underline{\mathbf{E}}$ and a second part, which is a nonlinear function of $\underline{\mathbf{E}}$. In most optical media at moderate optical powers the linear part dominates, and the interaction of the light with the medium is linear [20]. In a medium with linear interaction the optical waves propagating through the medium do not influence each other. If the second part is not negligible, the interaction of light with the medium is nonlinear. For all-optical switching, where it is intended to change the properties of an optical wave propagating through the medium by a second optical wave, a nonlinear interaction is needed.

As described in the introduction, the properties of all-optical switches depend strongly on whether the nonlinearity is resonant or non-resonant.

Non-resonant Nonlinearity

If the optical frequency of the wave is far away from any transition frequencies in the medium the nonlinearity is called non-resonant. An example are silica fibers at telecommunication wavelengths. In this case, the nonlinearity is small and can be treated as a perturbation [54]. $\underline{\mathbf{P}}$ can then be expressed as a power series in $\underline{\mathbf{E}}$:

$$\underline{\widetilde{\mathbf{P}}}(\omega) = \underbrace{\underline{\widetilde{\mathbf{P}}}^{(1)}(\omega)}_{\text{linear}} + \underbrace{\underline{\widetilde{\mathbf{P}}}^{(2)}(\omega) + \cdots + \underline{\widetilde{\mathbf{P}}}^{(n)}(\omega) + \cdots}_{\text{nonlinear response}} \tag{2.5}$$

with

$$\underline{\widetilde{\mathbf{P}}}^{(n)}(\omega) = \varepsilon_0 \int_{-\infty}^{+\infty} d\omega_{a1} \cdots \int_{-\infty}^{+\infty} d\omega_{an}\, \boldsymbol{\chi}^{(n)}(-\omega_\sigma; \omega_{a1}, \cdots, \omega_{an}) \mid \underline{\widetilde{\mathbf{E}}}(\omega_{a1}) \cdots \underline{\widetilde{\mathbf{E}}}(\omega_{an})\, \delta(\omega - \omega_\sigma) \tag{2.6}$$

and

$$\omega_\sigma = \omega_{a1} + \omega_{a2} + \cdots + \omega_{an}\ .$$

$\boldsymbol{\chi}^{(n)}$ is the nth-order susceptibility tensor, a tensor of rank $n+1$, which is independent of the electric field $\underline{\mathbf{E}}$. The susceptibility tensors $\boldsymbol{\chi}^{(n)}$ are in general complex and their imaginary and real parts can lead to different physical effects like nonlinear index or gain changes and the generation of new frequency components.

Resonant Nonlinearity

The nonlinearity is called resonant, if the optical frequencies are close to transition frequencies in the medium. This means that specific susceptibilities are enhanced (so called resonance enhancement) and the small-perturbation approximation, used in the non-resonant case, can no longer be applied. It is therefore not useful to write $\underline{\mathbf{P}}$ as a power series in $\underline{\mathbf{E}}$. A 'field corrected' susceptibility $\overline{\boldsymbol{\chi}}\,(\omega, \underline{\mathbf{E}})$ is introduced instead, which is depending on the electrical field, so that $\underline{\mathbf{P}}$ can be expressed as [55]

$$\underline{\mathbf{P}} = \epsilon_0\, \overline{\boldsymbol{\chi}}(\omega, \underline{\mathbf{E}})\, \underline{\mathbf{E}}\ . \tag{2.7}$$

Similar to the non-resonant case the susceptibility $\overline{\boldsymbol{\chi}}(\omega, \underline{\mathbf{E}})$ is in general complex and leads to a number of different nonlinear effects.

This chapter will concentrate on non-resonant nonlinearities. The more complicated resonant case, which is relevant for the description of the nonlinear properties of SOAs, will be discussed in section 3.1.1.

Nonlinear Refractive Index

Interferometric switching relies on refractive index changes, induced by the control signal, which lead to a phase change for the optical data signal propagating through the medium. In the following the origin of the nonlinear refractive index change will be discussed for the special case of an isotropic, non-resonant medium, such as the optical fiber. It is assumed that the data signal $\underline{\widetilde{\mathbf{E}}}_1(\omega_1)$ and the control signal $\underline{\widetilde{\mathbf{E}}}_2(\omega_2)$ oscillate at different frequencies $\omega_1 \neq \omega_2$. Both signals are linearly polarized and propagate in z-direction through the medium with either the same or orthogonal polarization states. Using (2.5) and (2.6) the polarization density $\underline{\widetilde{\mathbf{P}}}(\omega)$, arising in response to the data and control signal, can be calculated. For the investigation of the nonlinear refractive index changes at the frequency ω_1 of the data signal, only the polarization density $\underline{\widetilde{\mathbf{P}}}(\omega_1)$ oscillating at frequency ω_1 is considered.

– **Linear response:** $\underline{\widetilde{\mathbf{P}}}^{(1)}(\omega_1)$ describes the linear effects. In an isotropic medium the second rank tensor $\boldsymbol{\chi}^{(1)}$ can be written as a scalar quantity and the linear polarization density

$$\underline{\widetilde{\mathbf{P}}}^{(1)}(\omega_1) = \varepsilon_0 \, \chi^{(1)}(-\omega_1; \omega_1) \, \underline{\widetilde{\mathbf{E}}}_1(\omega_1) \tag{2.8}$$

has the same state of polarization as the incoming wave. The real and imaginary part of $\chi^{(1)}(-\omega_1, \omega_1)$ are linked to the linear refractive index $n_0(\omega_1)$ and to the absorption coefficient $\alpha(\omega_1)$. By substituting $\widetilde{\mathbf{P}}^{(1)}(\omega_1)$ into the wave equation 2.2 the following relation can be derived

$$n_0(\omega_1) + i \, \frac{\alpha(\omega_1) \, c}{2 \, \omega_1} = \sqrt{1 + \Re\left\{\chi^{(1)}(-\omega_1; \omega_1)\right\} + i \, \Im\left\{\chi^{(1)}(-\omega_1; \omega_1)\right\}} \, . \tag{2.9}$$

If $\left(\frac{\alpha(\omega_1)\, c}{2\omega_1}\right)^2 \ll n_0(\omega_1)^2$, the refractive index and the absorption coefficient can be directly linked to the real and imaginary part of $\chi^{(1)}(-\omega_1; \omega_1)$ respectively [56]

$$n_0^2(\omega_1) \approx 1 + \Re\left\{\chi^{(1)}(-\omega_1; \omega_1)\right\} \, , \qquad \alpha(\omega_1) \approx \frac{\omega_1}{c \, n_0(\omega_1)} \, \Im\left\{\chi^{(1)}(-\omega_1; \omega_1)\right\} \, . \tag{2.10}$$

– **Quadratic nonlinear response:** $\underline{\widetilde{\mathbf{P}}}^{(2)}(\omega_1)$ describes the quadratic effects. In a medium with inversion symmetry, such as optical fiber, $\boldsymbol{\chi}^{(2)}$ vanishes so that

$$\underline{\widetilde{\mathbf{P}}}^{(2)}(\omega_1) = 0. \tag{2.11}$$

– **Cubic nonlinear response:** $\underline{\widetilde{\mathbf{P}}}^{(3)}(\omega_1)$ describes the cubic effects. Note that in this case, the evaluation of (2.6) involves a summation over all sets of frequencies $\omega_{a1}, \omega_{a2}, \omega_{a3}$ which satisfy $\omega_1 - \omega_\sigma = 0$ ($\omega_{a1}, \omega_{a2}, \omega_{a3} \in \{\pm\omega_1, \pm\omega_2\}$) and the summation in the tensor product with the fourth rank tensor $\boldsymbol{\chi}^{(3)}$ (81 components).

The complexity of this tensor is strongly reduced in an isotropic medium. 60 of the tensor components are zero and the 21 non-zero components can be expressed by [57]

$$\chi^{(3)}_{\alpha\beta\gamma\delta} = \chi^{(3)}_{xxyy}\delta_{\alpha\beta}\,\delta_{\gamma\delta} + \chi^{(3)}_{xyxy}\delta_{\alpha\gamma}\,\delta_{\beta\delta} + \chi^{(3)}_{xyyx}\delta_{\alpha\delta}\,\delta_{\beta\gamma} \quad (\alpha,\beta,\gamma,\delta \in \{x,y,z\}) \tag{2.12}$$

The relative magnitude of the three independent elements $\chi^{(3)}_{xxyy}$, $\chi^{(3)}_{xyxy}$ and $\chi^{(3)}_{xyyx}$ depends on the physical mechanisms that contribute to $\boldsymbol{\chi}^{(3)}$. In the case of silica fibers the dominant contribution is of electronic origin and the three elements have nearly the same magnitude ($\chi^{(3)}_{xxyy} \approx \chi^{(3)}_{xyxy} \approx \chi^{(3)}_{xyyx}$) [20]. As a result, several terms in the evaluation of (2.6) can be combined and the third order polarization density at frequency ω_1 is given by

$$\begin{aligned}\widetilde{\underline{\mathbf{P}}}^{(3)}(\omega_1) \;=\; \varepsilon_0 \Big[& 3\,\chi^{(3)}_{xxxx}(-\omega_1;\omega_1,-\omega_1,\omega_1)\,\left|\widetilde{\underline{\mathbf{E}}}_1(\omega_1)\right|^2\,\widetilde{\underline{\mathbf{E}}}_1(\omega_1) \\ & + 3\,b\,\chi^{(3)}_{xxxx}(-\omega_1;\omega_1,-\omega_2,\omega_2)\,\left|\widetilde{\underline{\mathbf{E}}}_2(\omega_2)\right|^2\,\widetilde{\underline{\mathbf{E}}}_1(\omega_1)\Big] \;. \end{aligned} \tag{2.13}$$

The parameter b equals 2 if the control and data signal have the same state of polarization. For orthogonal polarization b is 2/3. By substituting (2.13) into the wave equation (2.2) it can be seen that the real part of $\chi^{(3)}_{xxxx}$ is associated with a refractive index change. This nonlinear refractive index change is described by the the nonlinear refractive index coefficient

$$\overline{n}_2(\omega_1) = \frac{3}{8\,n_0(\omega_1)}\,\Re\left\{\chi^{(3)}_{xxxx}(-\omega_1,\omega_1,-\omega_1,\omega_1)\right\} \;. \tag{2.14}$$

The imaginary part of $\boldsymbol{\chi}^{(3)}$ is small for silica fiber and only important for effects like stimulated Raman or Brillouin scattering. These effects are not discussed in this work.

– **Higher-order nonlinearity:** Higher order polarization densities $\widetilde{\underline{\mathbf{P}}}^{(n)}(\omega_1)$ $(n > 3)$ are not considered here, as they are normally very weak.

By combining the different orders of polarization density and substituting them into the wave equation 2.2 an expression for the refractive index $n(\omega_1)$ at the frequency of the data signal can be derived. It is approximately given by [21]

$$n(\omega_1) = n_0(\omega_1) + \overline{n}_2(\omega_1)\left|\widetilde{\underline{\mathbf{E}}}_1(\omega_1)\right|^2 + b\,\overline{n}_2(\omega_1)\left|\widetilde{\underline{\mathbf{E}}}_2(\omega_2)\right|^2 \;. \tag{2.15}$$

$n_0(\omega_1)$ is the linear refractive index and $\overline{n}_2(\omega_1)$ is the nonlinear refractive index coefficient defined in (2.14). Sometimes (2.15) is also written in terms of the optical intensity I

$$n(\omega_1) = n_0(\omega_1) \;+\; n_2(\omega_1)I_1 \;+\; b\,n_2(\omega_1)I_2 \quad \text{with} \quad n_2(\omega_1) = \frac{2\,\overline{n}_2(\omega_1)}{\varepsilon_0\,c\,n_0(\omega_1)}. \tag{2.16}$$

The second term in (2.15) with $\left|\widetilde{\underline{\mathbf{E}}}_1(\omega_1)\right|^2$ describes the refractive index change induced by the data signal itself (self-phase modulation). The third term with $\left|\widetilde{\underline{\mathbf{E}}}_2(\omega_2)\right|$ is the refractive index change induced by the control signal (cross-phase modulation)

Nonlinear Phase Shift

To calculate the phase shift for the data signal through self-phase and cross-phase modulation in an optical fiber, it has to be investigated how the propagation constant β is affected by the refractive index change. For the simplified case that control and data signal have equal transversal field distributions and equal propagation constants (approximately true for single mode fibers if walk off is neglected), β can be written as

$$\beta \approx \beta_0 + \gamma P_1(t) + b \gamma P_2(t) . \tag{2.17}$$

The first term $\beta_0 = n_0(\omega_1)/c$ is the propagation constant of the data signal at low optical power. The second term describes the change of the propagation constant due to self-phase modulation, the third term describes the effect of the cross-phase modulation. $P_1(t)$ and $P_2(t)$ are the powers of the data and control signal respectively,

$$\gamma = \frac{\omega_1 \, n_2(\omega_1)}{c \, A_{eff}} \tag{2.18}$$

is the nonlinear coefficient and A_{eff} is the effective area of the fiber, defined in (A.12). The phase shift incurred by the data signal, traveling a distance L in an optical fiber (which is assumed lossless) together with the control signal is

$$\begin{aligned} \Phi &= L \, \beta \\ &= \frac{\omega_1}{c} \, L \left[n_0(\omega_1) + n_2(\omega_1) \frac{P_1(t)}{A_{eff}} + b \, n_2(\omega_1) \frac{P_2(t)}{A_{eff}} \right] . \end{aligned} \tag{2.19}$$

The last term in (2.19) leads to the cross-phase modulation that is used in interferometric switches. The phase shift by cross-phase modulation increases linearly with the interaction length and with the power of the control signal. The phase shift is three times higher for linearly polarized data and control signals with the same state of polarization compared to orthogonal polarization states. Please note that (2.19) does not take into account the walk off between the data and control signals and also neglects the absorption inside the fiber. Both effects can have an important influence depending on the amount of absorption and dispersion in the fiber.

The characteristic time constant for the nonlinearities in optical fibers leading to cross-phase modulation is on the order of a few fs [21]. This enables very high switching speeds in interferometric switches based on fibers. On the other hand a good temporal and spatial overlap of the optical signals is needed. In the case of short optical pulses a sufficient interaction length can only be achieved, when the optical signals co-propagate inside the fiber and the group velocity dispersions are comparable.

A similar approach to derive the nonlinear phase shift by self- and cross-phase modulation, that was used in this section for the case of a non-resonant medium, will be discussed in chapter 3 for the SOA. The following section will investigate, how the nonlinear phase shift by cross-phase modulation is used in interferometric setups to realize all-optical gates.

2.2 Interferometer

An interferometer is an optical instrument that splits a single light beam or wave into a number of waves, delays them by equal or unequal distances and recombines them again

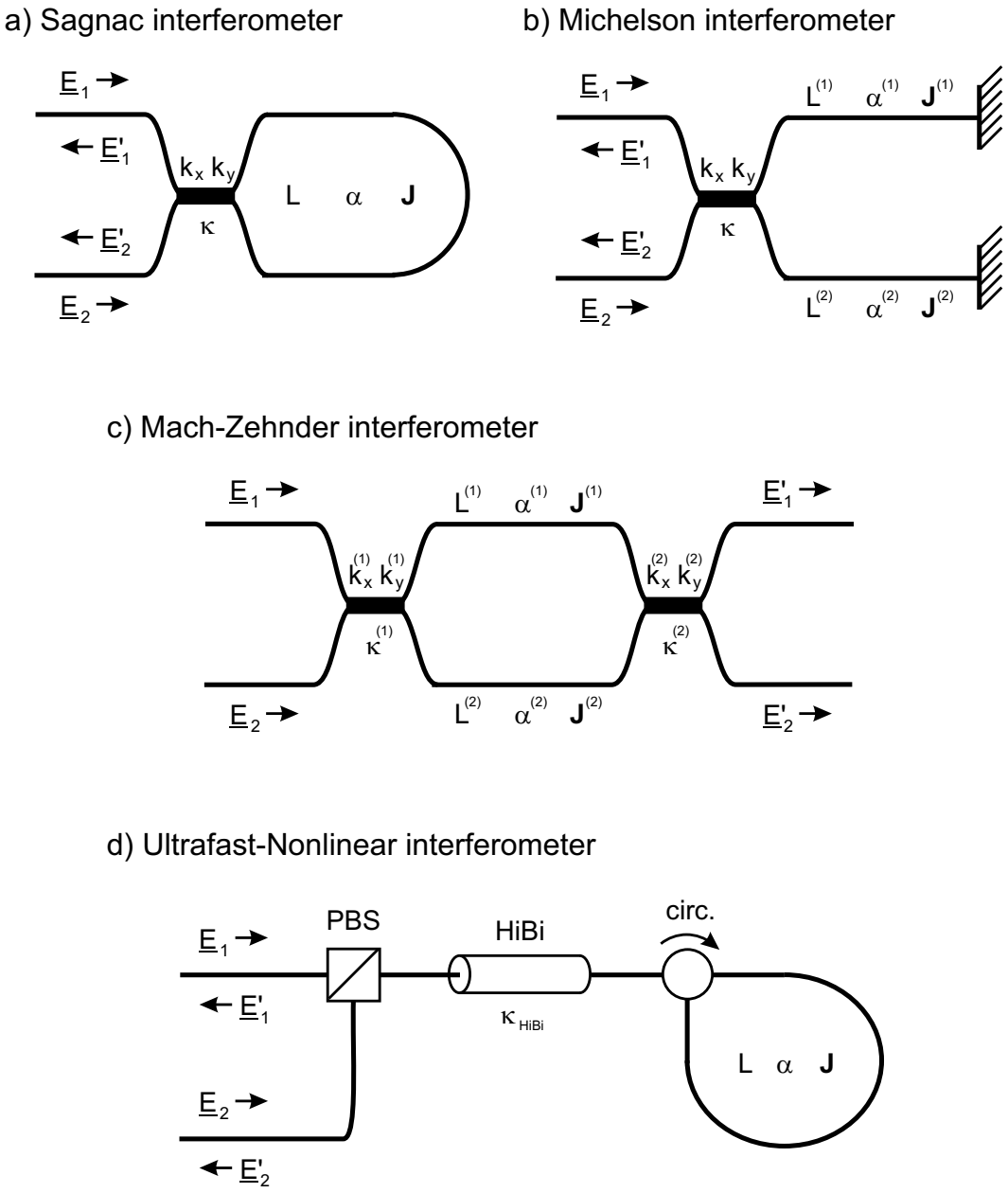

Figure 2.1: Schematic depiction of different types of two beam interferometers. The symbols used in the figure are defined in the following sections (2.2.1 to 2.2.3) and in Appendix A.5

[58]. The optical field at the output of the interferometer depends on the relative phase differences between the recombined waves. The phase difference between two of these waves is given by $\Delta\Phi = 2\pi\frac{\Delta n \Delta d}{\lambda}$, where λ is the vacuum wavelength of the waves, Δd is the difference between the distances they traveled and Δn is the difference between the refractive indices of the materials they traveled through. If a refractive index difference Δn is induced between the split waves, the resulting phase difference $\Delta\Phi$ leads to a change of the optical power transmitted through the interferometer. This means that the optical wave can be gated by controlling the refractive index difference Δn. For example

by incorporating a medium with high nonlinearity into one interferometer branch and applying a strong optical pulse (cross-phase modulation), as was discussed in section 2.1.

The interferometers used in optical signal processing to realize optical gates are almost exclusively two beam interferometers with division of amplitude. They can be subdivided according to the type of beamsplitter used. In the Sagnac or cyclic Interferometer (SI), the Michelson Interferometer (MI) and the Mach-Zehnder Interferometer (MZI), shown in Fig. 2.1 a) - c), partially reflecting beamsplitters or fused fiber couplers (evanescent field couplers) divide and recombine the two beams. In the Ultrafast-Nonlinear Interferometer (UNI, also called polarization discriminating Mach-Zehnder Interferometer) this is done by a polarizing beamsplitter (see Fig. 2.1 d)). The UNI is therefore called a polarization interferometer.

Three of the interferometers shown in Fig. 2.1 will be discussed in the following sections - the Sagnac, the Mach-Zehnder and the Ultrafast-Nonlinear Interferometer. A unified description based on the Jones formalism will be presented to describe their transmission properties and it will be shown, that for all three interferometers under ideal conditions the transmittance as a function of the phase difference $\Delta\Phi$ can be described by a simple interference equation.

2.2.1 Sagnac Interferometer

In the Jones formalism [53] (see Appendix A.4) an optical system, such as an interferometer, can be described by a transfer matrix $\mathbf{M}$, called the Jones matrix, given by

$$\underline{E}' = \mathbf{M}\,\underline{E}\ , \tag{2.20}$$

where $\underline{E} = \begin{pmatrix} E_x \\ E_y \end{pmatrix}$ and $\underline{E}' = \begin{pmatrix} E'_x \\ E'_y \end{pmatrix}$ are the Jones vectors of the input and output waves. The Jones vectors and also the Jones matrices are in general complex, but the tilde denoting complex quantities will be omitted in the following.

In order to describe the fiber based Sagnac Interferometer in the Jones formalism [59], it is useful to take a look at the schematic shown in Fig. 2.1 a). An incoming wave ($\underline{E}_1$ or $\underline{E}_2$) is separated at a fiber coupler in two waves, which propagate in opposite directions through the fiber loop. After a round trip in the loop they interfere again at the coupler and leave the interferometer. The Jones vectors $\underline{E}'_1$ and $\underline{E}'_2$, representing the output waves, can be written as

$$\underline{E}'_1 = \left[\mathbf{M}_{(11)}\underline{E}_1 + \mathbf{M}_{(21)}\underline{E}_2\right] \tag{2.21}$$

$$\underline{E}'_2 = \left[\mathbf{M}_{(12)}\underline{E}_1 + \mathbf{M}_{(22)}\underline{E}_2\right]\ . \tag{2.22}$$

The Jones matrices $\mathbf{M}_{(pq)}(\ p,q \in \{1,2\})$ are given by

$$\begin{aligned}
\mathbf{M}_{(11)} &= \mathbf{J}^{\text{cross}}\,\mathbf{J}^{C}\,\mathbf{J}^{\sigma_x}\,\mathbf{J}^{\text{bar}} + \mathbf{J}^{\text{bar}}\,\mathbf{J}^{\sigma_x}\,\mathbf{J}^{A}\,\mathbf{J}^{\text{cross}} \\
\mathbf{M}_{(12)} &= \mathbf{J}^{\text{bar}}\,\mathbf{J}^{C}\,\mathbf{J}^{\sigma_x}\,\mathbf{J}^{\text{bar}} + \mathbf{J}^{\text{cross}}\,\mathbf{J}^{\sigma_x}\,\mathbf{J}^{A}\,\mathbf{J}^{\text{cross}} \\
\mathbf{M}_{(21)} &= \mathbf{J}^{\text{cross}}\,\mathbf{J}^{C}\,\mathbf{J}^{\sigma_x}\,\mathbf{J}^{\text{cross}} + \mathbf{J}^{\text{bar}}\,\mathbf{J}^{\sigma_x}\,\mathbf{J}^{A}\,\mathbf{J}^{\text{bar}} \\
\mathbf{M}_{(22)} &= \mathbf{J}^{\text{bar}}\,\mathbf{J}^{C}\,\mathbf{J}^{\sigma_x}\,\mathbf{J}^{\text{cross}} + \mathbf{J}^{\text{cross}}\,\mathbf{J}^{\sigma_x}\,\mathbf{J}^{A}\,\mathbf{J}^{\text{bar}}\ ,
\end{aligned} \tag{2.23}$$

with

$$\mathbf{J}^{\text{bar}} = \sqrt{1-\kappa}\begin{pmatrix} \sqrt{1-k_x} & 0 \\ 0 & \sqrt{1-k_y} \end{pmatrix}\ ,\quad \mathbf{J}^{\text{cross}} = \sqrt{1-\kappa}\begin{pmatrix} i\sqrt{k_x} & 0 \\ 0 & i\sqrt{k_y} \end{pmatrix} \tag{2.24}$$

and

$$\mathbf{J}^{\sigma_x} = \begin{pmatrix} -1 & 0 \\ 0 & 1 \end{pmatrix} . \tag{2.25}$$

$\mathbf{J}^{\text{cross}}$ and $\mathbf{J}^{\text{bar}}$ represent the cross and bar coupling through the fiber coupler. k_x and k_y are the field intensity coupling coefficients for the x and y polarization, κ is the excess loss of the coupler. $\mathbf{J}^{\sigma_x}$ is a Jones matrix describing a reflection at the y-z plane (sign change of the x component). The Jones matrices $\mathbf{J}^A$ and $\mathbf{J}^C$ represent the clockwise and anticlockwise propagation in the fiber loop respectively.

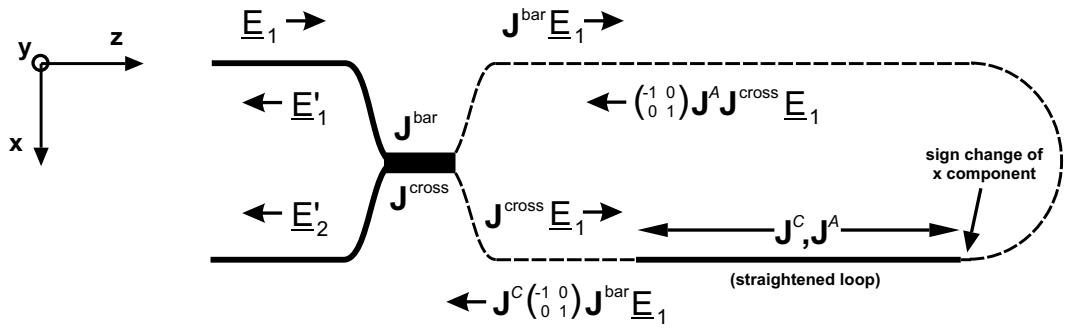

Figure 2.2: Schematic of the Sagnac Interferometer with straightened fiber loop in the case of a single input wave $\underline{E}_1$ to aid the understanding of the Jones matrices.

In order to understand the form of the Jones matrices $\mathbf{M}_{(pq)}$ in (2.23), we assume the fiber loop to be straightened out along the z axis as indicated in Fig. 2.2. Consider the first addend in the Jones matrices $\mathbf{M}_{(11)}$ and $\mathbf{M}_{(12)}$, which describe the clockwise propagation of the wave $\underline{E}_1$ through the loop. The wave passes the fiber coupler ($\mathbf{J}^{\text{bar}}$) and just before it enters the (straightened) loop it is assumed that the x component has changed sign (represented by multiplication with $\mathbf{J}^{\sigma_x}$ [59]). After propagation through the fiber loop ($\mathbf{J}^C$) the wave re-enters the coupler ($\mathbf{J}^{\text{bar}}$ or $\mathbf{J}^{\text{cross}}$) and leaves the interferometer ($\underline{E}'_1$ or $\underline{E}'_2$). The anticlockwise propagating through the loop is represented by the second addend in the Jones matrices $\mathbf{M}_{(pq)}$. Note that the anticlockwise propagating wave changes sign *after* propagation through the fiber (see [59]).

Equation (2.21) and (2.22) may be written in a more compact form

$$\begin{pmatrix} \underline{E}'_1 \\ \underline{E}'_2 \end{pmatrix} = \underbrace{\begin{pmatrix} \mathbf{M}_{(11)} & \mathbf{M}_{(21)} \\ \mathbf{M}_{(12)} & \mathbf{M}_{(22)} \end{pmatrix}}_{\mathcal{M}_{\text{Sagnac}}} \begin{pmatrix} \underline{E}_1 \\ \underline{E}_2 \end{pmatrix} , \tag{2.26}$$

where $\begin{pmatrix} \underline{E}_1 \\ \underline{E}_2 \end{pmatrix}$ and $\begin{pmatrix} \underline{E}'_1 \\ \underline{E}'_2 \end{pmatrix}$ are four-dimensional vectors representing the Jones vectors at the input and output of the interferometer respectively. The Jones matrices $\mathbf{M}_{(pq)}$ are combined to a 16×16 matrix, the so called transfer matrix $\mathcal{M}_{\text{Sagnac}}$ of the Sagnac Interferometer. The components of the transfer matrix can be used to derive the power reflectivity coefficient R_{qq} and the power transmission coefficient T_{pq} ($p \neq q$):

$$R_{qq} \left| \underline{E}_q \right|^2 = \left| \mathbf{M}_{(qq)} \underline{E}_q \right|^2 , \qquad T_{pq} \left| \underline{E}_p \right|^2 = \left| \mathbf{M}_{(pq)} \underline{E}_p \right|^2 . \tag{2.27}$$

The complete transfer matrix $\mathcal{M}_{\text{Sagnac}}$ is given in Appendix A.5. Here a simplified case is considered, without fiber absorption ($\alpha = 0$), no excess loss of the coupler ($\kappa = 0$) and an equal field intensity coupling for x and y polarization ($k_x = k_y = k$). With regard to interferometric switching, it is of interest how a refractive index difference Δn (which is assumed polarization independent), induced between the separated waves in the interferometer, changes the reflectivity and transmission coefficients. In the case of the Sagnac Interferometer this means that a polarization independent phase difference of $\Delta\Phi = \Phi_1 - \Phi_2$ is introduced between the anticlockwise and clockwise propagating waves in the loop. The Jones matrices $\mathbf{J}^C$ and $\mathbf{J}^A$ are then given by

$$\mathbf{J}^C = \begin{pmatrix} \mathrm{e}^{i\Phi_1} & 0 \\ 0 & \mathrm{e}^{i\Phi_1} \end{pmatrix}, \ \mathbf{J}^A = \begin{pmatrix} \mathrm{e}^{i\Phi_2} & 0 \\ 0 & \mathrm{e}^{i\Phi_2} \end{pmatrix}.$$

By substituting $\mathbf{J}^C$ and $\mathbf{J}^A$ into the transfer matrix $\mathcal{M}_{\text{Sagnac}}$ the reflectivity and transmission coefficient for a single incoming wave $\underline{E}_1$ can be derived as

$$R_{11} \left|\underline{E}_1\right|^2 = \left|\mathbf{M}_{(11)}\underline{E}_1\right|^2 = \left|-\sqrt{1-k}\; i\; \sqrt{k}\left(\mathrm{e}^{i\Phi_2} + \mathrm{e}^{i\Phi_1}\right)\right|^2 \left|\underline{E}_1\right|^2$$

$$\begin{aligned} \Rightarrow R_{11} &= (1-k)k + k(1-k) + 2k(1-k)\cos(\Delta\Phi) \\ &= 2k(1-k)(1+\cos(\Delta\Phi)) \end{aligned} \tag{2.28}$$

and

$$T_{12} \left|\underline{E}_1\right|^2 = \left|\mathbf{M}_{(12)}\underline{E}_1\right|^2 = \left|-(1-k)\mathrm{e}^{i\Phi_1} + k\mathrm{e}^{i\Phi_2}\right|^2 \left|\underline{E}_1\right|^2$$

$$\begin{aligned} \Rightarrow T_{12} &= (1-k)^2 + k^2 - 2k(1-k)\cos(\Delta\Phi) \\ &= 1 - R_{11}\ . \end{aligned} \tag{2.29}$$

Equation 2.28 and 2.29 are called interference equations. They describe the reflectance and transmittance of the Sagnac Interferometer for a given coupling ration k as a function of the phase difference $\Delta\Phi$. R_{11} and T_{12} are plotted in Fig. 2.3 for different coupling ratios. The curves show the typical behavior of an interferometer, a change of the phase difference from $\Delta\Phi = 0$ to $\Delta\Phi = \pi$ changes the reflectance (transmittance) from maximum to minimum (minimum to maximum).

The impact of a non-ideal coupling ratio is also shown in Fig. 2.3. For an ideal coupling ratio of $k = 1/2$ the reflectance (transmittance) of the interferometer is completely changed from 1 to 0 (0 to 1). For a non-ideal coupling coefficient of $k = 0.3$ or $k = 0.1$, the transmittance T_{12}, plotted on the right hand side, does no longer change completely from 1 to 0. However, the reflectance R_{11}, plotted on the left hand side, still reaches 0 at a phase difference of $\Delta\Phi = \pi$. This means that complete destructive interference is possible for the reflected signal, although the coupling ratio is not ideal.

In an ideal Sagnac Interferometer without birefringence in the fiber loop all incoming light is reflected. This is generally not achieved in practical applications, because the fiber loop has residual birefringence. The impact of the residual birefringence, which was neglected in the formulas derived so far, is that it introduces a phase difference between the orthogonal polarization states of the propagating light. This can lead to a change of the polarization state and a temporal delay, depending on the orientation

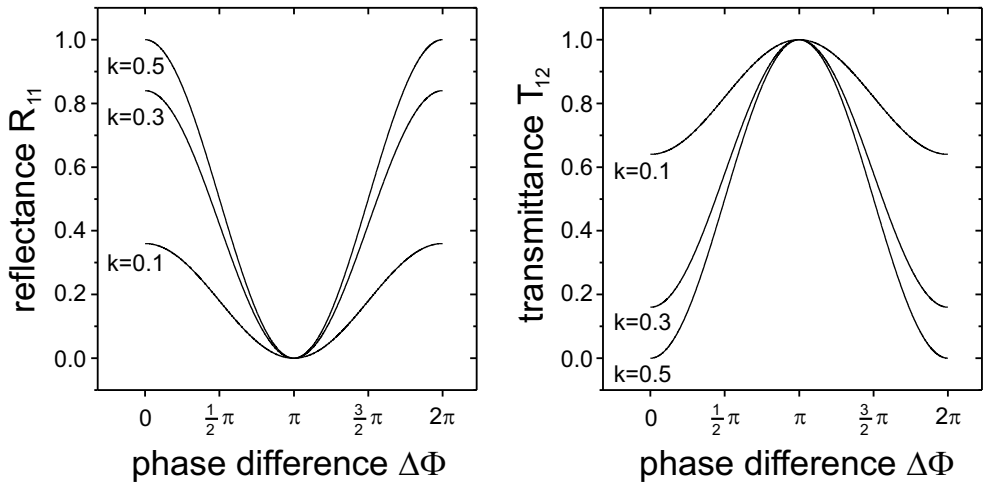

Figure 2.3: Reflectance and transmittance of the Sagnac Interferometer as a function of the phase difference $\Delta\Phi$ for different coupling coefficients k.

of the main axes of this birefringence. The change is not necessarily the same for light propagating in different directions, which leads to a change in transmission and reflection of the Sagnac Interferometer, depending on the loop birefringence. To use the Sagnac Interferometer as a switch, we need to be able to control the loop birefringence, in order to balance the interferometer for example such that all incoming light is reflected. A variable birefringent element can be used to control the loop birefringence [60]. In the experiments a polarization controller either fiber based or based on rotatable retardation plates ($\lambda/2$ or $\lambda/4$) is used for this.

In the simplified case considered above the transmission and reflection properties of the Sagnac Interferometer are independent of the polarization of the incoming wave. In general the intensity coupling coefficient of the fiber coupler is not independent of the polarization and the Jones matrices representing the fiber loop have a far more complex form, due to the residual birefringence of the fiber or polarization dependent loss. In this case the Sagnac Interferometer will become polarization dependent.

It was already mentioned, that the Sagnac Interferometer is a cyclic interferometer. This means that the separated beams propagate through the same fiber. Therefore the transmission and reflection is independent of the fiber loop length if the fiber attenuation is neglected. This is important for practical applications, because it makes an active stabilization of the interferometer unnecessary.

2.2.2 Mach-Zehnder Interferometer

The schematic of the Mach-Zehnder Interferometer is shown in Fig. 2.1 c). Similar to the Sagnac Interferometer, the incoming wave ($\underline{E}_1$ or $\underline{E}_2$) is separated at a fiber coupler in two waves. After propagation over a certain distance they interfere at a second coupler and leave the interferometer ($\underline{E}'_1$ or $\underline{E}'_2$). The main difference compared to the Sagnac

Interferometer is that the separated waves travel through different paths and that they recombine on a second fiber coupler.

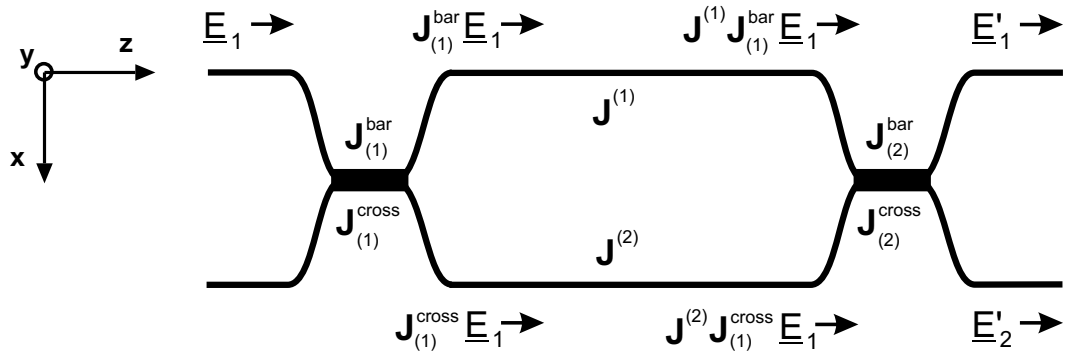

Figure 2.4: Schematic of the Mach-Zehnder Interferometer in the case of a single input wave $\underline{E}_1$ to aid the understanding of the Jones matrices.

The Jones vectors at the output of the Mach-Zehnder Interferometer can be derived from Fig. 2.4. They are given by

$$\begin{pmatrix} \underline{E}'_1 \\ \underline{E}'_2 \end{pmatrix} = \underbrace{\begin{pmatrix} \mathbf{M}_{(11)} & \mathbf{M}_{(21)} \\ \mathbf{M}_{(12)} & \mathbf{M}_{(22)} \end{pmatrix}}_{\mathcal{M}_{\mathrm{MZI}}} \begin{pmatrix} \underline{E}_1 \\ \underline{E}_2 \end{pmatrix} \ , \tag{2.30}$$

Equation 2.30 is written in the compact form introduced in the discussion of the Sagnac Interferometer (see (2.26)). $\mathcal{M}_{\mathrm{MZI}}$ is the transfer matrix of the Mach-Zehnder Interferometer, defined by the Jones matrices

$$\begin{aligned} \mathbf{M}_{(11)} &= \mathbf{J}^{\mathrm{bar}}_{(2)}\, \mathbf{J}^{(1)}\, \mathbf{J}^{\mathrm{bar}}_{(1)} + \mathbf{J}^{\mathrm{cross}}_{(2)}\, \mathbf{J}^{(2)}\, \mathbf{J}^{\mathrm{cross}}_{(1)} \\ \mathbf{M}_{(12)} &= \mathbf{J}^{\mathrm{cross}}_{(2)}\, \mathbf{J}^{(1)}\, \mathbf{J}^{\mathrm{bar}}_{(1)} + \mathbf{J}^{\mathrm{bar}}_{(2)}\, \mathbf{J}^{(2)}\, \mathbf{J}^{\mathrm{cross}}_{(1)} \\ \mathbf{M}_{(21)} &= \mathbf{J}^{\mathrm{bar}}_{(2)}\, \mathbf{J}^{(1)}\, \mathbf{J}^{\mathrm{cross}}_{(1)} + \mathbf{J}^{\mathrm{cross}}_{(2)}\, \mathbf{J}^{(2)}\, \mathbf{J}^{\mathrm{bar}}_{(1)} \\ \mathbf{M}_{(22)} &= \mathbf{J}^{\mathrm{cross}}_{(2)}\, \mathbf{J}^{(1)}\, \mathbf{J}^{\mathrm{cross}}_{(1)} + \mathbf{J}^{\mathrm{bar}}_{(2)}\, \mathbf{J}^{(2)}\, \mathbf{J}^{\mathrm{bar}}_{(1)} \ . \end{aligned} \tag{2.31}$$

$\mathbf{J}^{\mathrm{bar}}_{(1)}$, $\mathbf{J}^{\mathrm{bar}}_{(2)}$ and $\mathbf{J}^{\mathrm{cross}}_{(1)}$, $\mathbf{J}^{\mathrm{cross}}_{(2)}$ are the Jones matrices for bar and cross coupling in the fiber couplers, given in (2.24). The field intensity coupling coefficients of the fiber couplers for the x and y polarization are given by $k_x^{(1)}$, $k_y^{(1)}$ and $k_x^{(2)}$, $k_y^{(2)}$. The different optical paths are characterized by the Jones matrices $\mathbf{J}^{(1)}$ and $\mathbf{J}^{(2)}$.
The power transmission coefficient ($p, q \in \{1, 2\}$) is defined as

$$T_{pq} \left| \underline{E}_p \right|^2 = \left| \mathbf{M}_{(pq)} \underline{E}_p \right|^2 . \tag{2.32}$$

The complete transfer matrix $\mathcal{M}_{\mathrm{MZI}}$ is given in Appendix A.5. Here a simplified case is considered, where $L^{(1)} = L^{(2)} = L$ (equal length of the interferometer branches), $\alpha^{(1)} = \alpha^{(2)} = 0$ (no fiber absorption), $k_x^{(1)} = k_y^{(1)} = k^{(1)}$ and $k_x^{(2)} = k_y^{(2)} = k^{(2)}$ (polarization independent couplers) and $\kappa^{(1)} = \kappa^{(2)} = 0$ (no coupler excess loss). Similar to the discussion in section 2.2.1, we investigate the influence of a refractive index difference between the

separated waves in the interferometer on the transmission coefficient. The refractive index difference leads to a phase difference of $\Delta\Phi = \Phi_1 - \Phi_2$ between both interferometer branches. The Jones matrices are then given by

$$\mathbf{J}^{(1)} = \begin{pmatrix} \mathrm{e}^{i\Phi_1} & 0 \\ 0 & \mathrm{e}^{i\Phi_1} \end{pmatrix}, \; \mathbf{J}^{(2)} = \begin{pmatrix} \mathrm{e}^{i\Phi_2} & 0 \\ 0 & \mathrm{e}^{i\Phi_2} \end{pmatrix}.$$

By substituting $\mathbf{J}^{(1)}$ and $\mathbf{J}^{(2)}$ into the transfer matrix the transmission coefficients T_{11} and T_{12} for the upper and lower interferometer output can be calculated in the case of a single incoming wave $\underline{E}_1$

$$T_{12} \left|\underline{E}_1\right|^2 = \left|\mathbf{M}_{(12)}\underline{E}_1\right|^2 = \left|\sqrt{1-k^{(1)}}\sqrt{k^{(2)}}\,\mathrm{e}^{i\Phi_1} + \sqrt{1-k^{(2)}}\sqrt{k^{(1)}}\,\mathrm{e}^{i\Phi_2}\right|^2 \left|\underline{E}_1\right|^2$$

$$\Rightarrow T_{12} = \left(1-k^{(1)}\right)k^{(2)} + k^{(1)}\left(1-k^{(2)}\right) + 2\sqrt{1-k^{(1)}}\sqrt{k^{(2)}}\sqrt{k^{(1)}}\sqrt{1-k^{(2)}}\cos(\Delta\Phi) \tag{2.33}$$

and

$$T_{11} \left|\underline{E}_1\right|^2 = \left|\mathbf{M}_{(11)}\underline{E}_1\right|^2 = \left|-\sqrt{k^{(1)}}\sqrt{k^{(2)}}\,\mathrm{e}^{i\Phi_2} + \sqrt{1-k^{(1)}}\sqrt{1-k^{(2)}}\,\mathrm{e}^{i\Phi_1}\right|^2 \left|\underline{E}_1\right|^2$$

$$\begin{aligned} \Rightarrow T_{11} &= k^{(1)}k^{(2)} + \left(1-k^{(1)}\right)\left(1-k^{(2)}\right) - 2\sqrt{1-k^{(1)}}\sqrt{1-k^{(2)}}\sqrt{k^{(1)}}\sqrt{k^{(2)}}\cos(\Delta\Phi) \\ &= 1 - T_{12}\,. \end{aligned} \tag{2.34}$$

Equation 2.33 and 2.34 have the typical form of interference equations. For identical couplers ($k^{(1)} = k^{(2)} = k$) they are equal to the corresponding transmission and reflectivity coefficients of the Sagnac Interferometer (2.28 and 2.29). Please note that complete destructive and constructive interference is not possible in the Mach-Zehnder Interferometer, if the coupling ratios of the couplers are different ($k^{(1)} \neq k^{(2)}$). For the simplified case considered here, the Mach-Zehnder Interferometer is independent of the polarization of the incoming wave. As was already pointed out in the discussion of the Sagnac Interferometer this is no longer true for more practical cases, where the couplers are polarization dependent and the fiber shows residual birefringence.

In the transmission coefficients derived above the loss and birefringence in the interferometer branches were neglected. A different loss in both branches is similar to a non-ideal coupling ratio in the input coupler. A complete constructive and destructive interference of the split signals can no longer be achieved in this case, which reduces the on-off contrast of the interferometer. Different birefringence in the interferometer branches can also reduce the on-off contrast, because it leads to a different polarization of the split signals at the output coupler. In hybrid devices these effects are generally reduced by using optical attenuators and polarization controllers in the interferometer branches.

Also different optical path length in both interferometer branches were not taken into account so far. Unlike the Sagnac, the Mach-Zehnder Interferometer is no cyclic interferometer. This means that the separated waves travel through different paths. A small length difference $\Delta d = L^{(1)} - L^{(2)}$ between both paths, evoked by temperature differences, can therefore lead to an additional phase difference $\Delta\Phi$. This changes the transmission properties of the interferometer. Already small differences in length can lead to significant phase differences (e.g. $\Delta d \approx 0.75\ \mu\mathrm{m} \Rightarrow \Delta\Phi \approx \pi$). In order to use the

MZI as a switch, we need to be able to control these differences in length, to guarantee a stable operation and to balance the interferometer for example such that all incoming light leaves through the lower output port. Therefore an active stabilization, e.g. based on optical feedback and Peltier elements for heating or cooling the fiber in the interferometer branches, is needed in a hybrid device [27]. The active stabilization is not necessary for a monolithically integrated MZI, because all waveguides are close together on one chip and temperature differences across the chip are negligible. In this case, the interferometer has to be balanced by changing the injection current for the SOAs or by monolithically integrated phase shifters [61].

2.2.3 Ultrafast-Nonlinear Interferometer

The schematic of the Ultrafast-Nonlinear Interferometer is shown in Fig. 2.1 d). In contrast to the two interferometers discussed above, the Ultrafast-Nonlinear Interferometer is a polarization interferometer. The operation principle is as follows. The incoming wave ($\underline{E}_1$ or $\underline{E}_2$) passes a polarizing beamsplitter (PBS) and is coupled into a piece of highly birefringent fiber (HiBi, also called polarization maintaining fiber PMF) with two orthogonally polarized components along the principle axes of the HiBi fiber. In the HiBi fiber the orthogonally polarized components are separated by a temporal delay, which is given by the differential group delay (DGD) of the HiBi fiber. The split waves propagate through a fiber loop and are launched again in opposite direction into the HiBi fiber using an optical circulator (circ.). For the second passage through the HiBi fiber the polarization is chosen such that the temporal delay between the split waves is canceled, so that they recombine and interfere at the PBS ($\underline{E}'_1$ or $\underline{E}'_2$).

In order to describe the transmission properties with the Jones formalism, we consider the UNI in an unfolded geometry, shown in Fig. 2.5, which is equivalent to the configuration shown in Fig. 2.1 d). The waves at the UNI output can be written in the following compact form (see (2.26))

$$\begin{pmatrix} \underline{E}'_1 \\ \underline{E}'_2 \end{pmatrix} = \underbrace{\begin{pmatrix} \mathbf{M}_{(11)} & \mathbf{M}_{(21)} \\ \mathbf{M}_{(12)} & \mathbf{M}_{(22)} \end{pmatrix}}_{\mathcal{M}_{\mathrm{UNI}}} \begin{pmatrix} \underline{E}_1 \\ \underline{E}_2 \end{pmatrix} \ , \tag{2.35}$$

where the components of the transfer matrix $\mathcal{M}_{\mathrm{UNI}}$ are given by

$$\begin{aligned} \mathbf{M}_{(11)} &= \mathbf{J}_{\mathrm{PBS}}^{\mathrm{trans}}\, \mathbf{J}_{\mathrm{out}}^{\mathrm{HiBi}}\, \mathbf{J}\, \mathbf{J}_{\mathrm{in}}^{\mathrm{HiBi}}\, \mathbf{J}_{\mathrm{PBS}}^{\mathrm{trans}} \\ \mathbf{M}_{(12)} &= \mathbf{J}_{\mathrm{PBS}}^{\mathrm{ref}}\, \mathbf{J}_{\mathrm{out}}^{\mathrm{HiBi}}\, \mathbf{J}\, \mathbf{J}_{\mathrm{in}}^{\mathrm{HiBi}}\, \mathbf{J}_{\mathrm{PBS}}^{\mathrm{trans}} \\ \mathbf{M}_{(21)} &= \mathbf{J}_{\mathrm{PBS}}^{\mathrm{trans}}\, \mathbf{J}_{\mathrm{out}}^{\mathrm{HiBi}}\, \mathbf{J}\, \mathbf{J}_{\mathrm{in}}^{\mathrm{HiBi}}\, \mathbf{J}_{\mathrm{PBS}}^{\mathrm{ref}} \\ \mathbf{M}_{(22)} &= \mathbf{J}_{\mathrm{PBS}}^{\mathrm{ref}}\, \mathbf{J}_{\mathrm{out}}^{\mathrm{HiBi}}\, \mathbf{J}\, \mathbf{J}_{\mathrm{in}}^{\mathrm{HiBi}}\, \mathbf{J}_{\mathrm{PBS}}^{\mathrm{ref}} \ . \end{aligned} \tag{2.36}$$

$\mathbf{J}_{\mathrm{PBS}}^{\mathrm{trans}}$ and $\mathbf{J}_{\mathrm{PBS}}^{\mathrm{ref}}$ are the Jones matrices representing the transmission and reflection in the polarizing beamsplitters. It is assumed, that the PBS is lossless and that only light polarized along the x axis is transmitted, so that

$$\mathbf{J}_{\mathrm{PBS}}^{\mathrm{trans}} = \begin{pmatrix} 1 & 0 \\ 0 & 0 \end{pmatrix} \quad \text{and} \quad \mathbf{J}_{\mathrm{PBS}}^{\mathrm{ref}} = \begin{pmatrix} 0 & 0 \\ 0 & 1 \end{pmatrix} \ . \tag{2.37}$$

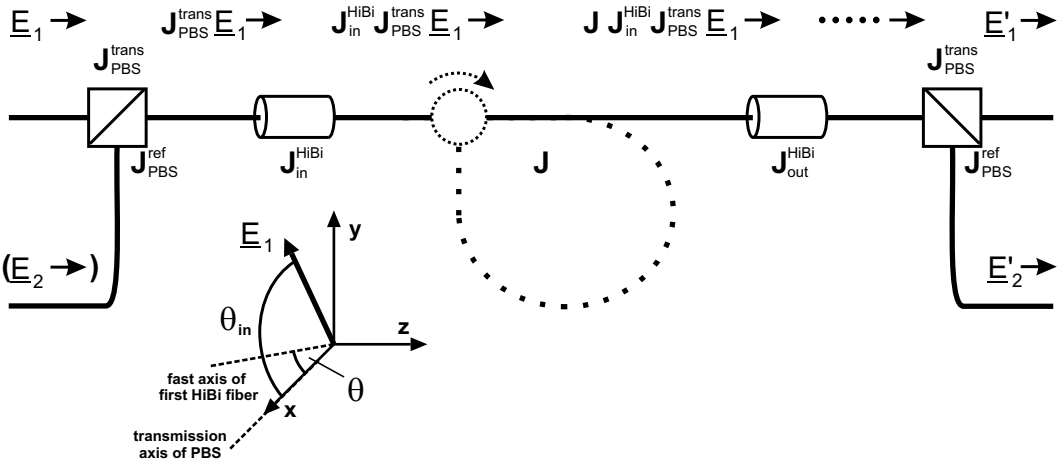

Figure 2.5: Schematic of the Ultrafast-Nonlinear Interferometer in the unfolded geometry, for the case of a single input wave $\underline{E}_1$.

In the unfolded geometry the UNI contains two pieces of HiBi fiber. One piece ($\mathbf{J}_{\text{in}}^{\text{HiBi}}$) to introduce the temporal delay between orthogonally polarized components of the incoming wave and the other ($\mathbf{J}_{\text{out}}^{\text{HiBi}}$) to cancel the delay. Their Jones matrices are derived using the coordinate transformation matrix $\mathbf{R}(\Theta)$ (A.18):

$$\begin{aligned}\mathbf{J}_{\text{in}}^{\text{HiBi}} &= \mathbf{R}(-\theta)\,\sqrt{1-\kappa_{\text{HiBi}}}\begin{pmatrix} e^{i\phi_{\text{DGD}}} & 0 \\ 0 & 1 \end{pmatrix}\mathbf{R}(\theta) \qquad (2.38)\\ &= \sqrt{1-\kappa_{\text{HiBi}}}\begin{pmatrix} e^{i\phi_{\text{DGD}}}\cos^2(\theta)+\sin^2(\theta) & \left(e^{i\phi_{\text{DGD}}}-1\right)\cos(\theta)\sin(\theta) \\ \left(e^{i\phi_{\text{DGD}}}-1\right)\cos(\theta)\sin(\theta) & e^{i\phi_{\text{DGD}}}\sin^2(\theta)+\cos^2(\theta) \end{pmatrix},\\ \mathbf{J}_{\text{out}}^{\text{HiBi}} &= \mathbf{J}_{\text{in}}^{\text{HiBi}}(\theta+\frac{\pi}{2}) \qquad (2.39)\\ &= \sqrt{1-\kappa_{\text{HiBi}}}\begin{pmatrix} e^{i\phi_{\text{DGD}}}\sin^2(\theta)+\cos^2(\theta) & -\left(e^{i\phi_{\text{DGD}}}-1\right)\sin(\theta)\cos(\theta) \\ -\left(e^{i\phi_{\text{DGD}}}-1\right)\sin(\theta)\cos(\theta) & e^{i\phi_{\text{DGD}}}\cos^2(\theta)+\sin^2(\theta) \end{pmatrix}.\end{aligned}$$

θ is the angle between the fast axis of $\mathbf{J}_{\text{in}}^{\text{HiBi}}$ and the x axis, κ_{HiBi} is the loss coefficient of the HiBi fibers and ϕ_{DGD} is the difference in phase between the wave components propagating along the fast axis and slow axis. In order to cancel the temporal delay, introduced by the first piece of HiBi fiber, the fast axis of $\mathbf{J}_{\text{out}}^{\text{HiBi}}$ is rotated by $\pi/2$ with respect to the fast axis of $\mathbf{J}_{\text{in}}^{\text{HiBi}}$. The Jones matrix $\mathbf{J}$ in (2.36) represents the propagation between the two pieces of HiBi fiber, which corresponds to the propagation through the fiber loop in the folded UNI geometry (Fig. 2.1 d)).

In the following, we want to derive the transmission coefficients of the UNI for a simplified case, where $\alpha = 0$ (no fiber absorption) and $\kappa_{\text{HiBi}} = 0$ (lossless HiBi fiber). Similar to the other two interferometers, the transmission coefficient is defined as

$$T_{pq}\left|\underline{E}_p\right|^2 = \left|\mathbf{M}_{(pq)}\underline{E}_p\right|^2 . \qquad (2.40)$$

Analogue to the discussion in section 2.2.1, the effect of a refractive index change, induced between the two pieces of HiBi fiber (or in the fiber loop) on the transmission coefficients is investigated. The refractive index change leads to a phase difference $\Delta\Phi = \Phi_1 - \Phi_2$

between the separated, orthogonally polarized data components. The Jones matrix **J** is in this case given by

$$\begin{aligned}\mathbf{J} &= \mathbf{R}(-\theta)\begin{pmatrix} e^{i\Phi_1} & 0 \\ 0 & e^{i\Phi_2}\end{pmatrix}\mathbf{R}(\theta) \\ &= \begin{pmatrix} \left(e^{i\Phi_1}\cos^2(\theta)+e^{i\Phi_2}\sin^2(\theta)\right) & \left(e^{i\Phi_1}-e^{i\Phi_2}\right)\sin(\theta)\cos(\theta) \\ \left(e^{i\Phi_1}-e^{i\Phi_2}\right)\sin(\theta)\cos(\theta) & \left(e^{i\Phi_1}\sin^2(\theta)+e^{i\Phi_2}\cos^2(\theta)\right)\end{pmatrix}, \end{aligned} \tag{2.41}$$

where θ is the angle between the fast axis of the first HiBi fiber and the x axis. By substituting (2.41) into (2.36) or (A.5), the transmission coefficients of the UNI can be calculated using (2.40) . For a single, linearly polarized wave $\underline{E}_1 = |\underline{E}_1|\begin{pmatrix}\cos(\theta_{in})\\ \sin(\theta_{in})\end{pmatrix}$, where θ_{in} is defined with respect to the x axis, the transmission coefficients become

$$T_{12}\,|\underline{E}_1|^2 = \left|\mathbf{M}_{(12)}\underline{E}_1\right|^2 = \left|\sin(\theta)\cos(\theta)\left(e^{i\Phi_1}-e^{i\Phi_2}\right)\right|^2\cos^2(\theta_{in})\,|\underline{E}_1|^2$$

$$\begin{aligned}\Rightarrow T_{12} &= \left[\sin^2(\theta)\cos^2(\theta)+\sin^2(\theta)\cos^2(\theta)-2\sin^2(\theta)\cos^2(\theta)\cos(\Delta\Phi)\right]\cos^2(\theta_{in}) \\ &= \left[2\ \sin^2(\theta)\cos^2(\theta)(1-\cos(\Delta\Phi))\right]\cos^2(\theta_{in})\end{aligned} \tag{2.42}$$

and

$$\begin{aligned}T_{11}\,|\underline{E}_1|^2 &= \left|\mathbf{M}_{(11)}\underline{E}_1\right|^2 = \left|e^{i\Phi_1}\sin^2(\theta)+e^{i\Phi_2}\cos^2(\theta)\right|^2\cos^2(\theta_{in})\,|\underline{E}_1|^2 \\ \Rightarrow T_{11} &= \left[\sin^4(\theta)+\cos^4(\theta)+2\sin^2(\theta)\cos^2(\theta)\cos(\Delta\Phi)\right]\cos^2(\theta_{in}).\end{aligned} \tag{2.43}$$

First of all, the transmission through the interferometer depends on the polarization state (θ_{in}) of the incoming wave, even under ideal conditions. This is obviously due to the polarizing beamsplitter at the input of the interferometer. In the following it will be assumed that the polarization state of the incoming wave is optimized for maximum transmission through the polarizing beamsplitter ($\theta_{in} = 0$).

The form of (2.42) and (2.43) is very similar to the interference equations derived for the Sagnac and Mach-Zehnder Interferometer. This becomes obvious when $\cos^2(\theta)$ is replaced by a field coupling constant k

$$T_{12} = 2(1-k)k(1-\cos(\Delta\Phi)) \tag{2.44}$$

$$T_{11} = (1-k)^2 + k^2 + 2(1-k)k\cos(\Delta\Phi) = 1 - T_{12}. \tag{2.45}$$

θ is the angle between the fast axis of the HiBi fiber and the x axis, which is the transmission axis of the polarizing beamsplitter. By changing θ, the amplitude ratio between the orthogonally polarized components is varied. This corresponds to a change of the coupling constant in the Sagnac or Mach-Zehnder Interferometer. Equation 2.44 and 2.45 are interference equations, very similar to those derived for the other two interferometers. They are, however, not identical, which becomes clear if a phase difference of zero ($\Delta\Phi = 0$) is assumed between the separated beams. In this case the transmission coefficients become constant ($T_{12} = 0, T_{11} = 1$) for the UNI. For the Sagnac and Mach-Zehnder Interferometer the coefficients still depend on the coupling coefficient k and are given by R_{11} or $T_{12} = (2k-1)^2$ and T_{12} or $T_{11} = 1-(2k-1)^2$.

The Ultrafast-Nonlinear Interferometer is a cyclic interferometer, because the separated beams travel through the same fiber. Therefore it can be operated without active stabilization, similar to the Sagnac Interferometer.

2.3 Interferometric Switches based on HNLF

In this section the formulas derived in section 2.1 and 2.2 are applied to derive the transmission properties of two interferometric gates, the Nonlinear Optical Loop Mirror (NOLM) and the Kerr-Switch. Both switches use highly nonlinear fiber (HNLF) as nonlinear medium. HNLF is a special type of fiber with an increased nonlinear coefficient γ, given by (2.18). A high γ value is generally unwanted in optical fibers for long-haul transmission, because they lead to severe nonlinear distortions of the transmitted data signal. In the case of interferometric switching, a γ value as high as possible is desirable, to increase the cross-phase modulation effect. Due to the non-resonant nature of the nonlinear effects in optical fiber, γ is rather low for conventional fiber (about 1 $\mathrm{W^{-1}km^{-1}}$). The high γ values in HNLF (up to 25 $\mathrm{W^{-1}km^{-1}}$) are realized by increasing n_2 (or in fact $\boldsymbol{\chi}^{(3)}$) and by reducing the effective area A_{eff} of the fiber. The first can be achieved by doping the core with e.g. Germanium. The second is realized by reducing the core diameter.

2.3.1 Nonlinear Optical Loop Mirror

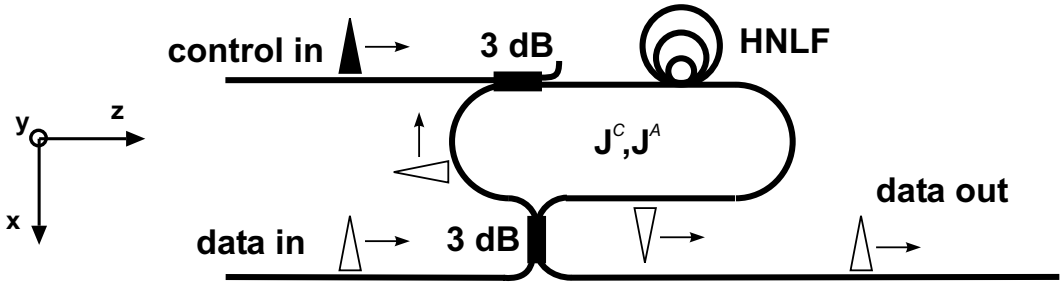

Figure 2.6: Schematic setup of the Nonlinear Optical Loop Mirror (NOLM).

The setup of the NOLM is shown in Fig. 2.6. It is based on the Sagnac Interferometer. The nonlinear medium is a piece of highly nonlinear fiber (HNLF), incorporated in the Sagnac loop. The operation principle of the switch is as follows. The incoming data signal is split at the 3 dB coupler. The split components travel in opposite direction through the fiber loop including the HNLF and interfere again at the 3 dB coupler. The power at the output of the interferometer depends on the phase difference $\Delta\Phi$ between the clock- and anticlockwise traveling data pulse components. This was discussed in detail in section 2.2.1. It was shown that for a phase difference of $\Delta\Phi = 0$ the Sagnac Interferometer works as a mirror and all incoming light is reflected. If a phase difference of $\Delta\Phi = \pi$ is induced between the split pulse components the data signal will be completely transmitted. In the NOLM the phase difference is induced by cross-phase modulation through optical control or pump pulses, inserted into the fiber loop via a second 3 dB coupler.

For the calculation of the transmission and reflectivity coefficients of the NOLM, the following simplifying assumptions are made:

– The optical fiber and the 3 dB coupler are lossless ($\alpha = 0$, $\kappa = 0$). The 3 dB coupler is polarization independent ($k_x = k_y = k$) and the influence of the second 3 dB cou-

pler to insert the pump pulses is completely neglected. The fiber loop is assumed to consist only of the HNLF.

– The HNLF has negligible polarization mode dispersion (PMD) and chromatic dispersion, to assure a complete overlap of data and pump pulses while traveling through the HNLF. The only nonlinear effects considered are self-phase modulation of the data signal and cross-phase modulation between the co-propagating data and pump signals. A nonlinear interaction between the counter-propagating data and pump signals is neglected.

– The pump signal is linearly polarized along the x axis. The data signal is also linearly polarized, either parallel or orthogonal to the pump. The data signal, given by the Jones vector $\underline{E}_{\text{in}}$, enters through the data in port.

By using the expression (2.19) derived in section 2.1 for the nonlinear phase shift in optical fiber, the Jones matrices $\mathbf{J}^C$ and $\mathbf{J}^A$ for clockwise and anticlockwise propagation through the HNLF are given by

$$\mathbf{J}^C = \begin{pmatrix} \mathrm{e}^{i\Phi_{C\parallel}} & 0 \\ 0 & \mathrm{e}^{i\Phi_{C\perp}} \end{pmatrix}, \quad \mathbf{J}^A = \begin{pmatrix} \mathrm{e}^{i\Phi_{A\parallel}} & 0 \\ 0 & \mathrm{e}^{i\Phi_{A\perp}} \end{pmatrix} \tag{2.46}$$

$$\Phi_{C\parallel} = \frac{\omega}{c} L \left[n_0 + n_2 \frac{P_c(t)}{A_{eff}} + 2n_2 \frac{P_{pump}(t)}{A_{eff}} \right], \quad \Phi_{C\perp} = \frac{\omega}{c} L \left[n_0 + n_2 \frac{P_c(t)}{A_{eff}} + \frac{2}{3} n_2 \frac{P_{pump}(t)}{A_{eff}} \right]$$

$$\Phi_{A\parallel} = \Phi_{A\perp} = \frac{\omega}{c} L \left[n_0 + n_2 \frac{P_a(t)}{A_{eff}} \right].$$

Compared to the Jones matrices $\mathbf{J}^C$ and $\mathbf{J}^A$ for the simple case considered in section 2.2.1, the diagonal elements in (2.46) are not equal. This is due to the polarization dependence of the nonlinear phase shift in HNLF. Φ_C and Φ_A are the phase of the clockwise and anticlockwise propagating data component for the case of parallel ($\parallel$) and orthogonal ($\perp$) polarization of the data and pump signal. $P_c(t)$ and $P_a(t)$ is the optical power of the clockwise and anticlockwise propagating data component, $P_{pump}(t)$ the power of the pump signal and L the length of the HNLF.

To calculate the transmission and reflectivity coefficients, given by (2.27), (2.46) is substituted into the transfer matrix $\mathcal{M}_{\text{Sagnac}}$ of the Sagnac Interferometer (see section 2.2.1 and Appendix A.5)

$$\begin{aligned} R_{11} \left| \underline{E}_{\text{in}} \right|^2 &= \left| \mathbf{M}_{(11)} \underline{E}_{\text{in}} \right|^2 \\ &= 2k\,(1-k) \left[\left(1 + \cos\left(\Delta\Phi_{\parallel} \right) \right) |E_{in,x}|^2 \right. \\ &\qquad \left. + \left(1 + \cos\left(\Delta\Phi_{\perp} \right) \right) |E_{in,y}|^2 \right] \end{aligned} \tag{2.47}$$

$$\begin{aligned} T_{12} \left| \underline{E}_{\text{in}} \right|^2 &= \left| \mathbf{M}_{(12)} \underline{E}_{\text{in}} \right|^2 \\ &= \left[1 - 2k\,(1-k) \left(1 + \cos\left(\Delta\Phi_{\parallel} \right) \right) \right] |E_{in,x}|^2 \\ &\quad + \left[1 - 2k\,(1-k) \left(1 + \cos\left(\Delta\Phi_{\perp} \right) \right) \right] |E_{in,y}|^2 \end{aligned} \tag{2.48}$$

with

$$\Delta\Phi_{\parallel} = \frac{\omega}{c} L n_2 \left[\frac{P_{in}(t)}{A_{eff}} (1-2k) + 2\frac{P_{pump}(t)}{A_{eff}} \right], \Delta\Phi_{\perp} = \frac{\omega}{c} L n_2 \left[\frac{P_{in}(t)}{A_{eff}} (1-2k) + \frac{2}{3}\frac{P_{pump}(t)}{A_{eff}} \right].$$

It can be seen that the transmission and reflection properties of the NOLM depend on the input polarization even for a polarization independent 3 dB coupler. This is due to the polarization dependence of the cross-phase modulation itself. (2.47) and (2.48) can be further simplified by assuming parallel polarization between data and pump pulses ($E_{in,y} = 0$) and an ideal coupling ratio of $k = \frac{1}{2}$ for the 3 dB coupler

$$\begin{aligned} R_{11} &= k(1-k) + k(1-k) + 2k(1-k)\cos\left(\Delta\Phi_{\parallel}\right) \\ &= \frac{1}{2} + \frac{1}{2}\cos\left(\Delta\Phi(\Delta t)\right) \end{aligned} \tag{2.49}$$

$$\begin{aligned} T_{12} &= k^2(1-k)^2 - 2k(1-k)\cos\left(\Delta\Phi_{\parallel}\right) \\ &= \frac{1}{2} - \frac{1}{2}\cos\left(\Delta\Phi(\Delta t)\right). \end{aligned} \tag{2.50}$$

The phase difference between the split signals is here given by

$$\Delta\Phi(\Delta t) = \frac{\omega}{c} L\, n_2\, 2\, \frac{P_{pump}(\Delta t)}{A_{eff}} = 2\,\gamma\,L\,P_{pump}(\Delta t)\,. \tag{2.51}$$

(2.49) and (2.50) are the familiar interferometer formulas. A temporal delay Δt has been introduced to account for a time difference between the data and pump signal. A temporal mismatch between data and pump pulses ($\Delta t \neq 0$) leads to a lower cross-phase modulation. In the simple model used here this can be taken into account by a delay dependent pump pulse power $P_{pump}(\Delta t)$. As a result the shape of the switching window of the NOLM is determined by $P_{pump}(\Delta t)$, which basically follows the shape of the pump pulse.

2.3.2 Kerr-Switch

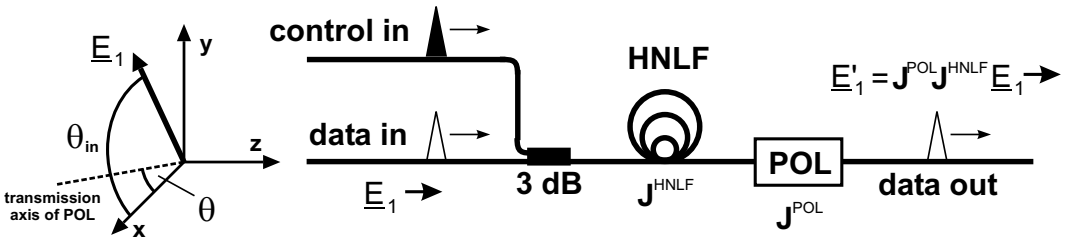

Figure 2.7: Schematic setup of the Kerr-Switch to aid the understanding of the Jones matrix $\mathbf{M}_{\mathrm{KS}}$.

Fig. 2.7 shows the setup of the Kerr-Switch. The switching effect relies on a polarization rotation of the data signal, induced by the pump pulses in the HNLF. The data

signal is launched into the HNLF and afterward blocked by a polarization filter (POL). If a pump pulse is inserted into the HNLF via the 3 dB coupler, such that it overlaps with the data signal, cross-phase modulation occurs. The component of the data signal parallel to the pump will experience a larger phase shift compared to the component orthogonal to the pump, because cross-phase modulation is a polarization dependent effect. This leads to a rotation of the polarization state for the data signal which can then pass the polarization filter.

For the calculation of the transmission coefficient we neglect the influence of the 3 dB coupler. Similar to the discussion of the NOLM, it is assumed that the HNLF has negligible polarization mode dispersion (PMD) and negligible chromatic dispersion, to assure a complete overlap of data and pump pulses while traveling through the HNLF. The only nonlinear effects considered are self-phase modulation of the data signal and cross-phase modulation between the data and pump signal. The pump signal is linearly polarized along the x axis.

The Kerr-Switch is a two-port device and the Jones vector at the interferometer output $\underline{E}'_1$ is straightforward given by

$$\underline{E}'_1 = \mathbf{M}_{(11)}\underline{E}_1 = \mathbf{J}^{\mathrm{POL}}\mathbf{J}^{\mathrm{HNLF}}\underline{E}_1 \ . \tag{2.52}$$

$\mathbf{J}^{\mathrm{HNLF}}$, the Jones matrix representing the HNLF, is identical to the Jones matrix for clockwise propagation in the NOLM given in (2.46). The Jones matrix for the polarization filter is calculated using the coordinate transformation matrix $\mathbf{R}(\Theta)$ (A.18):

$$\mathbf{J}^{\mathrm{POL}} = \mathbf{R}(-\theta)\begin{pmatrix}1 & 0\\ 0 & 0\end{pmatrix}\mathbf{R}(\theta) = \begin{pmatrix}\cos^2(\theta) & \sin(\theta)\cos(\theta)\\ \sin(\theta)\cos(\theta) & \sin^2(\theta)\end{pmatrix} \ , \tag{2.53}$$

where θ is the angle between the transmission axis and the x axis. The multiplication of the two matrices $\mathbf{J}^{\mathrm{POL}}$ and $\mathbf{J}^{\mathrm{HNLF}}$ yields the Jones matrix $\mathbf{M}_{\mathrm{KS}}$ for the Kerr-Switch

$$\mathbf{M}_{KS} = \mathbf{M}_{(11)} = \begin{pmatrix} \mathrm{e}^{i\Phi_{C\parallel}}\cos^2(\theta) & \mathrm{e}^{i\Phi_{C\perp}}\sin(\theta)\cos(\theta)\\ \mathrm{e}^{i\Phi_{C\parallel}}\sin(\theta)\cos(\theta) & \mathrm{e}^{i\Phi_{C\perp}}\sin^2(\theta)\end{pmatrix} \tag{2.54}$$

with

$$\Phi_{C\parallel} = \frac{\omega}{c}L\left[n_0 + n_2\frac{P_c(t)}{A_{eff}} + 2n_2\frac{P_{pump}(t)}{A_{eff}}\right], \quad \Phi_{C\perp} = \frac{\omega}{c}L\left[n_0 + n_2\frac{P_c(t)}{A_{eff}} + \frac{2}{3}n_2\frac{P_{pump}(t)}{A_{eff}}\right].$$

$\Phi_{C\parallel}$ and $\Phi_{C\perp}$ are the phases of the data pulse for parallel and orthogonal polarization of the data and pump signal. $P_c(t)$ is the optical power of the data signal, $P_{pump}(t)$ the optical power of the pump signal and L the length of the HNLF.

By the use of (2.54) the transmission coefficient T_{11} for a linearly polarized data signal $\underline{E}_{\mathrm{in}} = \begin{pmatrix}\cos(\theta_{\mathrm{in}})\\ \sin(\theta_{\mathrm{in}})\end{pmatrix}|\underline{E}_{\mathrm{in}}|$ is

$$T_{11}\,|\underline{E}_{\mathrm{in}}|^2 = |\mathbf{M}_{KS}\underline{E}_{\mathrm{in}}|^2$$

$$\begin{aligned}\Rightarrow T_{11} \ = \ & \cos^2(\theta_{\mathrm{in}})\cos^2(\theta) + \sin^2(\theta_{\mathrm{in}})\sin^2(\theta)\\ & + \sin(\theta_{\mathrm{in}})\cos(\theta_{\mathrm{in}})\sin(\theta)\cos(\theta)2\cos\left(\Delta\Phi(\Delta t)\right) \ ,\end{aligned} \tag{2.55}$$

where θ_{in} and θ are defined with respect to the x axis and

$$\Delta\Phi(\Delta t) = \frac{\omega}{c}\, L\, \frac{4}{3}\, n_2\, \frac{P_{pump}(\Delta t)}{A_{eff}}. \tag{2.56}$$

Similar to the discussion of the NOLM a temporal delay Δt between the pump and probe pulses is taken into account by a delay dependent pump pulse power $P_{pump}(\Delta t)$.

Equation 2.55 shows that the transmittance of the Kerr-Switch is polarization dependent. For an angle $\theta_{in} = 0$ the probe signal is polarized parallel to the pump signal and no polarization rotation occurs. In this case the switch does not work at all. The optimum angle is $\theta_{in} = \pi/4$, where the data components parallel and orthogonal to the pump signal have equal amplitudes. The transmittance also depends on the orientation of the polarization filter. For $\theta = 0$, which corresponds to a filter orientated parallel to the pump pulses, no switching is possible independent of the input state of polarization. The reason is, that an induced change of the polarization state will in this case not change the amplitude after the polarization filter. The optimum orientation for the polarization filter is $\theta = -\pi/4$. Substituting the optimum values $\theta_{in} = \pi/4$ and $\theta = -\pi/4$ into (2.55) yields

$$T_{11} = \frac{1}{2} - \frac{1}{2}\cos\left(\Delta\Phi(\Delta t)\right) = \sin^2\left(\frac{\Delta\Phi(\Delta t)}{2}\right) \tag{2.57}$$

for the transmission coefficient, with

$$\Delta\Phi(\Delta t) = \frac{4}{3}\, \gamma\, L\, P_{pump}(\Delta t)\ . \tag{2.58}$$

(2.57) is the familiar interferometer formula. As expected a rotation of the polarization filter by 90° ($\theta = +\pi/4$) leads to the complementary transmittance function $T = 1/2 + 1/2\cos(\Delta\Phi(\Delta t))$.

A direct comparison of (2.58) with the phase difference (2.51) for the NOLM reveals that the phase difference $\Delta\Phi$ is in principle lower for the Kerr-Switch. As a result, the pump power needed for a π phase shift under equal conditions is 1.5 times higher. The shape of the switching window is similar to the NOLM and mainly determined by the shape of the pump pulse, as long as chromatic dispersion is neglected. While the influence of chromatic dispersion on the switching performance of the Kerr-Switch is comparable to the NOLM, the impairments by PMD are more severe. The reason is, that in the Kerr-Switch $\Delta\Phi$ is reduced to 0 (no polarization rotation), when pump and data pulses have the same polarization state. In the NOLM $\Delta\Phi$ is only reduced by a factor of 3 in the worst case (pump and data pulses are orthogonally polarized).

Chapter 3

Characterization of Semiconductor Optical Amplifiers

3.1 Semiconductor Optical Amplifier

A semiconductor optical amplifier (SOA) is basically a semiconductor laser operated as a broadband single-pass device for amplification. The operation principle is the same as that of other laser amplifiers: the creation of a population inversion that renders stimulated emission more prevalent than absorption. The population inversion is achieved by electric current injection into the p-n junction, like in a semiconductor laser.

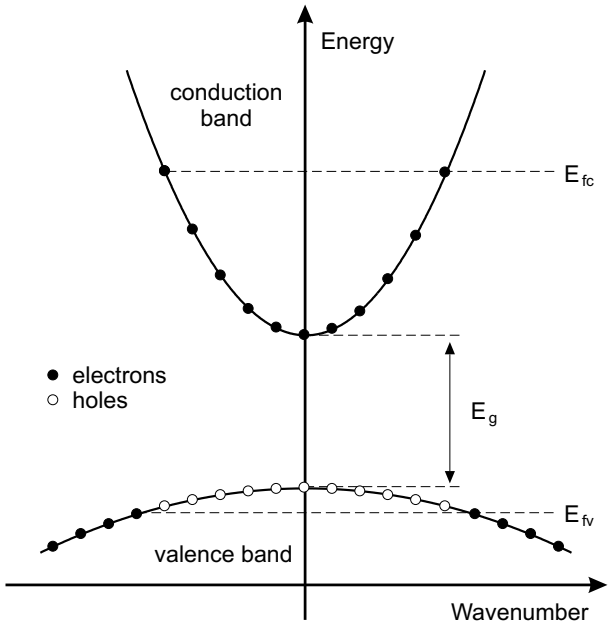

Figure 3.1: Simplified band structure of a direct-gap semiconductor in quasi-equilibrium.

As an example, Fig. 3.1 shows the simplified band structure of a direct-gap semiconductor. The conduction band and the valence band are separated by the bandgap energy E_g.

The current injection leads to the generation of electrons in the conduction band and an equal number of holes in the valence band. In quasi-equilibrium, which arises when the relaxation times for transitions within each of the bands are much shorter than the relaxation time between the two bands, it is appropriate to describe the carrier distribution within each band by separate Fermi functions. The two Fermi levels are then denoted E_{fc} and E_{fv} and are known as quasi-Fermi levels. The position of the quasi-Fermi levels is determined by the pumping rate (current injection). If the pumping rate is sufficiently large, so that the separation between the quasi-Fermi levels exceeds the bandgap energy ($E_{fc} - E_{fv} > E_g$), the semiconductor can act as an amplifier for optical frequencies ν with

$$E_g < h\nu < E_{fc} - E_{fv} \ . \tag{3.1}$$

For $h\nu < E_g$ the medium is almost transparent. For $h\nu > E_{fc} - E_{fv}$ the absorption dominates and the material acts as an attenuator instead of an amplifier.

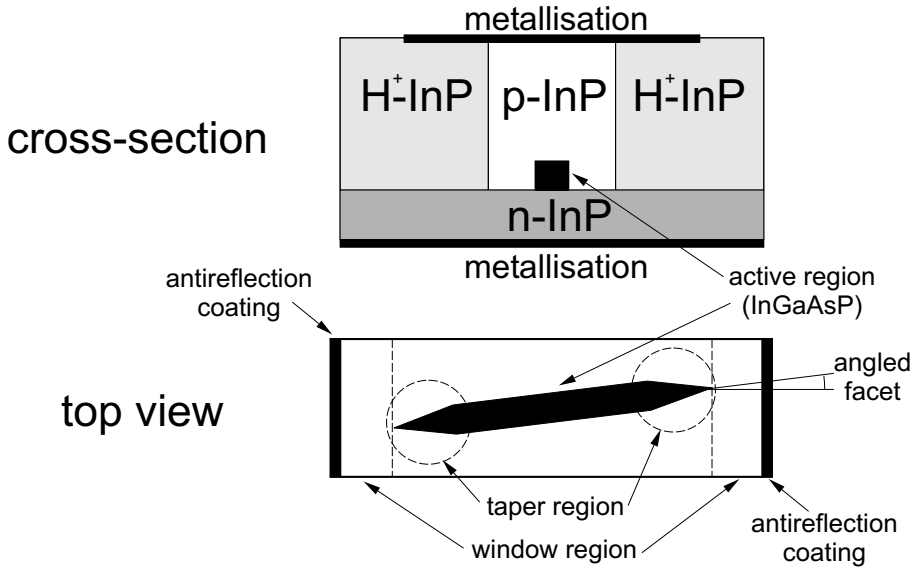

Figure 3.2: Schematic cross-section and top view of a buried ridge stripe SOA, showing a number of methods to reduce the effective facet reflectivity. H^+-InP denotes implanted hydrogen ions for current blocking and improved current injection into the active waveguide region.

SOAs can be classified into two main types: The Fabry-Perot SOA (FP-SOA), where reflections from the end facets are significant, and the traveling-wave SOA (TW-SOA), where reflections are negligible. The FP-SOA is operated below threshold and enables considerable amplification already at low injection currents, but it is more sensitive to fluctuations in bias current, temperature and signal polarization compared to the TW-SOA. In addition, the gain spectrum of the FP-SOA exhibits ripples caused by the reflections at the end facets, which make the device strongly frequency dependent. Therefore, the TW-SOA has replaced the FP-SOA in almost all practical applications. To achieve stable, controllable amplification in a TW-SOA (which will simply be called SOA from now on), care must be taken to reduce the facet reflectance to very low values. Due to the high population inversion, and therefore high single-pass gain achievable in an SOA, an

effective facet reflectivity below 10^{-4} is needed. A number of methods like antireflection coating, angled and window facet structures have been developed to reduce the effective facet reflectivity and are often used simultaneously. The antireflection coating has to consist of multiple layers to achieve wideband low facet reflectivity. In the angled facet structure the active region is slanted away from the facet cleaving plane, thereby reducing the effective facet reflectivity. The window facet structure is simply a transparent region between the active region and the cleaved end facets. The field that is partially reflected at the end facets broadens in space so that only a small fraction is coupled back into the active waveguide region. To improve fiber-chip coupling, sometimes a taper region is integrated in the SOA, in which the width of the active waveguide decreases continuously towards the end facets.

Fig. 3.2 shows the schematic of a typical InGaAsP/InP SOA architecture. The operation wavelength for applications in optical telecommunication is generally around 1.3 µm or 1.55 µm. The structure of the active region can be either bulk or multi quantum-well (MQW). An MQW-SOA has generally a larger gain bandwidth and, in the case of strained quantum-well structures, a low polarization dependence compared to bulk devices. Some characteristic values for an InGaAsP/InP MQW-SOA are shown in Tab. 3.1.

Parameters	typical values
Single-pass small signal gain (fiber-to-fiber)	$25 - 30$ dB
Polarization dependence of the gain	$0.5 - 1$ dB
3 dB saturation output power	$10 - 12$ dBm
3 dB gain bandwidth	≈ 100 nm
Driving current	$100 - 500$ mA
Temperature	25 °C
Length of active region	$300 - 1000$ µm
Width × height of active region	≈ 0.5 µm × 0.5 µm

Table 3.1: Compilation of typical parameters for an InGaAsP/InP MQW-SOA.

3.1.1 Nonlinear Properties

Due to the resonant nature of the nonlinearity, the SOA shows a strong nonlinear behavior, despite the short interaction length of only a few hundred microns. In this case, the polarization density can no longer be expanded in a power series of the electric field (see section 2.1). A field corrected susceptibility $\overline{\boldsymbol{\chi}}\left(\omega, \underline{\widetilde{\mathbf{E}}}\right)$ is often used instead and the wave equation is given by [55]

$$\nabla^2 \underline{\widetilde{\mathbf{E}}}(\omega) + \frac{\omega^2}{c^2}\left[1 + \frac{i\,\sigma}{\epsilon_0\,\omega} + \overline{\chi}\left(\omega, \underline{\widetilde{\mathbf{E}}}\right)\right] \underline{\widetilde{\mathbf{E}}}\left(\omega\right) = 0\ . \tag{3.2}$$

Compared to (2.2) the wave equation for the SOA has an additional term to include the conductivity σ. The susceptibility is treated as a scalar quantity. It is useful to decompose

$\overline{\chi}\left(\omega, \underline{\widetilde{\mathbf{E}}}\right)$ into two parts

$$\overline{\chi}\left(\omega, \underline{\widetilde{\mathbf{E}}}\right) = \overline{\chi}_0 + \overline{\chi}_p \ , \tag{3.3}$$

where $\overline{\chi}_0$ is the medium susceptibility in the absence of external pumping by current injection and $\overline{\chi}_p$ is the additional contribution to the susceptibility related to the strength of pumping.

Similar to equation 2.10 the refractive index n and the absorption coefficient α are linked to the real and imaginary part of $\overline{\chi}\left(\omega, \underline{\mathbf{E}}\right)$ [55]

$$n^2 \approx n_b^2 + \Re\left\{\overline{\chi}_p\right\}, \qquad \alpha \approx \frac{\omega}{c\,n}\left[\Im\left\{\overline{\chi}_0 + \overline{\chi}_p\right\} + \frac{\sigma}{\varepsilon_0\,\omega}\right], \tag{3.4}$$

where $n_b^2 \approx 1 + \Re\left\{\overline{\chi}_0\right\}$ is the background refractive index of the unpumped material. The refractive index n depends on the electric field, because $\overline{\chi}_0$ and $\overline{\chi}_p$ are functions of $\underline{\mathbf{E}}$. This leads to a number of nonlinear effects, including the nonlinear refractive index changes used in interferometric switching. The absorption coefficient in (3.4) has three contributions arising from different sources. The term $\Im\left\{\overline{\chi}_0\right\}$ accounts for the material absorption, while $\Im\left\{\overline{\chi}_p\right\}$ is responsible for its reduction with the external pumping. Their combined effect is generally described as the net optical gain [55]

$$\Gamma g = -\frac{\omega}{c n_b}\Im\left\{\overline{\chi}_0 + \overline{\chi}_p\right\} \ . \tag{3.5}$$

Similar to the refractive index, also the net optical gain g depends on the electric field, which leads to nonlinear changes of the optical gain in the SOA. The constant factor Γ, known as confinement factor, is introduced to describe the reduction in gain due to the spreading of the optical mode beyond the active region of the SOA. The last term in (3.4) accounts for other internal losses. They are summarized by

$$\alpha_{int} = \frac{\sigma}{c\,\varepsilon_0\,n} \ , \tag{3.6}$$

because the individual contributions to these losses are often difficult to estimate. Using (3.5) and (3.6) the standard formula [55]

$$\alpha = -\Gamma g + \alpha_{int} \ , \tag{3.7}$$

for the net absorption coefficient of the SOA can be derived.

In order to use (3.4) to determine the nonlinear phase changes, induced by optical control pulses, in a similar way as was discussed for non-resonant nonlinearities in section 2.1, an expression for the field corrected susceptibility is needed. To this aim a detailed analysis based on quantum mechanics is necessary, which is – because of its complexity – beyond the scope of this work and in most cases not possible. Instead a phenomenological approach is commonly used, based on a description of the carrier density in the SOA with a rate equation model. A differential equation for the gain coefficient g of the SOA has to be derived, which is solved numerically. The refractive index and the arising phase changes are calculated from the gain coefficient using the Kramers-Kronig relation. The rate equation model for the SOA and the relationship between the gain and phase changes, will be addressed briefly in the following section. The description will concentrate mainly on the dynamic processes in the SOA, as they are of particular interest in interferometric switching. A more detailed discussion, including the static behavior of SOAs, is described elsewhere [62, 63, 64].

3.1.2 Phenomenological Description

As stated above, the gain of the SOA results from transitions between the conduction and valence band. These transitions depend on the carrier density and on the carrier distribution in both bands. In order to distinguish the different physical processes, it is useful to consider interband and intraband processes separately. Thus, the gain coefficient can be expressed by

$$g = \underbrace{g_{cdp}(N)}_{interband} + \underbrace{g_{ch}(N,T) + g_{shb}(N,T)}_{intraband} \ . \tag{3.8}$$

$g_{cdp}(N)$ is the contribution caused by interband processes (carrier density pulsation) and depends on the carrier density N. The contributions by intraband processes are mainly due to carrier heating and spectral hole burning, described by separate gain coefficients $g_{ch}(N,T)$ and $g_{shb}(N,T)$ respectively. They depend also on the carrier distribution, described by an effective carrier temperature T.

Interband Processes : The interband processes change the carrier density N but do not affect the carrier distribution. Therefore, the rate equation for the carrier density can be used to derive a mathematical expression for the gain coefficient g_{cdp}. It has to take into account all mechanisms of carrier generation and loss in the active region of the SOA. The carrier diffusion is neglected and the electrons and holes in the SOA are interrelated, because of charge neutrality. It is therefore sufficient for this discussion to consider only the rate equation for the electrons. From now on, the carrier density N denotes the electron concentration in the conduction band and the carrier density rate equation is given by

$$\frac{\partial N}{\partial t} = \frac{J}{ed} - R(N) \ . \tag{3.9}$$

The first term on the right hand side represents the rate of injected electrons into the active layer of the SOA. J is the current density, e the electron charge and d the active-layer thickness. The second term $R(N)$ takes into account the carrier loss caused by various radiative and non-radiative recombination processes. It can be separated into

$$R(N) = R_{spon} + R_{stim} + R_{ASE} \ . \tag{3.10}$$

– For the spontaneous recombination rate

$$R_{spon} = A_{nonrad}N + B_{spon}N^2 + C_{Auger}N^3 \ , \tag{3.11}$$

is commonly used. The coefficients in (3.11) denote non-radiative processes, spontaneous emission and Auger recombination respectively.

– The stimulated recombination rate R_{stim} describes the impact of stimulated emission and absorption. It can be written as

$$R_{stim} = r_{st}S = v_g g S \ , \tag{3.12}$$

where S is the local signal photon density, v_g the group velocity of the signal, g the local gain coefficient and $r_{st} = v_g g$ the net rate of stimulated emission, which is the difference between the rate of stimulated emission and absorption.

– R_{ASE} accounts for the carrier recombination, stimulated by the spontaneously emitted photons, which are not included in the signal photon density S. R_{ASE} is only important for long SOAs at low input powers and will be neglected here.

Substituting (3.10), (3.11) and (3.12) into (3.9) yields

$$\frac{\partial N}{\partial t} = \frac{J}{ed} - R_{spon} - v_g g S \ . \tag{3.13}$$

In order to derive the differential equation for the gain coefficient $g_{cdp}(N)$ from (3.13), the following simplifications are made:

– R_{spon} is expressed by a constant spontaneous carrier lifetime τ_s, which is for small changes independent of N

$$R_{spon} = \frac{N}{\tau_s} \ . \tag{3.14}$$

– $g_{cdp}(N)$ is assumed to be wavelength independent and to depend linearly on the carrier density

$$g_{cdp}(N) = a_N(N - N_0) \quad \text{with} \quad a_N = \frac{\partial g}{\partial N} \ . \tag{3.15}$$

Here a_N is the differential gain coefficient and N_0 is the carrier density at transparency ($g = 0$).

Using these assumptions the differential equation for the gain coefficient g_{cdp} is

$$\frac{\partial g_{cdp}}{\partial t} = a_N \frac{\partial N}{\partial t} = \frac{g_{st} - g_{cdp}}{\tau_s} - \frac{1}{S_s \tau_s} g S \ . \tag{3.16}$$

In (3.16) the saturation photon density $S_s = (1/v_g a_N \tau_s)$ and the unsaturated gain $g_{st} = a_N(N_{st} - N_0)$ (in the absence of an input signal) are introduced. N_{st} is the unsaturated carrier density, given by $N_{st} = J\tau_s/ed$.

The time needed by the carriers to reach the initial distribution after saturation by an optical pulse, is described by an effective carrier lifetime τ_{cdp}. τ_{cdp} depends on the spontaneous lifetime τ_s and the rate of stimulated recombinations R_{stim}. τ_{cdp} is on the order of several hundred picoseconds.

Intraband Processes : The intraband processes change the carrier distribution in the conduction band. The two main processes are spectral hole burning (SHB) and carrier heating (CH). SHB is due to the fact that an incoming short optical pulse interacts only with a certain part of the carrier distribution, depending on the photon energy and the spectral width of the pulse. The pulse causes a reduction (hole) in the carrier distribution at the particular photon energy, resulting in a deviation from the Fermi distribution. The time τ_{shb}, which is the time needed to restore the Fermi distribution by scattering processes (mainly carrier-carrier scattering), is typically several tens of femtoseconds. The carrier-carrier scattering also leads to an increase in the effective carrier temperature, which is called carrier heating. The distribution cools down to the lattice temperature through phonon emission. The CH recovery time τ_{ch} is several hundreds of femtoseconds to a few picoseconds. The differential equations for the gain coefficients $g_{ch}(N,T)$ and $g_{shb}(N,T)$ are given by [17, 63]

$$\frac{\partial g_{ch}}{\partial t} = -\frac{g_{ch}}{\tau_{ch}} - \frac{\epsilon_{ch}}{\tau_{ch}} g S \ , \qquad \frac{\partial g_{shb}}{\partial t} = -\frac{g_{shb}}{\tau_{shb}} - \frac{\epsilon_{shb}}{\tau_{shb}} g S \ . \tag{3.17}$$

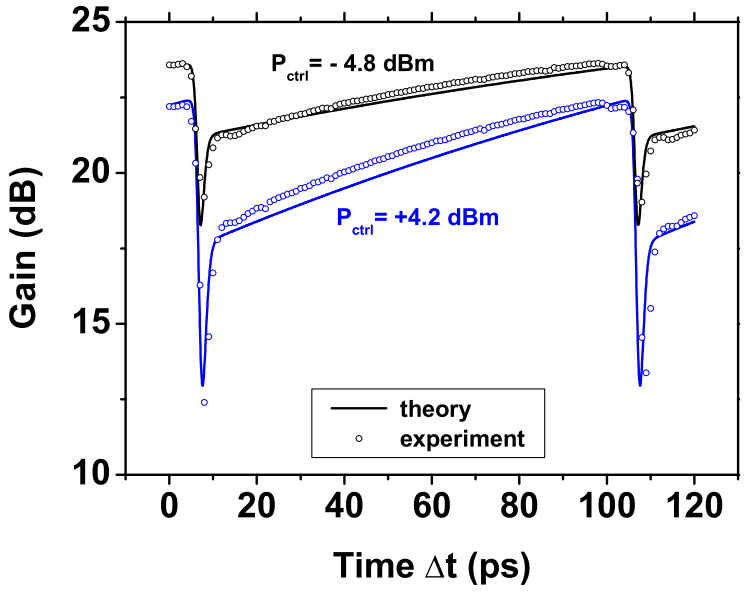

Figure 3.3: Measured and simulated gain dynamics of an MQW-SOA for two different average pump pulse powers P_{ctrl}.

Here ϵ_{ch} and ϵ_{shb} denote the reduction in gain due to carrier heating and spectral hole burning respectively, and are called the nonlinear gain suppression factors.

(3.16) and (3.17) can be used as basis for a numerical time domain model to derive the SOA gain coefficient g as a function of time t and position z. The total single-pass gain G of the SOA, defined as the power ratio between the SOA input and output signal, is linked to the gain coefficient g by

$$G = \exp\left(\int_0^L (\Gamma g(z) - \alpha_{int})\, dz\right) . \tag{3.18}$$

L is the length of the active region in the SOA. The temporal change of the SOA gain G after saturation by a strong optical pump pulse is called the gain dynamics. In Fig. 3.3 simulations of the gain dynamics, using a time domain model [63, 65], are plotted together with experimental results, obtained for an MQW-SOA with a static pump-probe setup (see Fig. 4.1). The device was operated at 300 mA driving current and has a spectral gain maximum around 1300 nm. A strong and fast decrease of the gain is observed, when the pump pulse enters the SOA. This is followed by a fast recovery due to the intraband effects and a slow recovery towards the initial gain level until the next optical pulse saturates the SOA. The different contributions to the fast recovery by spectral hole burning and carrier heating can not be distinguished in Fig. 3.3, because of the limited time resolution of the pump-probe measurement setup. A single nonlinear gain suppression factor is used in the simulations to account for the effects of CH and SHB. The slow recovery towards the initial gain level is governed by the current injection. The parameters used for the simulation are given in Appendix A.8.

In general the nonlinear phase change in the SOA is deduced from the gain changes by using linewidth enhancement factors. Over small ranges within the gain region of the SOA, the phase change can be approximated by [21]

$$\frac{\partial \Delta\Phi}{\partial z} = -\frac{1}{2}\left(\alpha_{cdp}\, g_{cdp} + \alpha_{ch}\, g_{ch} + \alpha_{shb}\, g_{shb}\right) \ , \tag{3.19}$$

where α_{cdp}, α_{ch} and α_{shb} are the linewidth enhancement factors for CDP, CH and SHB respectively. Integration of (3.19) along the propagation direction z yields the total induced nonlinear phase change $\Delta\Phi$. The linewidth enhancement factors for the SOA are in general complicated functions of N, T, z and t. Furthermore they depend on the wavelength and the SOA structure. For simplicity, however, they have to be treated as constants in most simulations. Typical values can be found in Appendix A.8.

Gain-Transparent Operation : The nonlinear phase change for an optical data signal, induced by an optical control signal, depends on the wavelength of both signals. The highest phase change is in general achieved, if the control signal is in the spectral gain region of the SOA. The influence of the wavelength of the data signal is depicted in Fig. 3.4.

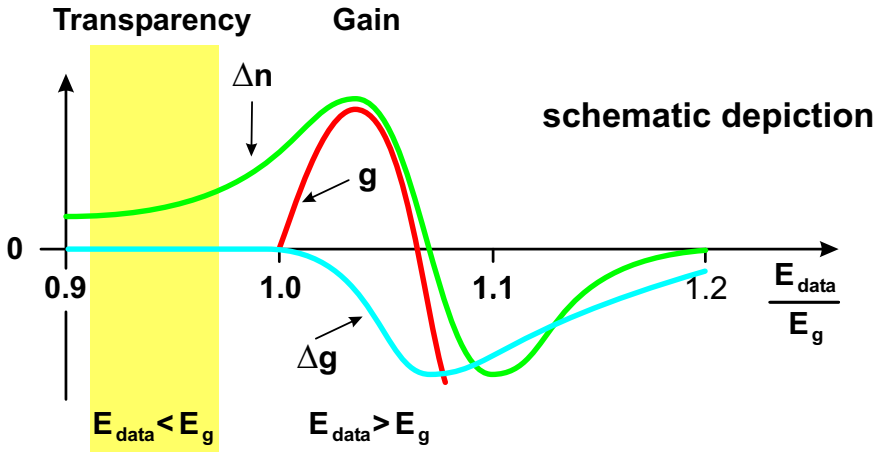

Figure 3.4: Schematic depiction of the SOA gain g, the gain change Δg and the refractive index change Δn as a function of the data signal energy relative to the bandgap energy after [21].

The gain g together with the gain and refractive index change Δg, Δn in the SOA, is shown schematically as a function of the data signal energy $E_{\text{data}} = h\ \nu$ relative to the bandgap energy E_g. It can be seen that Δn has a maximum for a data signal in the spectral gain region. In interferometric switching, an associated phase change

$$\Delta\Phi = \frac{\omega L}{c}\ \Delta n \tag{3.20}$$

as high as possible is desired, where $\omega = 2\pi\ \nu$ is the data signal wavelength and L the SOA length. Therefore the data signal, the control signal and the spectral gain maximum of the SOA are chosen to be in same wavelength range. This is the so called conventional mode of operation. Because the data wavelength in wide span signal transmission is fixed

around 1.55 µm, the spectral gain maximum and the control pulse wavelength are also chosen around 1.55 µm.

Fig. 3.4 also shows, that the refractive index change is not limited to the spectral gain region of the SOA. A considerable phase change can also occur in the transparency region, where the data energy is below the bandgap energy. It was shown in [62], that this phase change for a data signal in the transparency region can be used for interferometric switching. The advantage is, that the gain change for the data signal is significantly lower in the transparency region, which is favorable for interferometric switching. In addition, the noise of the SOA due to amplified spontaneous emission is outside the data wavelength region. If the data wavelength, which is fixed around 1.55 µm, shall be contained in the transparency region of an SOA, the maximum gain region and the wavelength of the control pulses have to be shifted to shorter wavelengths, e.g. 1.3 µm. This is the so called gain-transparent mode of operation, which was first presented in [66]. The name 'gain-transparent' denotes, that the control signal is in the gain region of the SOA, while the data signal is in the transparency region. In the following section, measurements of the gain and phase dynamics in gain-transparent operated SOAs under different operation conditions, as well as a comparison to a conventional operated SOA, is presented. The influence of gain and phase dynamics on the switching performance in interferometric gates is addressed. A detailed investigation on the advantages of gain-transparent versus conventional operation can be found in [62].

In the theoretical description of the SOA presented so far, only gain and refractive index changes within the maximum spectral gain region of the SOA were considered (conventional mode of operation). In the case of gain-transparent operation the gain and phase changes in the transparency region of the SOA have to be considered. For the phase change in the transparency region, the approximation (3.19) may also be used with the gain values for the gain region, but different linewidth enhancement factors [62]. Concerning the gain change it has to be noted, that in the transparency region, the data signal is below the bandgap of the semiconductor material ($h\nu < E_g$), where it experiences no gain by stimulated emission. This means, that the loss due to the fiber-chip coupling (loss parameter a_c) and waveguide scattering (α_w) cannot be compensated. These losses are independent of the number of carriers in the active region. Additional loss comes from carrier dependent effects, mainly free carrier absorption (α_{fca}), which depend on the SOA driving current. The total loss (total loss parameter a_{gt}) for the data signal in the transparency region of a gain-transparent operated SOA with length L amount to

$$a_{gt} = (\alpha_w + \alpha_{fca}(I))\, L + a_c \; . \tag{3.21}$$

The different loss contributions are discussed in section 3.2.3 on the basis of experimental results.

Similar to the dynamics in the gain region, the dynamics of the absorption in the transparency region is governed by the change of the carrier density and the carrier distribution. Experimental results are shown in section 3.2.2. The absorption changes are generally below 1 dB. Therefore, they have only minor impact on the switching performance and will not be discussed in detail in this work. For numerical simulations the dynamics of the phase in the transparency region is assumed to be similar to the phase dynamics in the gain region. This is backed by the experimental results presented in section 3.2.2. Additional information about the theoretical description and numerical

simulations of the gain and phase dynamics in gain-transparent operated SOAs can be found in [64].

3.2 Gain- and Phase Dynamics in SOAs

This section presents direct measurements of the phase and gain dynamics in SOAs, which arise in response to picosecond pulse excitations. The measurements are based on a pump-probe technique in conjunction with a hybrid Mach-Zehnder Interferometer [67]. In order to resolve the fast effects like carrier heating, the timing resolution of the measurement technique has to be in the order of picoseconds or less. Gain-transparent and conventionally operated SOAs are investigated under various operation conditions, especially for different repetition rates of the control or pump pulses and the influence of the gain and phase dynamics on the switching effect will be discussed.

3.2.1 Experimental Setup

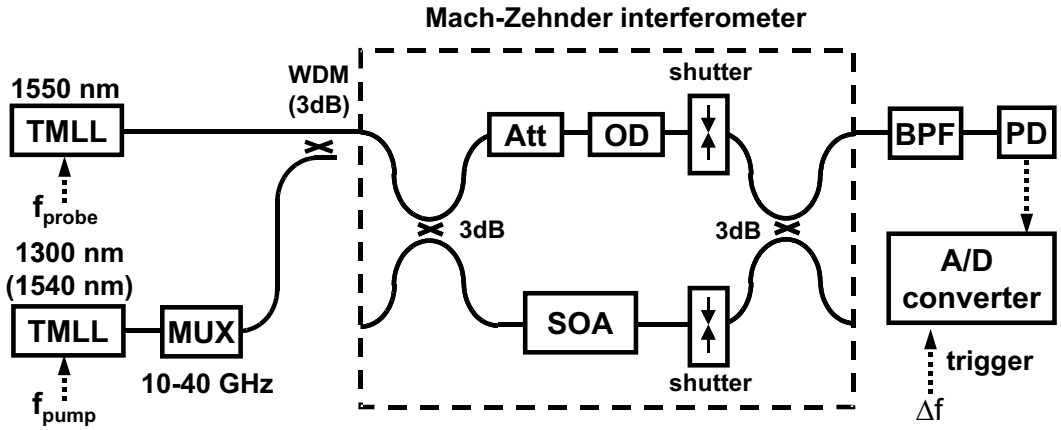

Figure 3.5: Schematic of the experimental setup for dynamic pump-probe measurements.

The experimental setup is shown schematically in Fig. 3.5. A pump-probe technique is used, where weak probe pulses sample the gain and phase changes induced by strong pump pulses. The optical pulses for pump and probe are generated by tunable mode locked lasers (TMLLs). The TMLLs are hybridly mode-locked to external RF-sources with frequencies f_{pump} and f_{probe}. The pulse widths are about 1.3 ps (FWHM). By choosing different frequencies ($f_{\mathrm{pump}} - f_{\mathrm{probe}} = \Delta f \approx 50\,\mathrm{kHz}$) the temporal delay Δt between the pump and probe pulses changes constantly. Therefore the complete gain and phase response is sampled after a period of $1/\Delta f$. The repetition rate of the pump pulses can be increased from 10 GHz up to 40 GHz using a passive fiber delay line multiplexer (MUX). For the investigation of the gain-transparent operated SOAs the pump and probe pulses are combined via a 1300/1550 nm WDM coupler. In the case of the conventional SOA a simple 3 dB coupler is used.
To measure the phase changes $\Phi(\Delta t)$ in the SOA, the phase changes are converted into

amplitude variations by incorporating the SOA in one branch of a hybrid fiber based Mach-Zehnder Interferometer (MZI). For optimum operation of the MZI the effective fiber length, as well as the polarization and the amplitude of the probe signal inside the interferometer have to be adjusted. This is achieved by using an attenuator (Att) and an optical delay line with built-in polarization controller (OD). The amplitude variation is determined by recording the average probe power at the MZI output P_{out} versus the pump-probe delay Δt with a slow photodetection system. It consists of a bandpass filter (BPF) centered at the probe wavelength (1550 nm), a photodiode (PD) and an A/D converter, triggered by a signal with the difference frequency Δf. In the case of the gain-transparent operated SOA a 1300/1550 nm WDM coupler was used instead of the BPF, to separate the probe from the pump signal. The power of the probe signal at the output of the MZI was too low for direct detection with the photodiode (between −10 dBm and −20 dBm), so that an EDFA was necessary to get sufficient probe signal.

An expression for P_{out} can be derived using the results from section 2.2. For a Mach-Zehnder Interferometer with an SOA in one interferometer branch, the Jones matrices $\mathbf{J}^{(1)}$ and $\mathbf{J}^{(2)}$ for the upper and lower interferometer branch are given by :

$$\mathbf{J}^{(1)} = \begin{pmatrix} \mathrm{e}^{\Phi_1} & 0 \\ 0 & \mathrm{e}^{\Phi_1} \end{pmatrix}, \quad \mathbf{J}^{(2)} = \begin{pmatrix} \sqrt{G(\Delta t)}\,\mathrm{e}^{\Phi(\Delta t)+\Phi_2} & 0 \\ 0 & \sqrt{G(\Delta t)}\,\mathrm{e}^{\Phi(\Delta t)+\Phi_2} \end{pmatrix} . \tag{3.22}$$

$G(\Delta t)$ and $\Phi(\Delta t)$ are the gain and phase in the SOA seen by the data pulse, which has a relative delay Δt with respect to the pump pulse. For simplicity it is assumed, that gain and phase are not depending on the polarization and the influence of the other components in the interferometer branches is neglected. Φ_1 and Φ_2 are static phase changes, which are independent of Δt. By substituting (3.22) into the transfer matrix for the Mach-Zehnder Interferometer (given in Appendix A.5, assuming lossless couplers and no fiber absorption) and using (2.32), the transmittance for the upper interferometer output is given by

$$\begin{aligned} T_{11}(\Delta t) &= k^{(1)}\,k^{(2)}\,G(\Delta t) + (1-k^{(1)})\,(1-k^{(2)}) \\ &\quad -2\sqrt{k^{(1)}}\sqrt{k^{(2)}}\sqrt{G(\Delta t)}\sqrt{1-k^{(1)}}\sqrt{1-k^{(2)}}\cos\left[\Delta\Phi(\Delta t)\right] , \end{aligned} \tag{3.23}$$

where $\Delta\Phi(\Delta t) = \Phi(\Delta t) + \Phi_2 - \Phi_1$ is the phase difference between both interferometer branches. In (3.23) polarization independent coupling constants ($k_x^{(1)} = k_y^{(1)}$ and $k_x^{(2)} = k_y^{(2)}$) are assumed. From the probe transmittance T_{11}, the average probe output power P_{out} can be derived

$$\begin{aligned} P_{\text{out}}(\Delta t) &= T_{11}(\Delta t)P_{in} \\ &= \underbrace{(k^{(1)}k^{(2)}G(\Delta t))P_{in}}_{P_1(\Delta t)} + \underbrace{((1-k^{(1)})(1-k^{(2)}))P_{in}}_{P_2} \\ &\quad -2\underbrace{\sqrt{k^{(1)}}\sqrt{k^{(2)}}\sqrt{G(\Delta t)}\sqrt{1-k^{(1)}}\sqrt{1-k^{(2)}}P_{in}}_{\sqrt{P_1(\Delta t)P_2}}\cos\left[\Delta\Phi(\Delta t)\right] , \end{aligned} \tag{3.24}$$

where $P_1(\Delta t) = P_{\text{out}}$ for the upper interferometer branch blocked and $P_2 = P_{\text{out}}$ for the lower interferometer branch blocked. The phase dynamics can be derived from (3.24) by measuring $P_{\text{out}}(\Delta t)$, $P_1(\Delta t)$ and P_2:

$$\Phi(\Delta t) + \Phi_2 - \Phi_1 = \Delta\Phi(\Delta t) = \arccos\left(\frac{P_1(\Delta t) + P_2 - P_{\text{out}}(\Delta t)}{2\sqrt{P_1(\Delta t)P_2}}\right) \tag{3.25}$$

In general, only the phase difference $\Delta\Phi(\Delta t)$ can be calculated and not $\Phi(\Delta t)$, because the static phase difference $\Phi_0 = \Phi_1 - \Phi_2$ is not known. But as Φ_0 is only a time independent offset (in the case of a stabilized interferometer), the dynamics is completely described by $\Delta\Phi(\Delta t)$. In order to compare different measurements, the static phase offset for the calculation of $\Delta\Phi(\Delta t)$ is chosen such, that the phase difference is zero just before the SOA is saturated by the pump pulse. The gain dynamics $G(\Delta t)$ is directly given by $P_1(\Delta t)$. Note that the interferometer has no active phase stabilization. As a result, the static phase difference Φ_0 is slowly varying with time and the average power $P_{\text{out}}(\Delta t)$ is constantly changing. However, this does not disturb the measurement, because the variation is slow compared to the measurement time.

Birefringence in the SOA, induced by the pump signal, can cause a dynamic polarization rotation of the probe signal, which would be misinterpreted as a phase change. This effect can play an important role, if the SOA shows a strong polarization dependence. The dynamic polarization rotation is reduced, when the probe signal is adjusted to propagate along the principle axis of the SOA. In the devices under test, the birefringence is very small, so that the influence of polarization rotation is negligible.

Mainly two effects reduce the accuracy of the measurements: First, a single measured phase dynamic curve $\Delta\Phi(\Delta t)$ is generally affected by noise, induced by power fluctuations in the detection system and by relative jitter between the laser sources. Even small noise contributions can lead to large errors in the phase change, because the inverse cosine is used in the calculation (see (3.25)). Especially if $\cos(\Delta\Phi(\Delta t))$ is close to ± 1, which corresponds to a $\Delta\Phi(\Delta t)$ close to zero or an integer multiple of π.

An example is shown in Fig. 3.6, where $\cos(\Delta\Phi(\Delta t))$, calculated from measurements of $P_{\text{out}}(\Delta t)$, $P_1(\Delta t)$ and P_2, is plotted for three different static phase differences Φ_0 (left hand side). On the right hand side, the corresponding phase dynamics curves $\Delta\Phi(\Delta t)$ are shown. Although the curves for $\cos(\Delta\Phi)$ look rather different, the corresponding phase change curves are very similar. As stated above, the noise in the phase dynamics curves increases, if $\cos(\Delta\Phi(\Delta t))$ is close to ± 1.

For the measurements shown in Fig. 3.6, the maximum phase change in the experiment is well below π. In this case, an optimum value for Φ_0 can be found, where $\cos(\Delta\Phi)$ is around 0 so that the noise level in the calculated phase dynamics curve is kept low. However, if the phase is changing by more than π, this is no longer possible. In this case the errors can be minimized by averaging over several measurements, recorded for different values of Φ_0. In the experiments this is achieved by omitting an active stabilization of the interferometer (see [68] for details on active stabilization of a hybrid MZI), so that thermal fluctuations are not compensated. This leads to a different static phase shift Φ_0 for each recorded $P_{\text{out}}(\Delta t)$.

The second effect, which reduces the accuracy of the measurement, is due to the EDFA that was used to amplify the signal before detection with the photodiode. The output power of the EDFA as a function of the input power is not perfectly linear. This did not affect the measurement of a single curve, because the gain dynamic of the EDFA is to slow to follow the changes in the interferometer (the phase and with it the transmittance of the interferometer changes with a period of $1/50$ kHz $= 20$ µs for a difference frequency of 50 kHz). But the phase dynamic is calculated from three recorded curves ($P_{\text{out}}(\Delta t)$, $P_1(\Delta t)$ and P_2), which have in general different average power levels. This leads to an error, which can be observed in Fig. 3.6 a). Under ideal conditions the $\cos(\Delta\Phi)$-curves would reach ± 1 for a phase shift of π, which is not the case. In addition the average power

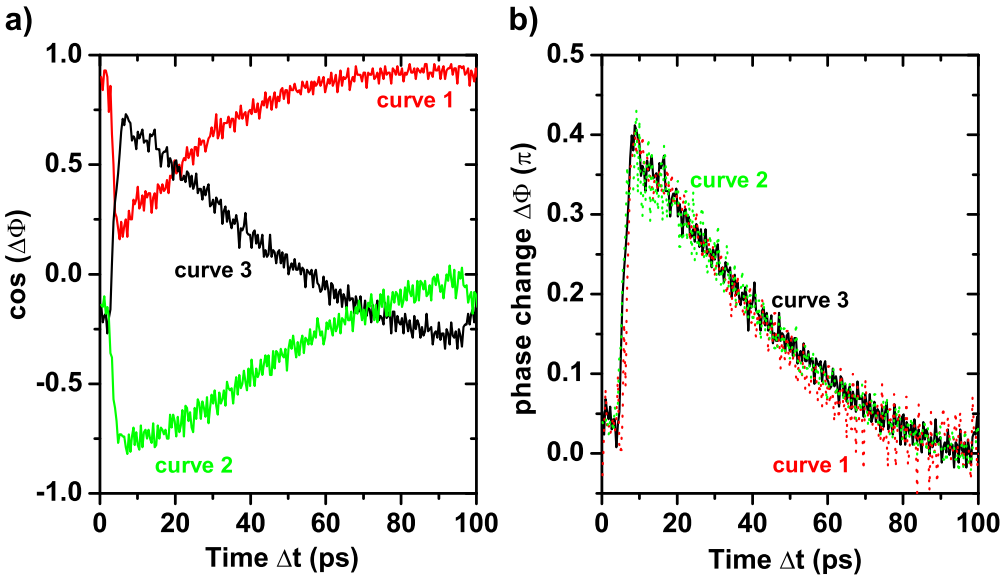

Figure 3.6: Phase dynamic curves for three different static phase differences. a) cosine of the phase difference $\Delta\Phi$ calculated from $P_{\text{out}}(\Delta t)$, $P_1(\Delta t)$ and P_2. b) corresponding phase difference $\Delta\Phi$

level of $P_{\text{out}}(\Delta t)$ varies for different values of the static phase difference Φ_0, which can also be seen from Fig. 3.6. This results in an error, when averaging over measurements with different Φ_0. To minimize these errors the detection system was made as linear as possible by saturating the EDFA with cw light and by taking care to operate the photodiode in the linear regime. All in all, the estimated uncertainty in the derived phase dynamic curves is about 5-10 %.

3.2.2 Conventional versus Gain-Transparent SOAs

In this section a conventionally and a gain-transparent operated SOA are investigated with the measurement setup described above, under comparable operation conditions. The conventionally operated SOA is a 750 µm long bulk device with a gain maximum around 1548 nm. For gain-transparent operation a MQW-SOA (length: 800 µm, gain maximum: 1308 nm) is used. More details about the SOAs can be found in Appendix A.7. For both SOAs a probe wavelength of 1550 nm is chosen. The average probe input power into the SOA is +6 dBm and −15 dBm for the gain-transparent and conventional mode of operation respectively.

10 GHz control pulse rate

The measured gain and phase dynamics for 10 GHz repetition rate of the control pulses are shown in Fig. 3.7. On the left hand side the results for the gain-transparent SOA are plotted. The wavelength of the pump was 1300 nm with an average input power

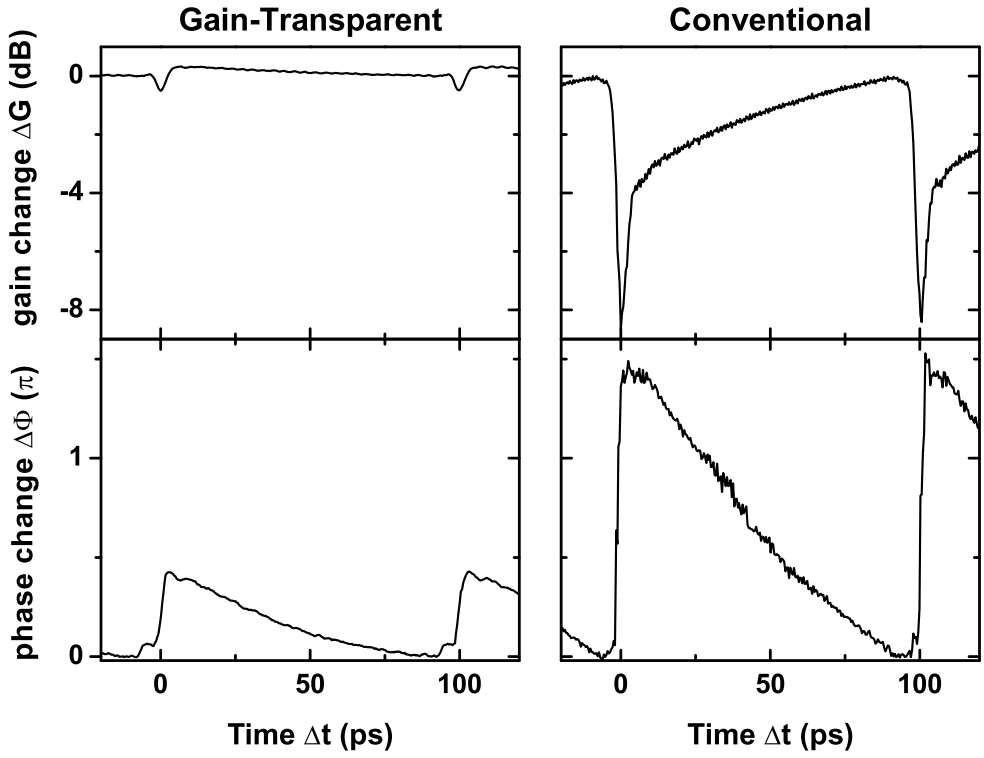

Figure 3.7: Gain and phase dynamics for a gain-transparent and a conventionally operated SOA at 10 GHz control pulse rate.

of +9 dBm (corresponds to a pulse energy of 800 fJ) into the SOA. On the right hand side the measurements for the conventionally operated device are shown. In this case, a 1540 nm pump with +9 dBm (800 fJ) average power was used. For the conventional SOA the predicted (see section 3.1) fast and strong decrease in gain (by about 8 dB), induced by the pump pulses, is observed. It is followed by a fast recovery, resulting from intraband effects like carrier heating (CH), and a slow recovery by electrical pumping towards the unsaturated value (carrier density pulsation, CDP). In the gain-transparent SOA the gain changes are much smaller (below 1 dB) and mainly caused by free carrier absorption. For the conventional SOA a maximum phase shift of 1.4 π is measured, while it is limited to about 0.4 π for the GT-SOA. The phase dynamics show no fast recovery, which suggests that for both SOAs the phase shift by intraband effects is much smaller than the phase changes by CDP.

40 GHz control pulse rate

In order to investigate the impact of an increasing base data rate on the switching performance of an SOA based interferometric switch, the gain and phase dynamics is also measured for a control pulse rate of 40 GHz. The results are shown in Fig. 3.8. The wavelength and average powers for the pump pulses are identical to those given for Fig. 3.7. Note that this results in a reduced pump pulse energy of 200 fJ. It is observed, that the

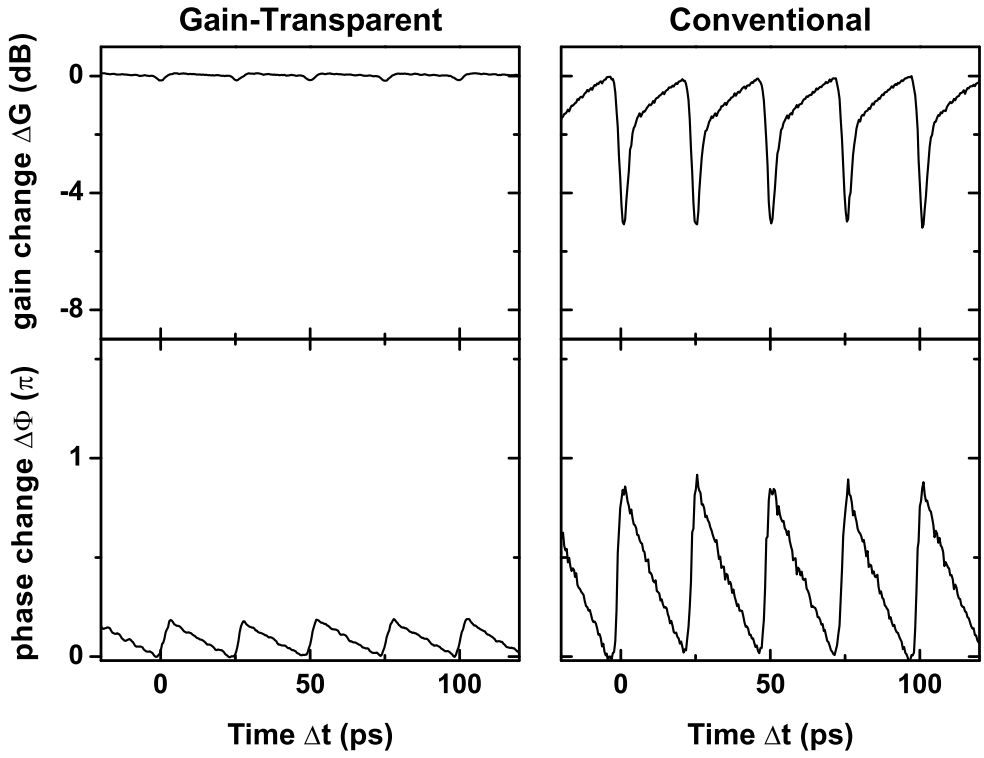

Figure 3.8: Gain and phase dynamics for a gain-transparent and a conventionally operated SOA at 40 GHz control pulse rate.

maximum gain and phase change is reduced for both SOAs, because the time to reach the recovered carrier density shortens with higher rates of the pump pulses. In the gain-transparent case the maximum phase change drops to about 0.2 π, while the maximum gain change stays well below 0.5 dB. For the conventional SOA the maximum gain and phase changes are approximately halved.

Discussion

Fig. 3.7 and Fig. 3.8 show, that the amount of gain and phase change is different for gain-transparent and conventionally operated SOAs and depend on the repetition rate of the control signal. The gain-transparent SOA has lower gain changes, but also a lower maximum phase change. The maximum phase change generally decreases for higher control pulse rates. In the following, the influence of the gain and phase changes on the switching windows of an SOA based interferometric switch will be discussed.

Phase change: The shape of the switching window in an interferometric switch is mainly determined by the shape of the phase change curve. For most applications, switching windows with steep rising and falling edges and a high on-off ratio are needed. The edges of the switching window are given by the steepness of the phase change, induced by the control pulses in the SOA. The steepness of the phase change is mainly determined

by the shape of the control pulses, because the phase change in the SOA occurs almost instantaneously. Only in the case of the SLALOM switch (see 4.1), where both split data components do not co-propagate with respect to the control pulses, the steepness is also influenced by the SOA length. For a good on-off ratio, a good suppression in the off state of the switch is needed, which means a phase difference of zero between the interferometer branches. In the differential switching scheme, explained in detail in the introduction, this is only achieved if the slow recovery of the phase Φ_1 and Φ_2 in both interferometer branches is identical. Under the assumption that both phase curves differ only by a constant factor and a phase offset ($\Phi_2(t) = A(\Phi_1(t) + \Phi_0)$), the condition for an optimum recovery curve is given by:

$$\begin{aligned} \Phi_1(t + t_0) &= \Phi_2(t) \\ &= A(\Phi_1(t) + \Phi_0) \ , \end{aligned} \tag{3.26}$$

where t_0 is the temporal separation between both phase curves. A solution of (3.26) is the exponential function

$$\Phi(t) = b\,\mathrm{e}^{t/\tau} + c \qquad (b, c \in \mathbb{R}) \ , \tag{3.27}$$

with $A = \mathrm{e}^{\frac{t_0}{\tau}}$, $\Phi_0 = c\,(\mathrm{e}^{-\frac{t_0}{\tau}} - 1)$ and a variable decay time τ. This means, that a good suppression in the off state of the switch is expected, if the slow recovery of the phase curve in the SOA follows an exponential function. This is the case for the gain-transparent and the conventionally operated SOAs. The switching windows will in general not have a flat top, unless the phase dynamic curve shows a linear recovery, which is not the case. The assumption made above to derive (3.26) is reasonable for the UNI switch (section 4.3), where the separated beams travel through the same SOA and for the MZI switch (section 4.2), where identical SOAs are normally used in both interferometer branches.

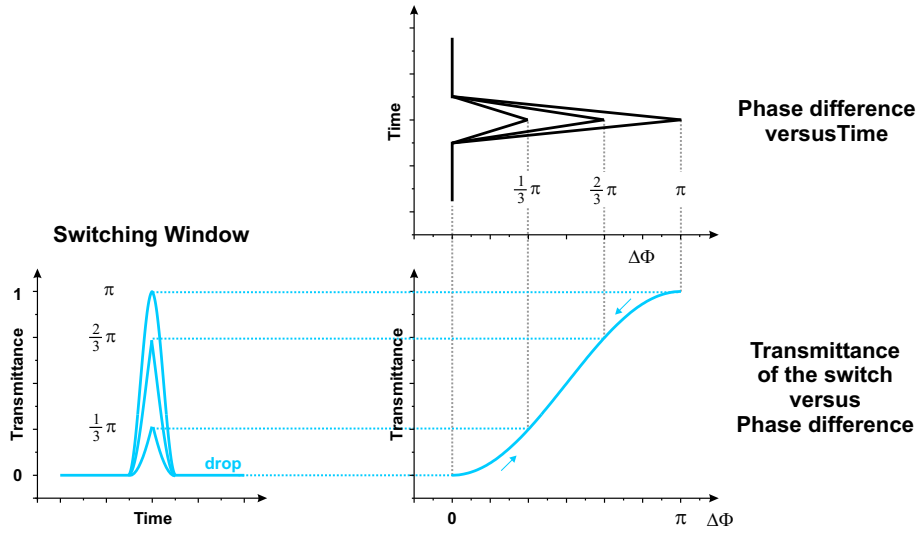

Figure 3.9: Influence of a maximum phase change below π on the switching windows of an interferometric switch.

In order to achieve the maximum possible transmittance in the differential switching scheme, the phase change has to be π (or an integer multiple). A phase change below or

above π results in a reduced transmittance. This is illustrated in Fig. 3.9. The switching windows of an ideal interferometric switch are plotted on the left hand side for maximum phase changes of $\frac{1}{3}\pi$, $\frac{2}{3}\pi$ and π. The phase difference between the interferometer branches over time (plotted in the upper part), is assumed to be an idealized triangular function. The transmittance function of the interferometer ($T(\Delta\Phi) = 0.5 - 0.5\cos(\Delta\Phi)$) is shown in the center.

It can be clearly seen that a maximum phase change below π results in a lower transmittance and therefore a lower maximum amplitude of the switching windows. Also the on-off contrast ratio is reduced. In addition, the switching window has a more pointed shape, so that the full width at half maximum is decreased. This makes the switch less tolerable to timing jitter in the data signal, which is especially disadvantageous for applications like 3R-Regeneration.

Gain change: A change of the SOA gain leads to an amplitude change for the signal propagating through the SOA. If the SOA is incorporated in an interferometric switch, this will invoke additional amplitude variations in the data signal, transmitted through the switch. Strong amplitude variations can significantly degrade the performance of SOA based switches, depending on the application. This is illustrated in Fig. 3.10, where the amplitude changes for a 16×10 Gbit/s = 160 Gbit/s OTDM data signal in the case of a gain-transparent and a conventionally operated SOA are shown schematically.

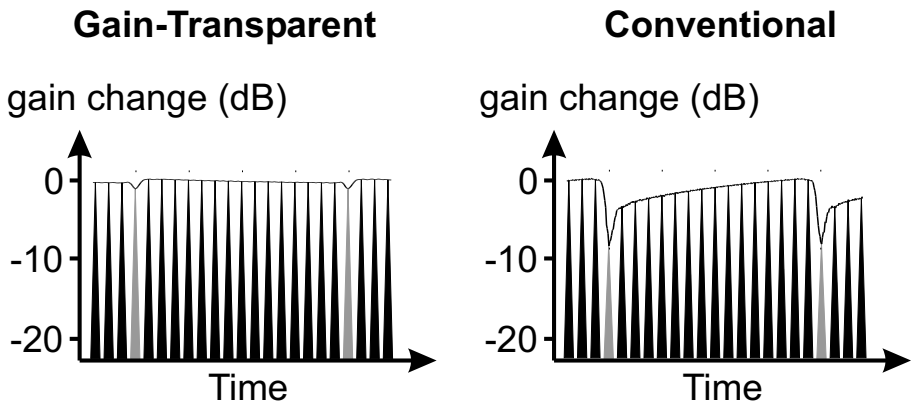

Figure 3.10: Schematic to illustrate the influence of the gain variation on the data signal transmitted through an interferometric switch based on a gain-transparent and a conventionally operated SOA.

For the gain-transparent SOA (left hand side), the modulation is significantly smaller compared to the conventional SOA (right hand side). In the application of the switch as demultiplexer, where one of the 10 Gbit/s base rate channels (indicated in gray) is extracted, the amplitude variation is not important, because the amplitudes of the pulses within a single base rate channel stays constant. However, if all OTDM channels are used (for example in add-drop multiplexing) the amplitude modulation leads to a severe degradation of the data signal. This will be explained in more detail in section 5.3.

Conclusion: For the gain-transparent operated SOA the gain variations are low (<1 dB) so that the impairments due to amplitude variations described above are negligible for most applications. However, the measurements of the phase dynamic showed that the maximum phase shift, which is achieved in a gain-transparent operated SOA is

four times lower compared to conventionally operated SOAs and well below π. In the case of conventionally operated SOAs it is possible to reduce the gain variations by using a lower SOA current, lower pump pulse power or by clamping the SOA with an additional cw-signal. However, this also reduces the maximum phase change that can be achieved. This means that for the application of conventionally operated SOAs in interferometric switching a compromise has to be found between the required phase change and the distortions induced in the switched signal by the gain variation in the SOA. The gain-transparent operated SOA has advantages due to the very small gain variation as long as no complete phase shift of π is required. The lower phase shift imposes no problems in applications like demultiplexing as will be shown in section 5.1 and 5.2. In applications like add-drop multiplexing where a phase shift of π is normally essential and gain changes are not tolerable a special switching geometry is found to make the use of gain-transparent SOAs possible (see section 5.3).

3.2.3 Gain-Transparent SOAs under various operation conditions

The following section concentrates on the gain-transparent operated SOAs. Measurements are presented, to investigate the phase dynamics under various operation conditions, like different average powers of the control pulses and different driving currents. The main concern is to identify the parameters to achieve a high phase shift. The figure of merit is the maximum phase shift $\Delta\Phi_{max}$, which is defined as the maximum phase variation in the measured phase dynamics curve. Two different types of GT-SOAs, a multi quantum well (MQW) and a bulk device are compared (for details about the investigated SOAs see Appendix A.7).

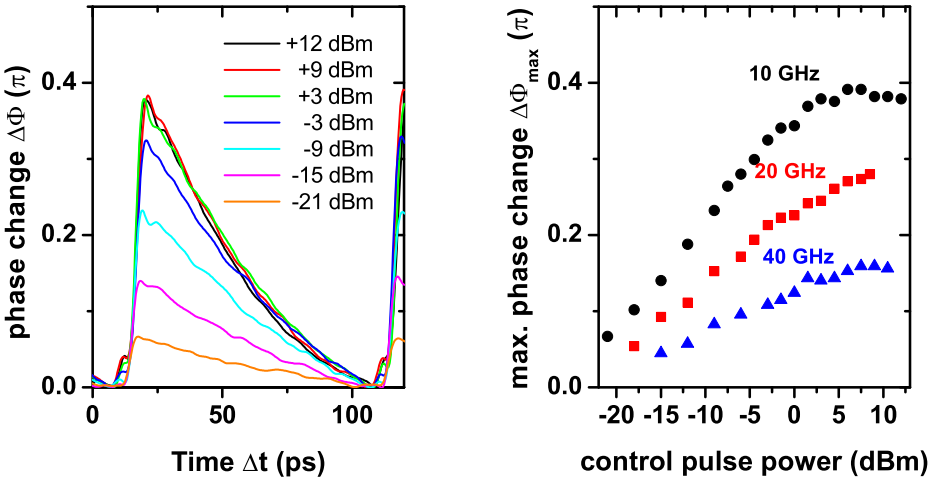

Figure 3.11: Phase dynamics of a gain-transparent operated MQW-SOA for different control pulse powers.

MQW-SOAs

The experimental setup described in section 3.2.1 is used to measure the phase dynamics of a gain transparent operated MQW-SOA (length: 800 µm, gain maximum: 1308 nm) for different control pulse powers and different driving currents. The wavelength of the pump pulses as well as the wavelength and average power of the probe pulses are identical to those used in section 3.2.1.

The results for different control pulse powers are shown in Fig. 3.11 for an SOA current of 300 mA. On the left hand side, the phase change $\Delta\Phi$ is plotted as a function of time for average control pulse powers from −21 dBm to +12 dBm. The repetition rate of the control pulses is 10 GHz. It can be seen, that the maximum phase shift increases with higher control pulse power and saturates above approximately 0 dBm. This becomes more obvious from the right hand side of Fig. 3.11, where the maximum phase shift is shown as a function of the control pulse power for control pulse repetition rates of 10 GHz, 20 GHz and 40 GHz. The maximum phase change saturates in all three curves. About 100 fJ pulse energy (corresponding to 0 dBm, +3 dBm and +6 dBm for 10 GHz, 20 GHz and 40 GHz respectively) is sufficient to reach the maximum possible phase change, independent of the pump pulse rate.

Fig. 3.12 shows the phase dynamic measurements for different SOA driving currents at an average control pulse power of +9 dBm. On the left hand side the phase change $\Delta\Phi$

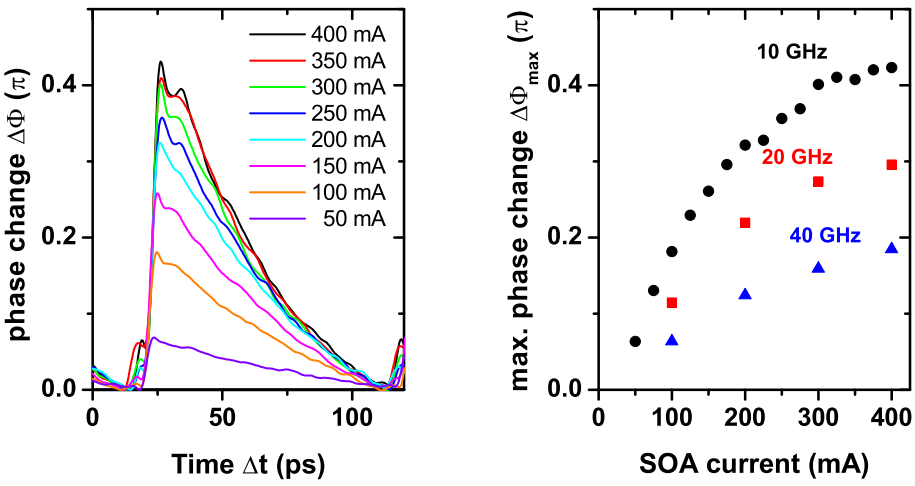

Figure 3.12: Phase dynamics of a gain-transparent operated MQW-SOA for different SOA currents.

is plotted as a function of time, for SOA currents from 50 mA to 400 mA. The repetition rate of the control pulses is 10 GHz. Similar to the results for different control pulse powers, described above, the maximum phase shift is increasing with higher SOA current. Also a slight saturation effect can be observed. On the right hand side of Fig. 3.12 the maximum phase shift as a function of SOA current is shown for three different repetition

rates of the control pulses. The saturation of the maximum phase shift with increasing SOA current is observed independent of the control pulse repetition rate, but not as distinct as with increasing control pulse power.

Bulk-SOAs

Phase curves for a bulk GT-SOA under different operation conditions are measured to investigate the influence of the SOA structure on the maximum phase shift. The gain-transparent bulk-SOA was a 500 µm long device with a gain maximum around 1304 nm. The wavelength of the probe and control pulses are not changed. The average probe power into the SOA was +6 dBm with a pulse width of 1.5 ps.

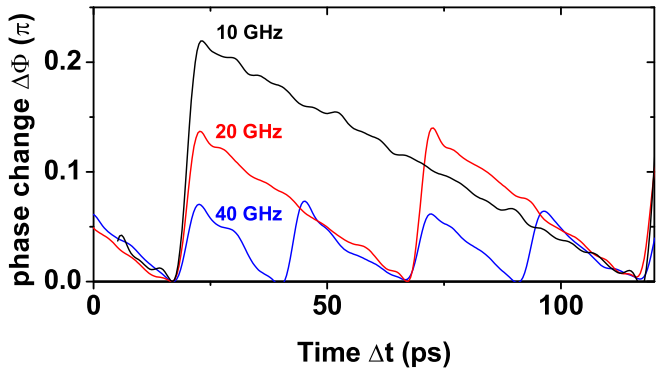

Figure 3.13: Phase dynamics of a gain-transparent bulk-SOA for different control pulse rates

Fig. 3.13 shows typical phase dynamic curves, measured for the bulk-SOA using different repetition rates of the control pulses. The SOA driving current was 250 mA and the control pulse energy was kept constant at 400 fJ. The curves look similar to the phase dynamics measured for the MQW-SOA. The maximum phase change is generally lower. A value of 0.22 π is achieved at 10 GHz, which decreases to 0.07 π at 40 GHz.

The bulk-SOA is investigated for different control pulse powers and SOA currents. The maximum phase change is determined from the measured phase dynamic curves and the results are shown in Fig. 3.14. On the left hand side the maximum phase change $\Delta\Phi$ is plotted as a function of the SOA driving current for different repetition rates of the control pulses. The current is varied from 100 mA to 250 mA for a constant control pulse energy of 200 fJ. Compared to the MQW-SOA the bulk device shows only a slight saturation with increasing current. The maximum phase shifts that are achieved correspond to those in Fig. 3.13. On the right hand side of Fig. 3.14 the maximum phase change is plotted as a function of the control pulse power, again for different control pulse repetition rates. The average control pulse power is changed from −9 dBm to +9 dBm. The SOA driving current is set to 400 mA. Also for the control pulse power no strong saturation of the maximum phase change is observed. The maximum phase change measured was 0.22 π for 10 GHz, 0.12 π for 20 GHz and 0.06 π for 40 GHz.

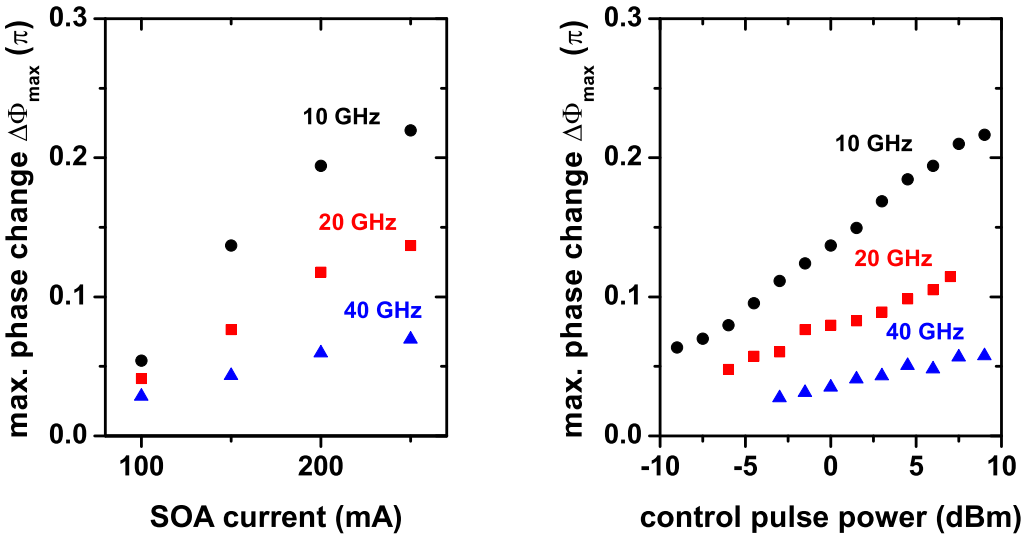

Figure 3.14: Maximum phase change of a gain-transparent operated bulk-SOA under different operation conditions.

Comparison: MQW versus bulk-SOAs

To investigate the influence of the SOA structure in gain-transparent operation, the measured maximum phase changes for the MQW and the bulk device are directly compared. The active region of the bulk-SOA is shorter compared to that of the MQW-SOA. Therefore, the maximum phase change per active region length is plotted in Fig. 3.15. On the left hand side, as a function of the SOA current per active region length for a constant control pulse energy of 800 fJ. On the right hand side, as a function of the control pulse energy for about 400 mA/mm SOA current per length. It can be seen that almost the same maximum phase shift per mm is reached for both devices. Both SOAs show a saturation of the maximum phase shift with increasing current and control pulse energy. While the saturation behavior with current is comparable, the MQW-SOA shows a stronger saturation with control pulse power compared to the bulk device. An SOA current of 500 mA/mm and a control pulse energy of 800 fJ (corresponds to +9 dBm average power at 10 GHz repetition rate) is the maximum that can be applied without risking a severe damage of the devices under test.

In conclusion, it can be said that by increasing the current or the control pulse power, the maximum phase shift in the investigated gain-transparent operated SOAs can not be increased above 0.4 π (0.22 π) for the MQW (bulk) device. The main reason are saturation effects, which are stronger in the MWQ-SOA compared to the bulk device. The different saturation behavior can be explained by the different gain of the devices (see Appendix A.7) and is not entirely due to the different SOA structures. A maximum phase shift of about 0.5 π/mm is achieved for high currents and pump powers in both devices. However, the control pulse energy to reach this value is significantly lower for

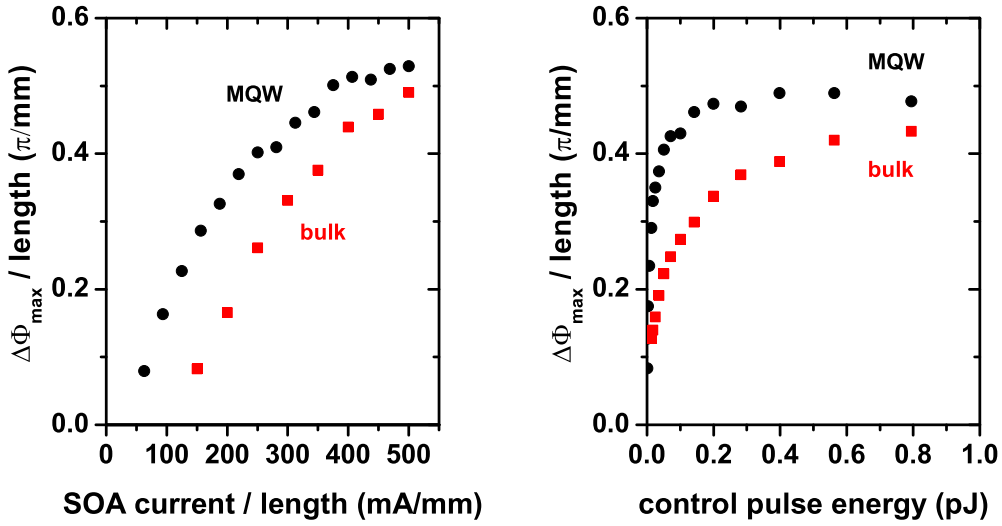

Figure 3.15: Comparison of the maximum phase change in a gain-transparent operated bulk and MQW-SOA under different operation conditions for 10 GHz control pulse rate.

the MQW-SOA (about 200 fJ compared to 800 fJ in the bulk device).

Influence of SOA current and length on transmittance

Another way to increase the phase shift in an SOA is to increase the length of the active region. This causes problems for gain-transparent operation, because the data signal in the transparency region of the SOA experiences no positive gain to compensate for the loss. The increase of the loss with driving current and length of the active region, which is called SOA loss in the following, is shown on the left hand side of Fig. 3.16. The transmittance of a data signal at 1550 nm is plotted as a function of the driving current for an MQW-SOA (800 µm long) and two bulk-SOAs (500 µm and 1500 µm long). The different contributions to the loss in gain-transparent SOAs were discussed in section 3.1.2 and an expression for the total loss parameter a_{gt} was derived (3.21). Using (3.21) the transmittance T of a data signal propagating through the gain-transparent operated SOA is given by:

$$T = \mathrm{e}^{-\left(\left(\alpha_w + \alpha_{fca}(I)\right)L + a_c\right)} \ , \tag{3.28}$$

or in logarithmic scale

$$\log(T) = -\log(\mathrm{e})\left(\left(\alpha_w + \alpha_{fca}(I)\right)L + a_c\right) \ . \tag{3.29}$$

By use of 3.29, the coupling loss a_c and the waveguide absorption coefficient α_w are calculated from the measured transmittance as follows:

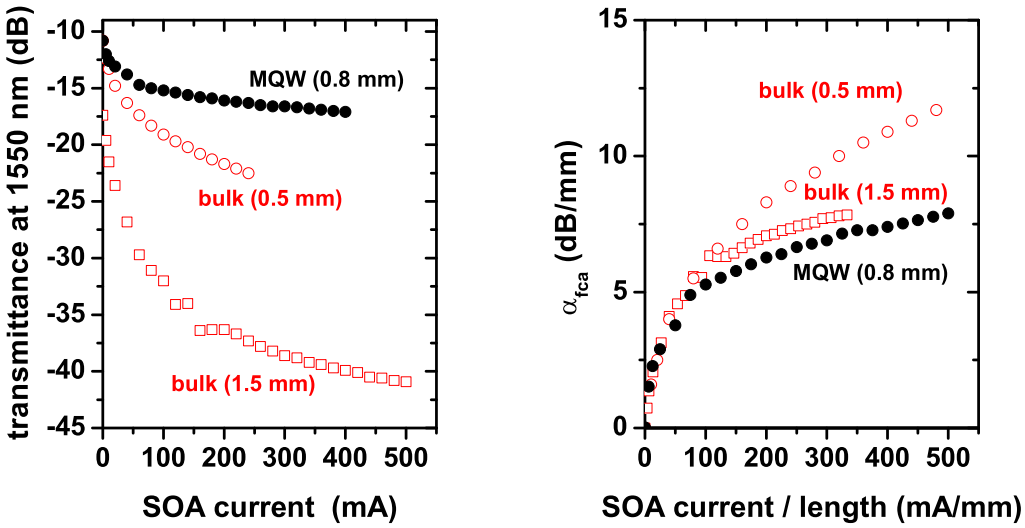

Figure 3.16: Left hand side: transmittance of the data signal in gain-transparent operated bulk and MQW-SOAs as a function of the driving current, Right hand side: absorption coefficient for free carrier absorption in gain-transparent operated bulk and MQW-SOAs.

- **Bulk-SOA:** The transmittance of the two bulk-SOAs with different lenght (500 µm and 1500 µm) at $I = 0$ was measured. Assuming that α_w and a_c are the same for both devices and that α_{fca} vanishes for $I = 0$, values for α_w and a_c can be calculated. The results are $a_c = 17.3$ (7.5 dB) and $\alpha_w = 15.2$/mm (6.6 dB/mm).
- **MQW-SOA:** The transmittance of the MQW-SOA (800 µm long) at $I = 0$ was measured. The coupling loss a_c is assumed to be identical to the value of the bulk devices. Assuming that α_{fca} vanishes for $I = 0$, a waveguide loss coefficient of α_w=4.1 dB/mm is deduced, which is slightly lower compared to the bulk-SOA case. The value for α_w is of course only a rough estimation, because the real coupling loss of the device is not known.

Substituting the values for a_c and α_w into 3.29, yields the free carrier absorption coefficients α_{fca} for the three investigated SOAs. They are plotted on the right hand side of Fig. 3.16 as a function of the driving current per length. For the two bulk-SOAs with different lengths (500 µm and 1500 µm) the free carrier absorption coefficient is not increasing linearly with the current, but start to saturate for higher currents. For currents below 100 mA/mm, α_{fca} seems to be independent of the SOA length. Above that value the coefficient increase faster for the short bulk-SOA. For the maximum applied current α_{fca} reaches 11.7 dB/mm for the short SOA at 480 mA/mm and 7.8 dB/mm for the long device at 333 mA/mm. The free carrier absorption coefficient for the MQW-SOA is also not linear and shows a far stronger saturation with current compared to the bulk devices. At a current of 500 mA/mm a value of 7.9 dB/mm is reached, which is significantly lower compared to the short bulk-SOA.

Up to now, only the influence of the SOA loss on the transmittance was discussed. In order to identify the optimum SOA current and length, with respect to the transmittance in an interferometric switch, also the switching loss has to be considered. In the ideal case of a π phase shift in the SOA, the transmittance in a lossless interferometer is 1 (or 0 dB). For lower phase shifts, the transmittance is reduced (see section 3.2.2). This is called switching loss. The switching loss is calculated from the maximum phase shifts measured for the MQW-SOA, shown in Fig. 3.12, under the assumption of an ideal interferometer (transmittance is given by $T = 0.5 - 0.5(\cos(\Delta\Phi))$). The switching loss for the MQW-SOA is plotted on the left hand side of Fig. 3.17 (dashed curve), as a function of the driving current, together with the SOA loss from Fig. 3.16 (solid curve). For increasing current the maximum phase shift increases, which leads to a decreases in the switching loss (increase in transmittance), as long as the phase shift is below π, which is the case here. The total loss (dotted curve) is the sum of the SOA loss and the switching loss. It can be seen, that up to a current of 300 mA the total loss decreases (transmittance increase), because the increase in transmittance due to the lower switching loss is stronger than the decrease by the SOA loss (free carrier absorption). Above 300 mA the total loss stays approximately constant.

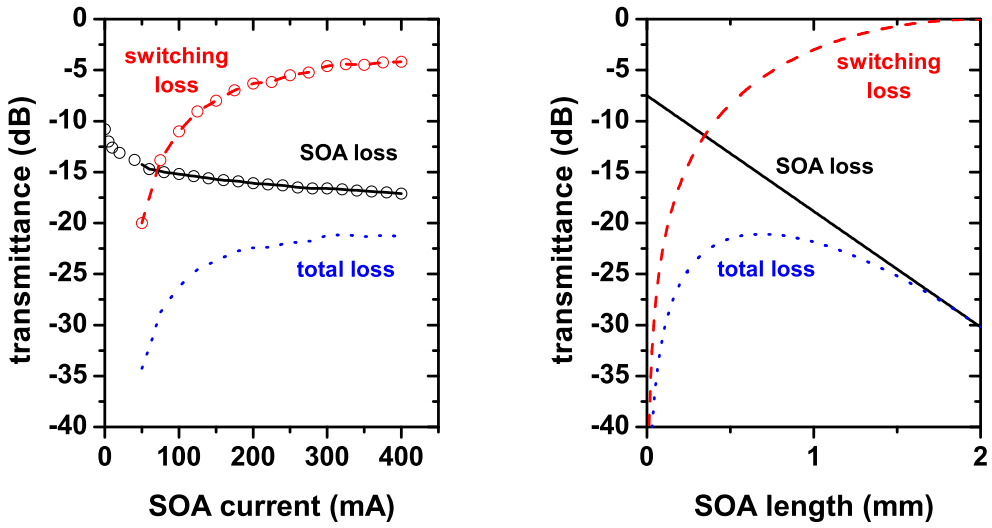

Figure 3.17: Estimation of the transmission loss in a switch using a gain-transparent operated MQW-SOA as a function of the driving current (left hand side) and the active region length (right hand side).

The influence of the SOA length on the transmittance of an interferometric GT-SOA switch, based on an MQW device, is shown on the right hand side of Fig. 3.17. The calculated switching loss, SOA loss and the total loss in the switch are plotted versus the SOA length. The following assumptions are made for the calculations:

– SOA loss: the coupling loss is given by a_c=7.5 dB, the loss coefficients are independent of the SOA length and given by $\alpha_w + \alpha_{fca}$=11.35 dB/mm (measured values for

the 800 µm long MQW-SOA at 300 mA)

– switching loss: ideal interferometer (transmittance $T = 0.5 - 0.5(\cos(\Delta\Phi))$), with $\Delta\Phi$=0.5 π/mm (measured value for the 800 µm long MQW-SOA at 300 mA and 0.5 pJ control pulse energy), independent of the SOA length. This is a best case approximation, because the phase shift per length generally decrease in longer devices.

It can be seen from Fig. 3.17, that the total loss is high for short SOAs, although the SOA loss is low, because of the small accumulated phase shift. For long SOAs the switching loss approaches 0 (transmittance of 0 dB), because the accumulated phase shift is close to π, but the SOA loss increases drastically. An optimum range for the SOA length is found to be between 0.4 mm and 1.2 mm.

Conclusion

In the following, the results for the gain-transparent operated SOA are summarized. The maximum phase shift in MQW and bulk-SOAs increases with driving current and control pulse power, but decrease with the control pulse repetition rate. A saturation effect with current and control pulse power is observed, which is stronger for the MQW device. The maximum phase shift, that could be reached was 0.4 π in the 800 µm long MQW-SOA and 0.22 π in the 500 µm long bulk-SOA at a control pulse repetition rate of 10 GHz. The maximum phase shift drops significantly for higher control pulse rates, because the time for the SOA to recover is shorter.

		MQW	**bulk**
control pulse energy to reach maximum phase shift[a]		100 fJ	800 fJ
$\frac{\text{phase shift}}{\text{length}}$ $\left[\frac{\pi}{\text{mm}}\right]$[b]	10 GHz	0.50	0.44
	40 GHz	0.09	0.12
$\frac{\text{transmission loss}}{\text{length}}$ $\left[\frac{\text{dB}}{\text{mm}}\right]$[c]	α_w	4.1	6.6
	α_{fca}	7.3	10.8[d] / 7.9[e]

[a] maximum phase shift means here the phase shift that was achieved for the highest control pulse power applied to the device

[b] the phase shift per length is generally not constant over SOA length

[c] assuming a constant coupling loss of a_c = 7.5 dB and an SOA driving current of about 300 mA/mm

[d] 0.5 mm long SOA

[e] 1.5 mm long SOA

Table 3.2: Comparison of a gain-transparent operated MQW and bulk-SOAs. The values were derived from measurements on a 800 µm long MQW and a 500 and 1500 µm long bulk-device.

It was also observed, that the transmission loss for 1550 nm light in the gain-transparent operated SOAs increases with current and SOA length. The influence of this effect on the

transmittance of interferometric GT-SOA switches based on MQW devices was estimated. It was found, that the maximum transmittance remains constant above a current of 300 mA, because the increase in transmittance by a maximum phase shift closer to π is compensated by the higher loss through free carrier absorption. An increase of the maximum phase shift by the use of longer GT-SOAs was found to be problematic, because the transmission loss increases drastically with length. A rough estimation showed, that an SOA length between 0.4 mm and 1.2 mm is ideal with respect to the total transmission loss in the switch. This does not take into account other important characteristics of the switch like the on-off contrast and the width of the switching window. Therefore, the ideal SOA length will depend on the application, in particular which switching speed and contrast values are required [69]. The main results of the comparison between the gain-transparent MQW and the bulk-SOAs are summarized in Tab. 3.2. The MQW-SOAs have clearly advantages over the bulk devices, due to the lower transmission loss and the lower control pulse power requirements.

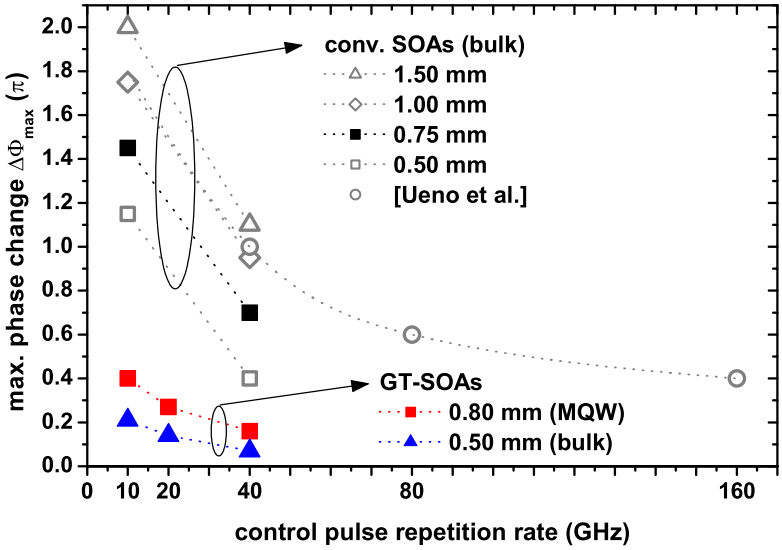

Figure 3.18: Maximum phase change in gain transparent and conventionally operated SOAs as a function of the repetition rate of the control pulses.

The influence of the control pulse rate on the phase shift is summarized in Fig. 3.18. It shows the maximum phase change, obtained for the gain-transparent MQW and bulk-SOAs discussed in this chapter and results for conventionally operated SOAs with different length. The measurements for the conventional SOAs, which are not discussed in detail in this work, are also done using the setup described in section 3.2.1. Details about the measurements can be found in [70]. The dotted lines are simple extrapolations of the maximum phase change. The gain-transparent operated MQW and bulk-SOAs show almost the same decrease in maximum phase change. Above 40 GHz, it is expected that $\Delta\Phi_{max}$ is even further reduced. It was already pointed out that increasing the phase change by using SOAs, longer than about 1.2 mm is not reasonable for gain-transparent

operation, as long as no way is found to reduce the SOA loss.

For the conventionally operated SOAs the phase shift can of course be increased by using longer SOAs, as can be seen from Fig. 3.18. A maximum phase change of 2.0 π is reached for a 1.5 mm long SOA at 10 GHz control pulse rate. At 40 GHz, the maximum phase shift is still above π. For comparison Fig. 3.18 shows the results from a publication by Ueno and his coworkers [71], where the maximum phase change above 40 GHz control pulse rate was measured using a spectral method. These measurements indicate that a reasonable phase shift might still be reached at 160 GHz. However, the results clearly show that it becomes increasingly difficult to reach a π-phase shift at high control pulse rates. Higher control pulse powers are generally needed, which is problematic for the conventionally operated SOA, because it leads to strong gain variations. Therefore SOA based interferometric gates are less attractive for applications like wavelength conversion and 3R-regeneration at high TDM bit rates (160 Gbit/s), which require high control pulse rates (160 GHz). As will be shown in section 5.5, interferometric gates based on fiber can be used instead.

Chapter 4

Interferometric Gates based on Semiconductor Optical Amplifiers

In this chapter, three different types of interferometric switches based on SOAs – the Semiconductor Laser Amplifier in a LOop Mirror (SLALOM), the Mach-Zehnder Interferometer switch (MZI) and the Ultrafast-Nonlinear Interferometer (UNI) – are discussed. The switching characteristics of all three switches are investigated by measurements of the switching windows under different operation conditions. In particular, the influence of the repetition rate of the control pulses is addressed. The switching windows are measured with a pump-probe technique. The experimental setup is shown schematically in Fig. 4.1.

Two tunable mode locked laser diodes (TMLLs) are used to generate the control (also called pump) and data (also called probe) pulses. The repetition rate of both lasers is 10 GHz. The control pulses can be multiplexed to 40 GHz by means of a fiber delay line multiplexer (MUX). Two different measurement modes, static and dynamic, are possible with the setup shown in Fig. 4.1. For the static measurements (Fig. 4.1 a)), both TMLLs are driven by the same RF frequency of 10 GHz and a controllable delay line (DLY) allows the probe pulses to be shifted in time with respect to the pump pulses. Measuring the power transmitted through the switch with an optical spectrum analyzer (OSA) as a function of the delay between the control and data pulses, yields the so called static switching window of the switch. The resolution bandwidth of the OSA is chosen such, that the optical power is integrated over the complete pulse spectrum. For a transform limited optical pulse with a sech^2 shape and 1.3 ps full width half maximum, the optical spectrum has a width of about 1.95 nm. The advantage of the static pump probe measurements are the high temporal resolution that can be reached by using small steps in the delay line and a high sensitivity by averaging the signal in the OSA. The disadvantage is the long measurement time, which depends on the chosen step width for the delay line.

The dynamic measurements (Fig. 4.1 b)) rely on the same principle already presented for the measurements of the phase and gain dynamics in SOAs (see section 3.2.1). By choosing different frequencies ($f_{\mathrm{pump}} - f_{\mathrm{probe}} = \Delta f \approx 50$ kHz) for the TMLLs, the temporal delay Δt between the pump and probe pulses changes constantly. This means that the complete switching window is sampled after a period of $1/\Delta f$ and can be observed online, after bandpass filtering (BPF) with a photo-detector (PD) and an A/D conversion. The A/D converter is triggered by the difference frequency Δf. The disadvantage of this method is, that it suffers from amplitude noise and a limited dynamic range. Also the temporal resolution is limited by the A/D converter.

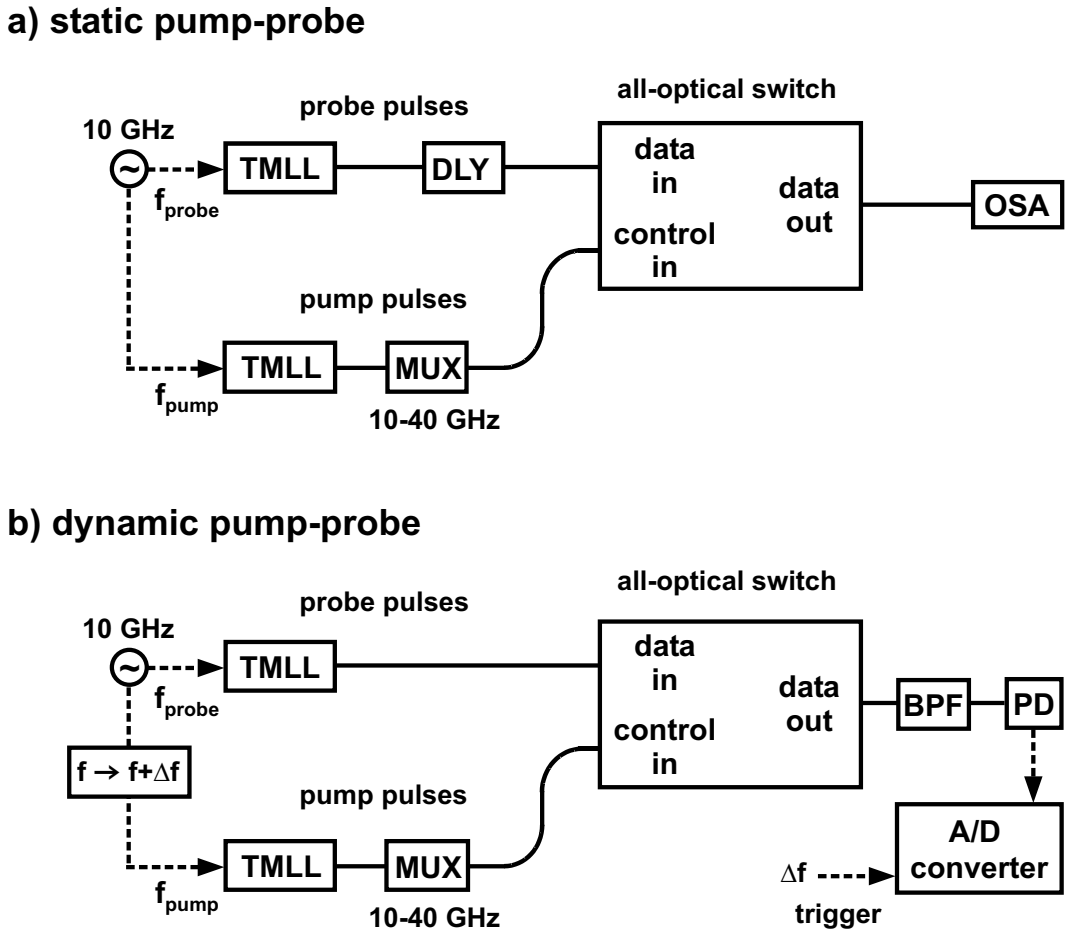

Figure 4.1: Schematic setup for the static (a) and dynamic (b) pump-probe measurements to determine the switching window.

The width and the on-off contrast of the measured switching windows are generally used as figures of merit for the switching performance. The on-off contrast is defined as the ratio between the optical power in the maximum and the minimum of the switching window. Although this simple definition of the contrast is not always suitable for comparing the switching windows, especially for different types of switches, it is used here for simplicity. A definition for the contrast adapted to the application of the switches as demultiplexer will be given in section 4.4, where different types of switches are compared under various operation conditions.

4.1 Semiconductor Laser Amplifier in a LOop Mirror (SLALOM)

4.1.1 Experimental Setup

The first switch which is discussed in detail is the Semiconductor Laser Amplifier in a LOop Mirror (SLALOM). This switch is based on the Sagnac Interferometer incorporating

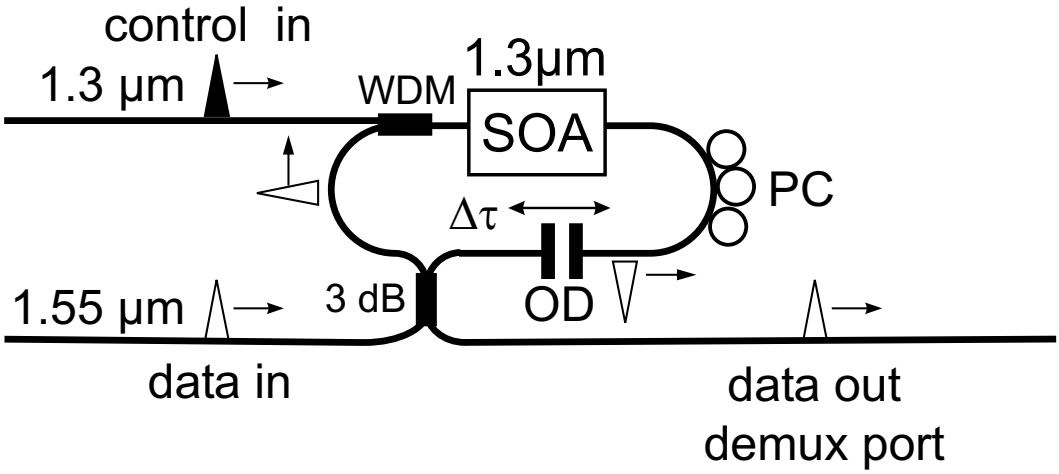

Figure 4.2: Experimental setup for the Semiconductor Laser Amplifier in a LOop Mirror (SLALOM) switch.

an SOA as nonlinear element in the fiber loop. The setup is shown in Fig. 4.2.

In the SLALOM switch an incoming data signal is split by a 3 dB coupler into two components, which propagate through the fiber loop in opposite directions. The SOA is placed slightly asymmetrically in the fiber loop, so that the two data components reach the SOA at different times. After one circulation in the loop, both components interfere again at the 3 dB coupler. Without a control pulse entering the SOA through a WDM coupler, the SLALOM is balanced (by means of a polarization controller PC) such that all data pulses are reflected (see section 2.2.1). The control pulse induces a phase change between the two counter-propagating data components. Thus the interferometer is unbalanced and switching to the 'demux port' will occur. Different widths of the switching windows are obtained by changing the position $\Delta\tau$ of the SOA in the fiber loop using an optical delay line (OD). The setup depicted in Fig. 4.2 is for the case of a gain-transparent operated SOA. For a conventional SOA, the control signal is around 1.5 µm and the WDM coupler is replaced by a 3 dB coupler.

The SLALOM can be described using the formalism derived in section 2.2.1. If the SOA is polarization independent and if we neglect the influence of the WDM coupler, the PC, the OD and additional fiber in the loop, the Jones matrices $\mathbf{J}^C$ and $\mathbf{J}^A$ for clockwise and anticlockwise propagation become

$$\mathbf{J}^C = \begin{pmatrix} \sqrt{G_C(\Delta t)}\, e^{i\Phi_C(\Delta t)} & 0 \\ 0 & \sqrt{G_C(\Delta t)}\, e^{i\Phi_C(\Delta t)} \end{pmatrix}, \tag{4.1}$$

$$\mathbf{J}^A = \begin{pmatrix} \sqrt{G_A(\Delta t-\Delta\tau)}\, e^{i\Phi_A(\Delta t-\Delta\tau)} & 0 \\ 0 & \sqrt{G_A(\Delta t-\Delta\tau)}\, e^{i\Phi_A(\Delta t-\Delta\tau)} \end{pmatrix} \tag{4.2}$$

where $G_C(\Delta t)$ and $\Phi_C(\Delta t)$ are the gain and phase for clockwise propagating pulses through the SOA, which were measured in section 3.2, having a relative delay Δt witch respect to the control pulses. $G_A(\Delta t-\Delta\tau)$ and $\Phi_A(\Delta t-\Delta\tau)$ are the gain and phase for the anticlockwise propagating pulses, which enter the SOA a time $\Delta\tau$ later. The gain and

phase curves for clockwise and anticlockwise propagation are not the same. The reason is that the clockwise pulse is co-propagating with the control pulse and experiences a constant gain and phase shift, while for the counter-propagating anticlockwise pulse the gain and phase shift is changing during propagation through the SOA. The impact of the different phase curves for clockwise and anticlockwise propagation on the switching windows will be discussed in the following section.

Substituting (4.1) and (4.2) into the transfer matrix $\mathcal{M}_{\text{Sagnac}}$ of the Sagnac Interferometer (see section 2.2.1 and appendix A.5) and using (2.27), yields the transmission coefficient T_{12} for the SLALOM (lossless 3 dB coupler assumed):

$$\begin{aligned} T_{12}\left(\underline{E}_{in}^{*}\underline{E}_{in}\right) &= \left(\mathbf{M}_{(12)}\underline{E}_{in}\right)^{*}\left(\mathbf{M}_{(12)}\underline{E}_{in}\right) \\ &= \Big[k_x^2 G_A(\Delta t-\Delta\tau)+(1-k_x)^2 G_C(\Delta t) \\ &\quad -2k_x(1-k_x)\sqrt{G_A(\Delta t-\Delta\tau)G_C(\Delta t)}\cos\left(\Phi_A(\Delta t-\Delta\tau)-\Phi_C(\Delta t)\right)\Big]\,|E_{in,x}|^2 \\ &\quad +\Big[k_y^2 G_A(\Delta t-\Delta\tau)+(1-k_y)^2 G_C(\Delta t) \\ &\quad -2k_y(1-k_y)\sqrt{G_A(\Delta t-\Delta\tau)G_C(\Delta t)}\cos\left(\Phi_A(\Delta t-\Delta\tau)-\Phi_C(\Delta t)\right)\Big]\,|E_{in,y}|^2 \end{aligned} \tag{4.3}$$

T_{12} describes the transmission to the 'demux port' for a single wave $\underline{E}_{in}$ entering through the data in port. It can be seen that the transmission to the 'demux port' depends on the input polarization, if the 3 dB coupler is polarization dependent, even if the SOA is not. (4.3) can be further simplified in the case of a polarization independent coupler ($k_x = k_y = k$):

$$\begin{aligned} T_{12} &= k^2 G_A(\Delta t-\Delta\tau)+(1-k)^2 G_C(\Delta t) \\ &\quad -2k(1-k)\sqrt{G_A(\Delta t-\Delta\tau)G_C(\Delta t)}\cos\left(\Delta\Phi(\Delta t)\right) \end{aligned}$$

The phase difference between the split signals is here given by $\Delta\Phi(\Delta t) = \Phi_A(\Delta t-\Delta\tau) - \Phi_C(\Delta t)$. The parameter $\Delta\tau$ gives the time delay for the counter-propagating signal to pass the SOA with respect to the co-propagating signal. Therefore $\Delta\tau$ determines the width of the switching window in the SLALOM. If the SOA is put symmetrical into the fiber loop $\Delta\tau$ will be 0.

In order to achieve a switching window with a high contrast and steep flanks, it was pointed out in section 3.2.2 that the slow recovery of the phase has to be identical for the separated beams. This is no longer true for the SLALOM, even in an ideal case, as the phase curves for the co- and counter-propagating signal can differ significantly, especially for long SOAs. This leads to a broadening of the switching window, which will be seen in the experimental results.

4.1.2 Switching Characteristics

The static pump-probe setup is used to measure the switching windows for a gain-transparent (GT) SLALOM switch at 10 GHz and 40 GHz repetition rate of the control pulses. The SOA in the GT-SLALOM was an MQW device with a gain maximum around 1300 nm (for details see Appendix A.7). The SOA driving current and the control pulse energy are kept constant at 300 mA and 400 fJ respectively. The pump pulses are at

1300 nm and have a width of 1.3 ps. The probe pulses have a wavelength of 1550 nm, an average power of 0 dBm and the pulse width is also 1.3 ps.

The results are shown in Fig. 4.3 for different switching window widths. The width was varied by changing the asymmetry of the SOA in the fiber loop with the optical delay line. In the upper part of Fig. 4.3, the switching windows and the derived contrast values are plotted for 10 GHz control pulse rate and in the lower part for 40 GHz. A characteristic of the SLALOM switching windows is the different steepness of the flanks, which is observed for both control pulse rates. It is due to the configuration of the Sagnac Interferometer, where the split signals travel in opposite directions with respect to the control signal through the SOA.

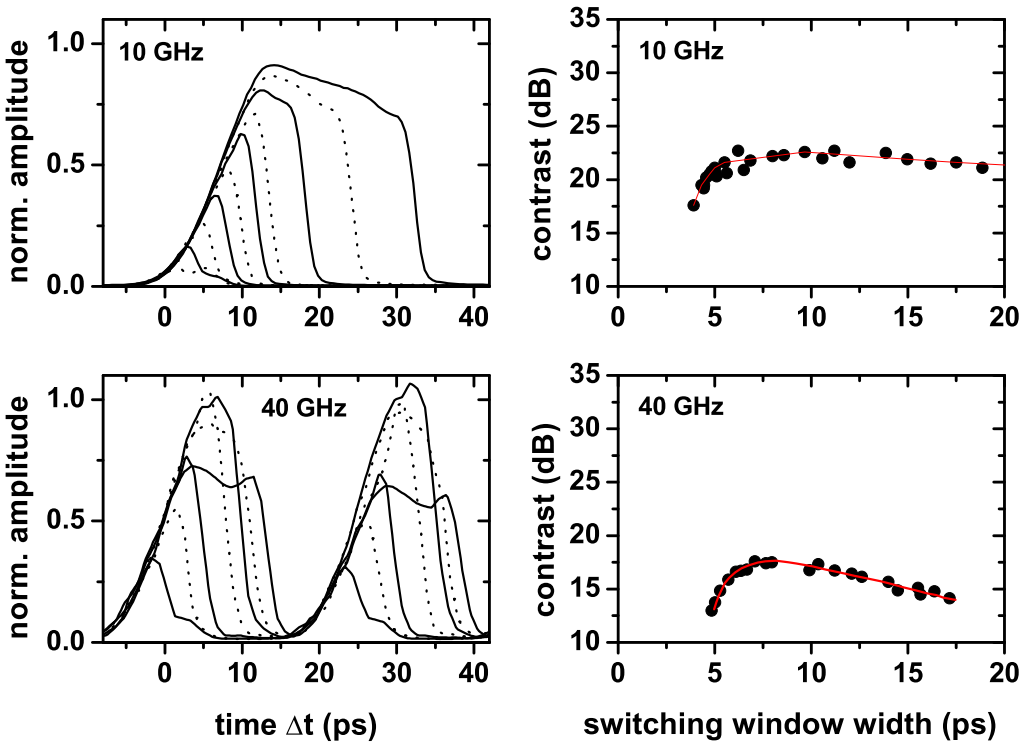

Figure 4.3: Switching windows with different widths, measured for the GT-SLALOM switch and the derived on-off contrast ratios. Upper part: 10 GHz control pulse rate, Lower part: 40 GHz control pulse rate.

Towards shorter switching window widths (below about 7 ps) the contrast decreases rapidly for 10 GHz and 40 GHz, because of the limited steepness of the phase dynamic curves, which leads to a significant decrease of the obtained phase difference in the differential scheme. Above 8 ps the contrast stays almost constant for 10 GHz, while it slowly decreases for 40 GHz. The reason is, that neighboring windows start to overlap at 40 GHz. The amount of overlap depends on the steepness of the switching window flanks and on the gap between neighboring switching windows, which is determined by the control pulse

rate. For 40 GHz, where the separation between adjacent switching windows is 25 ps, the contrast starts to decrease already at a width of about 10 ps. For 10 GHz, the contrast is not expected to decrease up to a switching window width of about 40 ps, which is beyond the measured parameter range. The overlap between neighboring switching windows is more severe for the Sagnac based SLALOM compared to switches based on other interferometer types, because of the slow rising edge of the SLALOM switching windows. Overall a switching contrast of about 22 dB for switching window widths down to 5 ps is reached at 10 GHz. The maximum contrast at 40 GHz was 17 dB, about 5 dB lower compared to 10 GHz, which is mainly due to the lower phase shift induced in the SOA for a higher control pulse rate (see section 3.2.2).

4.2 Mach-Zehnder Interferometer (MZI)

4.2.1 Experimental Setup

The setup of the Mach-Zehnder Interferometer switch is shown in Fig. 4.4. In the MZI

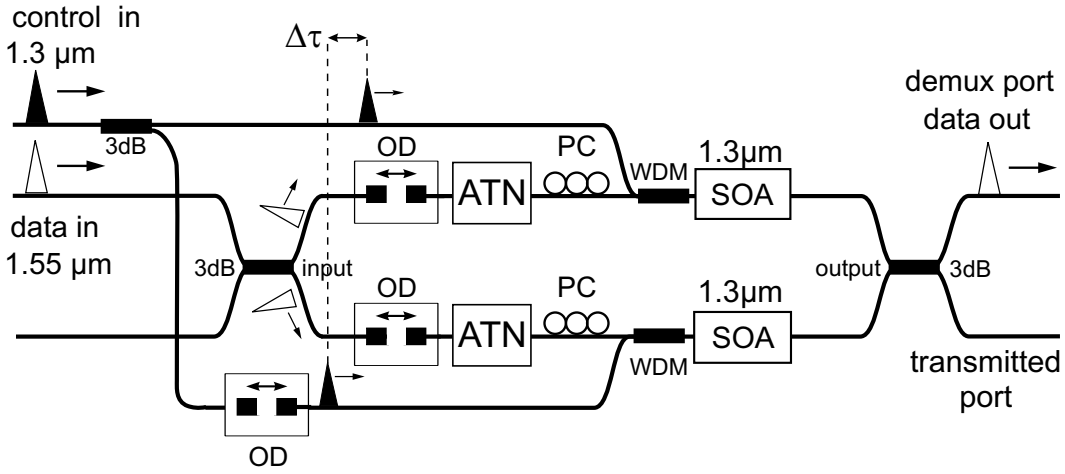

Figure 4.4: Experimental setup for the Mach-Zehnder Interferometer (MZI) switch

switch, the data signal is split by an input 3 dB coupler. The split components travel through physically separated branches of the interferometer and recombine at the output 3 dB coupler. The interferometer can be balanced such (by means of heating/cooling one interferometer branch, see section 2.2.2) that all data pulses leave the output 3 dB coupler through one port, the 'transmitted port'. A control pulse inserted into the SOA via a WDM coupler in the upper branch, induces a phase difference between both branches of the interferometer, which switches one bit of the data signal to the 'demux port'. A second control pulse, which enters the SOA in the lower branch via a WDM coupler a time $\Delta\tau$ later, cancels the phase difference between both branches again, thus closing the switching window. The width of the switching window is adjusted by changing the temporal delay $\Delta\tau$ between the control signals in both branches of the interferometer

using an optical delay line (OD). The setup depicted in Fig. 4.4 is for the case of a gain-transparent operated SOA. For a conventional SOA, the control signal is around 1.5 µm and the WDM couplers are replaced by 3 dB couplers.

The Jones formalism derived in section 2.2.2 can be used to discuss the switching properties of the MZI. The Jones matrices $\mathbf{J}^{(1)}$ and $\mathbf{J}^{(2)}$ for propagation through polarization insensitive SOAs in the upper and lower interferometer branch are given by

$$\mathbf{J}^{(1)} = \begin{pmatrix} \sqrt{G_1(\Delta t)}\ \mathrm{e}^{i\Phi_1(\Delta t)} & 0 \\ 0 & \sqrt{G_1(\Delta t)}\ \mathrm{e}^{i\Phi_1(\Delta t)} \end{pmatrix}, \tag{4.4}$$

$$\mathbf{J}^{(2)} = \begin{pmatrix} \sqrt{G_2(\Delta t-\Delta\tau)}\ \mathrm{e}^{i\Phi_2(\Delta t-\Delta\tau)} & 0 \\ 0 & \sqrt{G_2(\Delta t-\Delta\tau)}\ \mathrm{e}^{i\Phi_2(\Delta t-\Delta\tau)} \end{pmatrix}, \tag{4.5}$$

where $\sqrt{G_1(\Delta t)}$, $\sqrt{G_2(\Delta t-\Delta\tau)}$ and $\Phi_1(\Delta t)$, $\Phi_2(\Delta t-\Delta\tau)$ are the gain and phase for the signal propagating through the SOA in the upper and lower branch, having a relative delay Δt with respect to the control pulses. In the following, we consider the simplified case of two identical SOAs in the MZI, so that the gain $G_1 = G_2 = G$ and phase $\Phi_1 = \Phi_2 = \Phi$ for the upper an lower branch are equal. The fiber couplers are assumed lossless and the influence of all optical components between the input and output 3 dB coupler except the SOA is neglected. Under these assumptions, the transmission coefficient for the upper MZI output port ('demux port') is calculated by substituting (4.4) and (4.5) into the transfer matrix $\mathcal{M}_{\mathrm{MZI}}$ (section 2.2.2 and Appendix A.5) and using (2.32). For a single wave $\underline{E}_{in}$ entering through the upper input port of the MZI this yields

$$\begin{aligned} T_{11}\left(\underline{E}_{in}^{*}\underline{E}_{in}\right) &= \left(\mathbf{M}_{(11)}\underline{E}_{in}\right)^{*}\left(\mathbf{M}_{(11)}\underline{E}_{in}\right) \\ \Rightarrow T_{11} &= k^{(1)}k^{(2)}G(\Delta t-\Delta\tau) + \left(1-k^{(1)}\right)\left(1-k^{(2)}\right)G(\Delta t) \\ &\quad -2\sqrt{k^{(1)}k^{(2)}\left(1-k^{(1)}\right)\left(1-k^{(2)}\right)}\sqrt{G(\Delta t-\Delta\tau)G(\Delta t)}\cos\left(\Delta\Phi(\Delta t)\right) \end{aligned} \tag{4.6}$$

For identical couplers $\left(k^{(1)} = k^{(2)}\right)$ the transmission coefficient is similar to the transmission coefficient T_{12} for the SLALOM. The phase difference for the split signals in the MZI is given by $\Delta\Phi(\Delta t) = \Phi(\Delta t-\Delta\tau) - \Phi(\Delta t)$, where $\Delta\tau$ is the temporal delay between the control pulses in the upper and lower interferometer branch. (4.6) shows, that the transmission to the 'demux port' is not depending on the polarization state of the incoming signal, under the assumptions made above. However, in a hybrid setup, the MZI is in general polarization dependent, due to residual birefringence in the fiber and the polarization sensitivity of the SOAs and fiber couplers.

It was discussed in section 2.2.2, that the amplitude and polarization of the split signal pulses in the interferometer branches have to be controlled, especially in a hybrid setup. Attenuators (ATN) are incorporated in both interferometer branches, to equalize the amplitudes. The polarization state is changed by rotatable quarter- and half-wave plates in both branches (polarization controller, PC). If there is significant birefringence in the interferometer branches, which is generally the case, the polarization of the split signals can of course only be optimized for a single input polarization.

Different fiber lengths in the interferometer branches result in different traveling times, so that the pulses do not reach the output coupler at the same time to interfere properly. A

length difference of about 0.2 mm in standard single mode fiber corresponds to a temporal separation of 1 ps. To maintain good interference for pulse widths on the order of 1 ps, which is the typical pulse width in our experiments, the interferometer branches have to match better than a few ten μm. This is achieved in the hybrid setup by optical delay lines (OD), inserted into both interferometer branches.

It was already discussed in section 2.30 that the temperature dependence of the refractive index of the fiber makes the hybrid MZI vulnerable to temperature fluctuations. Therefore the hybrid MZI has to be actively stabilized [27], to achieve stable operation. The stabilization circuit can also be used to balance the interferometer (see section 2.2.2).

4.2.2 Switching Characteristics

The switching characteristic of a gain-transparent Mach-Zehnder Interferometer switch is investigated by measuring the switching windows with the static pump-probe technique. The experimental setup is described in Fig. 4.1. The switching windows are measured for different repetition rates of the control pulses. The GT-MZI that is used for these measurements is a hybrid fiber setup. The GT-SOAs incorporated in the MZI branches are identical to those 1300 nm MQW devices used in the SLALOM measurements (see appendix A.7 for details on the SOAs). The SOA driving current is 300 mA. The pump and probe signals are identical to those used for the switching window measurements of the GT-SLALOM. The GT-MZI is actively stabilized by a cw pilot signal (1530 nm) transmitted backwards through the GT-MZI and a slow feedback control circuit to hold the average phase difference in both branches at a preset value [27].

The measured switching windows with different window width are plotted in Fig. 4.5 – in the upper part for 10 GHz control pulse rate, in the lower part for 40 GHz. As figure of merit the derived on-off contrast is shown in each case on the right hand side. The switching windows of the GT-MZI show sharp rising and falling flanks, which is different from the GT-SLALOM switching windows plotted in Fig. 4.3. The reason is, that the split signal pulses co-propagate both with respect to the control pulses through the SOA. For larger window widths it can be seen that the top of the switching windows is not ideally flat. This is due to the exponential decay of the phase curves, as was explained in section 3.2.2. The dependence of the contrast on the window width is similar to the GT-SLALOM switch. For short width the switching windows collapse for both control pulse rates, because the phase difference in the differential switching scheme decreases. For long width, above about 6 ps, the contrast first stays relatively constant and then starts two decrease. For 10 GHz, this decrease occurs above a window width of about 40 ps, which is outside the range of the measured switching window widths. For 40 GHz, the contrast starts to decrease above a window width of about 10 ps, because the spacing between neighboring switching windows is closer (25 ps) compared to 10 GHz control pulse rate. Compared to the GT-SLALOM, the region of the window width with maximum contrast is broader for the GT-MZI. This is mainly due to the co-propagating switching scheme, which enables steep rising and falling flanks.

Contrast values above 30 dB are achieved at 10 GHz for window widths as short as $3 - 4$ ps. A maximum contrast of 25 dB, which is about 5 dB lower, is measured for 40 GHz at switching window widths down to about 4 ps. The lower contrast at the higher control pulse rate is mainly due to the lower maximum phase shift in the GT-SOAs.

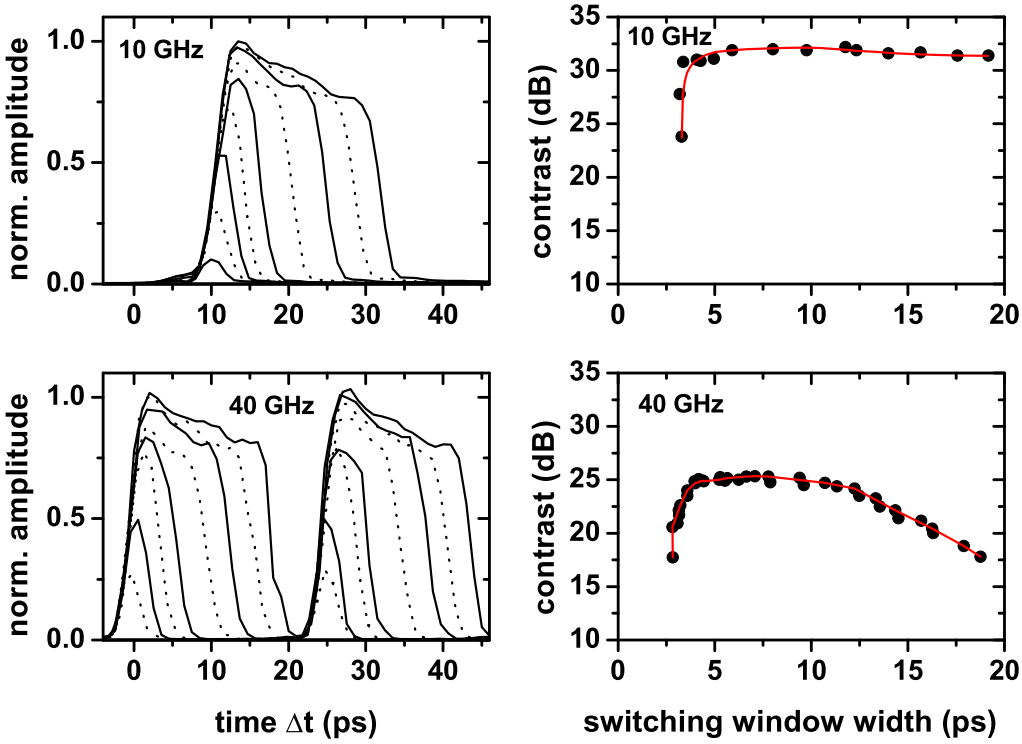

Figure 4.5: Switching windows with different widths, measured for the GT-MZI switch and the derived on-off contrast ratios. Upper part: 10 GHz control pulse rate, Lower part: 40 GHz control pulse rate.

Integrated MZI

The Mach-Zehnder Interferometer switch is the most suitable configuration for monolithic integration, due to its simple and symmetric structure. The advantage of a monolithic integration is that an active stabilization is not necessary, which simplifies the experimental setup. However, the polarization, amplitude and optical path length for the split signal can no longer be controlled independently in a monolithic device, but only together, by changing the driving current of the SOAs. This will of course also influence the gain and phase dynamics, which makes it more difficult to adjust the device for optimum switching conditions. Phase shifting sections, implemented into the interferometer branches, can be used to make the adjustment easier.
A number of research groups have successfully integrated MZI switches with conventionally operated SOAs on an InP-based chip and achieved error-free demultiplexing in high-speed OTDM experiments (see Table 1.1). The integration of a gain-transparent MZI switch is rather difficult, due to the large wavelength difference needed between the SOA gain maximum and the passive waveguides. At HHI, an integrated MZI was developed, which incorporated 1000 µm long MQW-SOAs with a gain maximum around 1500 nm [72]. Compared to the data wavelength of 1550 nm the SOA gain maximum

was slightly shifted to shorter wavelength to reduce the gain variations, similar to the gain-transparent scheme. This operation mode with only a slight shift of the SOA gain maximum is called gain-shifted. Typical switching windows for 10 GHz and 40 GHz control pulse rate, measured for such a gain-shifted integrated MZI fabricated at HHI, are shown in Fig. 4.6. A contrast of 13 dB is achieved at 10 GHz for a switching window

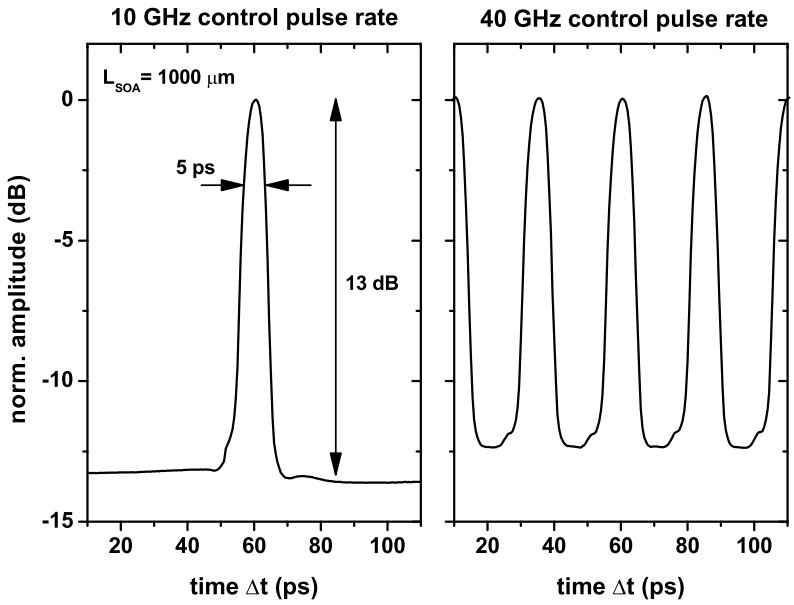

Figure 4.6: Typical switching windows measured for a monolithically integrated gain-shifted Mach-Zehnder Interferometer switch, for a control pulse rate of 10 GHz (left hand side) and 40 GHz (right hand side).

width of 5 ps. This is significantly lower compared to the GT-MZI. The reason is the strong amplified spontaneous emission (ASE) produced by the SOAs, which is in the case of the gain-shifted MZI still close to the wavelength of the data signal. This limits the measured on-off contrast. For 40 GHz control pulse rate the contrast is reduced to about 12 dB. Error-free demultiplexing was achieved with this device up to a data rate of 160 Gbit/s. Further details about the integrated MZI and the demultiplexing experiments can be found in [28, 61, 73].

4.3 Ultrafast-Nonlinear Interferometer (UNI)

4.3.1 Experimental Setup

The last interferometric switch to discuss in detail is the so called Ultrafast-Nonlinear Interferometer (UNI). The setup of the UNI switch in two different configurations is shown in Fig. 4.7. The operation principle of both configurations is similar and can be explained using Fig. 4.7 a) as follows: The data pulses are polarized by the polarization controller PC 1 such that they split into two orthogonal components of equal amplitude at port 2

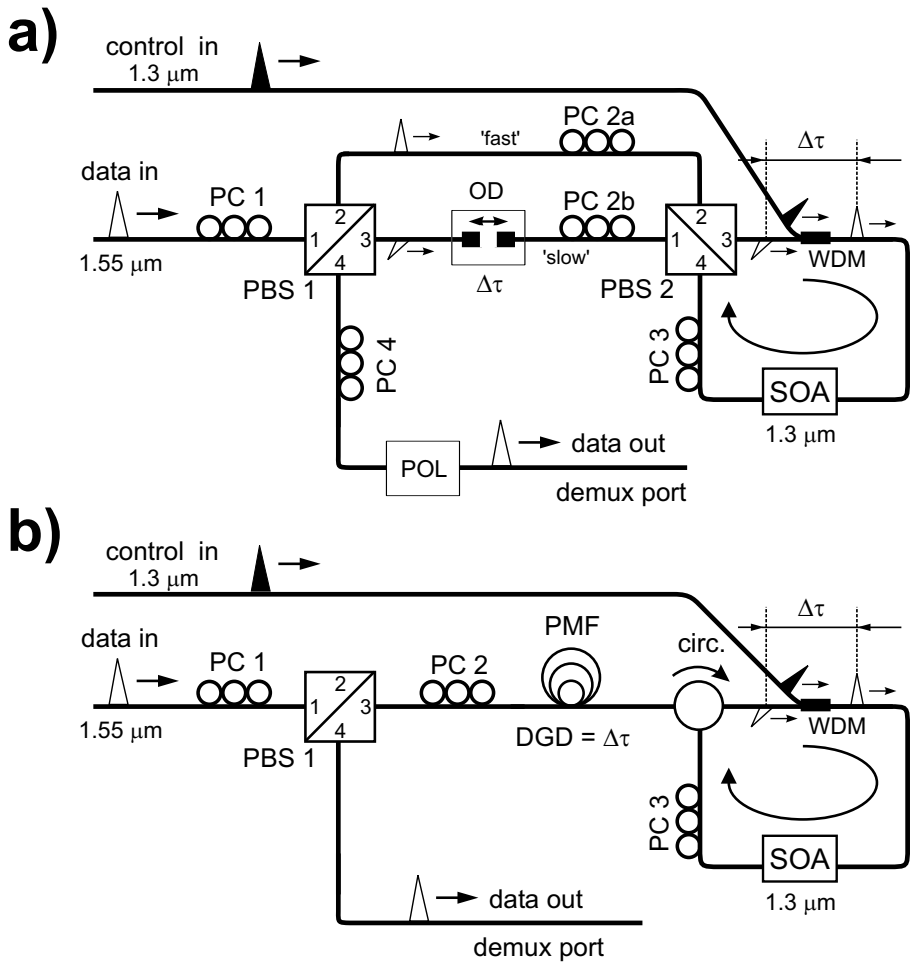

Figure 4.7: Experimental setup for the Ultrafast-Nonlinear Interferometer (UNI) switch. a) folded geometry using an optical delay line and polarizing beamsplitters. b) folded geometry using polarization maintaining fiber (= highly birefringent).

and 3 of the polarizing beamsplitter PBS 1. The two components are separated in time by a delay $\Delta\tau$ with an optical delay line (OD). The polarization controller PC 2a and PC 2b are adjusted such, that both components leave the polarizing beamsplitter PBS 2 through port 3. The two orthogonal pulse components pass the SOA and are launched again into PBS 2. By means of PC 3 it is made sure that the 'fast' component is coupled into the 'slow' branch and vice versa. Thereby the delay between both polarization components is canceled. The recombined data pulse leaves PBS 1 through port 4. Without a control pulse present, the UNI can be balanced such that all data is blocked at the polarizer (POL) by using PC 4. If a control pulse enters the SOA immediately after the leading ('fast') data component, the trailing ('slow') data component will experience a different phase shift, compared to the leading one. The two data components recombine to a different polarization behind PBS 1 and the data pulse can pass the polarizer. Switching of the data to the 'demux port' occurs. Similar to the MZI switch, the two data pulse components co-propagate with respect to the control pulses through the SOA. The window width of the switch is determined by the delay $\Delta\tau$ between the two components of the data pulses.

Fig. 4.7 b) shows a slightly different configuration of the UNI. In this configuration,

a piece of highly birefringent polarization maintaining fiber (PMF) is used to separate the split signal components by a fixed amount in time. The data signal is reinserted into the PMF via a circulator. The advantage of this configuration is the lower transmission loss, because less optical components are used. The contrast of the switching windows, measured for the UNI in the configuration b) is in general lower compared to the UNI in configuration a). This may be due to a better separation of the orthogonal pulse components in the PBS compared to the PMF. However, for the applications as demultiplexer, discussed in section 5.2, the configuration b) is used, because of the lower transmission loss. The setups depicted in Fig. 4.7 are for the case of a gain-transparent operated SOA. For a conventional SOA, the control signal is around 1.5 µm and the WDM coupler is replaced by a 3 dB coupler.

Similar to the discussion of the SLALOM and MZI switch, we can calculate the transmission coefficients for the UNI switch with the formalism derived in section 2.2.3. The Jones matrix $\mathbf{J}$, describing the propagation of the split signals through the SOA, which is assumed polarization insensitive, is given by

$$\mathbf{J} = \mathbf{R}(-\theta) \begin{pmatrix} \sqrt{G(\Delta t)}\, \mathrm{e}^{i\Phi(\Delta t)} & 0 \\ 0 & \sqrt{G(\Delta t-\Delta\tau)}\, \mathrm{e}^{i\Phi(\Delta t-\Delta\tau)} \end{pmatrix} \mathbf{R}(\theta)$$

$$= \begin{pmatrix} \sqrt{G(\Delta t)}\, \mathrm{e}^{i\Phi(\Delta t)} \sin^2(\theta) + \sqrt{G(\Delta t-\Delta\tau)}\, \mathrm{e}^{i\Phi(\Delta t-\Delta\tau)} \cos^2(\theta) & \\ \left[\sqrt{G(\Delta t)}\, \mathrm{e}^{i\Phi(\Delta t)} - \sqrt{G(\Delta t-\Delta\tau)}\, \mathrm{e}^{i\Phi(\Delta t-\Delta\tau)}\right] \cos(\theta) sin(\theta) & \\ & \left[\sqrt{G(\Delta t)}\, \mathrm{e}^{i\Phi(\Delta t)} - \sqrt{G(\Delta t-\Delta\tau)}\, \mathrm{e}^{i\Phi(\Delta t-\Delta\tau)}\right] \cos(\theta) sin(\theta) \\ & \sqrt{G(\Delta t)}\, \mathrm{e}^{i\Phi(\Delta t)} \cos^2(\theta) + \sqrt{G(\Delta t-\Delta\tau)}\, \mathrm{e}^{i\Phi(\Delta t-\Delta\tau)} \sin^2(\theta) \end{pmatrix}, \tag{4.7}$$

where θ is the angle between the leading data component in the SOA and the x axis (the same coordinate system as in section 2.2.3 is used). The orthogonally polarized, split data components are separated by a time delay $\Delta\tau$, so that the gain and phase for the trailing signal component in the SOA are given by $G(\Delta t)$ and $\Phi(\Delta t)$ and for the leading component by $G(\Delta t-\Delta\tau)$ and $\Phi(\Delta t-\Delta\tau)$. Δt is the relative delay of the signal components with respect to the control pulses.

Although the transfer matrix $\mathcal{M}_{\mathrm{UNI}}$ (see Appendix A.5) for the UNI, was derived in section 2.2.3 for a slightly different UNI setup, it can be used to a good approximation for calculating the transmission coefficient of the UNI configurations shown in Fig. 4.7. For a single wave $\underline{E}_{in}$ entering the UNI with the right polarization to pass the polarizing beamsplitter at the input, the transmission coefficient for the 'demux port' is

$$\begin{aligned} T_{11}\left(\underline{E}_{in}^{*}\underline{E}_{in}\right) &= \left(\mathbf{M}_{(11)}\underline{E}_{in}\right)^{*}\left(\mathbf{M}_{(11)}\underline{E}_{in}\right) \\ \Rightarrow T_{11} &= \cos^4(\theta)G(\Delta t-\Delta\tau) + \sin^4(\theta)G(\Delta t) \\ &\qquad +2\cos^2(\theta)\sin^2(\theta)\sqrt{G(\Delta t-\Delta\tau)G(\Delta t)}\cos\left(\Delta\Phi(\Delta t)\right) \\ &= k^2G(\Delta t-\Delta\tau) + (1-k)^2G(\Delta t) \\ &\qquad +2k(1-k)\sqrt{G(\Delta t-\Delta\tau)G(\Delta t)}\cos\left(\Delta\Phi(\Delta t)\right) \end{aligned} \tag{4.8}$$

Equation 4.8 is similar to the transmission coefficients of the other two switches, which becomes obvious if $\cos^2(\theta)$ is replaced by a coupling coefficient k (see section 2.2.3). The

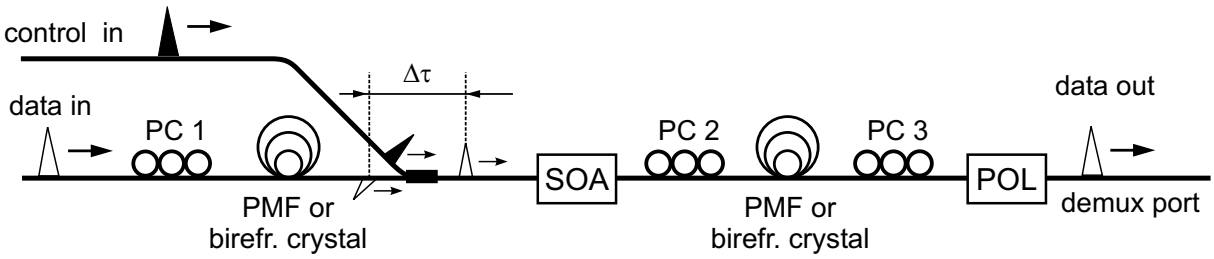

Figure 4.8: Experimental setup for the Ultrafast-Nonlinear Interferometer (UNI) switch without folded geometry [74].

phase difference between the split signals is given by $\Delta\Phi(\Delta t) = \Phi(\Delta t - \Delta\tau) - \Phi(\Delta t)$, where $\Delta\tau$ is the temporal delay between the split data pulse components.

The main advantage of the UNI configurations shown in Fig. 4.7 is the folded geometry, which makes them cyclic interferometers, like the SLALOM. This means that the data pulses are split and recombined in the same piece of fiber, so that all random phase shifts induced by temperature effects are canceled out. This UNI switch is therefore stable without any active stabilization, but unlike the SLALOM both split pulse components co-propagate with the control pulses through the SOA. In the initially proposed UNI switch, which is shown for comparison in Fig. 4.8, the pulses are split and recombined using separate birefringent elements, for example birefringent crystals [74]. In this case the random phase shifts are not canceled out, as they might differ in both birefringent elements. Stable long-term operation is difficult to achieve in such a setup, especially when PMF is used to delay the split pulse components instead of short birefringent crystals.

The main disadvantage of the UNI switch is the complete polarization dependence, due to the polarizing beamsplitter at the input. However, the switch can be modified to make it polarization independent by using a diversity scheme, which will be explained in section 5.2.2.

The UNI can be balanced, by introducing an additional phase difference between the orthogonally polarized, split pulse components. In the configuration shown in Fig. 4.7 a) this can be done even after the recombination of the split data components, by adding a birefringent element before the polarization filter. The balancing of the UNI will be discussed in more detail in section 5.3, because it plays an important role in realizing an add-drop multiplexer.

4.3.2 Switching Characteristics

Switching windows are measured for a gain-transparent (GT) UNI with the pump-probe setup shown in Fig. 4.1. The pump (control) and probe (data) signals are identical to those used for the other GT switches. The control pulse rate is set to 10 GHz and 40 GHz. For these measurements, the GT-UNI configuration shown in Fig 4.7 a) is used, which allows an easy change of the switching window width. The SOA incorporated in the GT-UNI is operated at 300 mA and identical to the one used in the GT-SLALOM.

Fig. 4.9 shows the measured switching windows. The results for a control pulse rate of 10 GHz are plotted in the upper part, the results for 40 GHz in the lower part. Although

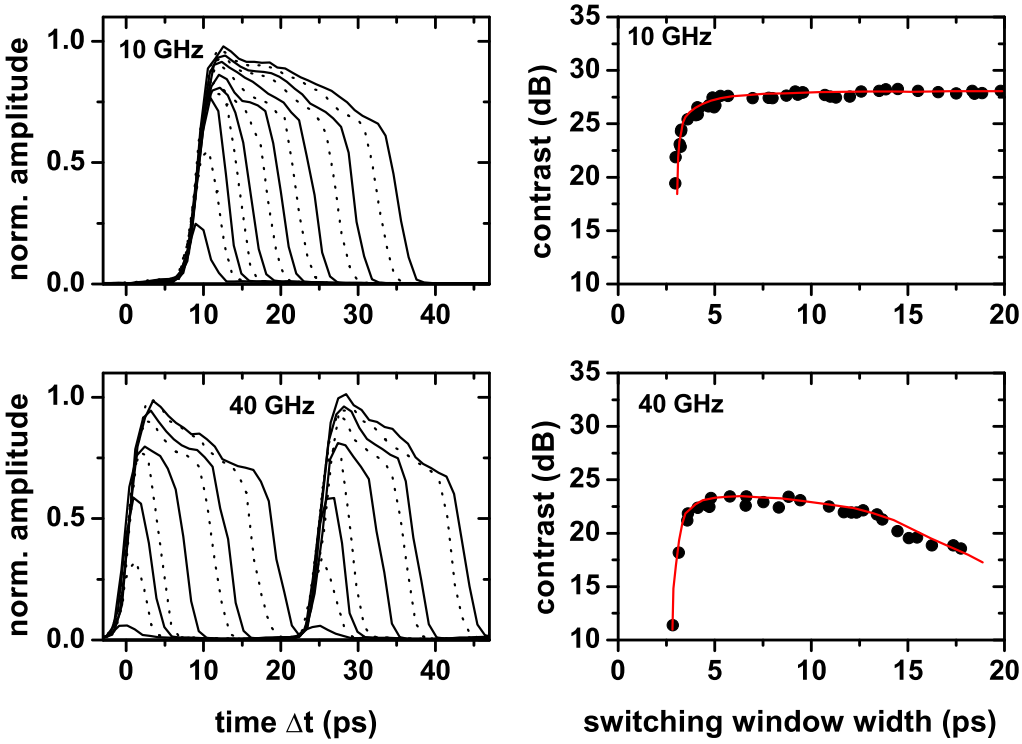

Figure 4.9: Switching windows with different widths, measured for the GT-UNI switch in the PBS configuration and the derived on-off contrast ratios. Upper part: 10 GHz control pulse rate, Lower part: 40 GHz control pulse rate.

the GT-UNI configuration used is based on a cyclic interferometer they look similar to the GT-MZI switching windows, with a sharp rising and falling flank. The reason is that unlike the GT-SLALOM, both split pulse components in the GT-UNI co-propagate with the control pulses through the SOA. The dependence of the switching contrast on the window width, shown for each case on the right hand side of Fig. 4.9, is similar to that of the GT-MZI. For 10 GHz, the contrast stays constant for window widths above 6 ps and decreases below about 5 ps. The decrease is due to the smaller phase difference in the differential switching scheme, which was already discussed in the case of the GT-SLALOM and GT-MZI. The maximum contrast that could be achieved was slightly lower compared to the GT-MZI. A value of 28 dB was measured for window widths down to $5-6$ ps. For the shortest measured window width of 3 ps the contrast was still around 25 dB. For 40 GHz a maximum contrast of 23 dB is reached between 5 ps and 10 ps. Below that range the switching windows collapse due to the decreasing phase difference, above that range the contrast decreases because neighboring switching windows begin to overlap. Compared to the switching windows at 10 GHz control pulse rate, the maximum contrast is about 5 dB lower at 40 GHz.

Conventional UNI

Also a conventional UNI switch incorporating a conventionally operated, 500 µm long bulk-SOA (see appendix A.7 for details) with a gain maximum around 1550 nm was realized within this work. The setup is almost identical to that of the GT-UNI shown in Fig 4.7 b), except that the WDM coupler to combine the control and data signal is exchanged by a 3 dB coupler. Switching windows measured for the conventional UNI using the static pump-probe setup (Fig. 4.1) at 10 GHz and 40 GHz repetition rate of the control pulses are shown in Fig. 4.10. The SOA is operated at 250 mA driving current. The wavelength of the pump (control) and probe (data) signal is 1539 nm and 1555 nm respectively. The average optical power at the input of the SOA module is +8 dBm for the pump signal and −8 dBm for the probe signal.

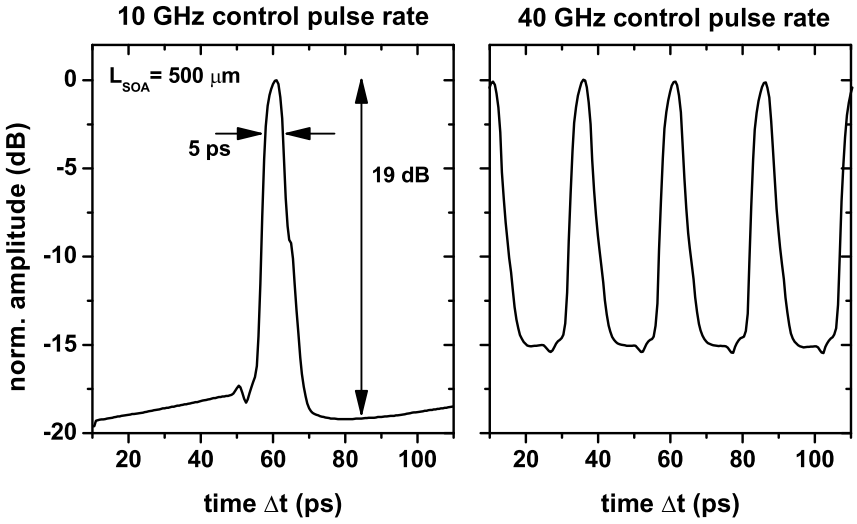

Figure 4.10: Switching windows measured for a conventional UNI switch for a control pulse rate of 10 GHz (left hand side) and 40 GHz (right hand side).

At 10 GHz a contrast of 19 dB is achieved for a switching window width of about 5 ps. At 40 GHz, the contrast is still 15 dB. A direct comparison to Fig. 4.9 is not possible, because of the different UNI configurations used. But the contrast values are comparable to those measured for the GT-UNI in the PMF configuration, presented in the demultiplexing applications (section 5.2). The contrast is not limited by the ASE of the SOA, as it was the case for the conventional MZI, shown in section 4.2.2. However, bit error rate measurements of the demultiplexing performance of the conventional UNI in an OTDM-system revealed severe problems due to pattern effects and relative jitter between the employed pulse sources. The switch was therefore not used in any system applications.

4.4 Comparison

In the following, the three different types of gain-transparent switches presented above are compared, especially regarding their application as demultiplexer in OTDM systems [75]. So far the on-off contrast ratio of the switching windows was used to evaluate the switching performance. The common definition of the contrast ratio leaves it to the evaluator, where to read the values for the maximum and minimum transmitted power in the switching window. As long as only a single type of switch is considered, where the shape of the switching window does not change significantly, this is a satisfactory approach. However, if different types of switches are compared, the simple on-off contrast ratio is not sufficient, because it does not take into account the full shape of the switching window. Therefore an integrative approach is introduced for the definition of the switching contrast, called the Integrated Contrast Ratio (ICR). The ICR is designed to evaluate the performance of the switch as demultiplexer in an OTDM system. It is defined as the ratio of the transmitted power in the switched channel to the sum of the transmitted powers in the neighboring OTDM channels. A high ICR value means a good switching performance with high transmission of the pulses in the switched channel and a good suppression of the pulses in the neighboring channels. The ICR is explained in more detail in Appendix A.2.

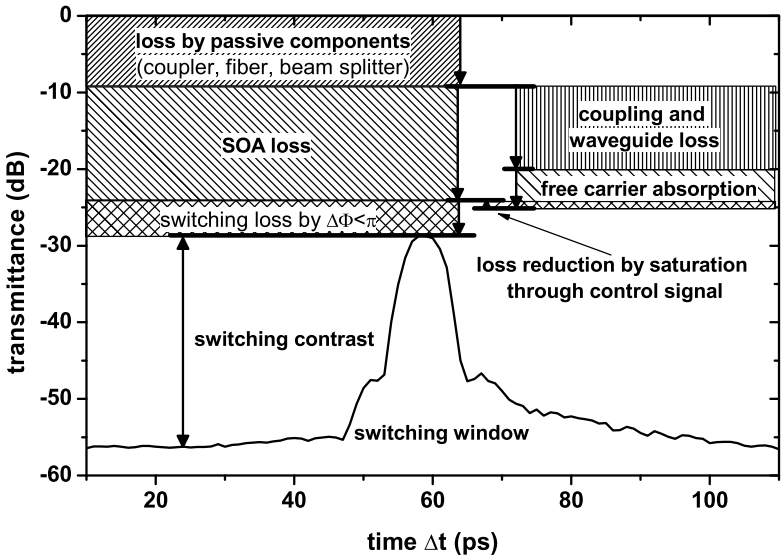

Figure 4.11: Summary of the different effects which contribute to the loss of the data signal in a switch based on a gain-transparent operated SOA.

The second property of a switch, which is crucial for its application as a demultiplexer and also for other switching applications, is the transmission loss. If the switch is used in a transmission system and the optical power at the output of the switch falls below the sensitivity of the receiver, error-free performance is no longer possible. This depends of course also on the maximum data power that can be input to the switch. In interferometric switches based on conventionally operated SOAs, the transmission loss is low (around

0 dB) or even a small positive gain is observed. But the maximum data power that can be applied is limited due to pattern effects. The pattern effects occur, because at high data powers (above about −20 dBm to −10 dBm) the data pulses start to change the SOA gain, similar to the control pulses. The exact limit for the data power depends on the SOA, the operation conditions and the application. For switches based on gain-transparent SOAs, the transmission loss is significantly higher (20 dB to 30 dB). But the pattern effects are negligible, because the data signal is far outside the SOA gain region, so that the maximum data power to the SOA is only limited by the destruction limit of the device. Data input powers of $15 - 20$ dBm are possible for the SOAs used in the experiments, so that the data power at the output of the gain-transparent switches was comparable to the conventional SOA switches.

The different contributions to the loss in a gain-transparent switch are summarized in Fig. 4.11. They mainly result from three different sources: loss by passive components (like fiber couplers, beamsplitter, etc.), loss in the SOA and loss by insufficient phase shift. The loss by passive components depends on the specific setup of the switch and is normally below 10 dB. The SOA loss was discussed in detail in section 3.2.3. If a control pulse saturates the SOA, this loss is slightly lower (by about 1 dB) because the number of free carriers, which absorb the data signal, is reduced. The loss by insufficient phase shift (switching loss) depends on the operation conditions (driving current, control pulse power, switching window width) of the switch. It results from the fact that a phase shift of π, which is needed for the maximum transmittance in an interferometer, is in general not reached for gain-transparent operated SOAs (see section 3.2.3).

4.4.1 10 GHz Control Pulse Rate

First the switches are compared at a control pulse rate of 10 GHz. The ICR values are calculated from the measured switching windows using (A.4). The results for TDM bit rates of 40 Gbit/s, 80 Gbit/s and 160 Gbit/s are shown in Fig. 4.12. The curves for all three switches have a similar shape. For small window widths, the ICR decreases, independent of the TDM bit rate, because the switching windows collapse (see the measured switching windows in Fig. 4.3, Fig. 4.5 and Fig. 4.9). For large window widths the ICR decreases when the switching windows become broader than the data bit period Δt_{bit} (6.25 ps for 160 Gbit/s, 12.5 ps for 80 Gbit/s). This is due to increasing cross talk from neighboring channels.

For TDM bit rates of 40 Gbit/s and 80 Gbit/s, all switches have a maximum ICR well above 10 dB. However, the GT-SLALOM switch already shows slightly lower values. The difference in ICR values between the GT-SLALOM and the other switches is even higher at 160 Gbit/s. While the ICR for the GT-MZI switch and the GT-UNI switch is still around 10 dB, the value for the GT-SLALOM switch drops to 6 dB. The reason is the co/counter propagation scheme in the SLALOM, which was already mentioned in section 4.1.2. Due to this operation scheme, the switching windows collapse earlier in the GT-SLALOM (contrast falls below 20 dB at about $5 - 6$ ps) compared to the other switches which collapse at about 3 ps. This is more critical for higher TDM bit rates (160 Gbit/s and above), where smaller switching windows are required. The maximum in the ICR curves also reveals information about the optimum switching window width for a certain TDM bit rate. The optimum is the same for all three switches, about 10 ps and 5 ps for a TDM bit rate of 80 Gbit/s and 160 Gbit/s respectively.

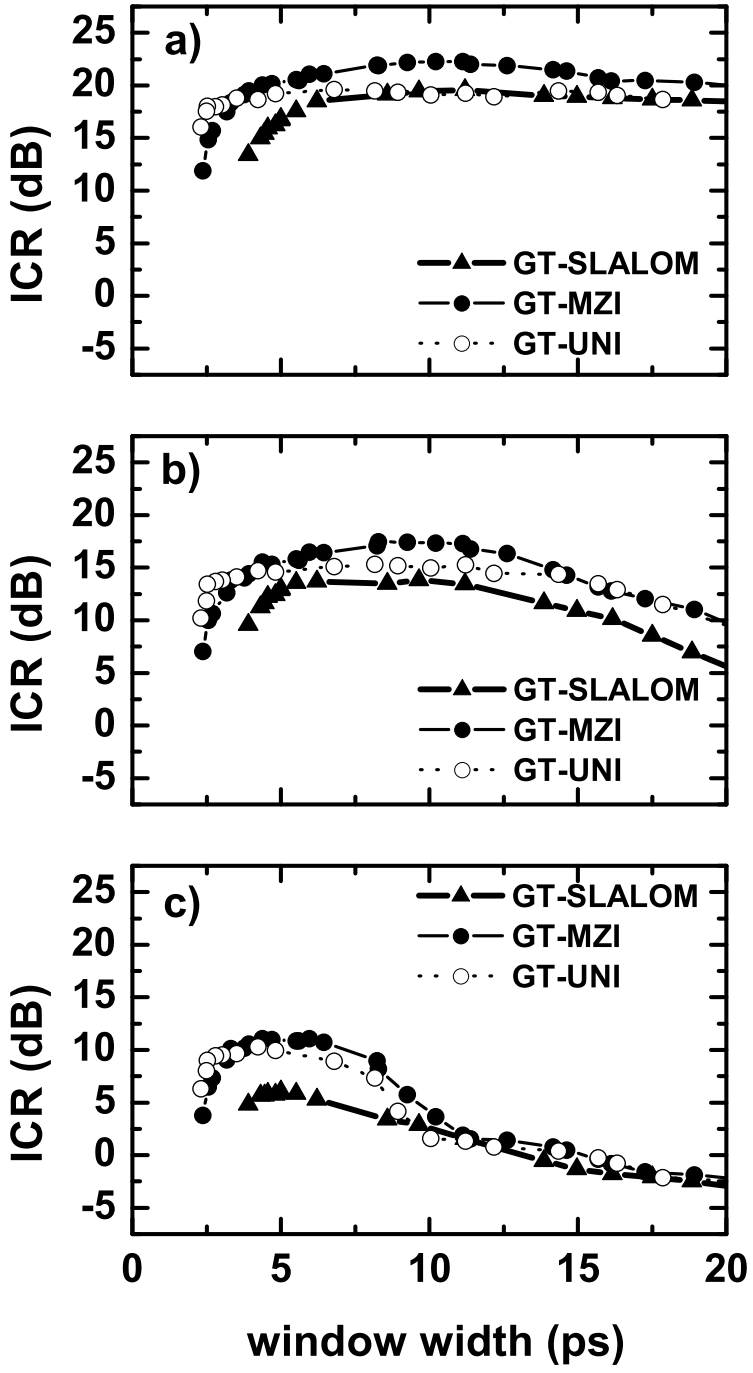

Figure 4.12: ICR values for the GT-SLALOM, the GT-MZI and the GT-UNI switch, calculated from measured switching windows with different widths for demultiplexing from a TDM bit rate of a) 40 Gbit/s, b) 80 Gbit/s and c) 160 Gbit/s to 10 Gbit/s base data rate.

The second important property of the switch is the transmittance in the maximum of the switching window (maximum transmittance), which determines the transmission loss for the switched data signal. The different loss contributions for a gain-transparent switch were summarized in Fig. 4.11. The loss by passive components and the SOA loss are independent of the switching window width, but differ for different switching configurations. In order to compare the influence of the switching window width on the transmittance for different types of switches, we have to eliminate the loss by passive components and the SOA loss. They are determined for each switch using the following method: For normal switching operation, the switch is balanced such that the on-off contrast ratio is high (see section 4.1 to 4.3 for details about the balancing of the switches). In order to measure the loss by passive components and the SOA loss, the interferometer is balanced for maximum transmission of the data signal (at 300 mA SOA driving current and +7 dBm average control pulse power). To a good approximation, this balance point corresponds to a phase difference of π in the switch, so that the switching loss is canceled and only the loss in the passive components and the SOA loss contribute to the measured loss. Subtracting this measured loss from the maximum transmittance for normal switching operation, yields the desired transmittance without the loss in the passive components and in the SOA, called corrected transmittance. The corrected transmittance is plotted in Fig. 4.13 for the three investigated switches as a function of the switching window width.

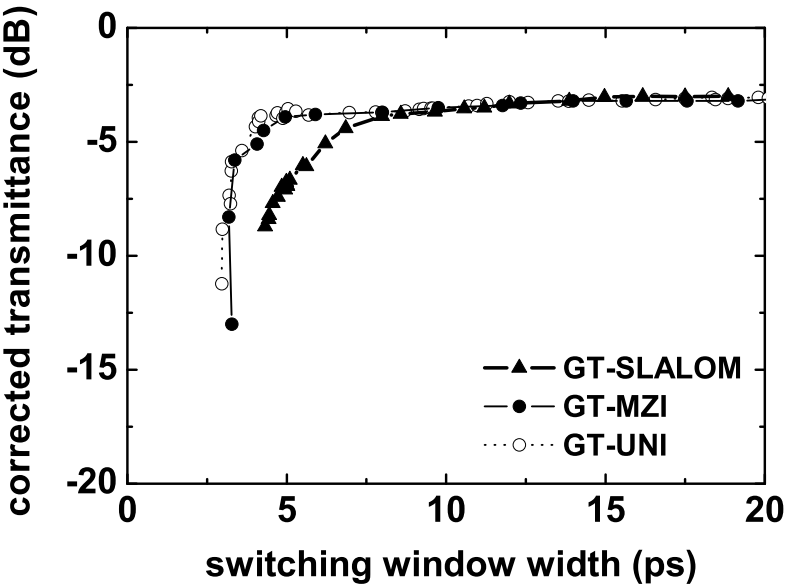

Figure 4.13: Corrected transmittance for different switching window widths in the case of the GT-SLALOM, the GT-MZI and the GT-UNI switch.

The shape of the curves is very similar to the measurements of the contrast over window width (Fig. 4.3, Fig. 4.5 and Fig. 4.9). The maximum transmittance stays constant down to about 5 ps (8 ps in the case of the GT-SLALOM) before it starts to decrease rapidly. Obviously, the decrease in contrast that was observed for short window width is

mainly due to this decrease of the corrected transmittance. The fact that the decrease starts earlier for the SLALOM compared to the UNI and MZI is explained by the different propagation directions of the split signals through the SOA in the SLALOM. The corrected transmittance do not reach 0 dB but stabilizes at about −3 dB to −3.5 dB. As the corrected transmittance takes into account only the switching loss, this indicates that the maximum phase difference is below π in the gain-transparent operated SOAs. A rough estimation of the phase difference from the corrected transmittance using the simple interferometer formula ($T = 0.5 + 0.5\cos(\Delta\Phi)$), yields a value of $\Delta\Phi = 0.4\ \pi$. This is in agreement with the phase differences determined by the direct phase measurements in section 3.2.

4.4.2 40 GHz Control Pulse Rate

To investigate the effect of a higher base data rate on the performance of the switches as demultiplexer, the corrected transmittance at 40 GHz control pulse rate was measured with the same method that was used at 10 GHz. In Fig. 4.14 the corrected transmittance of the GT-UNI and the GT-MZI as a function of the window width is compared for 10 GHz and 40 GHz.

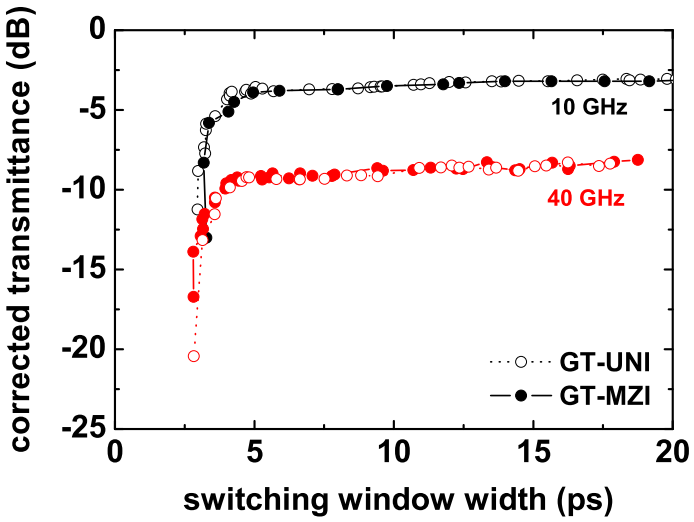

Figure 4.14: Corrected transmittance of the GT-MZI and the GT-UNI switch, as a function of the switching window width for 10 GHz and 40 GHz control pulse rate.

The overall shape of the curves is similar for both switches and also for both control pulse rates, but the corrected transmittance is in total about 5 dB lower at 40 GHz compared to 10 GHz. The reason is the lower phase shift at the higher control pulse rate, which was observed in the direct phase measurements in section 3.2.2.

The influence of the higher control pulse rate on the ICR is shown in Fig. 4.15 for the GT-SLALOM, the GT-MZI and the GT-UNI switch. The ICR for demultiplexing from

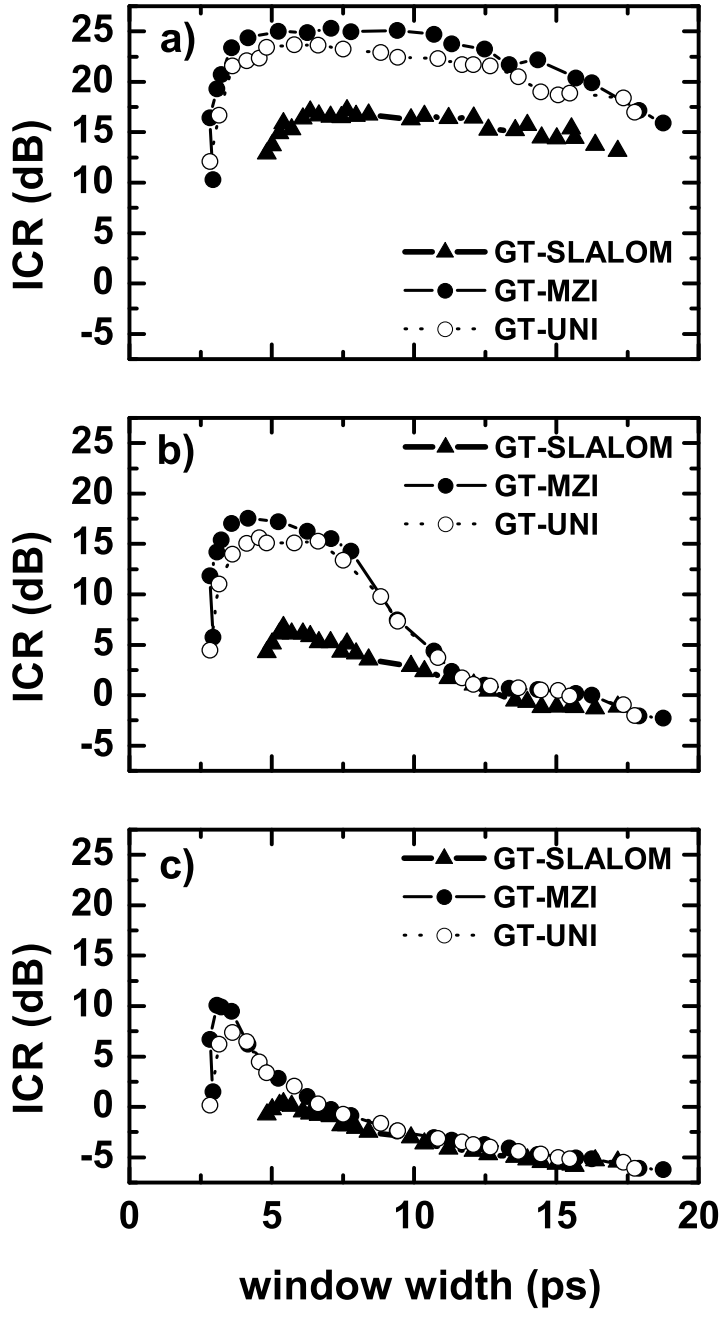

Figure 4.15: ICR values for the GT-SLALOM, the GT-MZI and the GT-UNI switch, calculated from measured switching windows with different widths for demultiplexing from a TDM bit rate of a) 80 Gbit/s, b) 160 Gbit/s and c) 320 Gbit/s to 40 Gbit/s base data rate.

a TDM bit rate of 80 Gbit/s, 160 Gbit/s and 320 Gbit/s to 40 Gbit/s base data rate is calculated from the switching windows measured at 40 GHz control pulse rate and plotted as a function of the window width.

Similar to the ICR values at 10 GHz, the overall shape of the curves is the same for all three switches. For shorter switching windows, the ICR decreases because the maximum transmittance decreases, while for broad switching windows the ICR decreases due to cross talk from neighboring channels. The point at which the switching windows collapse depends on the type of switch. The purely co-propagating switches like the GT-UNI and the GT-MZI can be operated at smaller window widths compared to the GT-SLALOM. At which point the cross talk leads to a decrease in ICR depends on the data bit period. For 80 Gbit/s, the decrease is slow and starts around 12.5 ps. For 160 Gbit/s and 320 Gbit/s, the decrease is significantly faster and starts at about 6 ps and 3 ps respectively.

Fig. 4.15 shows, that the ICR for the GT-SLALOM is significantly lower compared to the other two switches, already at 80 Gbit/s. At 320 Gbit/s it hardly reaches 0 dB. For the GT-UNI and the GT-MZI the ICR values are well above 10 dB for 80 Gbit/s and 160 Gbit/s. Even for 320 Gbit/s an ICR around 8 dB is measured. The optimum window width for demultiplexing from a certain TDM bit rate to 40 Gbit/s base rate is estimated from the calculated ICR values. For the GT-UNI and the GT-MZI it lies around 5 ps and 3 ps for 160 Gbit/s and 320 Gbit/s respectively.

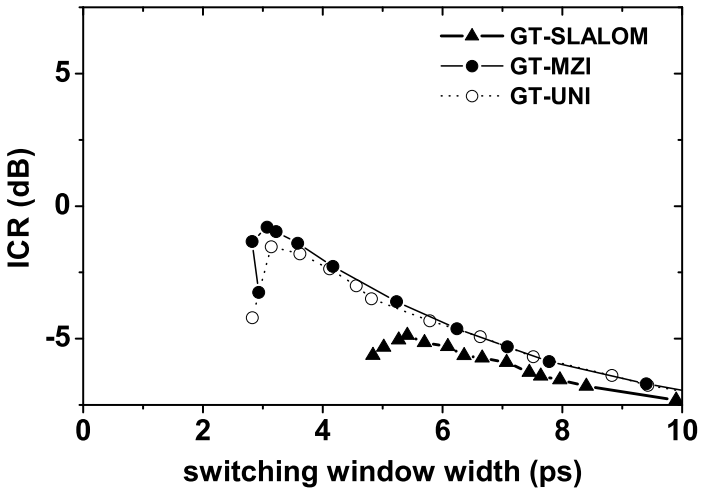

Figure 4.16: Calculated ICR values for demultiplexing from a TDM bit rate of 640 Gbit/s to 40 Gbit/s base data rate as a function of the window width for the GT-SLALOM, the GT-MZI and the GT-UNI switch.

A direct comparison of the ICR for 160 Gbit/s at the two different base data rates reveals, that the values at 40 Gbit/s are higher than at 10 Gbit/s. This seems to contradict with the results obtained for the maximum transmittance, where a significantly lower transmittance was observed for the higher base data rate. But the higher ICR values are reasonable, keeping in mind that for the same TDM bit rate the number of neighboring channels, which cause cross talk, reduces from 15 at 10 Gbit/s base data rate to 3 at

40 Gbit/s [76]. If the results for different base data rates are compared at the same multiplex level, which means ICR for 160 Gbit/s to 10 Gbit/s with ICR for 640 Gbit/s to 40 Gbit/s, a significantly lower ICR value at 40 Gbit/s is observed. This is illustrated in Fig. 4.16, where the ICR for demultiplexing from 640 Gbit/s to 40 Gbit/s is plotted for different switching configurations as a function of the window width. The ICR values are calculated with the same switching windows that were used for Fig. 4.15.

Even for the GT-MZI and the GT-UNI the ICR values are below 0 dB. This is partly due to the lower maximum transmittance observed at 40 GHz control pulse rate, but also because the achieved switching windows are too broad. The bit period at a TDM bit rate of 640 Gbit/s is 1.5625 ps, so that a window width below 2 ps is needed. As was pointed out earlier, the minimum window width that can be reached in the differential scheme, depends mainly on the width of the control pulses. By using shorter control pulses, a reduction in the minimum window width can be expected and higher ICR values at a TDM bit rate of 640 Gbit/s are possible. It should be mentioned that at such short window widths, the timing jitter between the control and data pulses plays an increasingly important role and has to be taken into account.

4.4.3 SOA Current and Control Pulse Power

In this section, the influence of the SOA driving current and the control pulse power at 10 GHz control pulse rate is investigated using the ICR and the maximum transmittance. In order to compare the maximum transmittance for different types of switches, we use the corrected transmittance, defined in section 4.4.1.

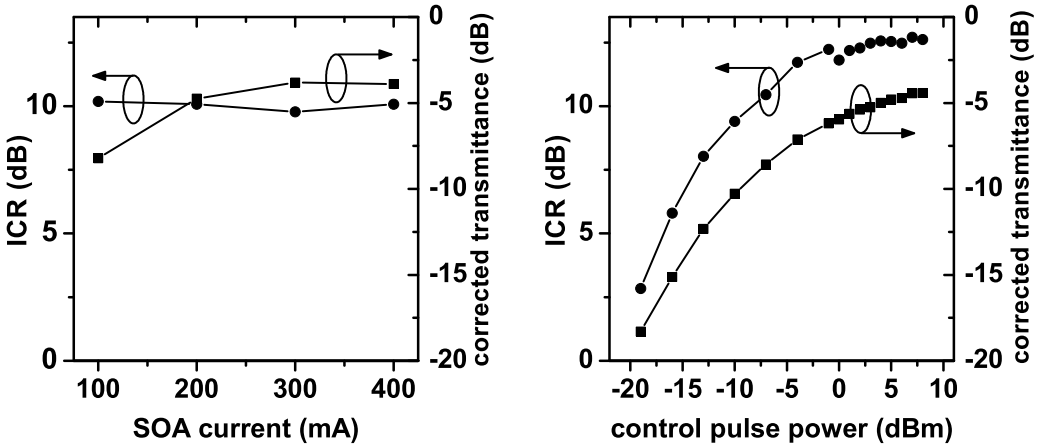

Figure 4.17: Corrected transmittance (squares) and ICR values (circles) for demultiplexing from a TDM bit rate of 160 Gbit/s to 10 Gbit/s base data rate. Left hand side: in a GT-MZI switch, for different SOA driving currents, Right hand side: in a GT-UNI switch, for different control pulse powers.

The ICR and the corrected transmittance versus the SOA driving current are shown on the left hand side of Fig. 4.17 for a GT-MZI switch. The control pulse power is +7 dBm

and the switching window width about 5 ps. The corrected transmittance decreases for lower currents, which is due to the reduced phase change observed in the direct phase measurements. The decrease is partly compensated by the lower SOA loss (4 to 6 dB), which occurs at lower driving currents (see Fig. 3.16). The ICR value stays constant, although the corrected transmittance decreases. This unexpected result is not completely understood and may as well be due to a slight misalignment in the GT-MZI for the higher driving currents. However, it can be concluded that above 200 mA the influence of the driving current on the corrected transmittance and the ICR is small.

The right hand side of Fig. 4.17 shows the corrected transmittance and the ICR as a function of the control pulse power. The results are for a GT-UNI switch with about 5 ps switching window width and an SOA driving current of 300 mA. The corrected transmittance and the ICR both decrease with decreasing control pulse power, which is mainly due to the lower phase shift observed in the direct phase measurements. Above a control pulse power of about 0 dBm the ICR stays almost constant and also the corrected transmittance is around its maximum value. The decrease of the corrected transmittance is enhanced by the higher SOA loss (about 1 dB), which occurs for lower pump pulse powers, because the number of free carriers and with it the free carrier absorption is higher.

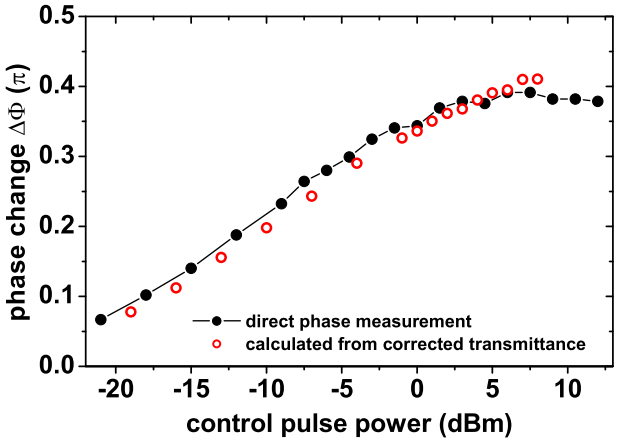

Figure 4.18: Comparison between the maximum phase change in the SOA measured with direct detection of the phase change (filled circles) and the maximum phase change calculated from measurements of the corrected transmittance (hollow circles).

To decide if the corrected transmittance over control pulse power is in agreement with the direct phase measurements shown in Fig. 3.11, the phase change was estimated from the corrected transmittance in Fig. 4.17 (right) using the simple interferometer formula (4.8). The result is plotted in Fig. 4.18 together with the direct phase measurements from Fig. 3.11. A good agreement is obtained between the calculated phase change and the results from the direct phase measurements.

4.4.4 Conclusion

		GT-UNI	GT-MZI	GT-SLALOM
corr. trans-	10 GHz	-3 to -3.5	-3 to -3.5	-6
mittance [dB][a]	40 GHz	-9	-9	–
ICR [dB][b]	10 Gbit/s	10	10	6
	40 Gbit/s	16	18	7
component loss [dB][c]		19 to 20	17 to 18	17 to 18
active stabilization needed		no	yes	no

[a]for 6 ps switching window width
[b]maximum value for 160 Gbit/s TDM bit rate
[c]at 300 mA SOA current

Table 4.1: Comparison of the main results for the GT-UNI, the GT-MZI and the GT-SLALOM switch.

Tab 4.1 summarizes the main results for the three investigated gain-transparent switches. For the GT-UNI and the GT-MZI, the corrected transmittance is almost equal. At a window width of about 6 ps, a corrected transmittance of −3 to −3.5 dB is obtained for a control pulse rate of 10 GHz and about −9 dB for 40 GHz. The GT-SLALOM shows a significantly lower corrected transmittance of −6 dB at 10 GHz.

The measured ICR values for the GT-UNI and the GT-MZI are also comparable. At a base data rate of 10 Gbit/s, the maximum ICR for 160 Gbit/s TDM bit rate is about 10 dB and at 40 Gbit/s base data rate between 16 dB and 18 dB. For the GT-SLALOM the maximum ICR is significantly lower. Only 6 dB and 7 dB are reached for 10 Gbit/s and 40 Gbit/s base data rate respectively. The switching window width, at which the highest ICR values for 160 Gbit/s TDM bit rate is reached, is about 6 ps for all switches independent of the base rate. Despite the lower maximum transmittance, the maximum ICR values are higher for 40 Gbit/s base data rate compared to 10 Gbit/s. This can be explained by the lower number of cross talk channels at the higher base rate. The GT-SLALOM shows the worst performance, which is mainly due to the switching scheme in the Sagnac Interferometer, where the split signals counter-propagate in the SOA. This leads to a switching window shape with only one steep flank, which is increasingly disadvantageous at high TDM bit rates. A shorter SOA can be used to overcome this problem, but this will also lead to lower phase changes, which worsens the switching performance especially in gain-transparent operation.

From the calculated ICR values, it is expected that the GT-SLALOM switch shows a considerably lower demultiplexing performance, compared to the other two switches, especially at higher TDM bit rates. This is in agreement with BER measurements in an OTDM system, where error-free demultiplexing up to a TDM bit rate of 160 Gbit/s is achieved using the GT-MZI switch and the GT-UNI switch, but only up to 80 Gbit/s with the GT-SLALOM. However, the ICR value alone is not sufficient to decide if a switch

is capable of error-free demultiplexing operation in a real system environment. Bit error rate measurements are still needed.

The loss in the passive components plus the loss in the SOA at 300 mA driving current is between 17 and 18 dB for the GT-MZI and the GT-SLALOM and slightly higher for the GT-UNI. The main part of the loss is due to the gain-transparent operated SOA. This loss can not be reduced easily without changing the structure of the SOA itself. Therefore, the loss of the passive components has to be kept as low as possible, to avoid that the power of the switched data signal drops below the receiver sensitivity. This is crucial especially for applications at 40 Gbit/s base data rate, because of the additional switching loss at the higher control pulse rate discussed in this chapter. Recent publications indicate, that an EDFA can be used in the loop of a GT-UNI switch to compensate for part of the loss [77]. In this case the EDFA needs low PMD and PDL values to maintain a good switching performance.

In conclusion, the GT-UNI and the GT-MZI switch clearly show the best performance. As the GT-MZI in a hybrid setup needs an active phase stabilization, the GT-UNI is the more practical device for a hybrid setup. A disadvantage is of course the strong polarization dependence of the GT-UNI. But as was discussed earlier, the MZI and the SLALOM, although ideally polarization independent, show a significant polarization dependence in hybrid setups. Therefore an automatic polarization controller or a polarization diversity scheme in conjunction with the GT-UNI is a viable solution. Experiments with a polarization independent GT-UNI demultiplexer using a diversity scheme are presented in section 5.2.2. The MZI has clearly the higher potential for monolithic integration and the polarization dependence can be reduced in the integration process by careful design. Therefore a monolithically integrated MZI is the best choice for most applications.

Chapter 5

Applications in High Speed OTDM-Systems

One of the main application of all-optical interferometric switches is in transmission systems, based on optical time division multiplexing (OTDM). In such systems, fast optical switches are needed as decision elements for demultiplexing, add-drop multiplexing, in sampling devices for signal monitoring and in signal regeneration, as was discussed in detail in the introduction. The interferometric switches, investigated in this work, were tested for a number of these applications and the experimental results are presented in this chapter. Two of the SOA based switches investigated in chapter 4 are promising candidates for demultiplexing signals at a high bitrate (e.g. 160 Gbit/s) – the GT-MZI and the GT-UNI switch.

5.1 Demultiplexing using GT-MZI

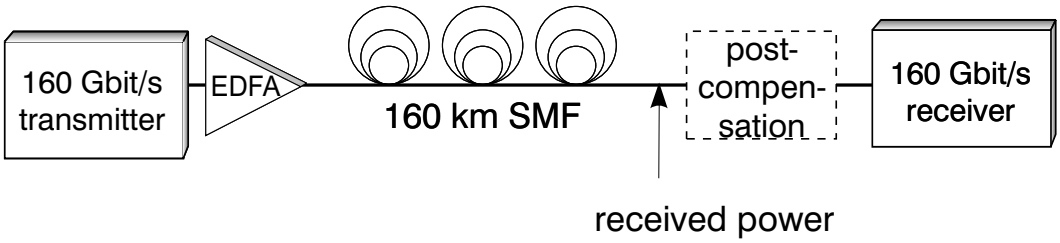

Figure 5.1: Experimental setup for the test of the GT-MZI as demultiplexer in a 160 Gbit/s receiver.

The experimental setup for the test of the GT-MZI as demultiplexer is shown in Fig. 5.1 [5]. A 160 Gbit/s RZ (return-to-zero) data signal (single wavelength channel) is transmitted over a transmission line, which comprises a single, unrepeatered (no EDFA within the transmission line), standard single mode fiber (SMF) span with a length of 160 km. For dispersion compensation, additional spans of DCF (dispersion compensating fiber) were used after the transmission (post-compensation).

The 160 Gbit/s data transmitter comprises a tunable mode-locked laser (TMLL), an external modulator and a fiber delay line multiplexer. The TMLL generated a 10 GHz pulse train, which was intensity modulated with a pseudo random bit-sequence (PRBS $2^7 - 1$), using the modulator. The 10 Gbit/s data signal was then multiplexed by the fiber delay-line multiplexer (4 stages) to a 160 Gbit/s, single polarization data signal. To ensure a multiplexed PRBS data stream, the bit sequences were shifted against each other by $(2^7 - 1)$/n bit periods with n = 2, 4, 8, 16. The generated data signal had a wavelength around 1550 nm and an rms timing jitter of approximately 300 fs. The pulses were almost transform limited with a sech^2 shape and had a full width at half maximum of about 1.5 ps. For longer word length, the pseudo-random characteristic of the generated 160 Gbit/s signal is not preserved in the multiplexer. Therefore, $2^7 - 1$ was chosen for almost all experiments in this chapter. In most of the presented applications gain-transparent SOA switches were used, which are not influenced by the data signal, so that no performance degradation at longer word lengths is expected.

The 160 Gbit/s data signal was transmitted over 160 km SMF [78]. In the receiver, the 160 Gbit/s data signal was optically demultiplexed to a 10 Gbit/s data signal using a gain-transparent Mach-Zehnder Interferometer in a hybrid setup.

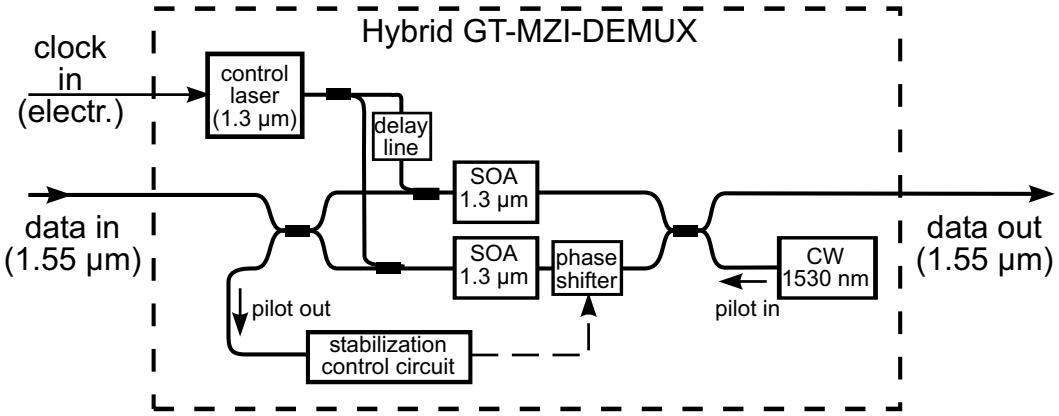

Figure 5.2: Setup of the GT-Mach-Zehnder Interferometer switch.

Fig. 5.2 shows schematically the GT-MZI switch, used as demultiplexer [27, 68]. The GT-MZI is similar to the device used for the switching window measurements in section 4.2. The optical delay lines, the attenuator and the polarization controller in the interferometer branches are not shown here. For the system experiments, the interferometer needed an active optical stabilization. A control circuit with a cw pilot light (1530 nm), propagating in opposite direction to the data signal through the MZI, was used for this. The control circuit equalized the difference of the optical path lengths of both interferometer branches, by heating or cooling a piece of the fiber using a Peltier-element. As a gain-transparent operated SOA is used, the pilot signal did not influence the switching performance. The TMLL, generating the control pulses (1300 nm, 1.2 ps sech^2) to gate the GT-MZI switch, is also shown in Fig. 5.2. To synchronize the control pulses with the data signal, the control pulse laser is locked to an electrical clock signal at the base data rate. This clock signal is either extracted from an optical signal at the base data rate, which is synchronous to the data signal and transmitted on a second wavelength channel (clock

transmission), or directly derived from the data signal at the full TDM bit rate (clock recovery). A switching window width of 6 ps was found to be the optimum value for the demultiplexing, which is consistent with the optimum value obtained using the ICR criteria in section 4.4.

To test the performance of the demultiplexer, the bit error rate (BER) of one demultiplexed OTDM channel was measured as a function of the input power to the 160 Gbit/s receiver. The results are plotted in Fig. 5.3, where the BER without (back-to-back) and with transmission line is shown.

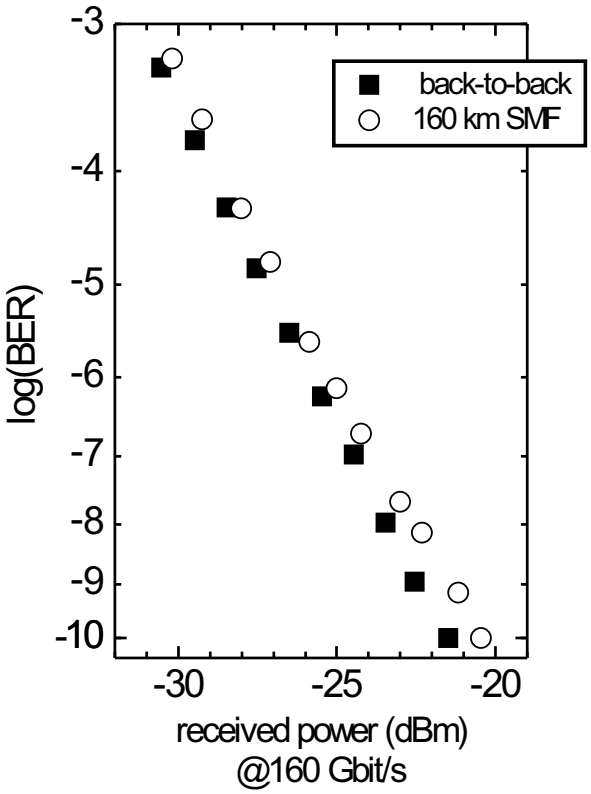

Figure 5.3: Bit error ratio for a 160 Gbit/s OTDM data signal without transmission (filled squares) and with transmission over 160 km fiber (hollow circles) using the GT-MZI as demultiplexer.

In both cases, error-free performance (which means that a BER of 10^{-9} is reached) was achieved. For the transmission, an average optical power of +11.5 dBm was used at the input of the transmission line. The receiver penalty for the transmission was about 1.5 dB (at BER=10^{-9}). From the back-to-back measurement a sensitivity of −22.4 dBm (at BER=10^{-9}) is derived for the 160 Gbit/s receiver.

5.2 Demultiplexing using GT-UNI

5.2.1 10 Gbit/s Base Data Rate

The GT-UNI switch was first tested as demultiplexer from 160 Gbit/s to 10 Gbit/s in a back-to-back system without transmission [25, 79]. Fig. 5.4 shows the experimental setup.

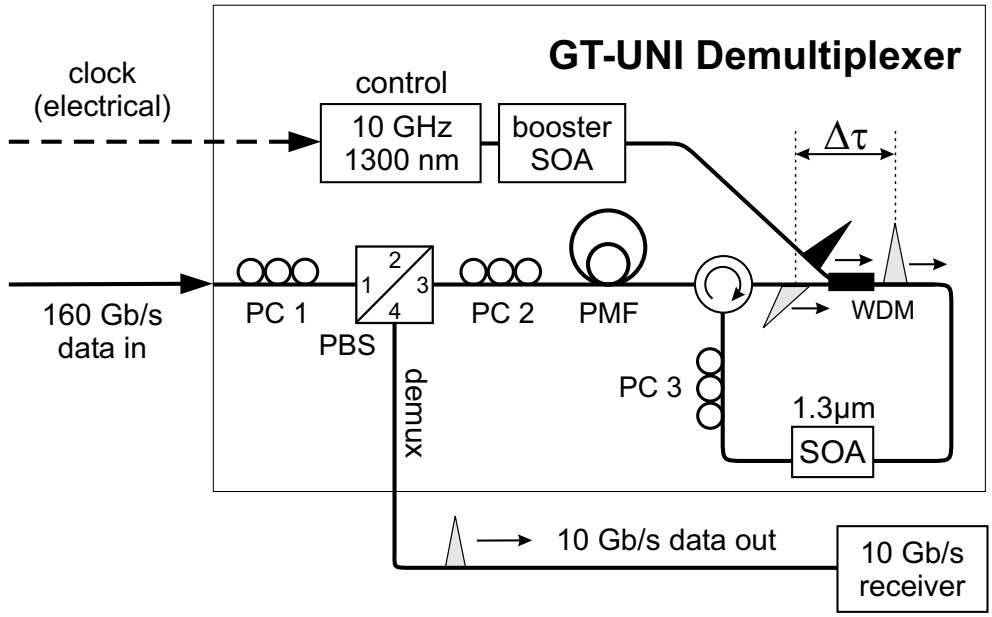

Figure 5.4: Setup of the GT-SOA based Ultrafast-Nonlinear Interferometer (GT-UNI) switch in its application as 160 Gbit/s to 10 Gbit/s all-optical demultiplexer.

The 160 Gbit/s data signal was generated in a 160 Gbit/s transmitter, identical to the one described in section 5.1. The operation principle of the GT-UNI switch was explained in section 4.3. The setup used for demultiplexing is identical to the one shown in Fig. 4.7 b). A piece of polarization maintaining fiber (PMF) is used to get a fixed switching window width. The width of the switching window can only be changed in this setup by replacing the PMF. The polarization controller PC 3 is used to adjust an appropriate interferometer bias for high suppression of the non-switched pulses at the 'demux port'. The 10 GHz optical control pulses (wavelength 1300 nm, 1.3 ps sech^2) are generated in a TMLL, also shown in Fig. 5.4 and amplified with a booster SOA. The control signal was synchronized to the data, by directly using the electrical clock signal from the receiver, which was possible because the data signal was not transmitted over a fiber span.

The switching window of the GT-UNI was measured for four different PMF lengths. The results are shown on the left hand side of Fig. 5.5. Switching window widths of 4.6 ps, 5.2 ps, 6.0 ps and 8.7 ps were obtained for PMF length of 3 m, 3.5 m, 4 m and 6 m respectively. The switching contrast was about 18 dB, which is slightly lower than the contrast values obtained for the GT-UNI switch in the PBS configuration (Fig. 4.7 a)), presented in section 4.3.

Bit error rate (BER) measurements were performed for demultiplexing from 160 Gbit/s to 10 Gbit/s, using the GT-UNI with PMF lengths of 3.0 m, 3.5 m and 4.0 m. The

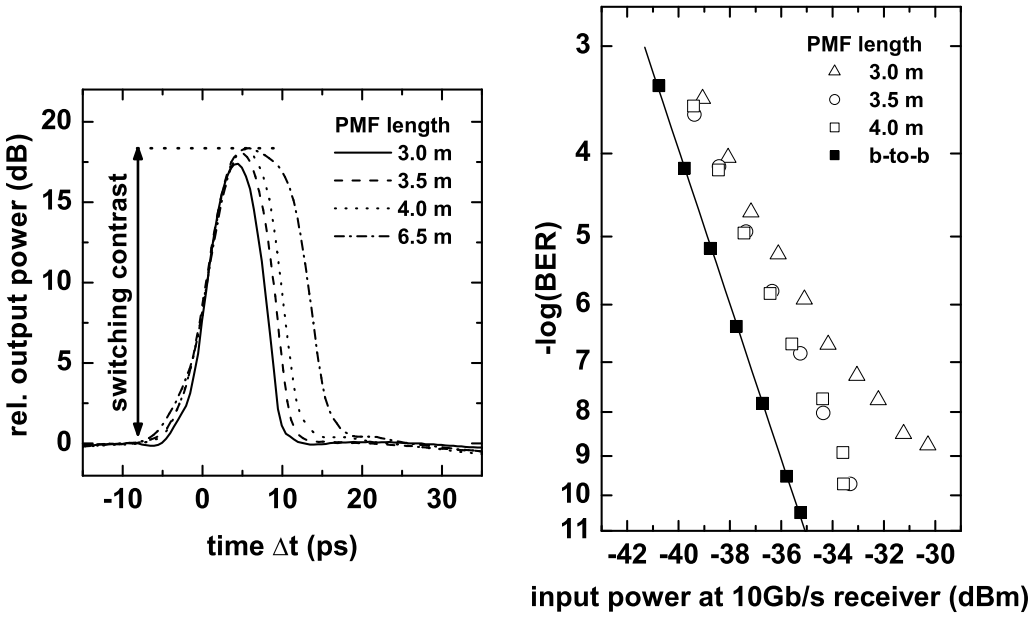

Figure 5.5: Left hand side: GT-UNI switching windows for different PMF lengths, Right hand side: BER for demultiplexing a 160 Gbit/s data signal with a GT-UNI switch, for different PMF lengths used in the GT-UNI. The BER for a non-multiplexed 10 Gbit/s signal (b-to-b) is shown for comparison.

average input power of the data signal into the GT-UNI was kept constant at +20 dBm. The average control pulse power before the WDM coupler was +10 dBm. The results are shown on the right hand side of Fig. 5.5. The BER of one demultiplexed OTDM channel is plotted over the average power of the demultiplexed signal before the 10 Gbit/s receiver. The performance with PMF lengths of 3.50 m and 4.0 m is very similar. The curves indicate a power penalty of about 2.3 dB (at BER=10^{-9}) compared to the BER of an unmultiplexed signal. No error-free demultiplexing was obtained with a fiber length of 3.0 m. This can not be explained by the slight decrease of the maximum transmittance, observed for a PMF length of 3.0 m. A possible explanation is the relative timing jitter between the data pulses and the control pulses, which can severely degrade the switching performance for very narrow switching windows. All BER measurements in Fig. 5.5 were performed with the word length $2^7 - 1$. Measurements with a longer word length $(2^{31} - 1)$ revealed a 1 dB larger penalty, which was entirely due to limitations in the electronics of the receiver. The BER of the demultiplexed signal was also measured as a function of the power at the 160 Gbit/s receiver. A penalty of 3.2 dB is observed, resulting in a receiver sensitivity of −22.3 dBm (at BER=10^{-9}). This is almost equal to the receiver sensitivity measured for the GT-MZI demultiplexer.

5.2.2 Polarization Diversity Scheme

The main disadvantage of the GT-UNI switch is the inherent polarization dependence. It is due to the operation principle of the UNI, which relies on a polarization rotation and subsequent polarization filtering of the incoming data signal. This only works for one linear input polarization. Apart from using an automatic polarization controller in front of the switch, which automatically adjusts the incoming data signal to the optimum linear state of polarization for the switch, a polarization diversity scheme can be employed to realize polarization independent operation. The idea of polarization diversity is, to split the data signal into two orthogonal polarization states, use separate switches for each polarization state and recombine the polarization states afterward. A polarization independent demultiplexer, based on the polarization diversity of a GT-UNI switch, will be presented in the following.

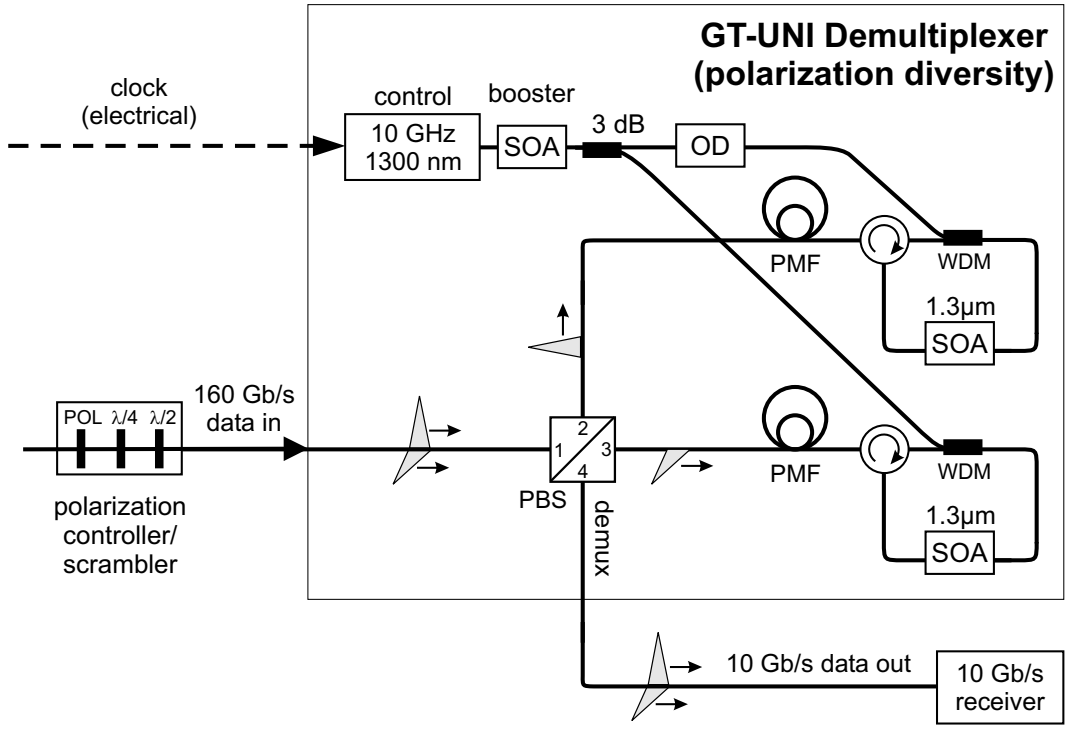

Figure 5.6: Schematic of the polarization insensitive GT-UNI demultiplexer based on a polarization diversity scheme.

Fig. 5.6 shows schematically the experimental setup of the polarization insensitive GT-UNI demultiplexer [80]. It comprises two GT-UNI switches, combined in a polarization diversity scheme. An incoming 160 Gbit/s data signal at port 1 of the polarizing beam-splitter (PBS) is split into two orthogonal components (port 2 and port 3). Each data component is demultiplexed separately by a GT-UNI switch. Then both are recombined again at the PBS. The setup of each single GT-UNI switch is identical to the GT-UNI demultiplexer shown in Fig. 5.4. The operation principle is explained in section 4.3. A piece of highly birefringent, polarization maintaining fiber (PMF) is used to delay the orthogonally polarized pulse components in the single switches. The length of the PMF was 3.5 m in both GT-UNI switches, which corresponds to a delay $\Delta\tau$ of about 5 ps. The

overall fiber length in both GT-UNI switches was also equalized, to make sure that the separately demultiplexed polarization components reach the receiver at approximately the same time (within a few picoseconds). The power of the recombined switched data signal at the receiver is independent of the relative phase between both components, because the components have orthogonal polarization. Therefore an active phase stabilization is not necessary, as long as a random polarization of the data signal at the receiver can be tolerated, which was the case in the experiments presented here.

The 10 GHz optical control pulses were generated by a TMLL (wavelength 1300 nm, 1.3 ps sech^2) and amplified with a booster SOA. They were split into two pulse trains (one for each GT-UNI switch) using a 3 dB coupler. An optical delay line (OD) in one branch, enabled to change the temporal delay between the control pulses transmitted to the single GT-UNI switches. Thus it provided an adjustment of the relative temporal position of the switching windows in both GT-UNI switches, relative to each other. The GT-UNI switches were insensitive to the control pulse polarization. The 160 Gbit/s optical data signal was generated using the 160 Gbit/s transmitter described in section 5.1.

In the experiments, a polarization controlling device (HP 8169A Polarization Controller) was used at the input of the GT-UNI demultiplexer. It comprises a linear polarizer (POL), a $\lambda/4$ and a $\lambda/2$ plate, which could each be rotated independently. With this device, the polarization of the data signal could, for example, be chosen such that the data signal left the PBS through only one port (port 2 or 3). In this case, the data signal is demultiplexed by one GT-UNI switch only. In addition, the $\lambda/4$ and the $\lambda/2$ plate could be rotated over time to obtain a quasi-randomly polarized signal (polarization scrambling). The control pulses were removed from the data signal behind the demultiplexer by the optical bandpass filter and the erbium-doped fiber amplifier, both included in the 10 Gbit/s receiver.

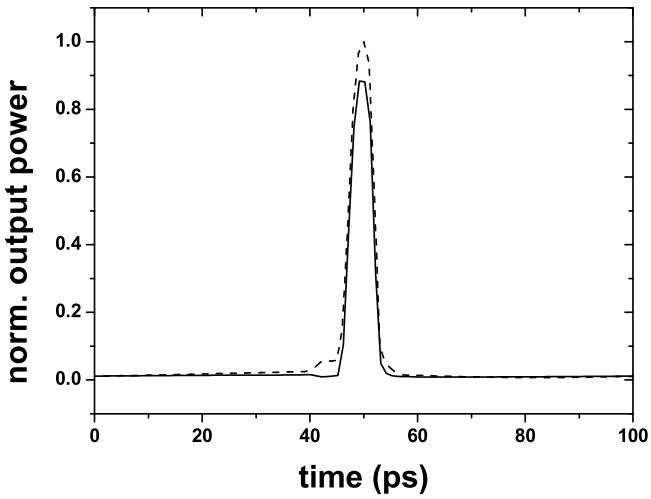

Figure 5.7: Switching windows of the solitary GT-UNI switches.

Fig. 5.7 shows the static switching windows of both GT-UNI switches. In this case, the state of polarization of the input signal was adjusted for the GT-UNI switch under study,

using the HP Polarization Controller, as described above. Both switching windows differ slightly in shape and amplitude. The window widths were about 5 ps and switching contrasts of about 18 dB were achieved.

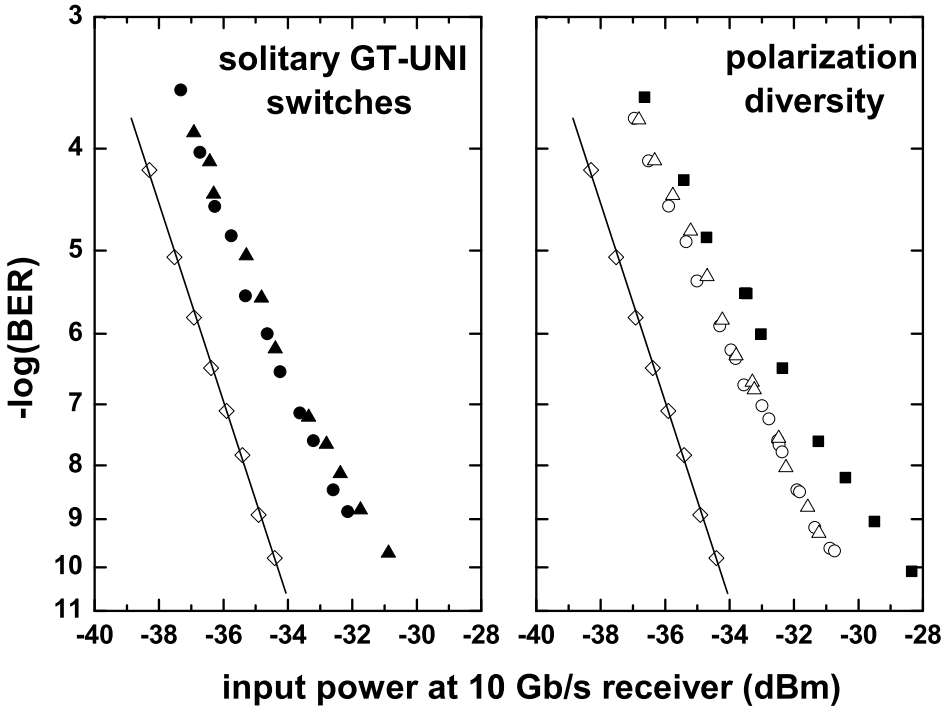

Figure 5.8: BER measurements: back-to-back (solid lines), with optimized state of polarization for one or the other GT-UNI switch (circles and triangles) and with scrambled polarization (filled squares).

The GT-UNI setup with polarization diversity was then tested as demultiplexer in an OTDM system without transmission. Fig. 5.8 shows bit error rate (BER) measurements for demultiplexing from 160 Gbit/s to 10 Gbit/s and back-to-back measurements (without multiplexer and demultiplexer). The BER curves on the left hand side of Fig. 5.8 were measured for each GT-UNI separately (either port 2 or port 3 of the PBS was disconnected and the data polarization was chosen appropriately). A power penalty of about 2.8 dB (at BER $= 10^{-9}$) was achieved for both switches. The BER curves on the right hand side of Fig. 5.8 depict measurements in the polarization diversity scheme using different states of polarization of the data signal. Two BER curves represent measurements, in which the HP Polarization Controller was set for optimum operation of one or the other of the two GT-UNI switches. In this case, the receiver was adjusted for optimum BER performance for each input polarization separately. The system performance was similar, with a power penalty of 3.4 dB. This is slightly higher than the results with the separately measured GT-UNI switches (see left hand side of Fig. 5.8). The difference may be due to some additional noise in the diversity scheme. The third BER curve on the right hand side of Fig. 5.8 depicts measurements in which the state of polarization of the data signal

was scrambled. During the measurement of each BER value, the state of polarization was rapidly changed over the whole Poincaré sphere. The BER curve shows a power penalty of 5.2 dB. This higher power penalty is attributed to the non-perfect relative adjustment of both GT-UNI switches in the polarization diversity scheme, which was observed in Fig. 5.7. All BER measurements were performed with the word length $2^7 - 1$. Measurements with a longer word length ($2^{31} - 1$, but no longer PRBS) revealed about 1 dB larger penalty, which is attributed entirely to limitations in the electronics of the receiver. In conclusion, the polarization insensitive GT-UNI shows a stable performance without the need of an active phase stabilization. The switch was also tested in a transmission experiment over field installed fiber at a data rate of 40 Gbit/s and error-free performance was achieved [81].

The polarization diversity scheme can in principle be applied to any polarization dependent switch. In the case of the UNI, the polarization splitter and combiner needed for the polarization diversity are already part of the switch itself, so that a simple setup with a minimum of additional components is possible. A problem arises, if the transmittance of the single switches used in the diversity is not linear with respect to the data input power. In that case the power of the demultiplexed signal depends on the input polarization, which would lead to a performance degradation. For interferometric switches based on conventionally operated SOAs, the switched output power is in general not linear to the input data power due to saturation effects inside the SOA. This would cause severe problems in polarization diversity schemes. Switches based on the gain-transparent scheme, like the GT-UNI switch, show a linear relation between the input data power and the output power (see Fig. 5.18). Those switches are therefore well suited to be used in a polarization diversity schemes. Of course a single, polarization independent switch still remains the optimum choice.

5.2.3 40 Gbit/s Base Data Rate

The single GT-UNI switch without polarization diversity was tested in a transmission experiment with a base data rate of 40 Gbit/s [26, 82]. The advantage of using a higher base data rate in an OTDM system is obvious. The number of receivers, which are needed in an OTDM system with 160 Gbit/s TDM bit rate to simultaneously detect all channels reduces from 16 at 10 Gbit/s base data rate to 4 at 40 Gbit/s. For demultiplexing to the base data rate of 40 Gbit/s, the repetition rate of the control pulses for the GT-UNI demultiplexer has to be increased to 40 GHz.

The setup of the 160 Gbit/s transmitter was identical to that used in the transmission experiment of the GT-MZI (see section 5.1). The wavelength of the transmitted data pulses was 1552 nm. The pulses were transform limited with sech^2 shape and a full width at half maximum (FWHM) of 1.2 ps. Two different receivers were used in this experiment to detect at both base data rates, 10 and 40 Gbit/s. For 10 Gbit/s, the receiver comprised the GT-UNI as optical DEMUX from 160 Gbit/s to 10 Gbit/s with subsequent electrical detection at 10 Gbit/s. In the 40 Gbit/s case, the GT-UNI was used with a higher rate of the control pulses as optical DEMUX for 160 Gbit/s to 40 Gbit/s with subsequent O/E conversion and electrical 40 Gbit/s to 10 Gbit/s demultiplexing [83].

The switching windows for the GT-UNI switch, used as demultiplexer in the receivers, are shown in Fig. 5.9 for 10 GHz and 40 GHz control pulse rate. In the 40 GHz case, about 6 dB lower contrast is observed. This was already discussed in section 4.4.2 and is

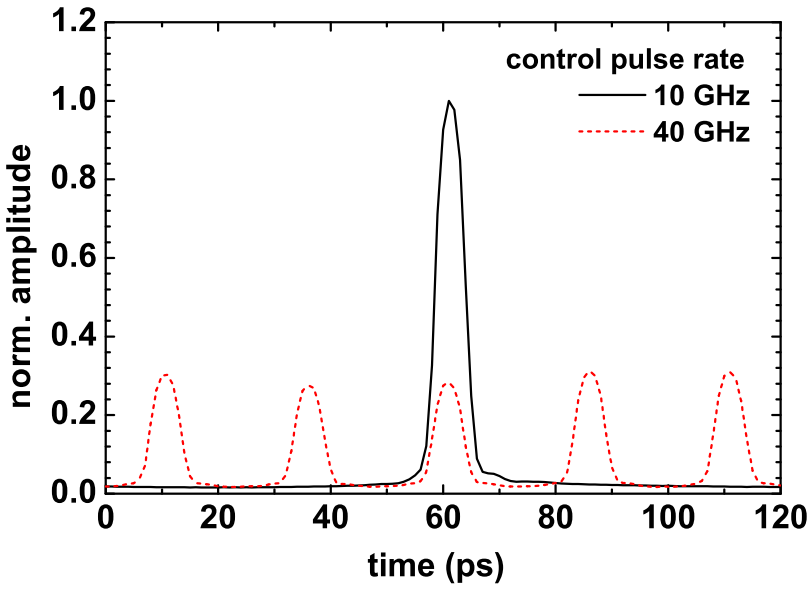

Figure 5.9: Switching windows of the GT-UNI optical demultiplexer for 10 GHz and 40 GHz control pulse rate.

mainly due to the lower nonlinear phase shift at the higher repetition rate of the control pulses (see also section 3.2.2). The phase shift is, however, sufficient for demultiplexing, due to the lower number of crosstalk channels at 40 Gbit/s base rate, as was discussed in section 4.4.4.

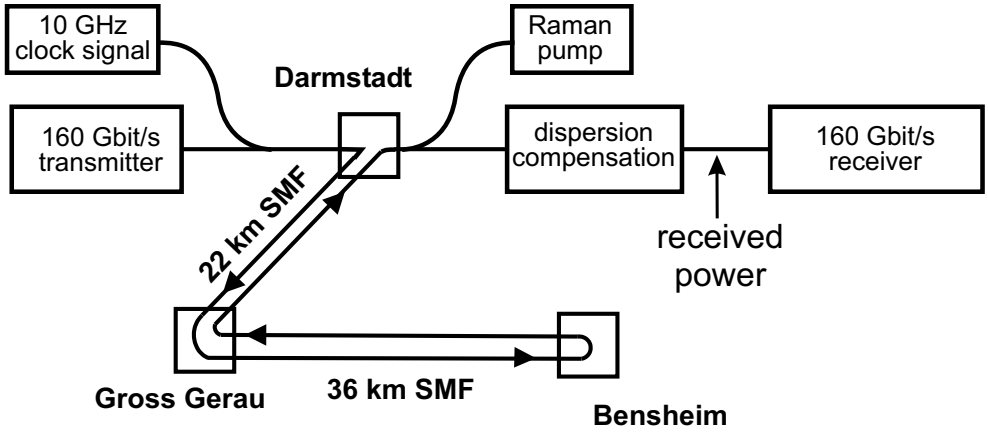

Figure 5.10: Schematic of the transmission link, with a total link length of 116 km SMF.

In this experiment, synchronization was achieved by transmitting a 10 GHz sinusoidal clock signal on a separate wavelength, which was detected at the receiver. This signal was then applied to synchronize the mode locked laser, which generated the optical control

signal for the GT-UNI demultiplexer at 1300 nm with a repetition rate of 10 GHz. For the experiments at 40 Gbit/s base data rate the control signal was multiplexed to 40 GHz by a delay line multiplexer. Two booster SOAs, one before and one after the multiplexer, were utilized to amplify the average power of the control signal to about +9 dBm.

The setup of the transmission link is shown in Fig. 5.10 [84]. An installed standard single mode fiber (SMF) link of the Deutsche Telekom between the cities of Darmstadt, Gross-Gerau and Bensheim was used. The total unrepeatered length of the fiber was 116 km and the total loss was about 32 dB, including all splices and connectors. To simplify the measurements, a Raman pump source was used for amplification of the data signal. The maximum power pumped backward into the transmission fiber was 945 mW, which resulted in a Raman gain of 14 dB. The dispersion was compensated after the transmission link.

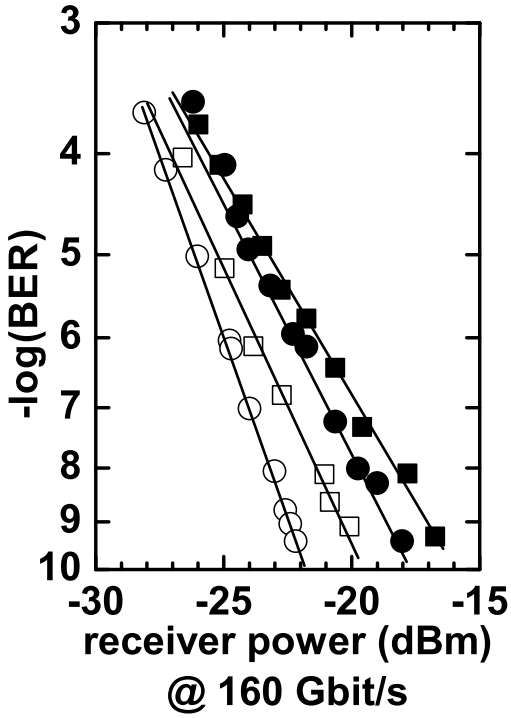

Figure 5.11: BER performance after transmission over 116 km SMF, for 160 Gbit/s to 10 Gbit/s (solid circles) and for 160 Gbit/s to 40 Gbit/s (solid squares). Back-to-back curves without transmission for 160 Gbit/s to 10 Gbit/s and to 40 Gbit/s (open circles and squares respectively) are included for comparison.

Fig. 5.11 shows the performance of the transmission system. The bit error rate (BER) dependence on the received optical power at the input of the optical demultiplexer was measured. For a TDM bit rate of 160 Gbit/s, receiver sensitivities (BER = 10^{-9}) of -22.4 dBm and -20.7 dBm were achieved at a base data rate of 10 Gbit/s and 40 Gbit/s respectively. The penalty for the higher base data rate is attributed to the fact that the

sensitivity of the 40 Gbit/s ETDM receiver was originally not optimized for RZ but for NRZ systems. For the transmission, the power launched into the SMF fiber span was approximately +12 dBm. For both base data rates, error free operation (BER = 10^{-9}) was achieved, with a penalty of about 4 dB compared to the BER curves taken without transmission.

These measurements confirm, that the GT-UNI switch can be used as demultiplexer in an OTDM system with a TDM bit rate of 160 Gbit/s and 40 Gbit/s base data rate. Despite the lower maximum transmittance of the switch at the higher repetition rate of the control pulses, the performance as demultiplexer was comparable to that at 10 Gbit/s base data rate. This is also in agreement with the results from section 4.4.2, where an even higher integrated contrast ratio was calculated for demultiplexing to the higher base data rate.

5.3 Add-Drop Multiplexing

Another essential operation in an OTDM network is to extract an individual channel at the base data rate from a multiplexed high bit rate data stream and to replace this dropped channel by a new channel, for instance in a network node. While for the simple extraction a demultiplexer is sufficient, simultaneous extraction and replacement requires an add-drop multiplexer (ADM). An add-drop multiplexer can also be realized with an interferometric switch, as was explained in the introduction. In this case, both output branches of the interferometer are needed. The branch that was used before in the application as demultiplexer ('demux port') and which contains the extracted channel, is called the 'drop port' of the ADM. The second branch, which has the complementary transmission characteristic, is called the 'add port'. All interferometric switches presented so far can in principle be used as add-drop multiplexer [85].

While for the application as demultiplexer only one output branch of the interferometer had to be optimized, add-drop multiplexing requires simultaneously good switching performance in both interferometer outputs. Two problems arise in this case for SOA based switches:

- As was shown in section 3.2.2, the gain changes in the SOA lead to amplitude variations in the data signal, transmitted through the switch. The repetition rate of the amplitude changes corresponds to the base data rate. For applications as demultiplexer, this does not influence the switching performance, because only one channel at the base data rate is extracted. For add-drop multiplexing however, also the other OTDM channels, which leave through the 'add port' and show the full amplitude modulation, have to be taken into account. Especially for conventionally operated SOAs, where amplitude changes of several dB might occur, this leads to a severe degradation in the transmitted data signal at the 'add port'.

- Two achieve a high on-off contrast in the 'add' and 'drop port' of a single interferometric switch simultaneously, a phase difference of exactly π between the split signals is needed in the standard interferometers, shown so far. This was already discussed in section 3.2.2. For a phase shift below π, the switch can only be optimized for good contrast in the 'add' or 'drop port', which is illustrated in Fig. 5.12. The switching windows of an ideal interferometric switch at the 'add' and 'drop port' are

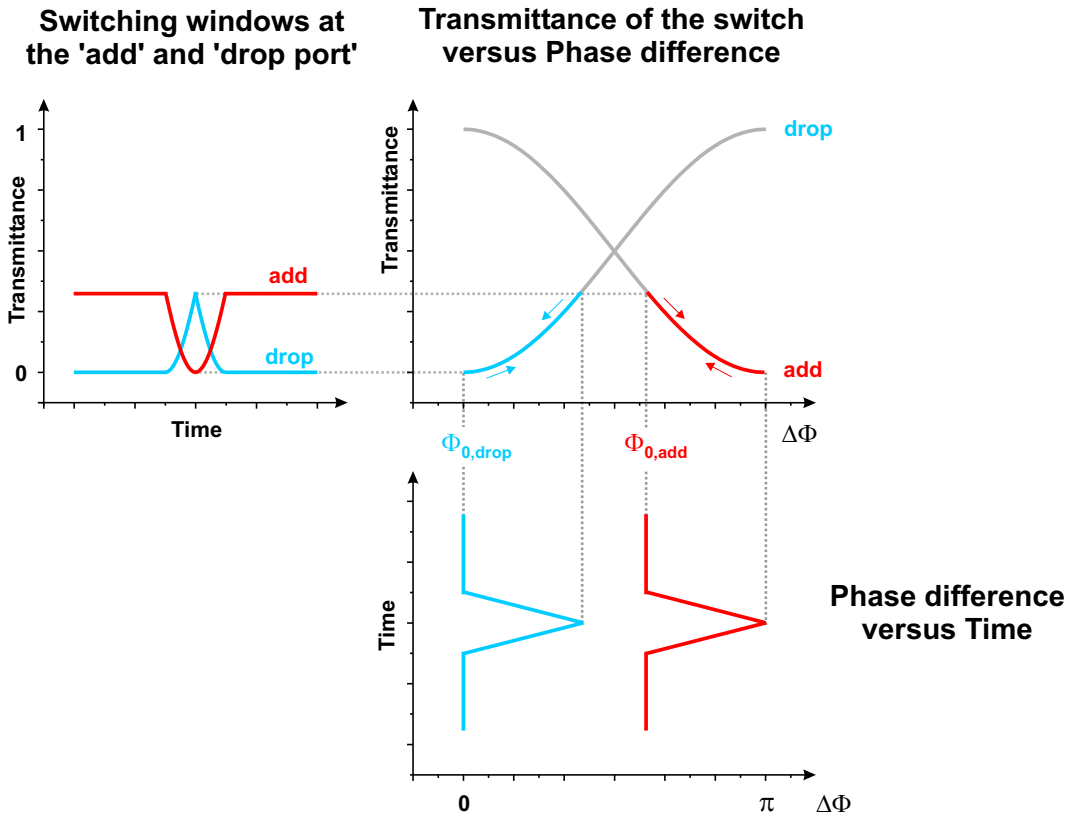

Figure 5.12: Impact of different phase offsets between the branches of an interferometric switch on the transmission characteristic in the add and drop port.

plotted on the left hand side for a phase shift below π. The change of the phase difference between the interferometer branches over time (plotted in the lower part), is assumed to be an idealized triangular function. The transmittance functions of the interferometer for the 'add' and 'drop port' ($T_{\mathrm{drop}}(\Delta\Phi) = 0.5 - 0.5\cos(\Delta\Phi - \Phi_{0,\mathrm{drop}})$ and $T_{\mathrm{add}}(\Delta\Phi) = 0.5 + 0.5\cos(\Delta\Phi - \Phi_{0,\mathrm{add}})$) are shown in the center. The absolute position of the phase difference curves depends on the static phase difference between both interferometer branches. Changing this static phase difference, called operation point Φ_0 in the following, results in a horizontal shift of the complete phase difference curve, which changes the shape of the switching window. From Fig, 5.12 it can be seen that a high on-off contrast in the switching window for the 'add' and 'drop port' simultaneously can not be achieved for a phase shift below π, because different operation points $\Phi_{0,\mathrm{add}}$ and $\Phi_{0,\mathrm{drop}}$ are needed.

While the amplitude modulation in the SOA can not be easily overcome, the problem due to the phase shift below π can be solved by using two switches in parallel. For one switch, the operation point is optimized for the drop operation ($\Phi_{0,\mathrm{drop}}$) and for the other switch the operation point is chosen for optimum add operation ($\Phi_{0,\mathrm{add}}$). This can in principle be realized with all interferometric switches, but it requires a rather complicated setup with a large number of components. In the case of the UNI, however, a simplified setup based on this idea was developed, which enables simultaneously a good add and drop performance in a single switch, despite a phase shift less than π [86]. Thus

a gain-transparent operated SOA can be used in the setup and the disturbing amplitude variations are avoided.

Experimental Setup

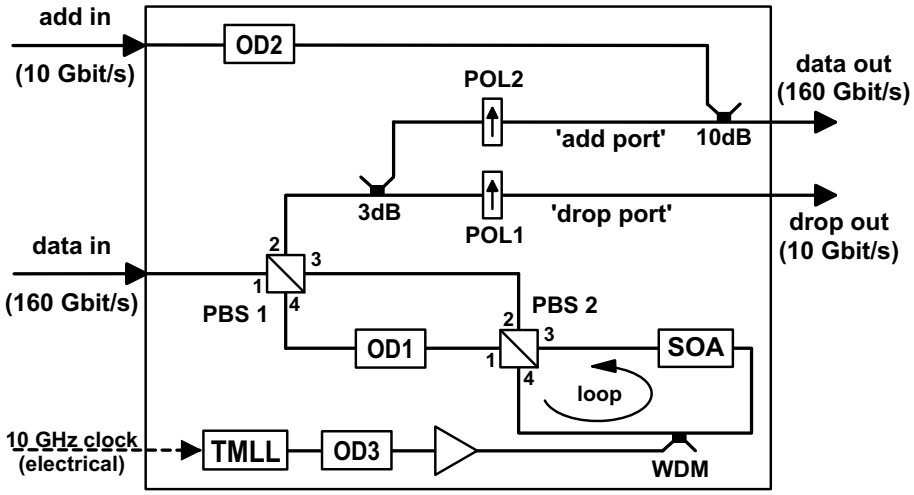

Figure 5.13: Setup of the add-drop multiplexer (ADM) based on a GT-UNI switch.

Fig. 5.13 shows schematically the setup of this ADM [44]. The polarization controllers for balancing the interferometer are omitted. The operation principle is similar to that of the GT-UNI in PBS configuration (Fig. 4.7 a)), discussed in section 4.3. By use of the polarizing beamsplitter (PBS 1), the incoming 160 Gbit/s data pulses are split into two orthogonally polarized components of equal amplitude at port 3 and 4 of PBS1. Both components propagate through different pass length (variable optical delay line, OD1) to PBS2, so that they leave PBS2 at port 4 with a relative time delay. They are then inserted into a polarization insensitive SOA (1.3 µm) together with the control pulses (wavelength 1300 nm, 1.3 ps sech^2 pulses at 10 GHz) via a 1300/1550 WDM coupler. The control pulses are generated in a TMLL. After traveling through the SOA, the temporal delay between the orthogonally polarized components is canceled, by launching them again into PBS2 through port 3 with the appropriate polarization. The pulse components recombine to a single data pulse, after leaving PBS1 at port 2. The state of polarization of the recombined data pulse is determined by the relative phase difference between the two orthogonally polarized pulse components. This phase difference changes, if a control pulse enters the SOA immediately after the leading data pulse component. For a phase shift of π, the polarization of the recombined data pulse is changed to the orthogonal state and can be completely separated with a single polarizing beamsplitter. This is no longer possible for a phase difference unequal to π. In this case, the 'add' and 'drop port' have to be optimized independently, by splitting the data signal after PBS1 and launching it into polarization filters POL1 and POL2. In the 'drop port', the orientation of POL1 is chosen such that only the dropped channel is transmitted (equivalent to a DEMUX operation). In the 'add port', POL2 is adjusted to suppress the dropped channel. The adjustment of the polarization filters corresponds to the setting of the optimum operation points $\Phi_{0,\text{add}}$

and $\Phi_{0,\mathrm{drop}}$, described above. The new 10 Gbit/s channel is inserted passively into the emptied time slot in the 'add port' via a 10 dB coupler.

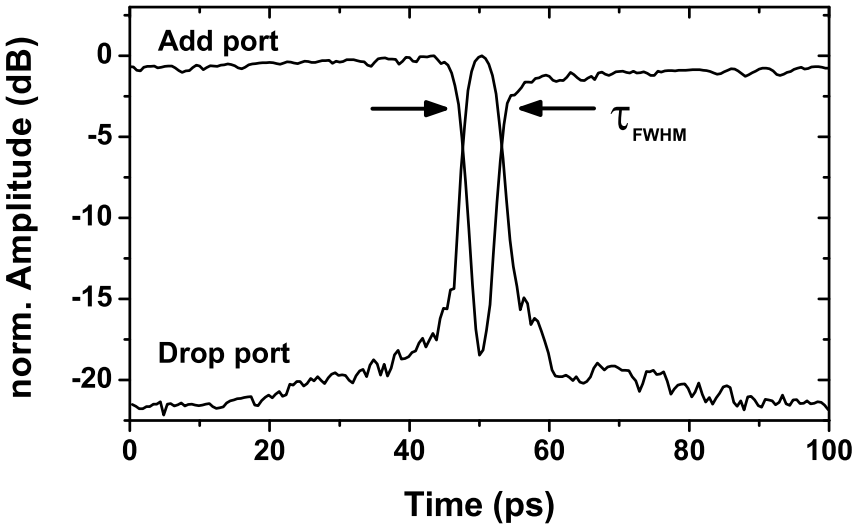

Figure 5.14: Switching windows for the 'add' and 'drop port' of the add-drop multiplexer.

Results

Switching windows, measured with the static pump-probe setup (Fig. 4.1) for the 'add' and 'drop port', are shown in Fig. 5.14. A high on-off contrast ratio of 20 dB and 17 dB was achieved for the 'add' and 'drop port' respectively. The switching window width, which is given by OD1, was chosen for optimum performance at 160 Gbit/s. This resulted in a full width at half maximum (τ_{FWHM}) of 7.0 ps for the 'add' and 4.4 ps for the 'drop port'. As can be seen from the schematic depiction in Fig. 5.12, the difference in switching window width is due to the phase shift of less than π. The OTDM channel that is dropped or cleared from the incoming data signal can be selected, by changing the relative delay between control and data pulses with the optical delay line OD3. The temporal position of the inserted channel with respect to the transmitted data signal is adjusted using OD2. The average input power of the control signal to the SOA was +8 dBm at a repetition rate of 10 GHz.

The add-drop multiplexer was tested in an OTDM system (without transmission) with 10 Gbit/s base data rate and a TDM bit rate of 160 Gbit/s. The experimental setup is shown schematically in Fig. 5.15. The data signal was generated in a 160 Gbit/s transmitter (see section 5.1). The 10 Gbit/s add-channel was taken directly from the 10 Gbit/s signal, generated in the transmitter. For the synchronization of the ADM, the 10 GHz electrical clock signal from the transmitter was used. The data signal at the output of the ADM (data out) was fed into a 160 Gbit/s receiver, which comprised a

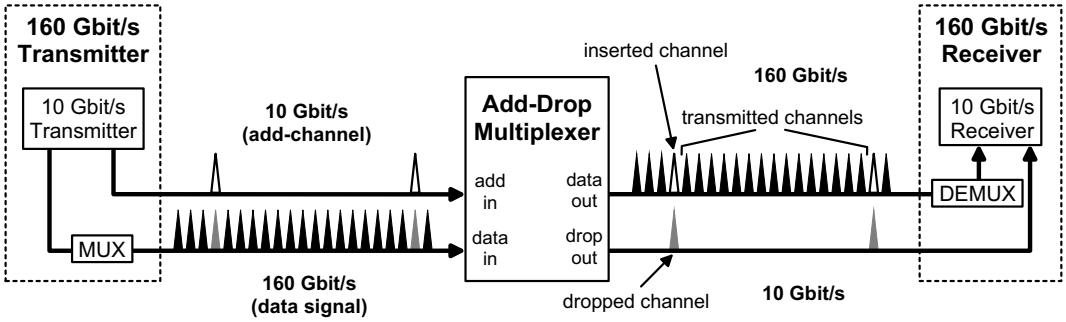

Figure 5.15: Schematic setup of the add-drop multiplexer in a 160 Gbit/s OTDM system with a base data rate of 10 Gbit/s.

GT-UNI demultiplexer (DEMUX) and a 10 Gbit/s receiver. The dropped channel (drop out) was transferred directly to the 10 Gbit/s receiver. The average powers at the add in and data in ports of the ADM were kept constant at −8 dBm and +20 dBm respectively. The inserted add-channel and the dropped channel were not identical and the amplitude and polarization of the add-channel was matched to the transmitted channels in the data out port.

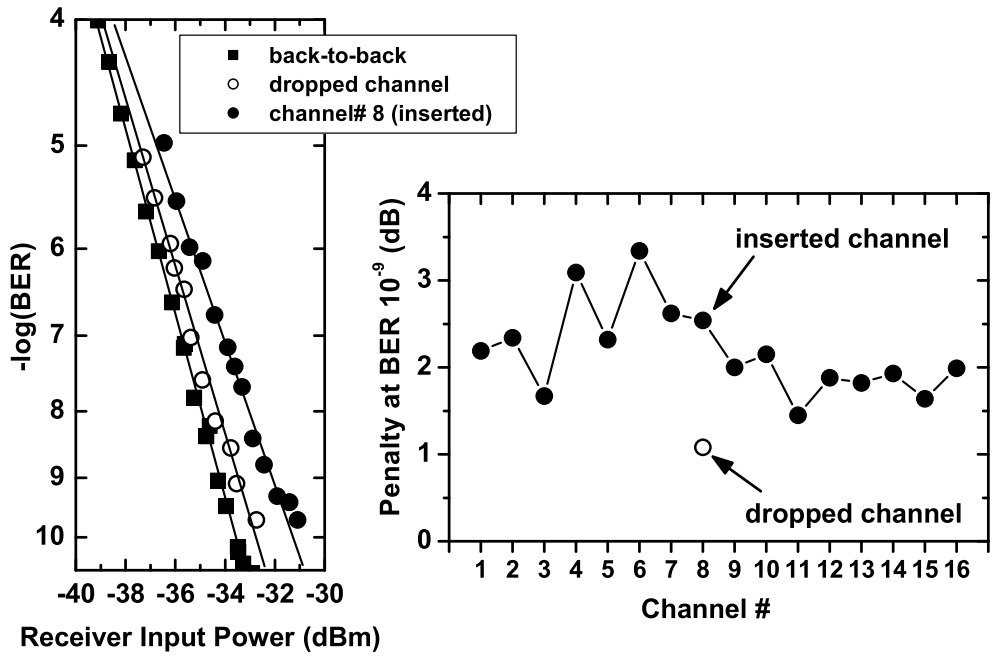

Figure 5.16: BER performance of the add-drop multiplexer at 160 Gbit/s.

The bit error rate (BER) of the inserted, the dropped and all transmitted channels was measured as a function of the average power at the 10 Gbit/s receiver. The results are shown in Fig. 5.16. On the left hand side, the BER curves for the dropped channel and

the inserted channel (channel number 8) are shown, together with the back-to-back curve for the 160 Gbit/s receiver. On the right hand side the power penalties, compared to the back-to-back curve, of all 16 channels in the data output of the ADM (including the inserted channel) and of the dropped channel are plotted. Error-free performance (BER = 10^{-9}) was achieved for all channels with a penalty of about 1 dB for the dropped channel and about 1.5 dB to 3.5 dB for the inserted and transmitted channels. Recently, transmission experiments have been reported in [87] using an ADM similar to the device presented here.

5.4 Optical Sampling

A crucial issue in high-speed OTDM systems (160 Gbit/s or above) is the in-service quality monitoring at the full TDM bit rate. Up to now, this is not possible with the standard electrical devices used at lower data rates, due to bandwidth limitations of the electric components. An alternative are optical sampling systems, which are similar in operation to electrical sampling systems, but use an optical gate. In order to enable sampling of high bitrate signals, these gates require a high timing resolution in the pico or sub-picosecond range. Optical sampling systems have been realized using switches based on four wave mixing in SOAs [88], cross-phase modulation in fibers [41], as well as second-harmonic or sum frequency generation in crystals [89, 90]. Also interferometric switches based on SOAs can be used. Especially switches using gain-transparent operated SOAs offer the advantage of high input to output linearity and wide wavelength tuneability of the input signal.

Therefore a GT-UNI switch was used as gate in an optical sampling system [40, 91]. Different from the application as optical demultiplexer, where the switching window has an optimum width, the window width in optical sampling should be as short as possible to achieve a high timing resolution.

Experimental Setup

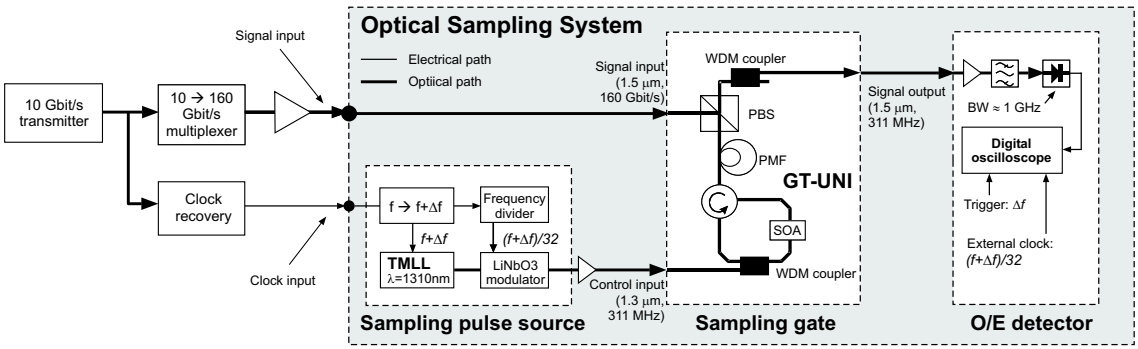

Figure 5.17: Schematic of the 160 Gbit/s sampling system with a GT-UNI as fast sampling gate.

Fig. 5.17 shows schematically the experimental setup of the sampling system, incorporating the GT-UNI as sampling gate. The setup of the GT-UNI is similar to that used as

demultiplexer (see section 5.2). The sampling system comprised three main parts: the sampling pulse source, the GT-UNI sampling gate and the opto-electrical (O/E) detector. As to the sampling pulse source, a TMLL at 1300 nm (1.5 ps sech^2 pulses, 0.2 ps rms timing jitter) was used. The laser was driven by the 10 GHz extracted clock signal, shifted by $\Delta f = 50$ kHz. Due to the limited clock speed of the digital oscilloscope in the O/E detector, the sampling pulse rate had to be reduced to 310 MHz by a $LiNbO_3$-Mach-Zehnder modulator. The sampling pulses were then fed into the control input of the GT-UNI. They open a switching window and part of the incoming data signal is gated to the signal output. The width of the switching window, which determines the timing resolution of the sampling system, is given by the differential group delay of the (high birefringent) PMF. The operation principle of the GT-UNI is described in detail in section 4.3. As the sampling pulses are at 1300 nm, the signal is easily separated from the sampling pulses by a 1550/1300 WDM coupler, independent of the signal wavelength. Then the signal is launched into the O/E detector, where the peak power of these optical samples is detected and displayed using a photodiode (1 GHz bandwidth) and a digital oscilloscope with external clock input. The oscilloscope is triggered by the frequency offset Δf, and allowed recording of eye diagrams with arbitrary persistence time. To increase the timing resolution of the sampling system, as compared to the demultiplexing experiments described in section 5.2, a shorter piece of PMF (1.8 m) was used in the GT-UNI switch. The GT-UNI configuration, used as sampling gate, was polarization dependent. In principle, also the polarization independent setup based on polarization diversity, shown in section 5.2.2, could be employed.

Results

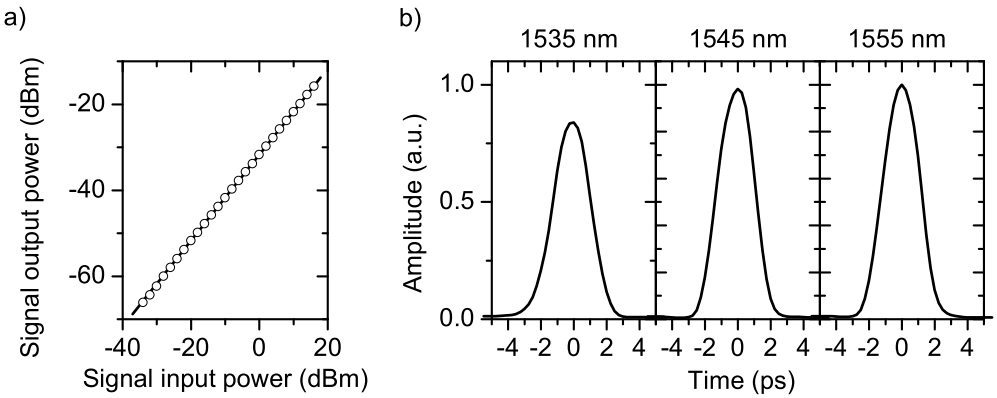

Figure 5.18: a) Linear dependence of the switched output power on the signal input power (open circles: measured values, solid line: ideal linear dependence) b) Switching windows of the GT-UNI sampling gate for different signal wavelengths.

First the sampling gate was investigated separately. The signal input to output linearity and the switching windows for different signal wavelengths were measured. For these

measurements, the signal output of the GT-UNI was directly connected to an optical spectrum analyzer and the sampling pulse rate was set to the 10 GHz extracted clock frequency, by omitting the frequency shifter and the modulator. The temporal delay between the sampling and signal pulses was changed by an optical delay line in the signal branch (not shown in Fig. 5.17). This corresponds to the static pump probe setup described in Fig. 4.1. The results are shown in Fig. 5.18. On the left hand side, the maximum switched output power is plotted as a function of the signal input power. A strictly linear dependence over a range of 50 dB was observed. This is typical for switches based on gain-transparent operated SOAs, because the signal pulses below the SOA band gap do not influence the carrier distribution in the SOA. The graph also indicates an insertion loss of the GT-UNI of about 30 dB. This fairly high value results mainly from the loss in the 1300 nm SOA (about 17 dB) and from the loss in the hybrid setup, as was discussed in detail in section 4.4. The energy of the sampling pulses was 0.5 pJ at the control input of the GT-UNI. The right hand side of Fig. 5.18 shows the switching windows of the GT-UNI for three different wavelengths. The available wavelength range of the signal was limited by the EDFA gain region and the TMLL, used in the 10 Gbit/s transmitter. Obviously, the shape of the switching windows is not depending on the wavelength. A width (FWHM) of 2.2 ps and a contrast of 20 dB was obtained for all three wavelengths. The lower maximum output power at 1535 nm is due to a slightly different alignment in the GT-UNI. The energy of the sampling and signal pulses was kept constant at 0.5 pJ and 20 pJ respectively (measured at input ports of the GT-UNI). The corresponding pulse width was 1.5 ps and 0.8 ps respectively.

The complete sampling system was tested by recording eye diagrams at a TDM bit rate of 160 Gbit/s. The 160 Gbit/s PRBS-RZ data signal was generated in a transmitter, identical to the one described in section 5.1. Part of the signal from the 10 Gbit/s transmitter was used to derive the 10 GHz electrical clock input to the sampling system, using a simple RF clock line extraction.

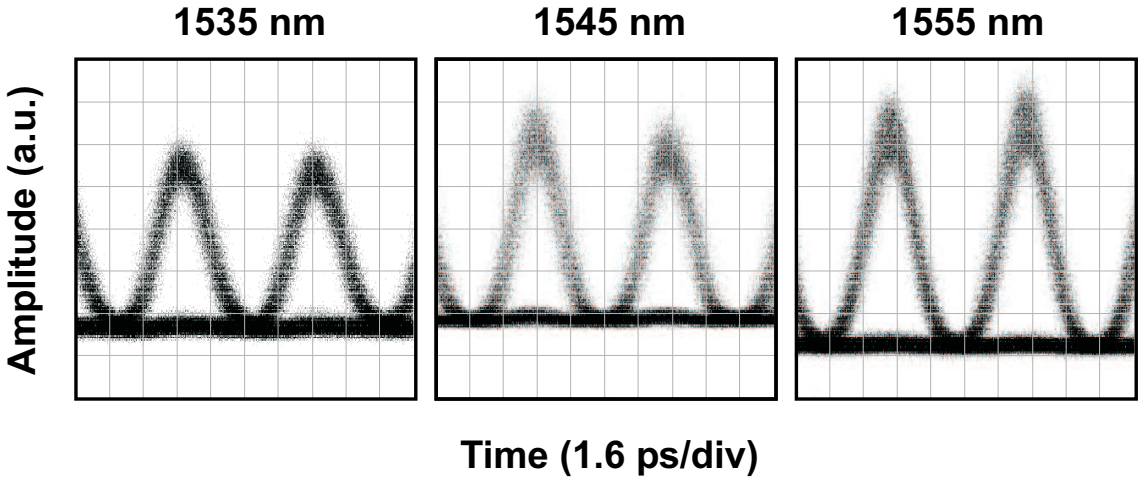

Figure 5.19: 160 Gbit/s eye diagrams, measured with the sampling system incorporating a GT-UNI gate for different wavelengths of the data signal.

Fig. 5.19 shows the measured eye diagrams for the three different data wavelengths. The energy of the sampling and data pulses for these measurements was 1 pJ and 5 pJ re-

spectively (measured at the input ports of the GT-UNI). Clearly open eyes with equal shape at a persistence of 200 traces can be observed over the whole wavelength range under investigation, due to the wavelength independence of the GT-UNI sampling gate. The eyes are also well separated, because of the high temporal resolution of the sampling system. The differences in the baseline and height of the eye diagrams can be explained by different amplifier gain and offset values of the oscilloscope in the O/E detector. From the eye diagram at 1545 nm a slightly higher jitter of the data signal can be derived. This is due to a higher jitter in the 10 Gbit/s transmitter at this wavelength, as was confirmed by rms timing jitter measurements.

In conclusion, the GT-UNI switch can be used as sampling gate in an all-optical sampling system for eye diagram monitoring at 160 Gbit/s. By gain-transparent SOA operation, a high input to output linearity and almost wavelength independent switching performance of the sampling gate is achieved. This leads to a very low wavelength dependence of the sampled eye diagrams over a range of 20 nm, only limited by the signal laser source and optical amplifiers available. Without these limitations, a wavelength range of more than 50 nm can be expected. The GT-UNI was chosen as sampling gate because of its stability as hybrid device. The same performance of the sampling system can be expected by using a Mach-Zehnder type switch, which has a high potential for monolithic integration.

The main disadvantage of the SOA based interferometric switches, compared to solutions based on fibers or crystals, is the switching window width, which depends on the steepness of the phase change. For the minimum control pulse width of about 1 ps available in the experiments, the shortest achievable window width was about 2 ps. Compared to this, window widths significantly below 1 ps can easily be achieved with switches based on fibers or crystals. In general, these switches suffer from the high average powers that are needed to achieve a good switching contrast for high control pulse repetition rates. In the case of optical sampling, the repetition rate of the control pulses is limited by the O/E converter and lower average powers are sufficient for switching. With a shorter piece of PMF in the GT-UNI and shorter sampling pulses, the timing resolution of the sampling system can be increased and monitoring of even 320 Gbit/s eye diagrams was shown [39]. However, switches using fibers or crystals have clearly the greater potential for sampling of even higher data rates.

5.5 3R-Regeneration and Wavelength Conversion

The possibility to regenerate a distorted data signal after transmission is an inevitable requirement in a transmission system. The regeneration becomes increasingly difficult at higher bit rates, as it has to be performed in the optical domain. For this so called 3R-regeneration (3R stands for re-amplification, re-shaping and re-timing), interferometric switches can be used. A second important function, in conjunction with WDM systems, is wavelength conversion at high bit rates. All-optical interferometric switches can combine both functions, wavelength conversion and 3R-regeneration (3R-wavelength conversion). In chapter 3 it was shown that a high repetition rate of the control pulses significantly reduces the phase shift in SOAs. Thus, SOAs are less attractive as nonlinear medium in interferometric gates for applications which require high repetition rates of the control pulses (160 GHz) like wavelength conversion and 3R-regeneration. Fiber based interfe-

rometric gates can be used instead, because the nonlinear phase shift in optical fiber by XPM is independent of the control pulse rate.

In the experiment presented here, a Kerr-Switch was used as decision gate in a 3R-wavelength converter at 160 Gbit/s [92, 51]. Especially to achieve re-timing in a wavelength converter, the data signal has to switch a re-timed pulse train, rather than a continuous wave signal, as was discussed in the introduction. Such 3R-wavelength converters have been under intensive study over the last years. The highest data rate reported so far was 84 Gbit/s [49], using semiconductor based switches.

Kerr-Switch

The setup and operation principle of the Kerr-Switch was discussed in detail in section 2.3.2. A typical switching window, measured for a Kerr-Switch with the static pump-probe setup (Fig. 4.1), is shown in Fig. 5.20.

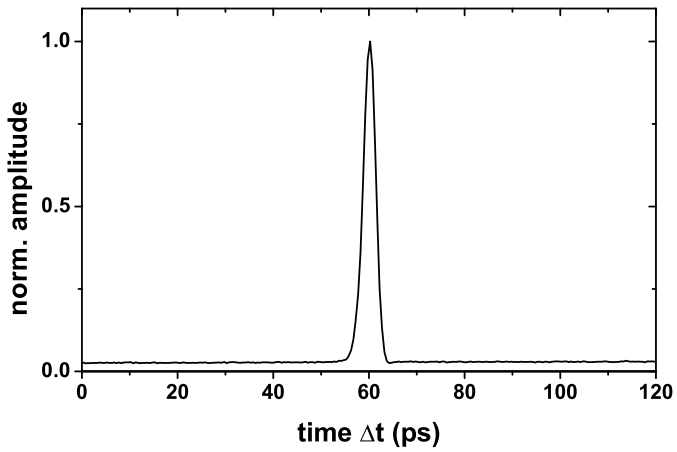

Figure 5.20: Switching window for the Kerr-Switch.

A short switching window width of about 3 ps is achieved, with a switching contrast of about 16 dB. The window width and the contrast are comparable to the values measured for the SOA based switches. However, in the fiber based Kerr-Switch, the contrast will not decrease at higher control pulse rates, because the nonlinear phase shift does not depend on the repetition rate of the control pulses. The HNLF used was 630 m long and had a zero-dispersion wavelength of λ_0=1550.5 nm. The nonlinear coefficient was $\gamma = 20\ \mathrm{W^{-1}km^{-1}}$. The data and the control signal had a repetition rate of 10 GHz. The wavelength was 1555.2 nm for the data signal and 1542.5 nm for the control signal. The average power for the data and control signal at the input of the HNLF was −5.0 dBm and −0.7 dBm respectively.

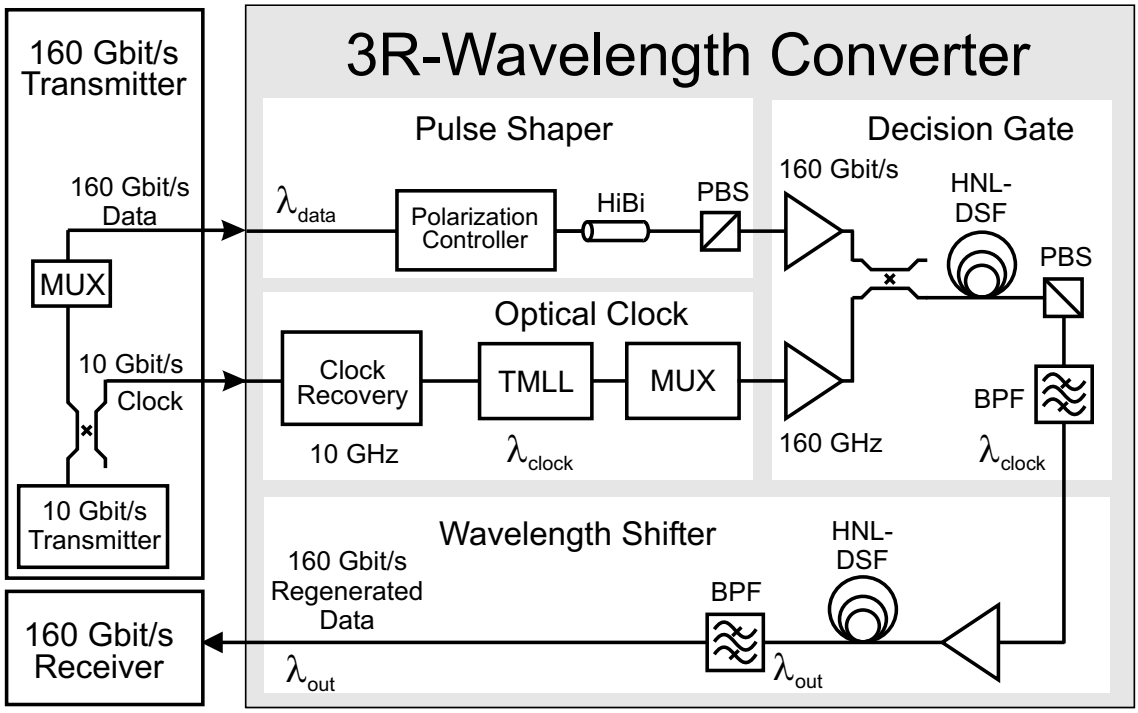

Figure 5.21: Experimental setup of the 3R-wavelength converter based on a Kerr-Switch as decision gate.

Experimental Setup

Fig. 5.21 shows a schematic diagram of the experimental setup. It comprised a 160 Gbit/s transmitter, the 3R-wavelength converter and a 160 Gbit/s receiver. The transmitter was described in section 5.1. The generated 160 Gbit/s pulses had a wavelength of 1554 nm and a width of 1.3 ps (FWHM) at the input of the 3R-wavelength converter. The 160 Gbit/s RZ data signal at the output of the 3R-wavelength converter had the wavelength 1541 nm, an average power of +10 dBm and consisted of pulses with 1.6 ps FWHM. The 3R-wavelength converter comprised four distinct elements: the **pulse shaper**, the **optical clock**, the **decision gate** and the **wavelength shifter**.

In the **pulse shaper**, the data pulses were transformed to an almost rectangular shape (FWHM = 2.9 ps), using a piece of high birefringent fiber (HiBi-fiber, 0.5 m long with a differential group delay of 0.85 ps) and a polarizing beamsplitter (PBS). The operation principle is explained in detail in Appendix A.1. The pulse shaping is aimed to prevent the transfer of phase noise of the input data pulses to amplitude noise of the output data pulses in the decision gate. This is especially important, if two separate pulse sources for data and clock are used (like in the present experiment), which will be the case in a complete transmission system.

The **optical clock** was based on a TMLL of the same kind, as used in the transmitter and in the receiver (all delivering transform limited sech^2 pulses). The 10 GHz output pulses of the TMLL were multiplexed (MUX) by a fiber delay line multiplexer to a 160 GHz, single polarization pulse train (wavelength 1537 nm, 1.8 ps FWHM). The TMLL was synchronized by a 10 GHz clock signal, extracted at the transmitter.

The **decision gate** was an optical Kerr-Switch (described in detail in section 2.3.2),

comprising 1.6 km highly nonlinear dispersion-shifted fiber (HNL-DSF). The HNL-DSF had a third-order nonlinear coefficient of 20 $W^{-1}km^{-1}$ with $\lambda_0 = 1552.5$ nm. The average input power of the control signal into the HNL-DSF was +18 dBm. The polarization state of the 160 GHz clock pulses was adjusted for zero transmittance through the Kerr-Switch, in the absence of the control pulses. The data signal switched the clock pulses by using XPM-induced rotation of the clock pulse polarization state in the HNL-DSF (see section 2.3.2). The polarization state of the 160 Gbit/s control pulses was then adjusted for optimum XPM.
In the **wavelength shifter**, supercontinuum (SC) generation in 850 m HNL-DSF with $\lambda_0 = 1550.3$ nm was used. The spectrum of the switched data at $\lambda_{clock} = 1537$ nm was broadened coherently by self-phase modulation (SPM) in the HNL-DSF, and then the wavelength-converted copy of the data was obtained by filtering out the generated SC light with an optical bandpass filter (center wavelength 1541 nm). The average input power of the switched data into the HNL-DSF was +20 dBm.

Results

Fig. 5.22 shows the obtained BER values versus the power at the 160 Gbit/s receiver for two different measurements.

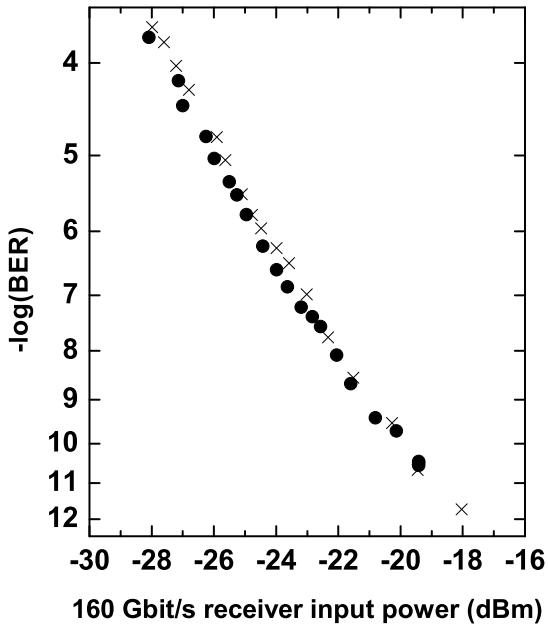

Figure 5.22: BER measurement of the wavelength converted 160 Gbit/s data signal after a 3R-wavelength converter (bullet), compared to a reference measurement (cross).

In the reference measurement, the 160 Gbit/s receiver was directly connected to the transmitter. In the second measurement, the 3R-wavelength converter was placed between

transmitter and receiver, as depicted in Fig. 5.21. No significant difference between both measurements is observed. Even considering, that a different pulse width and wavelength was used for the reference measurement, the results show no degradation of the data signal after the 3R-wavelength converter.

The experiment shows, that a Kerr-switch can be used as decision element in an all-optical wavelength converter with 3R-regenerating capabilities operated at 160 Gbit/s. This is the highest bit rate of a 3R-wavelength converter reported to date. Due to the polarization dependence of especially the Kerr-Switch and the pulse shaper, an automatic polarization controller is needed, when the 3R-wavelength converter is used in a transmission system. One critical issue of using a fast optical gate in a wavelength converter, is the conversion of jitter in the incoming data signal to amplitude noise in the output data signal. This effect was reduced by using a pulse shaper at the input of the decision gate. Recently, the 3R-wavelength converter presented here has been successfully tested in a recirculating loop experiment at 160 Gbit/s. Details about this experiment can be found in [50].

Chapter 6

Summary and Outlook

Summary

This work investigates all-optical interferometric gates based on Semiconductor Optical Amplifiers (SOA) and their application to all-optical signal processing. The objective was to realize interferometric gates for operations like demultiplexing, optical sampling, add-drop multiplexing, wavelength conversion and 3R-regeneration in a 160 Gbit/s OTDM system with 10 and 40 Gbit/s base data rate. After presenting the basics of interferometric switching in chapter 2, including a theoretical description of different interferometer configurations with the Jones formalism, the SOA as nonlinear medium was considered in detail. SOAs with different structures (bulk and multiple quantum-well, MQW) and in different operation modes (conventional and gain-transparent, GT) were investigated and compared. For interferometric switching the amount of refractive index change and the associated maximum phase change for an optical signal propagating through the SOA is of major importance. Therefore, the response of the SOA gain and refractive index upon saturation by a strong optical pulse was measured under different operation conditions (injection current, control pulse power, control pulse repetition rate). The aim was to derive the optimum operation parameters with respect to interferometric switching. It was found that the gain-transparent operated MQW-SOA is the best choice for almost all applications addressed in this work, in consideration of the available devices. Subsequently, interferometric SOA gates based on three different interferometer setups, namely the Semiconductor Laser Amplifier in a LOop Mirror (SLALOM), the Mach-Zehnder Interferometer (MZI) and the Ultrafast-Nonlinear Interferometer (UNI) were realized in hybrid setups using GT-SOAs. All three gates were characterized by measuring the switching windows under different operation conditions with a pump-probe technique. The switching windows were evaluated using different criteria, such as the switching window width, the on-off contrast ratio, the maximum transmittance and the integrated contrast ratio (ICR). Based on the results, the gates were compared with respect to their application in OTDM systems. Finally, the most promising gates were tested in OTDM system experiments at a TDM bit rate of 160 Gbit/s and base data rates of 10 Gbit/s and 40 Gbit/s. The GT-UNI turned out to be the best hybrid setup, interferometric gate for demultiplexing, add-drop multiplexing and the application as sampling gate. Wavelength conversion and 3R-regeneration could not be realized with SOA based gates and a fiber based solution was used instead. Error-free performance at 160 Gbit/s was demonstrated for all applications, in the case of add-drop multiplexing and 3R-regeneration for the first time.

In detail, the following results were obtained:

- **SOA Characterization:** A maximum phase change of 1.4 π, together with a gain variation of about 8 dB were determined for the conventionally operated SOA at 10 GHz control pulse rate. Compared to this, the GT-SOA showed 8 times smaller gain variations (below 1 dB), but also a 3 times lower phase change (about 0.4 π).

  For the GT-SOAs, the maximum phase change increases when applying higher driving currents or when increasing the optical power of the control pulses. A saturation of the phase change was observed for higher values. For the best GT-SOA under test, a 0.8 µm long MQW, a phase shift of about 0.4 π was reached at 300 mA driving current and a control pulse energy of 200 fJ.

  The investigation of GT-SOAs with different length showed that the loss by free carrier absorption increases significantly in longer devices. In general, the investigated bulk GT-SOAs showed a higher loss and a lower phase shift per length compared to the MQW device.

  An increase of the repetition rate from 10 to 40 GHz leads to a decrease of the phase shift to about half the value at 10 GHz. This was found for conventional and gain-transparent operated SOAs.

  Conclusion: The optimum operation parameters for the SOAs with regard to interferometric switching, depend on the operation mode. In gain-transparent operation, the phase shift is low ($< \pi$), so that high driving currents and control pulse powers are advantageous to achieve a phase shift closer to π. However, above a certain limit, which was 300 mA driving current and 200 fJ control pulse energy for the best investigated SOA, the phase shift cannot be increased significantly due to saturation effects. In conventionally operated SOAs, where a phase shift of π is easily obtained at moderate driving currents and control pulse powers, a compromise has to be found between the required phase shift and the distortions in the switched signal induced by the gain variations.

  The gain-transparent operated SOA has advantages due to the very small gain variations, as long as no complete phase shift of π is required. The phase shift can be increased by using longer GT-SOAs, but the loss due to free carrier absorption increases significantly with the SOA length. The optimum SOA length depends on the required phase shift and on how much loss is tolerated in the application. The 0.8 mm long MQW GT-SOAs, used to realize the interferometric gates in this work, are in agreement with the estimated optimum SOA length between 0.6 and 1.2 mm. Due to the lower loss and the higher phase shifts per length, MQW-SOAs are more suitable for gain-transparent operation than bulk devices.

  SOA based interferometric gates are not favorable for applications like wavelength conversion or 3R-regeneration, where the control pulse rate is given by the full TDM bit rate (160 Gbit/s and above), because of the lower phase shift at higher control pulse rates. For demultiplexing at the higher base data rate of 40 Gbit/s, the phase shift in the SOAs is still sufficient, even in gain-transparent operation.

- **GT-SOA based Interferometric Gates:** The shortest switching windows were measured for the GT-UNI and the GT-MZI with a value of 3 to 4 ps. The on-off contrast at 10 GHz control pulse rate was 28 to 30 dB. The on-off contrast of the

GT-SLALOM was lower compared to the other two switches. Due to the co/counter-propagating scheme in the Sagnac Interferometer it dropped to about 22 dB. At 40 GHz control pulse rate, the difference in switching performance is even more obvious. While for the GT-UNI and GT-MZI the on-off contrast is still between 23 and 25 dB, the value for the GT-SLALOM is below 15 dB.

A direct comparison of the three gates was done using the integrated contrast ratio (ICR) and the maximum transmittance. A high ICR value denotes a good switching performance and a high maximum transmittance means a low switching loss. The ICR values, in particular at higher TDM bit rates, and the maximum transmittance of the GT-UNI and the GT-MZI were higher compared to the GT-SLALOM. This was even more pronounced for the higher base data rate of 40 Gbit/s.

The increase in control pulse repetition rate to 40 GHz leads to a decrease in maximum transmittance for all three gates and as a result, to a decrease in on-off contrast by about 5 dB. Despite this lower contrast the ICR was higher compared to the 10 GHz case. This is due to the lower number of cross talk channels at 40 Gbit/s base data rate.

Conclusions: It can be concluded that with the given GT-SOAs, the UNI and the MZI configuration are more suitable for demultiplexing and add-drop multiplexing at high TDM bit rates ($>$ 80 Gbit/s), than the GT-SLALOM. Also for applications as sampling gate, where narrow switching windows are required, the UNI and the MZI configuration are the better choice. To decide whether the UNI or the MZI is the better configuration depends on the actual setup. As hybrid device, the MZI needs to be actively stabilized, which makes the handling difficult. In this case the UNI is preferred. However, a monolithically integrated MZI has the advantage of being more compact and can potentially be made polarization independent without the need of a diversity scheme.

The high ICR values at 40 GHz control pulse rate indicate, that the GT-UNI and the GT-MZI can be used as demultiplexer to the base rate 40 Gbit/s. Even demultiplexing up to a TDM bit rate of 320 Gbit/s should be possible. However, for stable operation at such a high TDM bit rate, steeper switching windows and pulse sources with low timing jitter will be necessary.

– **Applications:** The GT-MZI was used as **demultiplexer** in a 160 Gbit/s transmission experiment over 160 km standard single mode fiber at a base data rate of 10 Gbit/s. The GT-UNI was employed successfully to demultiplex from 160 Gbit/s to 10 and 40 Gbit/s and the first 160 Gbit/s field experiment with 40 Gbit/s base data rate was performed using the GT-UNI gate. A polarization independent GT-UNI demultiplexer was realized using a polarization diversity scheme. Error-free performance for a 160 Gbit/s input data signal with a rapidly varying polarization state was achieved. Due to the low amplitude variations in the GT-SOAs, **add-drop multiplexing** at 160 Gbit/s could be demonstrated for the first time. In this experiment a GT-UNI with a special configuration was used, which enabled high on-off contrast ratios in the transmitted and demultiplexed signal, despite a phase shift in the GT-SOA below π. The GT-UNI was also used as fast gate in an **optical sampling** system and clearly resolved eye diagrams at 160 Gbit/s were recorded.

Conclusions: Interferometric gates based on GT-SOAs are promising devices for

applications in 160 Gbit/s OTDM systems at 10 Gbit/s and 40 Gbit/s base data rate. As was shown in section 5.2, one of the main limitations for a further increase in the TDM bit rate is the relative timing jitter between the pulse source generating the optical control signal and the data signal. Recently electro-absorption modulators (EAM) have replaced interferometric gates in certain 160 Gbit/s OTDM applications. This was enabled by a significant increase in the bandwidth of commercially available EAMs. The EAM is an electro-optical gate and the limitations mentioned above are reduced, because the control signal to the EAM is electrical instead of optical and can be generated with very low timing jitter. In applications like demultiplexing, the EAM clearly has advantages, due to the more compact setup, the lower polarization sensitivity and the lower number of components needed. However, electro-optical operated EAM gates can only be used up to a TDM bit rate of 160 Gbit/s and at base data rates up to 40 Gbit/s at present.

Outlook

In chapter 3 it was shown that a high repetition rate of the control pulses significantly reduces the phase shift in SOAs. Thus, SOAs are less attractive as nonlinear media in interferometric gates for applications which require high repetition rates of the control pulses (160 GHz) like wavelength conversion and 3R-regeneration. Fiber based interferometric gates can be used instead, because the nonlinear phase shift in optical fiber by XPM is independent of the control pulse rate. The application of a fiber based gate was shown in section 5.5, where a fiber based Kerr-Switch is used as decision gate in a 160 Gbit/s 3R-wavelength converter. To reduce the impairments of relative timing jitter between the data signal and the narrow switching window of the Kerr-Switch, a pulse shaper was used for the control signal to form narrow gating windows with an almost rectangular shape. With this pulse shaping, error-free performance in the 3R-wavelength converter was achieved. Recent progress in the fabrication of optical fibers with high nonlinearity coefficients makes such fiber based switches attractive solutions for applications in all-optical signal processing.

It was demonstrated in this work, that GT-SOA based interferometric switches can be used as demultiplexer and add-drop multiplexer at a TDM bit rate of 160 Gbit/s. An increase of the TDM bit rate to 320 Gbit/s seems feasible, but operation of GT switches at a base data rate above 40 Gbit/s is extremely difficult with the currently available devices. To improve the gain-transparent switches, mainly to points have two be addressed: the low phase shift, especially at high control pulse rates and the high loss for the data signal in the GT-SOA. As was shown in this work, a higher phase shift in the GT-SOA cannot be achieved by changing the operation conditions in the current devices and also not by using longer SOAs. A new device structure is necessary, which reduces the free carrier absorption and increases the phase change. An interesting approach is the fabrication of SOAs with a gain maximum more close to the data wavelength region (1.55 µm). First experiments with so called gain-shifted SOAs, having a gain maximum around 1.5 µm, monolithically integrated in an MZI structure, were briefly discussed in this work. The investigated device still showed a strong gain variation and error-free performance in demultiplexing applications was difficult to achieve. The fabrication of SOAs with new structures was beyond the scope of this work, so that the answer to this question has to be left for further detailed investigations. In the case of the UNI configuration the loss in the GT-SOA can be compensated by using an EDFA in the fiber loop, as was shown by Turkiewicz and his coworkers [93].

Bibliography

[1] G. P. Agrawal, *Fiber-Optic Communication Systems*, 3rd ed. Wiley & Sons, 2002.

[2] K. E. Stubkjaer, "Semiconductor optical amplifier-based all-optical gates for high-speed optical processing," *IEEE J. Sel. Top. Quant.*, vol. 6, no. 6, pp. 1428–1435, November 2000.

[3] H. G. Weber, R. Ludwig, C. Schmidt, C. Schubert, J. Berger, E. Hilliger, M. Kroh, V. Marembert, C. Boerner, S. Ferber, and H. J. Ehrke, "160 Gbit/s TDM-transmission technology," in *Proc. 29th Europ. Conf. Opt. Commun., ECOC'03*, vol. 1, Copenhagen, Denmark, September 2002, invited paper 2.1.1.

[4] R. Ludwig, C. Schmidt, C. Schubert, J. Berger, E. Hilliger, M. Kroh, V. Marembert, C. Boerner, S. Ferber, H. J. Ehrke, and H. G. Weber, "Technologies for 160 Gbit/s transmission systems," in *Techn. Dig. of Optoelectronics and Commun. Conf., OECC'02*, Yokohama, Japan, July 2002, pp. 18–19, invited paper 9B1-1.

[5] R. Ludwig, U. Feiste, S. Diez, C. Schubert, C. Schmidt, H. J. Ehrke, and H. G. Weber, "Unrepeatered 160 Gb/s RZ single channel transmission over 160 km of standard fiber at 1.55 μm with hybrid MZI optical demux," *Electron. Lett.*, vol. 36, no. 16, pp. 1405–1406, August 2000.

[6] R. Ludwig and A. Ehrhardt, "Turn-key-ready wavelength-, repetition rate- and pulsewidth-tunable femtosecond hybrid modelocked semiconductor laser," *Electron. Lett.*, vol. 31, no. 14, pp. 1165–1167, July 1995.

[7] C. Schmidt, C. Schubert, J. Berger, M. Kroh, H. Ehrke, E. Dietrich, C. Börner, R. Luwig, H. G. Weber, F. Futami, S. Watanabe, and T. Yamamoto, "Optical Q-Factor Monitoring at 160 Gb/s Using an Optical Sampling System in an 80 km Transmission Experiment," in *Techn. Dig. of Conf. on Lasers and Electro-Optics, CLEO'02*, Washington DC, USA, May 2002, pp. 579–580, paper CThU3.

[8] C. Schmidt-Langhorst, "Optical Sampling," Ph.D. dissertation, Fakultät II - Mathematik und Naturwissenschaften der TU Berlin, to be handed in 2004.

[9] T. Yamamoto, L. K. Oxenløwe, C. Schmidt, C. Schubert, E. Hilliger, U. Feiste, J. Berger, R. Ludwig, and H. G. Weber, "Clock recovery from 160Gb/s data signals using a phase-locked loop with an interferometric optical switch based on a semiconductor optical amplifier," *Electron. Lett.*, vol. 37, no. 8, pp. 509–510, April 2001.

[10] L. Oxenløwe, C. Schubert, C. Schmidt, E. Hilliger, J. Berger, U. Feiste, R. Ludwig, and H. G. Weber, "Optical clock recovery employing an optical PLL using cross-phase modulation in a sagnac-interferometer," in *Techn. Dig. of Conf. on Lasers and Electro-Optics, CLEO'01*, Baltimore, USA, May 2001, pp. 525–526, paper CThU2.

[11] C. Boerner, C. Schubert, C. Schmidt, E. Hilliger, V. Marembert, J. Berger, S. Ferber, E. Dietrich, R. Ludwig, B. Schmauss, and H. G. Weber, "160 Gbit/s clock recovery with electro-optical PLL using a bidirectionally operated electroabsorption modulator as phase comparator," *Electron. Lett.*, vol. 39, no. 14, pp. 1071–1073, July 2003.

[12] E. Lach, M. Schmidt, K. Schuh, B. Junginger, and G. Veith, "Advanced 160 Gbit/s OTDM system based on wavelength transparent 4 x 40 Gbit/s ETDM transmitters and receivers," in *Proc. Optical Fiber Commun. Conf., OFC'02*, Anaheim, USA, March 2002, paper TuA2.

[13] D. T. K. Tong, K.-L. Deng, B. Mikkelsen, G. Raybon, K. F. Dreyer, and J. E. Johnson, "160 Gbit/s clock recovery using electroabsorption modulator-based phase-locked loop," *Electron. Lett.*, vol. 36, no. 23, pp. 1951–1952, November 2000.

[14] T. Yamamoto, U. Feiste, J. Berger, C. Schubert, C. Schmidt, R. Ludwig, and H. G. Weber, "160 Gbit/s demultiplexer with clock recovery using SOA-based interferometric switches and its application to 120 km fiber transmission," in *Proc. 27th Europ. Conf. Opt. Commun., ECOC'01*, Amsterdam, The Netherlands, September 2001, pp. 192–193, paper Tu.L.2.6.

[15] R. Ludwig, S. Ferber, C. Schubert, C. Boerner, A. Beling, H.-G. Bach, B. Schmauss, A. Wietfeld, J. Berger, C. Schmidt, and H. G. Weber, "160 Gbit/s DPSK transmission over 410 km dispersion-managed fiber," in *Proc. 8th European Conference on Networks & Optical Communications*, Vienna, Austria, July 2003, pp. 14–19.

[16] R. Ludwig, "Experimentelle Untersuchungen an Halbleiterlaserverstärkern für die optische Nachrichtentechnik," Ph.D. dissertation, Fachbereich 19 für Elektrotechnik der TU Berlin, 1993.

[17] R. Schreieck, "Ultrafast Dynamics in InGaAsP/InP Optical Amplifiers and Mode Locked Laser Diodes," Ph.D. dissertation, Swiss Federal Institute of Technology, Zurich, 2001, Diss. ETH No. 14337.

[18] L. Occhi, "Semiconductor Optical Amplifiers made of Ridge Waveguide Bulk InGaAsP/InP: Experimental Characterisation and Numerical Modelling of Gain, Phase, and Noise," Ph.D. dissertation, Swiss Federal Institute of Technology, Zurich, 2002, Diss. ETH No. 14788.

[19] M. J. Connelly, *Semiconductor Optical Amplifiers*. Kluwer Academic Publishers, 2002.

[20] G. P. Agrawal, *Nonlinear Fiber Optics*, 3rd ed. Academic Press, 2001.

[21] H. G. Weber, *Optische Kommunikationstechnik*. Springer-Verlag Berlin Heidelberg, 2002, ch. 16, pp. 555–593.

[22] E. Hilliger, "Optisches Schalten mit Elektroabsorptionsmodulatoren," Ph.D. dissertation, Fakultät II - Mathematik und Naturwissenschaften der TU Berlin, 2003.

[23] E. Hilliger, V. Marembert, C. Schubert, H. G. Weber, K. Yvind, and J. Hanberg, "Improved electroabsorption demultiplexer by tandem-arrangement with semiconductor optical amplifier," in *Proc. Optical Fiber Commun. Conf., OFC'02*, Anaheim, USA, March 2002, pp. 742–743, poster ThGG92.

[24] S. Nakamura, Y. Ueno, and K. Tajima, "Error-free all-optical demultiplexing at 336 Gb/s with a hybrid-integrated Symmetric-Mach-Zehnder switch," in *Proc. Optical Fiber Commun. Conf., OFC'02*, Anaheim, USA, March 2002, post-deadline paper FD3.

[25] C. Schubert, S. Diez, J. Berger, R. Ludwig, U. Feiste, H. G. Weber, G. Toptchiyski, K. Petermann, and V. Krajinovic, "160 Gb/s All-Optical Demultiplexing using a Gain-Transparent Ultrafast-Nonlinear Interferometer (GT-UNI)," *IEEE Photon. Technol. Lett.*, vol. 13, no. 5, pp. 475–477, May 2001.

[26] U. Feiste, R. Ludwig, C. Schubert, J. Berger, C. Schmidt, H. G. Weber, A. Munk, B. Schmauss, B. Buchhold, D. Briggmann, F. Kueppers, and F. Rumpf, "160 Gbit/s transmission over 116 km field-installed fiber using 160 Gbit/s OTDM and 40 Gbit/s ETDM," in *Proc. Optical Fiber Commun. Conf., OFC'01*, Anaheim, USA, March 2001, paper ThF3.

[27] S. Diez, C. Schubert, R. Ludwig, H.-J. Ehrke, U. Feiste, C. Schmidt, and H. G. Weber, "160 Gbit/s all-optical demultiplexer using hybrid gain-transparent SOA Mach-Zehnder interferometer," *Electron. Lett.*, vol. 36, no. 17, pp. 1484–1486, August 2000.

[28] T. Tekin, C. Schubert, J. Berger, M. Schlak, B. Mau, W. Brinker, R. Molt, H. Ehlers, and H.-P. N. M. Gravert, "160 Gbit/s error-free all-optical demultiplexing using monolithically integrated band gap shifted Mach-Zehnder interferometer (GS-MZI)," in *Techn. Dig. of Conf. on Integrated Photonics Research, IPR'02*, Vancouver, Canada, July 2002, paper IWC4.

[29] M. Heid, S. Spälter, G. Mohs, A. Färbert, W. Vogt, and H. Melchior, "160-Gbit/s demultiplexing based on a monolithically integrated Mach-Zehnder interferometer," in *Proc. 27th Europ. Conf. Opt. Commun., ECOC'01*, Amsterdam, The Netherlands, 2001, pp. 82–83, post-deadline paper PD.B.1.8.

[30] K. Suzuki, K. Iwatsuki, S. Nishi, and M. Saruwatari, "Error-free demultiplexing of 160 Gbit/s pulse signal using optical loop mirror including semiconductor laser amplifier," *Electron. Lett.*, vol. 30, no. 18, pp. 1501–1503, September 1994.

[31] I. Glesk, B. C. Wang, L. Xu, V. Baby, and P. R. Prucnal, "Ultra-fast all-optical switching in optical networks," *Prog. Optics*, vol. 45, pp. 53–117, 2003.

[32] N. K. Das, Y. Yamayoshi, T. Kawazoe, and H. Kawaguchi, "Analysis of Optical DEMUX Characteristics Based on Four-Wave Mixing in Semiconductor Optical Amplifiers," *J. Lightwave Technol.*, vol. 16, no. 2, pp. 237–246, February 2001.

[33] S. L. Jansen, M. Heid, S. Spälter, E. Meissner, C. J. Weiske, A. Schöpflin, D. Khoe, and H. de Waardt, "Demultiplexing 160 Gbit/s OTDM signal to 40 Gbit/s by FWM in SOA," *Electron. Lett.*, vol. 38, no. 17, pp. 978–980, August 2002.

[34] I. Shake, H. Takara, K. Uchiyama, I. Ogawa, T. Kitoh, T. Kitagawa, M. Okamoto, K. Magari, Y. Suzuki, and T. Morioka, "160 Gbit/s full optical time-division demultiplexing using FWM of SOA-array integrated on PLC," *Electron. Lett.*, vol. 38, no. 1, pp. 37–38, January 2002.

[35] M. Nakazawa, T. Yamamoto, and K. R. Tamura, "1.28 Tbit/s - 70 km OTDM transmission using third- and fourth-order simultaneous dispersion compensation with a phase modulator," in *Proc. 26th Europ. Conf. Opt. Commun., ECOC'00*, Munich, Germany, 2000, post-deadline paper 2.6.

[36] K. Schuh, M. Schmidt, E. Lach, B. Junginger, A. Klekamp, G. Veith, and P. Sillard, "4x160 Gb/s DWDM / OTDM transmission over 3x80 km TeraLight - Reverse TeraLight fibre," in *Proc. 28th Europ. Conf. Opt. Commun., ECOC'02*, Copenhagen, Denmark, September 2002, paper 2.1.2.

[37] E. Hilliger, V. Marembert, S. Ferber, M. Kroh, J. Berger, H. G. Weber, and B. Schmauss, "EAM with Improved Switching Performance by Self Cascading," in *Proc. Optical Fiber Commun. Conf., OFC'03*, Atlanta, USA, March 2003, paper TuP2.

[38] S. Kodama, T. Yoshimatsu, and H. Ito, "320-Gbit/s Error-Free Demultiplexing Operation of a Monolithic PD-EAM Optical Gate," in *Proc. Optical Fiber Commun. Conf., OFC'03*, Atlanta, USA, March 2003, paper ThX5.

[39] C. Schmidt, C. Schubert, S. Watanabe, F. Futami, R. Ludwig, and H. G. Weber, "320 Gb/s all-optical eye diagram sampling using gain-transparent Ultrafast Nonlinear Interferometer (GT-UNI)," in *Proc. 28th Europ. Conf. Opt. Commun., ECOC'02*, Copenhagen, Denmark, September 2002, paper 2.1.3.

[40] C. Schubert, C. Schmidt, C. Börner, E. Dietrich, S. Ferber, R. Ludwig, and H. G. Weber, "A gain-transparent Ultrafast-Nonlinear Interferometer (GT-UNI) in a 160 Gb/s optical sampling system," in *Techn. Dig. of Optical Amplifiers and their Applications, OAA'02*, Vancouver, Canada, July 2002, paper OTuD5.

[41] C. Schmidt, F. Futami, S. Watanabe, T. Yamamoto, C. Schubert, J. Berger, M. Kroh, H.-J. Ehrke, E. Dietrich, C. Börner, R. Ludwig, and H. G. Weber, "Complete optical sampling system with broad gap-free spectral range for 160 Gbit/s and 320 Gbit/s and its application in a transmission system," in *Proc. Optical Fiber Commun. Conf., OFC'02*, Anaheim, USA, March 2002, pp. 528–530, paper ThU1.

[42] M. Shirane, Y. Hashimoto, H. Kurita, H. Yamada, and H. Yokoyama, "Optical sampling measurement with all-optical clock recovery using mode-locked diode lasers," in *Proc. Optical Fiber Commun. Conf., OFC'01*, Anaheim, USA, March 2001, paper MG2.

[43] N. Yamada, S. Nogiwa, and H. Ohta, "Measuring eye diagram of 640 Gb/s OTDM signal with optical sampling system by using wavelength-tunable soliton pulse," in

Proc. 29th Europ. Conf. Opt. Commun., ECOC'03, Rimini, Italy, September 2003, pp. 138–139, paper Mo4.6.5.

[44] C. Schubert, C. Schmidt, S. Ferber, R. Ludwig, and H. G. Weber, "Error-free all-optical add-drop multiplexing at 160 Gbit/s," *Electron. Lett.*, vol. 39, no. 14, pp. 1074–1076, July 2003.

[45] H. N. Poulsen, A. T. Clausen, A. Buxens, L. Oxenløwe, C. Peucheret, C. Rasmussen, F. Liu, J. Yu, A. Kloch, T. Fjelde, D. Wolfson, and P. Jeppesen, "Ultra fast all-optical signal processing in semiconductor and fiber based devices," in *Proc. 26th Europ. Conf. Opt. Commun., ECOC'00*, Munich, Germany, September 2000, pp. 59–62, paper 7.4.1.

[46] S. Watanabe and F. Futami, "All-Optical Wavelength Conversion Using Ultra-Fast Nonlinearities in Optical Fiber," *IEICE Trans. electron.*, vol. E85-C, no. 4, pp. 889–895, April 2002.

[47] J. Leuthold, C. H. Joyner, B. Mikkelsen, G. Raybon, J. L. Pleumeekers, B. I. Miller, K. Dreyer, and C. A. Burrus, "100 Gbit/s All-Optical Wavelength Conversion with an Integrated SOA Delayed-Interference Configuration," in *Techn. Dig. of Optical Amplifiers and their Applications, OAA'00*, Quebec, Canada, July 2000, pp. 186–188, paper OWB3.

[48] S. Nakamura, Y. Ueno, and K. Tajima, "Error-free all-optical data pulse regeneration at 84 Gbps and wavelength conversion at 168 Gbps with Symmetric Mach-Zehnder all-optical switches," in *Techn. Dig. of Optical Amplifiers and their Applications, OAA'00*, Quebec, Canada, July 2000, post-deadline paper PDP4.

[49] Y. Ueno, S. Nakamura, and K. Tajima, "Penalty-free error-free all-optical data pulse regeneration at 84 Gb/s by using a symmetric-Mach-Zehnder-type semiconductor regenerator," *IEEE Photon. Technol. Lett.*, vol. 13, no. 5, pp. 469–471, May 2001.

[50] S. Watanabe, F. Futami, R. Okabe, Y. Takita, S. Ferber, R. Ludwig, C. Schubert, C. Schmidt, and H. G. Weber, "160 Gbit/s optical 3R-regenerator in a fiber transmission experiment," in *Proc. Optical Fiber Commun. Conf., OFC'03*, Atlanta, USA, March 2003, post-deadline paper PD16.

[51] C. Schubert, R. Ludwig, S. Watanabe, F. Futami, C. Schmidt, J. Berger, C. Boerner, S. Ferber, and H. G. Weber, "160 Gbit/s wavelength converter with 3R-regenerating capability," *Electron. Lett.*, vol. 38, no. 16, pp. 903–904, August 2002.

[52] W. Nolting, *Elektrodynamik*, 3rd ed., ser. Grundkurs: Theoretische Physik. Verlag Zimmermann-Neufang, 1993, no. 3.

[53] B. E. A. Saleh and M. C. Teich, *Fundamentals of Photonics*. John Wiley & Sons, Inc., 1991.

[54] P. N. Butcher and D. Cotter, *The Elements of Nonlinear Optics*, ser. Cambridge Studies in Modern Optics. Cambridge University Press, 1990, no. 9.

[55] G. P. Agrawal and N. K. Dutta, *Long-Wavelength Semiconductor Laser*. van Nostrand Reinhold Company Inc., 1986.

[56] H. G. Weber, "Grundlagen und Anwendungen der linearen und nichtlinearen Faseroptik," lecture given at the Technical University Berlin, SS03/WS04.

[57] R. W. Boyd, *Nonlinear Optics*, 2nd ed. Academic Press, 2003.

[58] W. H. Steel, *Interferometry*, 2nd ed., ser. Cambridge Studies in Modern Optics. Cambridge University Press, 1987, no. 1.

[59] D. B. Mortimore, "Fiber Loop Reflectors," *J. Lightwave Technol.*, vol. 6, no. 7, pp. 1217–1224, July 1988.

[60] G. Toptchiyski, S. Randel, K. Petermann, S. Diez, E. Hilliger, C. Schmidt, C. Schubert, R. Ludwig, and H. G. Weber, "Analysis of switching windows in a gain-transparent-SLALOM configuration," *J. Lightwave Technol.*, vol. 18, no. 12, pp. 2188–2195, October 2000.

[61] T. Tekin, "Monolithically Integrated Gain-shifted Mach-Zehnder Interferometer for All-Optical Demultiplexing," Ph.D. dissertation, Fakultät IV (Elektrotechnik und Informatik) der TU Berlin, to be handed in 2004.

[62] S. Diez, "All-Optical Signal Processing by Gain-Transparent Semiconductor Switches," Ph.D. dissertation, Fachbereich 4 (Physik) der TU Berlin, 2000.

[63] G. Toptchiyski, S. Kindt, K. Petermann, E. Hilliger, S. Diez, and H. G. Weber, "Time-domain Modeling of Semiconductor Optical Amplifiers for OTDM Applications," *J. Lightwave Technol.*, vol. 17, no. 12, pp. 2577–2583, December 1999.

[64] G. Toptchiyski, "Analysis of All-Optical Interferometric Switches Based on Semiconductor Optical Amplifiers," Ph.D. dissertation, Fakultät IV (Elektrotechnik und Informatik) der TU Berlin, 2002.

[65] A. Melo, K. Petermann, and C. Schubert, "Frequency vs. Time-domain Amplified Spontaneous Emission (ASE) noise modeling of Semiconductor Optical Amplifiers (SOAs)," in *CLEO/Europe-EQEC Conference*, Munich, Germany, June 2003, poster EA1T.

[66] R. Ludwig, S. Diez, and H. G. Weber, "A Novel All-Optical Switch for Demultiplexing in OTDM-Systems demonstrated in a 640 Gbit/s WDM/TDM Experiment," in *Proc. Optical Fiber Commun. Conf., OFC'98*, San Jose, USA, February 1998, post-deadline paper PD22.

[67] C. Schubert, L. Schares, C. Schmidt, G. Guekos, and H. G. Weber, "Phase dynamics in gain-transparent semiconductor optical amplifiers," in *Proc. 29th Europ. Conf. Opt. Commun., ECOC'03*, Rimini, Italy, September 2003, pp. 1062–1063, paper Th3.5.2.

[68] S. Diez, C. Schubert, R. Ludwig, H.-J. Ehrke, U. Feiste, C. Schmidt, and H. G. Weber, "160 Gb/s all-optical demultiplexer using a hybrid gain-transparent SOA Mach-Zehnder-Interferometer," in *Techn. Dig. of Optical Amplifiers and their Applications, OAA'00*, Quebec, Canada, July 2000, pp. 195–197, paper OWB6.

[69] A. Melo, G. Toptchiyski, K. Petermann, and C. Schubert, "Crosstalk analysis of longer SOAs for demultiplexing to the base data rate of 10 Gbit/s and 40 Gbit/s," in *Tech. Dig. of IEEE Summer Topical Meeting 2002*, Mont Tremblant, Canada, July 2002, pp. 11–12, paper TuC2.

[70] L. Schares, C. Schubert, C. Schmidt, H. G. Weber, L. Occhi, and G. Guekos, "Phase Dynamics of Semiconductor Optical Amplifiers at 10 to 40 GHz," *IEEE J. Quantum Electron.*, vol. 39, no. 11, pp. 1394–1408, November 2003.

[71] Y. Ueno, S. Nakamura, and K. Tajima, "Nonlinear phase shifts induced by semiconductor optical amplifiers with control pulses at repetition frequencies in the 40-160 GHz range for use in ultrahigh-speed all-optical signal processing," *J. Opt. Soc. Am. B*, vol. 19, no. 11, pp. 2573–2589, November 2002.

[72] T. Tekin, M. Schlak, W. Brinker, J. Berger, C. Schubert, B. Maul, and R. Molt, "Ultrafast all-optical demultiplexing performance of monolithically integrated band gap shifted Mach-Zehnder interferometer," in *Proc. 27th Europ. Conf. Opt. Commun., ECOC'01*, Amsterdam, The Netherlands, September 2001, pp. 504–505, paper Th.F.1.3.

[73] T. Tekin, C. Schubert, J. Berger, M. Schlak, B. Maul, W. Brinker, R. Molt, and H. Ehlers, "160 Gbit/s error-free all-optical demultiplexing using monolithically integrated band gap shifted Mach-Zehnder interferometer," in *International Congress for Optics XIX: Optics for the Quality of Life*, Firenze, Italy, August 2002, pp. 605–606.

[74] N. S. Patel, K. A. Rauschenbach, and K. L. Hall, "40 Gb/s demultiplexing using an ultrafast nonlinear interferometer (UNI)," *IEEE Photon. Technol. Lett.*, vol. 8, no. 12, pp. 1695–1697, December 1996.

[75] C. Schubert, J. Berger, S. Diez, H. J. Ehrke, R. Ludwig, U. Feiste, C. Schmidt, H. G. Weber, G. Toptchiyski, S. Randel, and K. Petermann, "Comparison of interferometric all-optical switches for demultiplexing applications in high-speed OTDM systems," *J. Lightwave Technol.*, vol. 20, no. 4, pp. 618–624, April 2002.

[76] G. Toptchiyski, S. Randel, K. Petermann, C. Schubert, J. Berger, and H. G. Weber, "Characterization of switching windows of an 160 Gb/s all-optical demultiplexer with data base rates of 10 and 40 Gb/s," *IEEE Photon. Technol. Lett.*, vol. 14, no. 4, pp. 534–536, April 2002.

[77] J. Turkiewicz, E. Tangdiongga, H. Rohde, W. Schairer, G. Lehmann, G. Khoe, and H. de Waardt, "Simultaneous high speed OTDM add-drop multiplexing using GT-UNI switch," *Electron. Lett.*, vol. 39, no. 10, pp. 795–796, May 2003.

[78] R. Ludwig, U. Feiste, S. Diez, C. Schubert, C. Schmidt, H. J. Ehrke, and H. G. Weber, "Unrepeatered 160 Gbit/s RZ single channel transmission over 160 km of standard fiber at 1.55 μm with hybrid MZI optical DEMUX," in *Proc. 26th Europ. Conf. Opt. Commun., ECOC'00*, Munich, Germany, September 2000, pp. 135–136, paper 6.1.3.

[79] S. Diez, C. Schubert, U. Feiste, R. Ludwig, J. Berger, and H. G. Weber, "160 Gb/s all-optical demultiplexing using a gain-transparent Ultrafast-Nonlinear Interferometer," in *Techn. Dig. of Optical Amplifiers and their Applications, OAA'00*, Quebec, Canada, July 2000, post-deadline paper PD9.

[80] C. Schubert, J. Berger, U. Feiste, R. Ludwig, C. Schmidt, and H. G. Weber, "160 Gb/s polarization insensitive all-optical demultiplexing using a gain-transparent Ultrafast-Nonlinear Interferometer (GT-UNI)," *IEEE Photon. Technol. Lett.*, vol. 13, no. 11, pp. 1200–1202, November 2001.

[81] H. Rosenfeldt, C. Knothe, R. Ulrich, E. Brinkmeyer, U. Feiste, C. Schubert, J. Berger, R. Ludwig, H. G. Weber, and A. Ehrhardt, "Automatic PMD compensation at 40 Gbit/s and 80 Gbit/s using a 3-dimensional DOP evaluation for feedback," in *Proc. Optical Fiber Commun. Conf., OFC'01*, Anaheim, USA, March 2001, post-deadline paper PD27.

[82] U. Feiste, R. Ludwig, C. Schubert, J. Berger, C. Schmidt, H. G. Weber, A. Munk, B. Schmauss, B. Buchhold, D. Briggmann, F. Kueppers, and F. Rumpf, "160 Gbit/s transmission over 116 km field-installed fiber using 160 Gbit/s OTDM and 40 Gbit/s ETDM," *Electron. Lett.*, vol. 37, no. 7, pp. 443–445, March 2001.

[83] U. Feiste, R. Ludwig, C. Schubert, J. Berger, S. Diez, C. Schmidt, H. G. Weber, A. Munk, and B. Schmauss, "160 Gbit/s transmission using 160 to 40 Gbit/s OTDM and 40 to 10 Gbit/s ETDM DEMUX-techniques," in *Proc. 26th Europ. Conf. Opt. Commun., ECOC'00*, Munich, Germany, September 2000, post-deadline paper PD 1.10.

[84] U. Feiste, R. Ludwig, C. Schubert, J. Berger, C. Schmidt, H. G. Weber, B. Schmauss, A. Munk, B. Buchhold, D. Briggmann, F. Kueppers, and F. Rumpf, "160 Gbit/s field transmission over 116 km standard single mode fibre using 160 Gbit/s OTDM and 40 Gbit/s ETDM demultiplexer," *Proc.-Optoelectron.*, vol. 148, no. 4, pp. 171–175, August 2001.

[85] A. Melo, G. Toptchiyski, K. Petermann, and C. Schubert, "Analysis of ADD/DROP multiplexing at 160 Gbit/s to base data rates of 10 Gbit/s and 40 Gbit/s," in *Proc. 28th Europ. Conf. Opt. Commun., ECOC'02*, Copenhagen, Denmark, September 2002, paper 11.4.3.

[86] C. Schubert, C. Schmidt, S. Ferber, R. Ludwig, and H. G. Weber, "Error-free all-optical add-drop multiplexing at 160 Gbit/s," in *Proc. Optical Fiber Commun. Conf., OFC'03*, Atlanta, USA, March 2003, post-deadline paper PD17.

[87] J. Turkiewicz, H. Rohde, W. Schairer, G. Lehmann, E. Tangdiongga, G. D. Khoe, and H. de Waardt, "All-optical OTDM Add-Drop Node at 16x10 Gbit/s in between two Fibre Links of 150 km," in *Proc. 29th Europ. Conf. Opt. Commun., ECOC'03*, Rimini, Italy, September 2003, pp. 84–85, post-deadline paper Th4.4.5.

[88] M. Shirane, Y. Hashimoto, H. Yamada, and H. Yokoyama, "A compact optical sampling measurement system using mode-locked laser-diode modules," *IEEE Photon. Technol. Lett.*, vol. 12, no. 11, pp. 1537–1539, November 2000.

[89] N. Yamada, H. Ohta, and S. Nogiwa, "Jitter-free optical sampling system using passively modelocked fibre laser," *Electron. Lett.*, vol. 38, no. 18, pp. 1044–1045, August 2002.

[90] S. Nogiwa, Y. Kawaguchi, H. Ohta, and Y. Endo, "Highly sensitive and time-resolving optical sampling system using thin PPLN crystal," *Electron. Lett.*, vol. 36, no. 20, pp. 1727–1728, September 2000.

[91] C. Schmidt, C. Schubert, C. Börner, C. Weinert, H. Bülow, E. Lach, and H. G. Weber, "Investigation of intra-channel four-wave mixing at 160 Gb/s using an optical sampling system," in *Proc. 29th Europ. Conf. Opt. Commun., ECOC'03*, Rimini, Italy, September 2003, pp. 990–991, paper Th2.5.2.

[92] R. Ludwig, C. Schubert, S. Watanabe, F. Futami, C. Schmidt, J. Berger, C. Boerner, S. Ferber, and H. G. Weber, "160 Gb/s 3R-regenerating wavelength converter," in *Techn. Dig. of Optoelectronics and Commun. Conf., OECC'02*, Yokohama, Japan, July 2002, post-deadline Paper PD-1-3.

[93] J. Turkiewicz, E. Tangdiongga, H. Rohde, W. Schairer, G. Lehmann, , G. D. Khoe, and H. de Waardt, "Simultaneous high speed OTDM add-drop multiplexing using GT-UNI switch," *Electron. Lett.*, vol. 39, no. 10, pp. 795–796, May 2003.

[94] C. Schubert, R. Ludwig, S. Watanabe, F. Futami, S. Ferber, J. Berger, C. Schmidt, and H. G. Weber, "Improved performance of a 160 Gb/s fibre based all-optical switch using rectangular gating pulses," in *Proc. 28th Europ. Conf. Opt. Commun., ECOC'02*, Copenhagen, Denmark, September 2002, paper 8.3.7.

Appendix A

Appendix

A.1 Pulse Shaping using Highly Birefringent Fiber

In section 3.2.2 it was pointed out that the ideal switching window for most applications is a switching window with steep rising and falling flanks and a flat top (rectangular shape). Especially for very short switching window widths, deviations of the switching window from this ideal shape can result in conversion of phase jitter to amplitude noise in the gate. In the case of interferometric switches based on highly nonlinear fiber, the shape of the switching window is determined by the shape of the control pulse, in particular if the phase shift is below π. One possibility to achieve a switching window with the desired shape is therefore to shape the control pulses appropriately. In the following, a simple pulse shaper based on highly birefringent fiber will be presented to form almost rectangular shaped pulses at high bit rates [94]. These pulses are applied to gate a fiber based switch, providing an almost rectangular switching window. This pulse shaper was used in the 3R-wavelength converter, presented in section 5.5, and in a regeneration experiment with recirculating loop [50].

Pulse Shaper

The setup of the pulse shaper is shown schematically in Fig. A.1.

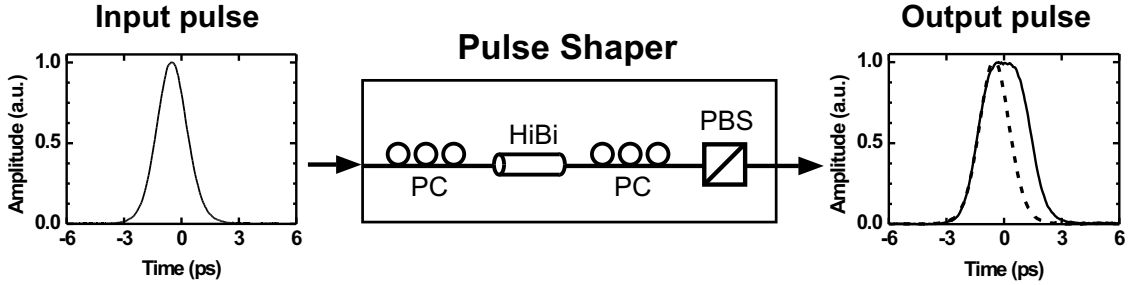

Figure A.1 : Schematic of the pulse shaper with measured input and output pulses.

An incoming pulse is launched into a piece of highly-birefringent (HiBi) fiber with the polarization state adjusted for equal amplitude in both principal axis, by using a polarization

controller (PC). On passage through the HiBi fiber, the pulse is split into two orthogonal components, separated by a delay τ, which is determined by the differential group delay (DGD) of the HiBi fiber. If τ is comparable or less than the pulse width of the incoming pulse, the two orthogonal components interfere at the polarizing beamsplitter (PBS). The pulse shape after the PBS depends on the polarization and the phase difference of the orthogonal pulse components, which can be changed with a PC before the PBS. As example, Fig. A.1 shows the pulses at the input and output of the pulse shaper, for an input pulse with sech^2 shape and 1.3 ps full width at half maximum (FWHM). The pulses at the input and output were measured by cross-correlation with a 650 fs sech^2 pulse. It can be seen that with a 0.5 m long piece of HiBi fiber (which corresponds to 0.85 ps DGD), an almost rectangular shaped, single polarization pulse with 5.8 ps FWHM is achieved. The insertion loss of the pulse shaper is about 4 dB. For polarization insensitive operation, an automatic polarization controller before the pulse shaper is needed.

The pulse shaper was used, to shape the 10 GHz control pulses of a Kerr-Switch (see section 2.3.2 for details on the Kerr-Switch).The effect of the pulse shaper on the switching window of the Kerr-Switch, is shown in Fig. A.2. The switching window was measured by recording the transmission of a 10 Gbit/s data signal through the gate as a function of the temporal delay between the control and data signal. An almost rectangular shaped window with 5.8 ps FWHM is obtained.

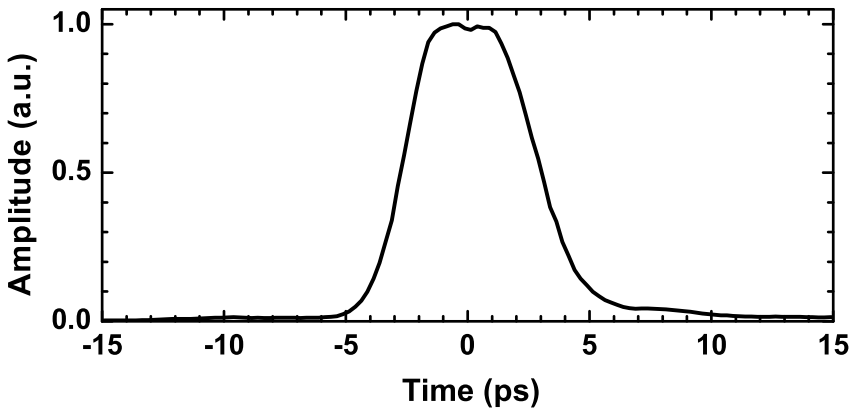

Figure A.2 : Switching window of a Kerr-Switch with shaped control pulse (average control power +7.7 dBm)

In conclusion, a simple pulse shaper was presented, to form almost rectangular shaped single polarization pulses. By using this pulse shaper to form the gating pulses of a fiber based Kerr-Switch, an almost rectangular switching window is achieved. The pulse shaper can also be used in other types of fiber based switches (e.g. Nonlinear Optical Loop Mirror) and at data rates of 160 Gbit/s and above.

A.2 The Integrated Contrast Ratio (ICR)

A switching window is usually described by the window width and the on-off contrast ratio. These quantities are not always sufficient to characterize the performance of a switch. The common definition of the contrast leaves it to the evaluator, where to read the values for the maximum and the minimum transmitted power in the switching window. Moreover, it does not convey any information about the overall shape of the switching window. The shape, however, is heavily dependent on the actual operation conditions of the switch and has a strong influence on, for example the demultiplexing performance. This makes it difficult to compare different types of interferometric switches, using the on-off contrast ratio. An integrative approach for the definition of the switching contrast is therefore reasonable.
This is the so called Integrated Contrast Ratio (ICR), which characterizes the performance of a switch, e.g. as demultiplexer in an OTDM system, and takes into account the overall shape of the switching window. It is defined as

$$\mathrm{ICR} = 10 \log \frac{\int_{\Delta t_{bit}} P_{data}(t)\, T_{int}(t+t_0)\, dt}{\int_{\Delta t_{out}} P_{data}(t)\, T_{int}(t+t_0)\, dt} \,, \tag{A.1}$$

where $P_{data}(t)$ is the data signal and $T_{int}(t)$ is the intrinsic switching window. For a data signal with a repetition frequency $\nu_{line} = k\, \nu_{base}$ (k: multiplex factor), $\Delta t_{bit} = 1/\nu_{line}$ and $\Delta t_{out} = 1/\nu_{base} - \Delta t_{bit}$ denote the integration periods for the switched and the unwantedly switched OTDM channels respectively. The parameter t_0 determines the temporal position of the data pulses with respect to the maximum of the switching window.
Equation A.1 can be simplified for a particular data signal $P_{data}(t)$. In the system experiments, the data signal consists of short optical pulses, with a repetition frequency of ν_{line}. In this case, for a time period of $1/\nu_{base}$, $P_{data}(t)$ can be written as

$$P_{data}(t) = \sum_{i=1}^{k} A_i(t)\, s(t - i/\nu_{line}) \,, \tag{A.2}$$

where $s(t)$ is the pulse shape, $A_i(t)$ stands for the amplitude modulation of the i-th channel (RZ modulation format) and k is the number of OTDM channels. It will be assumed that an ideal modulator is used and $A_i(t)$ equals 1 for all channels.
The experimental switching windows within this work, are obtained with an OSA (see Fig. 4.1), using a pump-probe technique. The probe signal also consists of short optical pulses with a pulse shape given by $s(t)$ and a repetition frequency of ν_{base}. Thus the measured switching windows $T_{exp}(t)$ are a convolution between the probe signal and the intrinsic switching window $T_{int}(t)$

$$T_{exp}(t) = \int_{\infty} s(t')\, T_{int}(t - t')\, dt' \,. \tag{A.3}$$

For the calculation, we assume that the integration period in (A.3) is reduced to Δt_{bit}. The resulting error is small, as long as the width of the data pulses (FWHM) is small compared to the bit period Δt_{bit}. This is always true for high bit rate OTDM systems,

because the FWHM of the data pulses in such systems has to be smaller than $\Delta t_{bit}/4$, in order to avoid a degradation of the data signal by coherent superposition of adjacent pulses. With this assumption, and using equation A.1, A.2 and A.3, a simple formula for calculating the ICR from the experimental switching windows is deduced

$$\mathrm{ICR} = 10 \log \frac{T_{exp}(t_0 + l/\nu_{line})}{\sum_{i=1\cdots l-1,l+1}^{k} T_{exp}(t_0 + i/\nu_{line})} , \tag{A.4}$$

where l denotes the switched channel. With equation A.4 it is possible to estimate the demultiplexing performance at a given base data rate (e.g. 10 Gbit/s) for any TDM bit rate from just one switching window measurement. This is of course only true when the data pulses do not degrade significantly by increasing the TDM bit rate. Fig. A.3 shows in a schematic picture, how the ICR is determined.

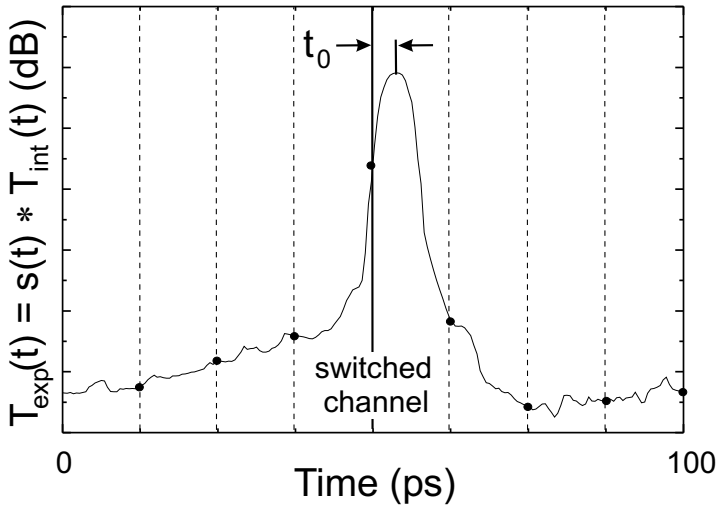

Figure A.3 : Schematic picture for calculating the ICR for 80 Gbit/s TDM bit rate and 10 Gbit/s base data rate. The solid curve is the measured switching window, which is the convolution of the probe pulses (10 GHz sech^2 pulse stream) and the intrinsic switching window $T_{int}(t)$. The vertical dotted lines denote the positions of the eight 10 Gbit/s data channels, where the values for calculating the ICR are taken. The parameter t_0 (relative position of the switching window with respect to the data channels) has to be chosen such that a maximum ICR is obtained.

Two characteristics of an optical switch, which can also influence the demultiplexing performance, are not included in the ICR. The first is the optical loss in the switch. In general, the loss is uncritical, because it can be compensated with an EDFA, without significant performance degradation. This is of course only true, as long as the optical power stays above the sensitivity of the receiver. The second characteristic value is the jitter of the control pulses, gating the switch. If the jitter is too high, the BER will start to fluctuate, because the switching window itself jitters.

A.3 Optical Waves, Intensity, Power

Throughout this work, the following expression to describe the optical waves will be used :

$$\underline{\mathbf{E}}(\underline{\mathbf{r}}\,,t) = \underline{\widetilde{\mathbf{E}}}_0(\underline{\mathbf{r}}\,,t)\,\mathrm{e}^{-i\omega t} + \underline{\widetilde{\mathbf{E}}}^*_0(\underline{\mathbf{r}}\,,t)\,\mathrm{e}^{+i\omega t} = 2\,\Re\{\underline{\widetilde{\mathbf{E}}}_0(\underline{\mathbf{r}}\,,t)\,\mathrm{e}^{-i\omega t}\}\;, \tag{A.5}$$

where

$$\underline{\widetilde{\mathbf{E}}}_0(\underline{\mathbf{r}}\,,t) = \frac{1}{2}\,\underline{\widetilde{\mathbf{A}}}\,(\underline{\mathbf{r}},\;t)\,\mathrm{e}^{+i\,\underline{\mathbf{k}}\,\underline{\mathbf{r}}}$$

is the slowly varying amplitude of the optical wave with center frequency ω, which is in general complex and time-dependent [21]. In an optical waveguide, such as optical fiber or the active region of an SOA, with orientation along the z axis, $\underline{\widetilde{\mathbf{E}}}_0\,(\underline{\mathbf{r}}\,,t)$ can be written as

$$\underline{\widetilde{\mathbf{E}}}_0(\underline{\mathbf{r}}\,,t) = \frac{1}{2}\,F(x,y)\,\underline{\widetilde{\mathbf{A}}}(z,t)\,\mathrm{e}^{(i\beta-\alpha/2)z}\;. \tag{A.6}$$

Here the wavenumber $\underline{\mathbf{k}}$ was replaced by the propagation constant $\beta = \frac{\omega}{c}\,n_0$ and the absorption coefficient α. $F(x,y)$ describes the transversal field distribution.
The intensity $I(\underline{\mathbf{r}}\,,t)$ of the optical wave is given by

$$I(\underline{\mathbf{r}}\,,t) = \varepsilon_0\;n_0\;c\;\left\langle|\underline{\mathbf{E}}(\underline{\mathbf{r}}\,,t)|^2\right\rangle\;, \tag{A.7}$$

where n_0 is the linear refractive index of the medium. The operation $\langle\,\cdot\,\rangle$ denotes averaging over a time interval, that is much longer than the time of an optical cycle ($2\pi/\omega$), but much shorter than any time of interest, which would be in this case the duration of the optical pulses used for data transmission (a few hundred femtoseconds to a few picoseconds). Substituting equation A.5 into equation A.7 yields

$$\begin{aligned} I(\underline{\mathbf{r}}\,,t) &= \varepsilon_0\;n_0\;c\;\left\langle\left|\underline{\widetilde{\mathbf{E}}}_0(\underline{\mathbf{r}}\,,t)\,\mathrm{e}^{-i\omega t} + \underline{\widetilde{\mathbf{E}}}^*_0(\underline{\mathbf{r}}\,,t)\,\mathrm{e}^{+i\omega t}\right|^2\right\rangle \\ &= 2\;\varepsilon_0\;n_0\;c\;\left\langle\left|\underline{\widetilde{\mathbf{E}}}_0(\underline{\mathbf{r}}\,,t)\right|^2\right\rangle + 2\;\varepsilon_0\;n_0\;c\;\left\langle\Re\left\{\underline{\widetilde{\mathbf{E}}}_0(\underline{\mathbf{r}}\,,t)\,\mathrm{e}^{-2i\,\omega t}\right\}\right\rangle\;. \end{aligned} \tag{A.8}$$

For a monochromatic wave, $\underline{\widetilde{\mathbf{E}}}_0(\underline{\mathbf{r}}\,,t)$ is time-independent and the second term in equation A.8 vanishes for averaging over a time interval much longer than $2\pi/\omega$. Thus the optical intensity of the monochromatic wave is proportional to the absolute square of $\underline{\widetilde{\mathbf{E}}}_0(\underline{\mathbf{r}})$ and does not vary with time

$$I(\underline{\mathbf{r}}) = 2\;\varepsilon_0\;n_0\;c\;\left|\underline{\widetilde{\mathbf{E}}}_0(\underline{\mathbf{r}})\right|^2\;. \tag{A.9}$$

For an optical pulse train, the optical signal can be regarded as a quasi-monochromatic wave with central frequency $2\pi/\omega_0$ and a spectral width $\Delta\omega \ll \omega_0$. The time average to determine the intensity, is in this case taken over a time interval much longer than the time of an optical cycle $2\pi/\omega_0$ but much shorter than $2\pi/\Delta\omega_0$. The first term in equation A.8 contains only frequency differences on the order of $\Delta\omega \ll \omega_0$. It therefore varies slowly and is unaffected by the time-averaging operation. The second term, which has components oscillating at frequencies $\approx \pm 2\pi/\omega_0$, is washed out by the averaging operation. Thus the expression for the intensity is similar to the monochromatic case

$$I(\underline{\mathbf{r}}\,,t) = 2\;\varepsilon_0\;n_0\;c\;\left|\underline{\widetilde{\mathbf{E}}}_0(\underline{\mathbf{r}}\,,t)\right|^2\;. \tag{A.10}$$

The optical power in the waveguide is given by

$$P(z,t) = \iint I(\underline{\mathbf{r}}\,,t)\,dxdy \approx 2\;\varepsilon_0\;n_0\;c\;A_{eff}\;\left|\underline{\widetilde{\mathbf{E}}}_0(z,t)\right|^2\;. \tag{A.11}$$

The integration is performed over the whole cross-section of the waveguide. Alternatively, the effective area A_{eff} of the waveguide can be used, which is calculated by integrating the transversal field distribution $F(x,y)$

$$A_{eff} = \frac{\left[\iint |F(x,y)|^2\,dx\,dy\right]^2}{\iint |F(x,y)|^4\,dx\,dy}\;. \tag{A.12}$$

In most of the experiments presented in this work, the average power P of the optical signals is given, which is the optical power $P(t)$, averaged over a time interval long compared to the width of the optical pulses used.

In some cases, the energy E_{pulse} and the peak power P_{peak} of a single pulse in a pulse train of well separated pulses with average power P is of interest. The pulse energy depends on the repetition rate ν_{rep} of the pulse train and is given by

$$E_{\text{pulse}} = \frac{P}{\nu_{rep}}\;. \tag{A.13}$$

The peak power depends on the pulse shape and can, for a decent pulse shape, be written as

$$P_{\text{peak}} = \frac{E_{\text{pulse}}}{a_{sh}\;\tau_{\text{FWHM}}} = \frac{P}{a_{sh}\;\tau_{\text{FWHM}}\;\nu_{rep}}\;, \tag{A.14}$$

where τ_{FWHM} is the full width at half maximum of the pulse and a_{sh} is a constant factor, to take into account the pulse shape. For a rectangular pulse shape $a_{sh} = 1$, for a pulse with sech envelope $a_{sh} = 1/\text{arccosh}(\sqrt{2}) \approx 1.135$ and for a pulse with gaussian shape $a_{sh} = \sqrt{\pi}/(2\sqrt{\ln 2}) \approx 1.065$. A 10 GHz pulse train with $P = 10$ dBm (10 mW) and 1 ps, sech shaped pulses has a pulse energy of 1 pJ and a peak power of 0.881 W. Note that for a pulse train, amplitude modulated with a pseudo-random bit sequence, the pulse energy is twice as high, because on average the amplitude of every second pulse is zero.

A.4 The Jones Formalism

The Jones formalism provides a compact mathematical description for the transformation of the polarization state of a fully polarized electromagnetic wave while traveling through an optical element. The polarization states are described by complex Jones vectors. The Jones vector is defined by the components of the complex electric field vector in a plane perpendicular to the propagation direction. In the case of an optical waveguide with an optical wave propagating in z direction, given by equation A.6, the Jones vector is

$$\underline{\widetilde{E}} = \begin{pmatrix} \widetilde{E}_{0,x} \\ \widetilde{E}_{0,y} \end{pmatrix} = \begin{pmatrix} E_{0,x} \mathrm{e}^{i\Phi_x} \\ E_{0,y} \mathrm{e}^{i\Phi_y} \end{pmatrix} \ . \tag{A.15}$$

The ratio $E_{0,x}/E_{0,y}$ and the phase difference $\Phi_y - \Phi_x$ determines the orientation and shape of the polarization ellipse. The Jones vectors for some special polarization states are provided in Table A.1.

Linearly polarized wave, in x direction	$\begin{pmatrix} 1 \\ 0 \end{pmatrix}$
Linearly polarized wave, plane of polarization making angle Θ with x axis direction	$\begin{pmatrix} \cos\Theta \\ \sin\Theta \end{pmatrix}$
Right circularly polarized wave	$\frac{1}{\sqrt{2}} \begin{pmatrix} 1 \\ i \end{pmatrix}$
Left circularly polarized wave	$\frac{1}{\sqrt{2}} \begin{pmatrix} 1 \\ -i \end{pmatrix}$

Table A.1 : Jones vectors for some special polarization states.

As the Jones vectors represent electric fields, the coherent superposition of split waves, for instance in an interferometer, can be described by the sum of the corresponding Jones vectors. If two waves have orthogonal states of polarization, the complex scalar product of their Jones vectors is zero. An optical element is described in the Jones formalism by a complex 2×2 Jones matrix $\mathbf{M}$. The Jones vector of an optical wave after propagation through a number of optical elements $\mathbf{M}_1 \ldots \mathbf{M}_n$ is than given by

$$\underline{\widetilde{E}}_{\,out} = \mathbf{M}_n \cdots \mathbf{M}_1 \underline{\widetilde{E}}_{\,in} \ . \tag{A.16}$$

In the special case of a lossless optical element the corresponding Jones matrix is a unitary matrix ($\mathbf{M}^\dagger \, \mathbf{M} = \mathbf{1}$).

The elements of the Jones vectors and Jones matrices depend on the choice of the coordinate system. If these elements are known in one coordinate system, they can be determined in another coordinate system by using matrix methods. Assume that an optical system is represented by the Jones matrix $\mathbf{M}'$ in a x'-y' coordinate system, which is rotated anticlockwise by an angle Θ against a given x-y coordinate system. The Jones matrix $\mathbf{M}$ representing the optical system in the x-y coordinate system is then given by

$$\mathbf{M} = \mathbf{R}(-\Theta) \ \mathbf{M}' \ \mathbf{R}(\boldsymbol{\Theta}) \ , \tag{A.17}$$

where

$$\mathbf{R}(\Theta) = \begin{pmatrix} \cos(\Theta) & \sin(\Theta) \\ -\sin(\Theta) & \cos(\Theta) \end{pmatrix} \tag{A.18}$$

is the coordinate transformation matrix.

A.5 Jones Transfer Matrices

The Jones transfer matrices $\mathcal{M}$ for the three different interferometer types, discussed in this work are given here in the following form

$$\mathcal{M} = \begin{pmatrix} \mathbf{M}_{(11)} & \mathbf{M}_{(21)} \\ \mathbf{M}_{(12)} & \mathbf{M}_{(22)} \end{pmatrix} \ , \quad \text{with}$$

$$\mathbf{M}_{(11)} = \begin{pmatrix} a & b \\ e & f \end{pmatrix} \ , \quad \mathbf{M}_{(21)} = \begin{pmatrix} c & d \\ g & h \end{pmatrix} \ , \quad \mathbf{M}_{(12)} = \begin{pmatrix} i & j \\ m & n \end{pmatrix} \ , \quad \mathbf{M}_{(22)} = \begin{pmatrix} k & l \\ o & p \end{pmatrix} \ .$$

Sagnac Interferometer

$$\begin{aligned}
a &= -\sqrt{1-k_x}\, i \sqrt{k_x} \left[J^A_{xx} + J^C_{xx}\right] \mathcal{K}\, \mathrm{e}^{-\frac{\alpha}{2}L} & i &= \left[k_x\, J^A_{xx} - (1-k_x)\, J^C_{xx}\right] \mathcal{K}\, \mathrm{e}^{-\frac{\alpha}{2}L} \\
b &= \big[-\sqrt{1-k_x}\, i \sqrt{k_y}\, J^A_{xx} & j &= \big[\sqrt{k_x}\sqrt{k_y}\, J^A_{xy} \\
&\quad +\sqrt{1-k_y}\, i \sqrt{k_x}\, J^C_{xy}\big] \mathcal{K}\, \mathrm{e}^{-\frac{\alpha}{2}L} & &\quad +\sqrt{1-k_x}\sqrt{1-k_y}\, J^C_{xy}\big] \mathcal{K}\, \mathrm{e}^{-\frac{\alpha}{2}L} \\
c &= \left[-(1-k_x)\, J^A_{xx} + k_x\, J^C_{xx}\right] \mathcal{K}\, \mathrm{e}^{-\frac{\alpha}{2}L} & k &= a \\
d &= -\big[\sqrt{1-k_x}\sqrt{1-k_y}\, J^A_{xy} & l &= -\big[\sqrt{1-k_y}\, i \sqrt{k_x}\, J^A_{xy} \\
&\quad +\sqrt{k_x}\sqrt{k_y}\, J^C_{xy}\big] \mathcal{K}\, \mathrm{e}^{-\frac{\alpha}{2}L} & &\quad +\sqrt{1-k_x}\, i \sqrt{k_y}\, J^C_{xy}\big] \mathcal{K}\, \mathrm{e}^{-\frac{\alpha}{2}L} \\
e &= \big[\sqrt{1-k_y}\, i \sqrt{k_x}\, J^A_{yx} & m &= -\big[\sqrt{k_x}\sqrt{k_y}\, J^A_{yx} \\
&\quad -\sqrt{1-k_x}\, i \sqrt{k_y}\, J^C_{yx}\big] \mathcal{K}\, \mathrm{e}^{-\frac{\alpha}{2}L} & &\quad +\sqrt{1-k_x}\sqrt{1-k_y}\, J^C_{yx}\big] \mathcal{K}\, \mathrm{e}^{-\frac{\alpha}{2}L} \\
f &= \sqrt{1-k_y}\, i \sqrt{k_y} \left[J^A_{yy} + J^C_{yy}\right] \mathcal{K}\, \mathrm{e}^{-\frac{\alpha}{2}L} & n &= \left[-k_y\, J^A_{yy} + (1-k_y)\, J^C_{yy}\right] \mathcal{K}\, \mathrm{e}^{-\frac{\alpha}{2}L} \\
g &= \big[\sqrt{1-k_x}\sqrt{1-k_y}\, J^A_{yx} & o &= \big[\sqrt{1-k_x}\, i \sqrt{k_y}\, J^A_{yx} \\
&\quad -\sqrt{k_x}\sqrt{k_y}\, J^C_{yx}\big] \mathcal{K}\, \mathrm{e}^{-\frac{\alpha}{2}L} & &\quad -\sqrt{1-k_y}\, i \sqrt{k_x}\, J^C_{yx}\big] \mathcal{K}\, \mathrm{e}^{-\frac{\alpha}{2}L} \\
h &= \left[(1-k_y)\, J^A_{yy} - k_y\, J^C_{yy}\right] \mathcal{K}\, \mathrm{e}^{-\frac{\alpha}{2}L} & p &= f
\end{aligned}$$

$\mathcal{K} = 1 - \kappa$ describes the excess loss in the coupler, where κ is the loss coefficient.
L and α are the fiber loop length and fiber absorption coefficient respectively.
k_x , k_y : field intensity coupling coefficients of the coupler for x and y polarization.

$\mathbf{J}^C = \begin{pmatrix} J^C_{xx} & J^C_{xy} \\ J^C_{yx} & J^C_{yy} \end{pmatrix}$, $\mathbf{J}^A = \begin{pmatrix} J^A_{xx} & J^A_{xy} \\ J^A_{yx} & J^A_{yy} \end{pmatrix}$: Jones matrices, representing the clockwise and anticlockwise propagation in the fiber loop.

Mach-Zehnder Interferometer

$$
\begin{aligned}
a &= \mathcal{K}\left[-\sqrt{k_x^{(2)}}\sqrt{k_x^{(1)}}\,J_{xx}^2\,e^{-\frac{1}{2}\alpha^{(2)}L^{(2)}}\right.\\
&\quad\left.+\sqrt{1-k_x^{(2)}}\sqrt{1-k_x^{(1)}}\,J_{xx}^1\,e^{-\frac{1}{2}\alpha^{(1)}L^{(1)}}\right]\\
b &= \mathcal{K}\left[-\sqrt{k_y^{(1)}}\sqrt{k_x^{(2)}}\,J_{xy}^2\,e^{-\frac{1}{2}\alpha^{(2)}L^{(2)}}\right.\\
&\quad\left.+\sqrt{1-k_x^{(2)}}\sqrt{1-k_y^{(1)}}\,J_{xy}^1\,e^{-\frac{1}{2}\alpha^{(1)}L^{(1)}}\right]\\
c &= \mathcal{K}\left[i\sqrt{1-k_x^{(1)}}\sqrt{k_x^{(2)}}\,J_{xx}^2\,e^{-\frac{1}{2}\alpha^{(2)}L^{(2)}}\right.\\
&\quad\left.+i\sqrt{1-k_x^{(2)}}\sqrt{k_x^{(1)}}\,J_{xx}^1\,e^{-\frac{1}{2}\alpha^{(1)}L^{(1)}}\right]\\
d &= \mathcal{K}\left[i\sqrt{1-k_y^{(1)}}\sqrt{k_x^{(2)}}\,J_{xy}^2\,e^{-\frac{1}{2}\alpha^{(2)}L^{(2)}}\right.\\
&\quad\left.+i\sqrt{1-k_x^{(2)}}\sqrt{k_y^{(1)}}\,J_{xy}^1\,e^{-\frac{1}{2}\alpha^{(1)}L^{(1)}}\right]\\
e &= \mathcal{K}\left[-\sqrt{k_y^{(2)}}\sqrt{k_x^{(1)}}\,J_{yx}^2\,e^{-\frac{1}{2}\alpha^{(2)}L^{(2)}}\right.\\
&\quad\left.+\sqrt{1-k_y^{(2)}}\sqrt{1-k_x^{(1)}}\,J_{yx}^1\,e^{-\frac{1}{2}\alpha^{(1)}L^{(1)}}\right]\\
f &= \mathcal{K}\left[-\sqrt{k_y^{(2)}}\sqrt{k_y^{(1)}}\,J_{yy}^2\,e^{-\frac{1}{2}\alpha^{(2)}L^{(2)}}\right.\\
&\quad\left.+\sqrt{1-k_y^{(2)}}\sqrt{1-k_y^{(1)}}\,J_{yy}^1\,e^{-\frac{1}{2}\alpha^{(1)}L^{(1)}}\right]\\
g &= \mathcal{K}\left[i\sqrt{k_y^{(2)}}\sqrt{1-k_x^{(1)}}\,J_{yx}^2\,e^{-\frac{1}{2}\alpha^{(2)}L^{(2)}}\right.\\
&\quad\left.+i\sqrt{1-k_y^{(2)}}\sqrt{k_x^{(1)}}\,J_{yx}^1\,e^{-\frac{1}{2}\alpha^{(1)}L^{(1)}}\right]\\
h &= \mathcal{K}\left[i\sqrt{k_y^{(2)}}\sqrt{1-k_y^{(1)}}\,J_{yy}^2\,e^{-\frac{1}{2}\alpha^{(2)}L^{(2)}}\right.\\
&\quad\left.+i\sqrt{1-k_y^{(2)}}\sqrt{k_y^{(1)}}\,J_{yy}^1\,e^{-\frac{1}{2}\alpha^{(1)}L^{(1)}}\right]
\end{aligned}
\qquad
\begin{aligned}
i &= \mathcal{K}\left[i\sqrt{k_x^{(1)}}\sqrt{1-k_x^{(2)}}\,J_{xx}^2\,e^{-\frac{1}{2}\alpha^{(2)}L^{(2)}}\right.\\
&\quad\left.+i\sqrt{k_x^{(2)}}\sqrt{1-k_x^{(1)}}\,J_{xx}^1\,e^{-\frac{1}{2}\alpha^{(1)}L^{(1)}}\right]\\
j &= \mathcal{K}\left[i\sqrt{k_y^{(1)}}\sqrt{1-k_x^{(2)}}\,J_{xy}^2\,e^{-\frac{1}{2}\alpha^{(2)}L^{(2)}}\right.\\
&\quad\left.+i\sqrt{k_x^{(2)}}\sqrt{1-k_y^{(1)}}\,J_{xy}^1\,e^{-\frac{1}{2}\alpha^{(1)}L^{(1)}}\right]\\
k &= \mathcal{K}\left[\sqrt{1-k_x^{(2)}}\sqrt{1-k_x^{(1)}}\,J_{xx}^2\,e^{-\frac{1}{2}\alpha^{(2)}L^{(2)}}\right.\\
&\quad\left.-\sqrt{k_x^{(2)}}\sqrt{k_x^{(1)}}\,J_{xx}^1\,e^{-\frac{1}{2}\alpha^{(1)}L^{(1)}}\right]\\
l &= \mathcal{K}\left[\sqrt{1-k_x^{(2)}}\sqrt{1-k_y^{(1)}}\,J_{xy}^2\,e^{-\frac{1}{2}\alpha^{(2)}L^{(2)}}\right.\\
&\quad\left.-\sqrt{k_x^{(2)}}\sqrt{k_y^{(1)}}\,J_{xy}^1\,e^{-\frac{1}{2}\alpha^{(1)}L^{(1)}}\right]\\
m &= \mathcal{K}\left[i\sqrt{1-k_y^{(2)}}\sqrt{k_x^{(1)}}\,J_{yx}^2\,e^{-\frac{1}{2}\alpha^{(2)}L^{(2)}}\right.\\
&\quad\left.+i\sqrt{1-k_x^{(1)}}\sqrt{k_y^{(2)}}\,J_{yx}^1\,e^{-\frac{1}{2}\alpha^{(1)}L^{(1)}}\right]\\
n &= \mathcal{K}\left[i\sqrt{1-k_y^{(2)}}\sqrt{k_y^{(1)}}\,J_{yy}^2\,e^{-\frac{1}{2}\alpha^{(2)}L^{(2)}}\right.\\
&\quad\left.+i\sqrt{1-k_y^{(1)}}\sqrt{k_y^{(2)}}\,J_{yy}^1\,e^{-\frac{1}{2}\alpha^{(1)}L^{(1)}}\right]\\
o &= \mathcal{K}\left[\sqrt{1-k_y^{(2)}}\sqrt{1-k_x^{(1)}}\,J_{yx}^2\,e^{-\frac{1}{2}\alpha^{(2)}L^{(2)}}\right.\\
&\quad\left.-\sqrt{k_y^{(2)}}\sqrt{k_x^{(1)}}\,J_{yx}^1\,e^{-\frac{1}{2}\alpha^{(1)}L^{(1)}}\right]\\
p &= \mathcal{K}\left[\sqrt{1-k_y^{(2)}}\sqrt{1-k_y^{(1)}}\,J_{yy}^2\,e^{-\frac{1}{2}\alpha^{(2)}L^{(2)}}\right.\\
&\quad\left.-\sqrt{k_y^{(2)}}\sqrt{k_y^{(1)}}\,J_{yy}^1\,e^{-\frac{1}{2}\alpha^{(1)}L^{(1)}}\right]
\end{aligned}
$$

$k_x^{(1)}, k_y^{(1)}$, $k_x^{(2)}, k_y^{(2)}$ are field intensity coupling coefficients of the couplers for x and y polarization. $L^{(1)}, L^{(2)}$ and $\alpha^{(1)}, \alpha^{(2)}$ are the fiber lengths and the fiber absorption coefficients in the two interferometer branches. $\mathcal{K} = \sqrt{1-\kappa^{(1)}}\sqrt{1-\kappa^{(2)}}$ is excess loss in the couplers, where $\kappa^{(1)}$ and $\kappa^{(2)}$ are the loss coefficients for the input and output coupler respectively.

$\mathbf{J}^{(1)} = \begin{pmatrix} J_{xx}^1 & J_{xy}^1 \\ J_{yx}^1 & J_{yy}^1 \end{pmatrix}$, $\mathbf{J}^{(2)} = \begin{pmatrix} J_{xx}^2 & J_{xy}^2 \\ J_{yx}^2 & J_{yy}^2 \end{pmatrix}$: Jones matrices, representing the propagation in the upper and lower interferometer branch.

Ultrafast-Nonlinear Interferometer

$$
\begin{aligned}
a \;=\; \Big[& \; \mathrm{e}^{i\,2\,\phi_{\mathrm{DGD}}} \left[\sin^2\Theta\,\cos^2\Theta\,(J_{xx}-J_{yy}) + \sin\Theta\,\cos\Theta\left(J_{xy}\,\sin^2\Theta - J_{yx}\,\cos^2\Theta\right)\right] \\
& + \mathrm{e}^{i\,\phi_{\mathrm{DGD}}} \left[J_{xx}\left(\sin^4\Theta+\cos^4\Theta\right) + J_{yy}\,2\,\cos^2\Theta\,\sin^2\Theta \right. \\
& \qquad \left. + \sin\Theta\,\cos\Theta\,\left(\cos^2\Theta-\sin^2\Theta\right)(J_{xy}+J_{yx})\right] \\
& + \left[\sin^2\Theta\,\cos^2\Theta\,(J_{xx}-J_{yy}) + \sin\Theta\,\cos\Theta\left(J_{yx}\,\sin^2\Theta - J_{xy}\,\cos^2\Theta\right)\right]\Big]\mathcal{K}\,\mathrm{e}^{-\frac{\alpha}{2}L}
\end{aligned}
$$

$$
\begin{aligned}
d \;=\; \Big[& \; \mathrm{e}^{i\,2\,\phi_{\mathrm{DGD}}} \left[\sin^3\Theta\,\cos\Theta\,(J_{xx}-J_{yy}) + \sin^2\Theta\left(J_{xy}\,\sin^2\Theta - J_{yx}\,\cos^2\Theta\right)\right] \\
& + \mathrm{e}^{i\,\phi_{\mathrm{DGD}}} \left[-\sin\Theta\,\cos\Theta\left(\sin^2\Theta-\cos^2\Theta\right)(J_{xx}-J_{yy}) \right. \\
& \qquad \left. + 2\,\sin^2\Theta\,\cos^2\Theta\,(J_{xy}+J_{yx})\right] \\
& + \left[-\cos^3\Theta\,\sin\Theta\,(J_{xx}-J_{yy}) + \cos^2\Theta\left(J_{xy}\,\cos^2\Theta - J_{yx}\,\sin^2\Theta\right)\right]\Big]\mathcal{K}\,\mathrm{e}^{-\frac{\alpha}{2}L}
\end{aligned}
$$

$$
\begin{aligned}
m = \Big[& \; \mathrm{e}^{i\,2\,\phi_{\mathrm{DGD}}} \left[-\cos^3\Theta\,\sin\Theta\,(J_{xx}-J_{yy}) - \cos^2\Theta\left(J_{xy}\,\sin^2\Theta - J_{yx}\,\cos^2\Theta\right)\right] \\
& + \mathrm{e}^{i\,\phi_{\mathrm{DGD}}} \left[\sin\Theta\,\cos\Theta\left(\cos^2\Theta-\sin^2\Theta\right)(J_{xx}-J_{yy}) \right. \\
& \qquad \left. + 2\,\sin^2\Theta\,\cos^2\Theta\,(J_{xy}+J_{yx})\right] \\
& + \left[\sin^3\Theta\,\cos\Theta\,(J_{xx}-J_{yy}) - \sin^2\Theta\left(J_{xy}\,\cos^2\Theta - J_{yx}\,\sin^2\Theta\right)\right]\Big]\mathcal{K}\,\mathrm{e}^{-\frac{\alpha}{2}L}
\end{aligned}
$$

$$
\begin{aligned}
p \;=\; \Big[& \; \mathrm{e}^{i\,2\,\phi_{\mathrm{DGD}}} \left[-\sin^2\Theta\,\cos^2\Theta\,(J_{xx}-J_{yy}) - \sin\Theta\,\cos\Theta\left(J_{xy}\,\sin^2\Theta - J_{yx}\,\cos^2\Theta\right)\right] \\
& + \mathrm{e}^{i\,\phi_{\mathrm{DGD}}} \left[2\,\cos^2\Theta\,\sin^2\Theta\,J_{xx} + \left(\sin^4\Theta+\cos^4\Theta\right)J_{yy} \right. \\
& \qquad \left. + \sin\Theta\,\cos\Theta\left(\sin^2\Theta-\cos^2\Theta\right)(J_{xy}+J_{yx})\right] \\
& + \left[-\cos^2\Theta\,\sin^2\Theta\,(J_{xx}-J_{yy}) + \cos\Theta\sin\Theta\left(J_{xy}\,\cos^2\Theta - J_{yx}\,\sin^2\Theta\right)\right]\Big]\mathcal{K}\,\mathrm{e}^{-\frac{\alpha}{2}L}
\end{aligned}
$$

$b,\ c,\ e,\ f,\ g,\ h,\ i,\ j,\ k,\ l,\ n,\ o = 0$

The transmission axis of the polarizing beamsplitter is orientated along the x axis. $\tau_{\mathrm{DGD}} = |L_{\mathrm{HiBi}}/v_{g,f} - L_{\mathrm{HiBi}}/v_{g,s}|$ is the differential group delay (DGD) of the HiBi fibers, where L_{HiBi} is the length of each HiBi fiber and $v_{g,f}$, $v_{g,s}$ are the group velocities of the fast and slow axis respectively.

$\mathcal{K} = (1-\kappa_{\mathrm{HiBi}})$ is the loss in both HiBi fibers with loss coefficient κ_{HiBi} for a single HiBi fiber.

L and α are the fiber length and fiber absorption coefficient in between the two pieces of HiBi fiber.

Θ : angle between the fast axis of the first HiBi fiber and the x axis.

ϕ_{DGD} : phase difference between the orthogonal data components after propagation through the HiBi fiber ($\phi_{\mathrm{DGD}} = \omega\,\tau_{\mathrm{DGD}}$).

$\mathbf{J} = \begin{pmatrix} J_{xx} & J_{xy} \\ J_{yx} & J_{yy} \end{pmatrix}$: Jones matrix, representing the propagation in between the two pieces of HiBi fiber.

A.6 Decibel Units: dB and dBm

The units dB (decibel) and dBm are widely used in fiber optics and telecommunication to describe optical power ratios and powers in a logarithmic scale. The optical power ratio T in dB between two optical powers P_1 and P_2, given in watt, is defined as

$$T\,[\mathrm{dB}] = 10\ \log\left(\frac{P_1\,[\mathrm{W}]}{P_2\,[\mathrm{W}]}\right)\ . \tag{A.19}$$

If P_1 and P_2 are the input and output power to an optical component, then T is the attenuation of the component in dB.

The absolute optical power is described by dBm. One milliwatt of optical power is used as a reference, when specifying the absolute optical power level P in terms of dBm

$$P\,[\mathrm{dBm}] = 10\ \log\left(\frac{P\,[\mathrm{mW}]}{1\ \mathrm{mW}}\right)\ . \tag{A.20}$$

As an example, some optical power values in dBm, calculated using (A.20), are listed below.

dBm	**mW**
-20	0.010
-10	0.100
-3	0.501
0	1.000
3	1.995
10	10.000
20	100.000

Also electrical powers are sometimes described using dB and dBm. As the electrical power is proportional to the square root of the optical power, generating the electrical signal on a detector, the $\mathrm{dB_{el}}$ and $\mathrm{dBm_{el}}$ values are twice as large as the $\mathrm{dB_{opt}}$ and $\mathrm{dBm_{opt}}$ values. Throughout this work only optical dB and dBm are used.

A.7 Parameters of utilized SOAs

The active material of all SOAs is InGaAsP. All average optical power and gain values are given in the fiber, including the fiber-chip coupling loss (on the order of $2-3$ dB). All parameters are given for an operation wavelength at the maximum SOA gain, except for the JDS Uniphase booster SOA.

ETH

Supplier: ETH - Zurich
Type: Bulk-SOA,

Parameter	typical value
single-pass small signal gain	26 dB
polarization dependence of the gain	$2-4$ dB
wavelength of maximum gain	1545 nm
3 dB saturation output power	not available
length of active region	750 µm

The parameters given above are for 375 mA driving current and at 20 °C. The SOA was fabricated and provided by colleagues from the Swiss Federal Institute of Technology (ETH) in Zurich. It was used for measurements of the gain and phase dynamics, to compare conventionally and gain-transparent operated SOAs. The measurements were performed together with colleagues from the ETH. Further details may be found in [70].

JDS Uniphase Inline

Supplier: JDS Uniphase
Type: MQW-SOA, CQF 882/0 No. 475

Parameter	typical value
single-pass small signal gain	28 dB
polarization dependence of the gain	0.5 dB
wavelength of maximum gain	1307 nm
3 dB saturation output power	11.5 dBm
length of active region	800 µm

The parameters given above are for 300 mA driving current and at 25 °C. The SOA was a commercially available device from JDS Uniphase. This SOA or a similar type was used for the SOA based interferometric switches, investigated in this work. Also the measurements of the gain and phase dynamics were performed with this device.

JDS Uniphase Booster

Supplier: JDS Uniphase
Type: MQW-SOA, CQF 881/0 No. 481

Parameter	typical value
single-pass small signal gain	15 dB
polarization dependence of the gain	[a]
wavelength of maximum gain	1240 nm
3 dB saturation output power	17.9 dBm
length of active region	400 µm

[a] strong polarization dependence, optical isolator integrated in the module

The parameters given above are for 262 mA driving current and at 25 °C. The operation wavelength was 1300 nm. The SOA was a commercially available device from JDS Uniphase. This SOA or a similar type was used to amplify the 1300 nm control signals, which are used in the gain-transparent SOA switches.

Optospeed 1

Supplier: Optospeed
Type: Bulk-SOA, SOA1300MRI/P - C1120

Parameter	typical value
single-pass small signal gain	21.4 dB
polarization dependence of the gain	0.8 dB
wavelength of maximum gain	1304 nm
3 dB saturation output power	7.9 dBm
length of active region	500 µm

The parameters given above are for 250 mA driving current and at 20 °C. The SOA was a commercially available device from Optospeed. This SOA was used to investigation the gain and phase dynamics in gain-transparent operated bulk-SOAs.

Optospeed 2

Supplier: Optospeed
Type: Bulk-SOA, SOA1300MRI/X1500 - C1182

Parameter	typical value
single-pass small signal gain	23.3 dB
polarization dependence of the gain	0.9 dB
wavelength of maximum gain	1321 nm
3 dB saturation output power	9.3 dBm
length of active region	1500 µm

The parameters given above are for 500 mA driving current and at 20 °C. The SOA was a commercially available device from Optospeed. This SOA was used to investigate the transmission loss for the data signal in gain-transparent operated bulk-SOAs.

Optospeed 3

Supplier: Optospeed
Type: Bulk-SOA, SOA1550MRI/P - L1105

Parameter	typical value
single-pass small signal gain	20.4 dB
polarization dependence of the gain	0.5 dB
wavelength of maximum gain	1550 nm
3 dB saturation output power	6.5 dBm
length of active region	500 µm

The parameters given above are for 250 mA driving current and at 20 °C. The SOA was a commercially available device from Optospeed. This SOA was used to build a conventional UNI switch.

A.8 Parameters used for SOA Time-Domain Model

Parameter	value
length of active region L	800 µm
area of active region	0.27 μm^2
current I	300 mA
group refractive index n_g	3.5
internal loss α_{int}	4000 m^{-1}
coupling loss a_c	4 dB
confinement factor Γ	0.35
differential gain a_N	$22 \cdot 10^{-21}$ m^2
unsaturated carrier density N_{st}	$3.0 \cdot 10^{24}$ m^{-3}
carrier density at transparency N_0	$1.0 \cdot 10^{24}$ m^{-3}
recombination coefficients	
A_{nonrad}	$0.15 \cdot 10^{9}$ s^2
B_{spon}	$0.1 \cdot 10^{-15}$ m^{-3} s^{-1}
C_{Auger}	$1.5 \cdot 10^{-40}$ m^6 s^{-1}
linewidth enhancement factor α_{cdp}	3.0
linewidth enhancement factor α_{ch+shb}	1.0
CH and SHB recovery time τ_{ch+shb}	$500 \cdot 10^{-15}$ s
nonlinear gain suppression factor ϵ_{ch+shb}	$0.8 \cdot 10^{-3}$ m W^{-1}

These parameters are used in the time-domain model, to simulate the SOA gain dynamics, shown in Fig. 3.3. Details about the model can be found in [65].

Appendix B

Symbols and Abbreviations

Symbols

Roman Symbols

A	real number
$\underline{\widetilde{\mathbf{A}}}\,(\underline{\mathbf{r}}\,,t), \underline{\widetilde{\mathbf{A}}}\,(z,t)$	slowly varying envelope of the optical wave [Vm^{-1}]
$A_i(t)$	amplitude modulation for the ith channel in the data signal [–]
A_{eff}	effective area of a waveguide [m^2]
A_{nonrad}	coefficient for non-radiative processes [s^{-1}]
a	real number; also, Jones matrix element
a_c	loss in an SOA due to fiber coupling [–]
a_{gt}	total loss in a gain-transparent operated SOA [–]
a_N	differential gain coefficient [m^2]
a_{sh}	pulse shape factor [–]
B_{spon}	coefficient for spontaneous emission [$\mathrm{s}^{-1}\ \mathrm{m}^3$]
b	weighting factor between different polarization states in XPM; also, an arbitrary real number; also, Jones matrix element
C_{Auger}	coefficient for Auger recombination [$\mathrm{s}^{-1}\ \mathrm{m}^6$]
c	speed of light in free space [ms^{-1}]; also, an arbitrary real number; also, Jones matrix element
$\underline{\mathbf{D}}$	electric flux density [$\mathrm{As}\ \mathrm{m}^{-2}$]
d	thickness of the active layer in a semiconductor [m]; also, Jones matrix element
$\underline{\mathbf{E}}, \underline{\mathbf{E}}(t), \underline{\mathbf{E}}(\underline{\mathbf{r}}\,,t)$	electric field [Vm^{-1}]
$E_i(t)$	components of the electric field vector ($i \in \{x,y,z\}$) [Vm^{-1}]
$\underline{\widetilde{\mathbf{E}}}\,(\omega), \widetilde{E}_i(\omega)$	Fourier transform of the electric field and its vector components ($i \in \{x,y,z\}$) [$\mathrm{Vm}^{-1}\ \mathrm{s}$]
$\underline{\widetilde{\mathbf{E}}}_{\,0}(\underline{\mathbf{r}}\,,t), \widetilde{E}_{\,0,i}$	slowly varying complex amplitude of an optical wave and its vector components ($i \in \{x,y,z\}$) [Vm^{-1}]
$E_{0,i}$	absolute value of the vector components of the complex wave amplitude ($i \in \{x,y,z\}$) [–]
E_g	bandgap energy [J]
E_{fc}	quasi-Fermi energy for the conduction band [J]
E_{fv}	quasi-Fermi energy for the valence band [J]

$\underline{E}, \underline{E}', \underline{E}_{in}, \underline{E}_{out}$	Jones vectors [−]
$E_i, E_i', E_{in,i}$	Jones vector components ($i \in \{x, y\}$) [−]
$\underline{E}_1, \underline{E}_2, \underline{E}_1', \underline{E}_2'$	Jones vectors at the inputs and outputs of an interferometer [−]
E_{pulse}	energy in a single pulse [Ws]
E_{data}	energy of the data signal [Ws]
e	magnitude of electron charge [As]; also, Jones matrix element; also, base of natural logarithm
$F(x, y)$	transversal field distribution [−]
f	Jones matrix element
$f_{\text{pump}}, f_{\text{probe}}$	frequency RF-sources used in the pump-probe setup [s^{-1}]
G	gain for optical intensity; also, single-pass gain of an SOA [−]
G_c, G_a	gain for clock- (c) and anticlockwise (a) propagation through a SLALOM [−]
G_1, G_2	gain for both branches of an MZI [−]
g	optical gain coefficient [m^{-1}]; also, Jones matrix element
g_{cdp}, g_{ch}, g_{shb}	gain coefficients for carrier density pulsation, carrier heating and spectral hole burning [m^{-1}]
g_{st}	unsaturated gain coefficient [m^{-1}]
h	Planck's constant [J s]; also, Jones matrix element
$I, I(\underline{\mathbf{r}}, t)$	optical intensity [Wm^{-2}]; also, injection current [A]
i	imaginary operator ($i^2 = -1$); also, Jones matrix element; also, variable index
J	absolute value of the electric current density [Am^{-2}]
$\mathbf{J}, \mathbf{J}_{ij}$	Jones matrix and its matrix elements ($i, j \in \{x, y\}$)
$\mathbf{J}^{\sigma_x}$	Jones matrix representing a reflection at the y-z plane
$\mathbf{J}^C_{\lambda/2}, \mathbf{J}^A_{\lambda/2}$	Jones matrices for a half-wave plate
$\mathbf{J}^C, \mathbf{J}^A$	Jones matrices for clock- (C) and anticlockwise (A) propagation through a fiber loop
$\mathbf{J}^{(1)}, \mathbf{J}^{(2)}$	Jones matrices for the two branches of an MZI
$\mathbf{J}^{\text{cross}}, \mathbf{J}^{\text{bar}}$	Jones matrices for cross and bar coupling in a fiber coupler
$\mathbf{J}^{\text{trans}}_{\text{PBS}}, \mathbf{J}^{\text{ref}}_{\text{PBS}}$	Jones matrices for propagation through a polarizing beamsplitter
$\mathbf{J}^{\text{HiBi}}$	Jones matrix for a highly birefringent fiber
$\mathbf{J}^{\text{POL}}$	Jones matrix for a polarization filter
$\mathbf{J}^{\text{HNLF}}$	Jones matrix for a highly nonlinear fiber
$\underline{\mathbf{j}}$	electric current density [Am^{-2}]
j	Jones matrix element; also, variable index
$\mathcal{K}$	constant describing excess loss of couplers, etc.
$\underline{\mathbf{k}}$	wave vector [m^{-1}]
k_0	free-space wavenumber [m^{-1}]
k	Jones matrix element; also, variable index
$k, k^{(1)}, k^{(2)}, k_x, k_y, \ldots$	intensity coupling coefficient of a fiber coupler [−]
$L, L^{(1)}, L^{(2)}$	length or traveling distance [m]
L_{HiBi}	length of the HiBi fiber [m]
L_{SOA}	active region length of an SOA [m]
l	Jones matrix element; also, variable index
$\mathbf{M}$	Jones matrix
$\mathbf{M}_{KS}$	Jones matrix for the Kerr-switch

$\mathcal{M}_{Sagnac}, \mathcal{M}_{MZI}, \ldots$	transfer matrices for transmission through an interferometer, consisting of four Jones sub-matrices $\mathbf{M}_{(pq)}$ $(p, q \in \{1, 2\})$
m	Jones matrix element
N	carrier density $[\mathrm{m}^{-3}]$
N_0	carrier density at transparency (gain equal to zero) $[\mathrm{m}^{-3}]$
N_{st}	unsaturated carrier density (steady-state) $[\mathrm{m}^{-3}]$
n	order of nonlinearity, integer number; also, Jones matrix element; also, refractive index $[-]$
n_0	linear refractive index $[-]$
$\overline{n}_2, n_2$	nonlinear refractive index coefficients $[\mathrm{m}^2\mathrm{V}^{-2}\mathrm{s}^{-2}]$, $[\mathrm{m}^2\mathrm{W}^{-1}]$
n_b	background refractive index in an SOA $[-]$
n_g	group refractive index $[-]$
$n(\omega)$	refractive index at frequency ω $[-]$
$\underline{\mathbf{P}}, \underline{\mathbf{P}}(t)$	electric polarization density $[\mathrm{As\ m}^{-2}]$
$\underline{\widetilde{\mathbf{P}}}\,(\omega), \widetilde{P}_i(\omega)$	Fourier transform of the polarization density and its vector components $(i \in \{x, y, z\})$ $[\mathrm{As\ m}^{-2}\ \mathrm{s}]$
$\underline{\widetilde{\mathbf{P}}}^{(n)}(\omega)$	Fourier transform of nth-order polarization density $[\mathrm{As\ m}^{-2}\ \mathrm{s}]$
$P(t), P(z, t)$	optical power $[\mathrm{W}]$
$P_c(t), P_a(t)$	optical powers for the clock- (c) and anticlockwise (a) propagating pulses in the NOLM $[\mathrm{W}]$
$P_{pump}\,(t)$	optical power for the pump pulses in the NOLM $[\mathrm{W}]$
$P_{in}\,(t)$	optical power for the data pulses at the NOLM input $[\mathrm{W}]$
$P_{data}\,(t)$	optical power for the data signal $[\mathrm{W}]$
$P, P_{in}, P_{\mathrm{out}}, P_1, P_2$	average optical powers $[\mathrm{dBm}]$ or $[\mathrm{W}]$
P_{ctrl}	average control pulse power $[\mathrm{dBm}]$ or $[\mathrm{W}]$
P_{peak}	maximum optical power in a pulse (peak power) $[\mathrm{W}]$
p	Jones matrix element; also, variable index
q	variable index
R	power reflectivity coefficient or reflectance $[-]$
$\mathbf{R}(\Theta)$	coordinate transformation matrix for rotation by an angle Θ
$\mathbf{R}^{(n)}(\tau_1, \cdots, \tau_n)$	nth-order polarization response function $[\mathrm{s^{-n}m^{n-1}V^{1-n}}]$
$R(N)$	recombination rate in a semiconductor $[\mathrm{s}^{-1}\ \mathrm{m}^{-3}]$
R_{qq}	power reflectivity coefficient or reflectance $(q \in \{1, 2\})$ $[-]$
$R_{spon}, R_{stim}, R_{ASE}$	rate of spontaneous (spon) and stimulated (stim) recombinations and of recombinations stimulated by spontaneously emitted photons (ASE) $[\mathrm{s}^{-1}\ \mathrm{m}^{-3}]$
$\underline{\mathbf{r}}$	position vector $[\mathrm{m}]$
r_{st}	net rate of stimulated emission $[\mathrm{s}^{-1}]$
S	local photon density $[\mathrm{m}^{-3}]$
S_s	saturation photon density $[\mathrm{m}^{-3}]$
$s\,(t)$	pulse shape function $[\mathrm{W}]$
T	carrier temperature $[\mathrm{K}]$; also, power transmission coefficient or transmittance $[-]$
T_{int}, T_{exp}	intrinsic and measured (experimental) switching window $[-]$
T_{max}, T_{min}	maximum and minimum transmittance of an interferometer $[-]$
T_{pq}	power transmission coefficient or transmittance $(p, q \in \{1, 2\})$ $[-]$
t	time $[\mathrm{s}]$

t_0	temporal offset between two phase curves; also, temporal position of a switching window relative to the data pulses [s]
v_g	group velocity of a wave [m s^{-1}]
$v_{g,f}, v_{g,s}$	group velocities along fast and slow axis of a HiBi fiber [ms^{-1}]
x, y, z	position coordinates (Cartesian coordinates) [m]

Greek Symbols

α	absorption coefficient [m^{-1}]
$\alpha^{(1)}, \alpha^{(2)}$	absorption coefficients for the two branches of an MZI [m^{-1}]
α_w	absorption coefficient in SOAs by waveguide scattering [m^{-1}]
α_{fca}	absorption coefficient in SOAs by free carrier absorption [m^{-1}]
α_{int}	absorption coefficient in SOAs by internal waveguide loss [m^{-1}]
$\alpha_{cdp}, \alpha_{ch}, \alpha_{shb}$	linewidth enhancement factors for carrier density pulsation, carrier heating and spectral hole burning [–]
β	propagation constant [m^{-1}]
β_0	propagation constant at low optical power [m^{-1}]
γ	nonlinear coefficient [W^{-1}m^{-1}],
$\kappa, \kappa^{(1)}, \kappa^{(2)}$	field excess loss coefficient of a fiber coupler [–]
κ_{HiBi}	field loss coefficient of a HiBi fiber [–]
Γ	confinement factor [–]
$\delta(\,\cdot\,)$	delta function or impulse function
$\Delta\beta$	change of the propagation constant [m^{-1}]
$\Delta\tau$	temporal delay, e.g. between the optical pulses traveling through different branches of an interferometer [s]
$\Delta\Phi$	phase change induced in an optical wave by refractive index changes; also, phase difference between two optical waves [rad]
$\Delta\Phi_{max}$	maximum phase shift in an interferometer [rad]
$\Delta\omega_0$	spectral width of a quasi-monochromatic wave [rad/s]
Δd	difference in traveling distance in a two beam interferometer [m]
Δf	frequency difference [s^{-1}]
Δn	refractive index change, also refractive index difference in a two beam interferometer [–]
Δt	time difference or temporal delay, e.g. between two optical pulses [s]
Δt_{bit}	bit period, reciprocal of the TDM bit rate [s]
Δt_{out}	time period without one bit [s]
ε_0	electric permittivity of free space [AsV^{-1} m^{-1}]
$\epsilon_{ch}, \epsilon_{shb}$	nonlinear gain suppression factor by carrier heating and spectral hole burning [m^3]
$\theta, \theta_1, \theta_2$	angle [rad]
θ_{in}	angle between the y axis and the polarization direction of a linearly polarized wave at the input of an interferometer [rad]
$\lambda, \lambda_1, \lambda_2$	free-space wavelength [m]
λ_0	zero-dispersion wavelength of a fiber [m]
ν	frequency [s^{-1}]
ν_{rep}	repetition frequency of a periodic signal [s^{-1}]
ν_{base}	repetition frequency of a signal at the base data rate [s^{-1}]

ν_{line}	repetition frequency of a multiplexed signal [s^{-1}]
π	3.14159265358979323846264338327 95 . . . [rad]
ρ	charge density [$\mathrm{As\ m}^{-3}$]
σ	conductivity [$\mathrm{VA}^{-1}\ \mathrm{m}^{-1}$]
$\tau,\ \tau_1, \ldots, \tau_n$	time variable, also decay time of an exponential function [s]
τ_s	spontaneous carrier lifetime [s]
$\tau_{cdp},\ \tau_{ch},\ \tau_{shb}$	recovery time for carrier density pulsation, carrier heating and spectral hole burning [s]
τ_{FWHM}	full-width of an optical pulse or a switching window, measured at half maximum [s]
τ_{DGD}	differential group delay of a highly birefringent fiber [s]
Φ, Φ_1, Φ_2	phase variable [rad]
Φ_C, Φ_A	phase for the clockwise and anticlockwise traveling pulses in a Sagnac fiber loop [rad]
Φ_x, Φ_y	phase components along the x and y axis for an optical wave with arbitrary polarization state [rad]
$\Phi_0, \Phi_{0,add}, \Phi_{0,drop}$	static phase difference between interferometer branches [rad]
$\boldsymbol{\chi}^{(1)}$	first-order susceptibility tensor; in an isotropic medium its elements are given by $\chi^{(1)}_{\alpha\beta} = \chi^{(1)}\delta_{\alpha\beta}$ $(\alpha, \beta \in \{x, y, z\})$ [–]
$\boldsymbol{\chi}^{(2)}$	second-order susceptibility tensor [$\mathrm{s\ mV}^{-1}$]
$\boldsymbol{\chi}^{(3)}, \chi^{(3)}_{\alpha\beta\gamma\delta}$	third-order susceptibility tensor and its elements [$\mathrm{s}^2\mathrm{m}^2\mathrm{V}^{-2}$] $(\alpha, \beta, \gamma, \delta \in \{x, y, z\})$
$\boldsymbol{\chi}^{(n)}(-\omega_\sigma; \omega_{a1}, \ldots, \omega_{an})$	nth-order susceptibility tensor [$\mathrm{s}^{\mathrm{n}-1}\mathrm{m}^{\mathrm{n}-1}\mathrm{V}^{1-\mathrm{n}}$]
$\overline{\boldsymbol{\chi}}\ (\omega, \underline{\mathbf{E}})$	'field corrected' susceptibility [–]
$\overline{\chi}_0$	susceptibility in an SOA without external pumping [–]
$\overline{\chi}_p$	additional susceptibility in an SOA due to external pumping [–]
$\omega,\ \omega_1,\ \omega_2,\ \omega_{a1}, \ldots, \omega_{an}$	angular frequency [rad/s]
ω_σ	sum of frequencies, $\omega_{a1} + \cdots + \omega_{an}$ [rad/s]
ω_0	center angular frequency of a quasi-monochromatic wave [rad/s]

Mathematical Symbols

d	differential
∂	partial differential
∇	gradient operator
$\nabla\cdot$	divergence operator
$\nabla\times$	curl operator
∇^2	laplacian operator
$\Re\{\cdot\}$	real part of a complex number
$\Im\{\cdot\}$	imaginary part of a complex number
$\mathbb{R}$	real number
$\in$	element of
$\cdot\,\vert\,\cdot$	tensor product
$\langle\cdot\rangle$	time average
$\vert\cdot\vert^2$	absolute square
$\tilde{\cdot}$	complex quantity, not consistently used

$\cdot^*$	complex conjugate
$\cdot^{\mathrm{T}}$	transpose matrix
$\cdot^\dagger$	adjoint matrix, identical to the transpose of the complex conjugate matrix ($\cdot^\dagger = (\cdot^*)^{\mathrm{T}}$)
$\underline{\cdot}$	vector

Abbreviations

3R	re-timing, re-shaping, re-amplification
$\lambda/2$ plate	half-wave plate
$\lambda/4$ plate	quarter-wave plate
A/D	analogue-to-digital converter
ADM	add-drop multiplexer (time-domain)
AND	boolean AND operation
ASE	amplified spontaneous emission
ATN	attenuator (optical)
BER	bit error rate
birefr.	birefringent
BPF	band-pass filter
BW	bandwidth
CDP	carrier density pulsation
CH	carrier heating
circ.	circulator (optical)
conv.	conventional
CW	continuous wave
DCF	dispersion-compensating fiber
DEMUX	demultiplexer (time-domain)
DGD	differential group delay
DIC	delayed interference configuration
EAM	electro-absorption modulator
EDFA	erbium-doped fiber amplifier
ETDM	electrical time division multiplexing
ETH	Eidgenössische Technische Hochschule
FP-SOA	Fabry-Perot semiconductor optical amplifier
FWHM	full width at half maximum
FWM	four-wave mixing
GT	gain-transparent
HHI	Heinrich-Hertz Institut
HiBi	highly birefringent
HNL-DSF	highly nonlinear dispersion shifted fiber
HNLF	highly nonlinear fiber
HP	Hewlett Packard
ICR	integrated contrast ratio
InGaAsP	indium gallium arsenide phosphide
InP	indium phosphide
$LiNbO_3$	lithium niobium trioxide (lithium niobate)

MI	Michelson interferometer
MOD	amplitude modulator
MQW	multiple quantum-well
MUX	multiplexer (time-domain)
MZI	Mach-Zehnder Interferometer
NOLM	nonlinear optical loop mirror
NRZ	non-return to zero
O/E	opto-electric conversion
OD	optical delay line
OSA	optical spectrum analyzer
OTDM	optical time division multiplexing
PBS	polarizing beamsplitter
PC	polarization controller
PD	photo diode
PD-EAM	photo diode electro-absorption modulator
PDL	polarization dependent loss
PD-MZI	polarization discriminating Mach-Zehnder Interferometer
PMD	polarization mode dispersion = HiBi fiber
PMF	polarization maintaining fiber
POL	polarization filter (polarizer)
ppLiNbO$_3$	periodically poled lithium niobate
PRBS	pseudo-random bit sequence
RF	radio frequency
RZ	return to zero
SHB	spectral hole burning
SHG	second-harmonic generation
SI	Sagnac Interferometer
SLALOM	semiconductor laser amplifier in a loop mirror
SMF	single-mode fiber
SOA	semiconductor optical amplifier
SPM	self-phase modulation
TDM	time division multiplexing
TMLL	tunable mode-locked laser
TW-SOA	traveling-wave semiconductor optical amplifier
UNI	ultrafast-nonlinear interferometer
WDM	wavelength-division multiplexing
XAM	cross-absorption modulation
XGM	cross-gain modulation
XOR	boolean XOR operation
XPM	cross-phase modulation

Appendix C

Publications by the Author

Journal Articles

1. R. Ludwig, U. Feiste, S. Diez, C. Schubert, C. Schmidt, H. J. Ehrke, and H. G. Weber, "Unrepeatered 160 Gbit/s RZ single-channel transmission over 160 km of standard fiber at 1.55 μm with hybrid MZI optical demultiplexer," *Electron. Lett.*, vol. 36, no. 16, pp. 1405–1406, July 2000.

2. S. Diez, C. Schubert, R. Ludwig, H. J. Ehrke, U. Feiste, C. Schmidt, and H. G. Weber, "160 Gbit/s all-optical demultiplexer using hybrid gain-transparent SOA Mach-Zehnder interferometer," *Electron. Lett.*, vol. 36, no. 17, pp. 1484–1486, August 2000.

3. G. Toptchiyski, S. Randel, K. Petermann, S. Diez, E. Hilliger, C. Schmidt, C. Schubert, R. Ludwig, and H. G. Weber, "Analysis of switching windows in a gain-transparent-SLALOM configuration," *J. Lightwave Technol.*, vol. 18, no. 12, pp. 2188–2195, October 2000.

4. S. Diez, E. Hilliger, M. Kroh, C. Schmidt, C. Schubert, H. G. Weber, L. Occhi, L. Schares, G. Guekos, and L. K. Oxenløwe, "Optimization of SOA-based Sagnac-Interferometer switches for demultiplexing to 10 and 40 Gb/s," *Opt. Commun.*, vol. 189, no. 4-6, pp. 241–249, March 2001.

5. U. Feiste, R. Ludwig, C. Schubert, J. Berger, C. Schmidt, H. G. Weber, A. Munk, B. Schmauss, B. Buchhold, D. Briggmann, F. Kueppers, and F. Rumpf, "160 Gbit/s transmission over 116 km field-installed fiber using 160 Gbit/s OTDM and 40 Gbit/s ETDM," *Electron. Lett.*, vol. 37, no. 7, pp. 443–445, March 2001.

6. T. Yamamoto, L. Oxenløwe, C. Schmidt, C. Schubert, E. Hilliger, U. Feiste, J. Berger, R. Ludwig, and H. G. Weber, "Clock recovery from 160 Gbit/s data signals using phase-locked loop with interferometric optical switch based on semiconductor optical amplifier," *Electron. Lett.*, vol. 37, no. 8, pp. 509–510, April 2001.

7. C. Schubert, S. Diez, J. Berger, R. Ludwig, U. Feiste, H. G. Weber, G. Toptchiyski, K. Petermann, and V. Krajinovic, "160 Gb/s all-optical demultiplexing using a gain-transparent Ultrafast-Nonlinear Interferometer (GT-UNI)," *IEEE Photon. Technol. Lett.*, vol. 13, no. 5, pp. 475–477, May 2001.

8. M. Gunkel, F. Küppers, J. Berger, U. Feiste, R. Ludwig, C. Schubert, C. Schmidt, and H. G. Weber, "Unrepeatered 40 Gbit/s RZ transmission over 252 km SMF using Raman amplification," *Electron. Lett.*, vol. 37, no. 10, pp. 646–648, May 2001.

9. U. Feiste, R. Ludwig, C. Schubert, J. Berger, C. Schmidt, H. G. Weber, B. Schmauss, A. Munk, B. Buchhold, D. Briggmann, F. Kueppers, and F. Rumpf, "160 Gbit/s field transmission over 116 km standard single mode fibre using 160 Gbit/s OTDM and 40 Gbit/s ETDM demultiplexer," *Proc.-Optoelectron.*, vol. 148, no. 4, pp. 171–175, August 2001.

10. C. Schubert, J. Berger, U. Feiste, R. Ludwig, C. Schmidt, and H. G. Weber, "160 Gb/s polarization insensitive all-optical demultiplexing using a gain-transparent Ultrafast-Nonlinear Interferometer (GT-UNI)," *IEEE Photon. Technol. Lett.*, vol. 13, no. 11, pp. 1200–1202, November 2001.

11. C. Weinert, J. Berger, U. Feiste, E. Hilliger, B. Konrad, M. Kroh, R. Ludwig, K. Petermann, C. Schmidt, C. Schubert, H. G. Weber, and T. Yamamoto, "High bit rate OTDM-transmission on standard fibre," *Int. J. Electron. Commun.*, vol. 55, no. 5, pp. 349–353, 2001.

12. C. Schubert, J. Berger, S. Diez, H. J. Ehrke, R. Ludwig, U. Feiste, C. Schmidt, H. G. Weber, G. Toptchiyski, S. Randel, and K. Petermann, "Comparison of interferometric all-optical switches for demultiplexing applications in high-speed OTDM systems," *J. Lightwave Technol.*, vol. 20, no. 4, pp. 618–624, April 2002.

13. G. Toptchiyski, S. Randel, K. Petermann, C. Schubert, J. Berger, and H. G. Weber, "Characterization of switching windows of an 160 Gb/s all-optical demultiplexer with data base rates of 10 and 40 Gb/s," *IEEE Photon. Technol. Lett.*, vol. 14, no. 4, pp. 534–536, April 2002.

14. C. Schubert, R. Ludwig, S. Watanabe, F. Futami, C. Schmidt, J. Berger, C. Börner, S. Ferber, and H. G. Weber, "160 Gbit/s wavelength converter with 3R-regenerating capability," *Electron. Lett.*, vol. 38, no. 16, pp. 903–904, August 2002.

15. C. Schubert, C. Schmidt, S. Ferber, R. Ludwig, and H. G. Weber, "Error-free all-optical add-drop multiplexing at 160 Gbit/s," *Electron. Lett.*, vol. 39, no. 14, pp. 1074–1076, July 2003.

16. C. Börner, C. Schubert, C. Schmidt, E. Hilliger, V. Marembert, J. Berger, S. Ferber, E. Dietrich, R. Ludwig, B. Schmauss, and H. G. Weber, "160 Gbit/s clock recovery with electro-optical PLL using a bidirectionally operated electroabsorption modulator as phase comparator," *Electron. Lett.*, vol. 39, no. 14, pp. 1071–1073, July 2003.

17. A. Beling, H.-G. Bach, D. Schmidt, G. G. Mekonnen, R. Ludwig, S. Ferber, C. Schubert, C. Börner, B. Schmauss, J. Berger, C. Schmidt, U. Troppenz, and H. G. Weber, "Monolithically integrated balanced photodetector and its application in OTDM 160 Gbit/s DPSK transmission," *Electron. Lett.*, vol. 39, no. 16, pp. 1204–1205, August 2003.

18. S. Ferber, R. Ludwig, C. Börner, A. Wietfeld, B. Schmauss, J. Berger, C. Schubert, G. Unterboersch, and H. G. Weber, "Comparison of DPSK and OOK modulation format in a 160 Gb/s transmission system," *Electron. Lett.*, vol. 39, no. 20, pp. 1458–1459, October 2003.

19. L. Schares, C. Schubert, C. Schmidt, H. G. Weber, L. Occhi, and G. Guekos, "Phase dynamics of semiconductor optical amplifiers at 10 to 40 GHz," *IEEE J. Quantum Electron.*, vol. 39, no. 11, pp. 1394–1408, November 2003.

Conference Contributions

1. S. Diez, C. Schubert, R. Ludwig, H.-J. Ehrke, U. Feiste, C. Schmidt, and H. G. Weber, "160 Gb/s all-optical demultiplexer using a hybrid gain-transparent SOA Mach-Zehnder-Interferometer," in *Techn. Dig. of Optical Amplifiers and their Applications, OAA'00*, Quebec, Canada, July 2000, pp. 195–197, paper OWB6.

2. S. Diez, C. Schubert, U. Feiste, R. Ludwig, J. Berger, and H. G. Weber, "160 Gb/s all-optical demultiplexing using a gain-transparent Ultrafast-Nonlinear Interferometer," in *Techn. Dig. of Optical Amplifiers and their Applications, OAA'00*, Quebec, Canada, July 2000, post-deadline paper PD9.

3. R. Ludwig, U. Feiste, S. Diez, C. Schubert, C. Schmidt, and H. G. Weber, "Towards the all-optical 3R regenerator: Present status and challenges," in *Techn. Dig. of Optoelectronics and Commun. Conf., OECC'00*, Chiba, Japan, July 2000, pp. 560–561, paper 14D1.

4. R. Ludwig, U. Feiste, S. Diez, C. Schubert, C. Schmidt, H. J. Ehrke, and H. G. Weber, "Unrepeatered 160 Gbit/s RZ single channel transmission over 160 km of standard fiber at 1.55 μm with hybrid MZI optical DEMUX," in *Proc. 26th Europ. Conf. Opt. Commun., ECOC'00*, Munich, Germany, September 2000, pp. 135–136, paper 6.1.3.

5. U. Feiste, R. Ludwig, C. Schubert, J. Berger, S. Diez, C. Schmidt, H. G. Weber, A. Munk, and B. Schmauss, "160 Gbit/s transmission using 160 to 40 Gbit/s OTDM and 40 to 10 Gbit/s ETDM DEMUX-techniques," in *Proc. 26th Europ. Conf. Opt. Commun., ECOC'00*, Munich, Germany, September 2000, post-deadline paper PD 1.10.

6. M. Gunkel, F. Küppers, J. Berger, U. Feiste, R. Ludwig, C. Schubert, C. Schmidt, and H. G. Weber, "40 Gbit/s RZ unrepeatered transmission over 252 km SMF using Raman amplification," in *Proc. Optical Fiber Commun. Conf., OFC'01*, Anaheim, USA, March 2001, paper TuU3.

7. U. Feiste, R. Ludwig, C. Schubert, J. Berger, C. Schmidt, H. G. Weber, A. Munk, B. Schmauss, B. Buchhold, D. Briggmann, F. Kueppers, and F. Rumpf, "160 Gbit/s transmission over 116 km field-installed fiber using 160 Gbit/s OTDM and 40 Gbit/s ETDM," in *Proc. Optical Fiber Commun. Conf., OFC'01*, Anaheim, USA, March 2001, paper ThF3.

8. G. Toptchiyski, S. Randel, K. Petermann, C. Schubert, J. Berger, and H. G. Weber, "Comparison of switching windows of an all-optical 160 Gbit/s demultiplexer with base data rates of 10 Gbit/s and 40 Gbit/s," in *Proc. Optical Fiber Commun. Conf., OFC'01*, Anaheim, USA, March 2001, paper MB5.

9. H. Rosenfeldt, C. Knothe, R. Ulrich, E. Brinkmeyer, U. Feiste, C. Schubert, J. Berger, R. Ludwig, H. G. Weber, and A. Ehrhardt, "Automatic PMD compensation at 40 Gbit/s and 80 Gbit/s using a 3-dimensional DOP evaluation for feedback," in *Proc. Optical Fiber Commun. Conf., OFC'01*, Anaheim, USA, March 2001, post-deadline paper PD27.

10. C. Schubert, J. Berger, E. Hilliger, H. G. Weber, G. Toptchiyski, S. Randel, and K. Petermann, "All-optical switching using gain-transparent Semiconductor Optical Amplifiers," in *Techn. Dig. of Nonlinear Guided Waves and their Applications, NLGW'01*, Washington DC, USA, March 2001, pp. 23–25, paper MB2.

11. H. G. Weber, R. Ludwig, U. Feiste, C. Schmidt, E. Hilliger, C. Schubert, J. Berger, M. Kroh, and T. Yamamoto, "Optical signal processing for high speed communication systems," in *Proc. 10th Europ. Conf. on Integrated Optics, ECIO'01*, Paderborn, Germany, April 2001, pp. 147–152, paper THP1.2.

12. T. Tekin, M. Schlak, W. Brinker, J. Berger, C. Schubert, B. Maul, and R. Molt, "All-optical demultiplexing using monolithically integrated Mach-Zehnder interferometer based on band gap shifted semiconductor optical amplifier," in *Proc. 10th Europ. Conf. on Integrated Optics, ECIO'01*, Paderborn, Germany, April 2001, post-deadline paper.

13. L. Oxenløwe, C. Schubert, C. Schmidt, E. Hilliger, J. Berger, U. Feiste, R. Ludwig, and H. G. Weber, "Optical clock recovery employing an optical PLL using cross-phase modulation in a Sagnac-interferometer," in *Techn. Dig. of Conf. on Lasers and Electro-Optics, CLEO'01*, Baltimore, USA, May 2001, pp. 525–526, paper CThU2.

14. T. Yamamoto, C. Schubert, C. Schmidt, L. Oxenløwe, U. Feiste, and H. G. Weber, "A semiconductor laser amplifier in a loop mirror as a phase comparator in PLL-based clock recovery for 160 Gb/s data signals," in *Techn. Dig. of Optical Amplifiers and their Applications, OAA'01*, Stresa, Italy, July 2001, paper OTuC2.

15. C. Schubert, J. Berger, U. Feiste, R. Ludwig, C. Schmidt, and H. G. Weber, "160 Gb/s polarization insensitive all-optical demultiplexing using a gain-transparent Ultrafast-Nonlinear Interferometer (GT-UNI)," in *Techn. Dig. of Optical Amplifiers and their Applications, OAA'01*, Stresa, Italy, July 2001, paper OWA4.

16. R. Ludwig, A. Sizmann, U. Feiste, C. Schubert, M. Kroh, C. M. Weinert, and H. G. Weber, "Experimental verification of noise squeezing by an optical intensity filter in high-speed transmission," in *Proc. 27th Europ. Conf. Opt. Commun., ECOC'01*, Amsterdam, The Netherlands, September 2001, pp. 178–179, paper Tu.B.2.7.

17. T. Yamamoto, U. Feiste, J. Berger, C. Schubert, C. Schmidt, R. Ludwig, and H. G. Weber, "160 Gbit/s demultiplexer with clock recovery using SOA-based interferometric switches and its application to 120 km fiber transmission," in *Proc. 27th Europ. Conf. Opt. Commun., ECOC'01*, Amsterdam, The Netherlands, September 2001, pp. 192–193, paper Tu.L.2.6.

18. T. Tekin, M. Schlak, W. Brinker, J. Berger, C. Schubert, B. Maul and R. Molt, "Ultrafast all-optical demultiplexing performance of monolithically integrated band gap shifted Mach-Zehnder interferometer," in *Proc. 27th Europ. Conf. Opt. Commun., ECOC'01*, Amsterdam, The Netherlands, September 2001, pp. 504–505, paper Th.F.1.3.

19. T. Yamamoto, C. Schmidt, E. Dietrich, C. Schubert, J. Berger, R. Ludwig, and H. G. Weber, "40 GHz optical clock extraction from 160 Gbit/s data signals using PLL-based clock recovery," in *Proc. Optical Fiber Commun. Conf., OFC'02*, Anaheim, USA, March 2002, pp. 86–87, paper TuN5.

20. C. Schmidt, F. Futami, S. Watanabe, T. Yamamoto, C. Schubert, J. Berger, M. Kroh, H. J. Ehrke, E. Dietrich, C. Börner, R. Ludwig, and H. G. Weber, "Complete optical sampling system with broad gap-free spectral range for 160 Gbit/s and 320 Gbit/s and its application in a transmission system," in *Proc. Optical Fiber Commun. Conf., OFC'02*, Anaheim, USA, March 2002, pp. 528–530, paper ThU1.

21. R. Ludwig, U. Feiste, C. Schmidt, C. Schubert, J. Berger, E. Hilliger, M. Kroh, T. Yamamoto, C. M. Weinert, and H. G. Weber, "Enabling transmission at 160 Gbit/s," in *Proc. Optical Fiber Commun. Conf., OFC'02*, Anaheim, USA, March 2002, pp. 1–2, paper TuA1.

22. E. Hilliger, V. Marembert, C. Schubert, H. G. Weber, K. Yvind, and J. Hanberg, "Improved electroabsorption demultiplexer by tandem-arrangement with semiconductor optical amplifier," in *Proc. Optical Fiber Commun. Conf., OFC'02*, Anaheim, USA, March 2002, pp. 742–743, poster ThGG92.

23. T. Yamamoto, C. Schmidt, E. Dietrich, C. Schubert, J. Berger, R. Ludwig, and H. G. Weber, "40 GHz optical clock extraction from 160 Gbit/s data signals using PLL-based clock recovery," in *Proc. 2002 IEICE General Conference*, Tokyo, Japan, March 2002, p. 609, paper B-10-172.

24. C. Schmidt, C. Schubert, J. Berger, M. Kroh, H. Ehrke, E. Dietrich, C. Börner, R. Luwig, H. G. Weber, F. Futami, S. Watanabe, and T. Yamamoto, "Optical Q-factor monitoring at 160 Gb/s using an optical sampling system in an 80 km transmission experiment," in *Techn. Dig. of Conf. on Lasers and Electro-Optics, CLEO'02*, Washington DC, USA, May 2002, pp. 579–580, paper CThU3.

25. H. G. Weber, R. Ludwig, U. Feiste, C. Schmidt, C. Schubert, J. Berger, E. Hilliger, M. Kroh, and T. Yamamoto, "High-speed all-optical signal processing in optical communications systems," in *Techn. Dig. of Conf. on Lasers and Electro-Optics, CLEO'02*, Washington DC, USA, May 2002, p. 610, paper CThAA3.

26. T. Tekin, H. Ehlers, M. Schlak, J. Berger, C. Schubert, B. Maul, and R. Ziegler, "All-optical demultiplexing performance of monolithically integrated GS-MZI module," in *Intern. Workshop on Optical MEMS and Integrated Optics*, Dortmund, Germany, June 2001.

27. T. Tekin, C. Schubert, J. Berger, M. Schlak, B. Mau, W. Brinker, R. Molt, H. Ehlers, M. Gravert, and H.-P. Nolting , "160 Gbit/s error-free all-optical demultiplexing using monolithically integrated band gap shifted Mach-Zehnder Interferometer (GS-MZI)," in *Techn. Dig. of Conf. on Integrated Photonics Research, IPR'02*, Vancouver, Canada, July 2002, paper IWC4.

28. T. Tekin, C. Schubert, J. Berger, M. Schlak, B. Maul, W. Brinker, R. Molt, and H. Ehlers, "160 Gbit/s error-free all-optical demultiplexing using monolithically integrated band gap shifted Mach-Zehnder Interferometer," in *International Congress for Optics XIX: Optics for the Quality of Life*, Firenze, Italy, August 2002, pp. 605–606.

29. C. M. Weinert, A. Sizmann, R. Ludwig, C. Schubert, U. Feiste, and H. G. Weber, "Nonlinear optical intensity filters: Experiment and Design," in *Proc. 27th Europ. Conf. Opt. Commun., ECOC'01*, Amsterdam, The Netherlands, September 2001, pp. 274–275, paper We.L.1.4.

30. H. Rosenfeldt, R. Ulrich, E. Brinkmeyer, U. Feiste, C. Schubert, J. Berger, R. Ludwig, H. G. Weber, and A. Ehrhardt, "Feed-forward approach for automatic PMD compensation at 80 Gbit/s over 45 km installed single mode fiber," in *Proc. 27th Europ. Conf. Opt. Commun., ECOC'01*, Amsterdam, The Netherlands, September 2001, post-deadline paper PD.B.1.1.

31. A. Melo, G. Toptchiyski, K. Petermann, and C. Schubert, "Crosstalk analysis of longer SOAs for demultiplexing to the base data rate of 10 Gbit/s and 40 Gbit/s," in *Tech. Dig. of IEEE Summer Topical Meeting 2002*, Mont Tremblant, Canada, July 2002, pp. 11–12, paper TuC2.

32. R. Ludwig, C. Schubert, S. Watanabe, F. Futami, C. Schmidt, J. Berger, C. Börner, S. Ferber, and H.G. Weber, "160 Gb/s 3R-regenerating wavelength converter," in *Techn. Dig. of Optoelectronics and Commun. Conf., OECC'02*, Yokohama, Japan, July 2002, post-deadline Paper PD-1-3.

33. R. Ludwig, C. Schmidt, C. Schubert, J. Berger, E. Hilliger, M. Kroh, V. Marembert, C. Börner, S. Ferber, H. J. Ehrke, and H.G. Weber, "Technologies for 160 Gbit/s transmission systems," in *Techn. Dig. of Optoelectronics and Commun. Conf., OECC'02*, Yokohama, Japan, July 2002, pp. 18–19, paper 9B1-1.

34. C. Schubert, C. Schmidt, C. Börner, E. Dietrich, S. Ferber, R. Ludwig, and H. G. Weber, "A Gain-Transparent Ultrafast-Nonlinear Interferometer (GT-UNI) in a 160 Gb/s optical sampling system," in *Techn. Dig. of Optical Amplifiers and their Applications, OAA'02*, Vancouver, Canada, July 2002, paper OTuD5.

35. H. G. Weber, R. Ludwig, C. Schmidt, C. Schubert, J. Berger, E. Hilliger, M. Kroh, V. Marembert, C. Börner, S. Ferber, and H. J. Ehrke, "160 Gbit/s TDM-transmission technology," in *Proc. 28th Europ. Conf. Opt. Commun., ECOC'02*, Copenhagen, Denmark, September 2002, paper 2.1.1.

36. C. Schubert, R. Ludwig, S. Watanabe, F. Futami, S. Ferber, J. Berger, C. Schmidt, and H. G. Weber, "Improved performance of a 160 Gb/s fibre based all-optical switch using rectangular gating pulses," in *Proc. 28th Europ. Conf. Opt. Commun., ECOC'02*, Copenhagen, Denmark, September 2002, paper 8.3.7.

37. C. Schmidt, C. Schubert, S. Watanabe, F. Futami, R. Ludwig, and H. G. Weber, "320 Gb/s all-optical eye diagram sampling using Gain-Transparent Ultrafast Nonlinear Interferometer (GT-UNI)," in *Proc. 28th Europ. Conf. Opt. Commun., ECOC'02*, Copenhagen, Denmark, September 2002, paper 2.1.3.

38. A. Melo, G. Toptchiyski, K. Petermann, and C. Schubert, "Analysis of add/drop multiplexing at 160 Gbit/s to base data rates of 10 Gbit/s and 40 Gbit/s," in *Proc. 28th Europ. Conf. Opt. Commun., ECOC'02*, Copenhagen, Denmark, September 2002, paper 11.4.3.

39. F. Buchali, H. Blow, W. Baumert, M. Schmidt, K. Schuh, E. Lach, E. Corbel, J. Berger, R. Ludwig, C. Schubert, and H. G. Weber, "Adaptive PMD compensation in a 160 Gb/s RZ transmission system using eye monitor feedback," in *Proc. 28th Europ. Conf. Opt. Commun., ECOC'02*, Copenhagen, Denmark, September 2002, paper 7.1.3.

40. C. Börner, C. Schubert, C. Schmidt, E. Hilliger, V. Marembert, J. Berger, S. Ferber, E. Dietrich, R. Ludwig, B. Schmauss, and H. G. Weber, "160Gbit/s clock recovery with electro-optical PLL using a bidirectionally operated electroabsorption modulator as phase comparator," in *Proc. Optical Fiber Commun. Conf., OFC'03*, Atlanta, USA, March 2003, pp. 670–671, paper FF3.

41. C. Schubert, C. Schmidt, S. Ferber, R. Ludwig, and H. G. Weber, "Error-free all-optical add-drop multiplexing at 160 Gbit/s," in *Proc. Optical Fiber Commun. Conf., OFC'03*, Atlanta, USA, March 2003, post-deadline paper PD17.

42. S. Watanabe, F. Futami, R. Okabe, Y. Takita, S. Ferber, R. Ludwig, C. Schubert, C. Schmidt, and H. G. Weber, "160 Gbit/s optical 3R-regenerator in a fiber transmission experiment," in *Proc. Optical Fiber Commun. Conf., OFC'03*, Atlanta, USA, March 2003, post-deadline paper PD16.

43. A. Beling, H.-G. Bach, D. Schmidt, G. Mekonnen, R. Ludwig, S. Ferber, C. Schubert, C. Börner, J. Berger, C. Schmidt, U. Troppenz, and H. G. Weber, "Monolithically integrated balanced photodetector and its application in OTDM 160 Gbit/s DPSK transmission," in *Techn. Dig. of Conf. on Integrated Photonics Research, IPR'03*, Washington DC, USA, June 2003, post-deadline paper PDP-4.

44. R. Ludwig, S. Ferber, C. Schubert, C. Börner, A. Beling, H.-G. Bach, B. Schmauss, A. Wietfeld, J. Berger, C. Schmidt, and H. G. Weber, "160 Gbit/s DPSK transmission over 410 km dispersion-managed fiber," in *Proc. 8th European Conference on Networks & Optical Communications*, Vienna, Austria, July 2003, pp. 14–19.

45. S. Ferber, R. Ludwig, C. Börner, A. Wietfeld, B. Schmauss, J. Berger, C. Schubert, G. Unterboersch, and H. G. Weber, "Comparison of DPSK and OOK modulation format in a 160 Gb/s transmission system," in *Proc. 29th Europ. Conf. Opt. Commun., ECOC'03*, Rimini, Italy, September 2003, pp. 1004–1005, paper Th2.6.2.

46. A. Melo, K. Petermann, and C. Schubert, "Frequency vs. Time-domain Amplified Spontaneous Emission (ASE) noise modeling of Semiconductor Optical Amplifiers (SOAs)," in *CLEO/Europe-EQEC Conference*, Munich, Germany, June 2003, poster EA1T.

47. C. Schmidt, C. Schubert, C. Börner, C. M. Weinert, H. Bülow, E. Lach, and H. G. Weber, "Investigation of intra-channel four-wave mixing at 160 Gb/s using an optical sampling system," in *Proc. 29th Europ. Conf. Opt. Commun., ECOC'03*, Rimini, Italy, September 2003, pp. 990–991, paper Th2.5.2.

48. C. Schubert, L. Schares, C. Schmidt, G. Guekos, and H. G. Weber, "Phase dynamics in gain-transparent Semiconductor Optical Amplifiers," in *Proc. 29th Europ. Conf. Opt. Commun., ECOC'03*, Rimini, Italy, September 2003, pp. 1062–1063, paper Th3.5.2.

Appendix D

Acknowledgements

First of all, I would like to thank my supervisors, Prof. Dr. Hans-Joachim Eichler of the Technical University Berlin (TU) and Prof. Dr. Hans-Georg Weber of the Fraunhofer Institute for Telecommunications, Heinrich-Hertz-Institut (HHI), for granting me the opportunity to work on the topic of this dissertation. During my work at HHI, Prof. Weber provided me any support possible and has always been open for discussions and problems, both during the time of the experiments and during the writing of the thesis.

I would like to thank Carsten Schmidt-Langhorst and Dr. Reinhold Ludwig for many productive hours in the lab and inspiring discussions. I would also like to thank all my other colleagues at HHI for their great support, especially the former and present members of the OTDM-group, Dr. Uwe Feiste, Dr. Stefan Diez, Christof Börner, Sebastian Ferber, Vincent Marembert, Hans-Jürgen Ehrke, Lothar Küller, Dr. Enno Hilliger, Dr. Jörn Berger, Marcel Kroh, Erik Dietrich and Herbert Knupke. I am indebted to Dr. Stefan Diez for his great support and guidance during the first part of my thesis and to Andreas Hermerschmidt (TU Berlin) for many fruitful discussions.

During the work on my thesis, I was fortunate to collaborate with a number of researchers from other groups and I would like to thank in particular Prof. Dr. Klaus Petermann, Dr. Gueorgui Toptchiyski and Alessandro Melo of the Technical University Berlin (Germany), Laurent Schares of the ETH Zürich (Switzerland), Dr. Leif Oxenløwe of the Research Center COM (Denmark), Harald Rosenfeld of Adaptif Photonics (formerly with Technical University Hamburg-Harburg, Germany) and Prof. Dr.-Ing. Bernhard Schmauss of the Fachhochschule Regensburg, University of Applied Sciences (formerly with Lucent Technologies Nürnberg, Germany).

I very much appreciate the collaboration with Dr. Shigeki Watanabe and Dr. Fumio Futami from Fujitsu Laboratories in Japan and I am especially grateful that I had the opportunity to visit them for a joint experiment in Japan. I spend a work-filled, nevertheless wonderful time there, thanks to their kindness and support. I also would like to thank Tsuyoshi Yamamoto from Fujitsu Laboratories, who was a research fellow in our group for one year, for his support and an impressive view on Mount Fuji.

Furthermore, I would like to express my thanks to Dr. Ronald Kaiser (HHI), Carsten Schmidt-Langhorst, Christof Börner, Dr. Stefan Diez and Andreas Hermerschmidt for reading parts of the manuscript, as well as to Prof. Dr. Gebhard von Oppen (TU Berlin) for his willingness to chair the examination committee.

Last, but not least I wish to thank my parents and my brother Martin Schubert for their everlasting support and in particular my wife Carola for her love, understanding, and patience, especially during the final year of my thesis.

Appendix E

Curriculum Vitae

Name:	Colja Schubert
Date of birth:	17. May 1973
Place of birth:	Berlin, Germany
Citizenship:	German
Marital Status:	married to Dr. Carola Schubert since 2003

Education and Professional Experience

School	Sep. 1979 - Aug. 1985	Primary School: 'Schlüter Grundschule' in Berlin-Charlottenburg
	Sep. 1985 - June 1992	Secondary School: 'Sophie-Charlotte-Oberschule (Gymnasium)', Degree: 'Abitur' (A-levels)
University	Oct. 1992 - Nov. 1998	Study of Physics at the Technical University of Berlin, Degree: Diploma in Physics
	Sep. 1996 - Mar. 1997	*Project at the University of Strathclyde in Glasgow, United Kingdom in the field of high-resolution molecular spectroscopy*
	Oct. 1997 - Sep. 1998	*Diploma thesis work at the Max-Born-Institute for Nonlinear Optics and Short Pulse Spectroscopy. Topic: Time and space resolved detection of metastable Helium atoms*
Community Service	Dec. 1998 - Dec. 1999	at 'Heilpädagogisches Zentrum Berlin-Kladow' for mentally handicapped people
Heinrich-Hertz -Institut	Jan. 2000 - present	Scientist at the Fraunhofer Institute for Telecommunications, Heinrich-Hertz-Institut in the group of Prof. H. G. Weber and work towards Ph.D. Research area: Interferometric all-optical switches and high bit rate transmission